

**Femtosecond Time-Resolved Spectroscopy
of Anionic Systems:
Dynamics of Mesoscopic Solvation and
Gas-Phase Organic Reactions**

Thesis by
Daniel Hern Paik

*In Partial Fulfillment of the Requirements
for the Degree of
Doctor of Philosophy*

California Institute of Technology
Pasadena, California
2004

(submitted May 13, 2004)

© 2004
Daniel Hern Paik
All rights reserved

To My Parents

Acknowledgments

I wish to express the deepest gratitude to my adviser, Professor Ahmed Zewail, for his patient guidance throughout my graduate studies. I have learned invaluable lessons from many stimulating discussions with Professor Zewail. It has been a truly honorable experience to witness his scientific intuition on a personal level.

I have been privileged to work with a number of outstanding scientists. First, I must acknowledge the immense contributions by Dr. Thorsten Bernhardt in the initial stage of the anion project. All the detailed outlines for the experiment were blueprinted by Dr. Bernhardt. He is one of the most modest scientists that I've known. I will never forget that exhilarating moment when we obtained our first time-dependent signal.

I'd like to thank Dr. Nam Joon Kim for his collaboration. Many challenging experiments continued thanks to his persistent effort and determination. I also extend my gratitude to two dedicated graduate students, Ding-Shuye Yang and I-Ren Lee who have provided tremendous help in the recent work. I wish the very best as they embark on their own graduate studies. I also extend my gratitude to the members in the Zewail Group. I would especially like to thank Dr. Spencer Baskin for his valuable input on the rotational coherence and hydrated electron studies.

I would like to note special thanks to some of staff members in the Department of Chemistry at Caltech. I thank Mr. Mike Roy, Mr. Ray Garcia and Mr. Guy Duremberg in the chemistry machine shop for their technical support. Similarly, Mr. Tom Dunn at the electric shop deserves heartfelt acknowledgment for his assistance. I'd also like to thank Ms. Dian Buchness for her sincerity and friendship.

Finally, I express my sincere gratitude to my parents for their blessing.

Abstract

This thesis work presents the femtosecond time-resolved spectroscopy of anionic systems ranging from gas-phase organic molecules to the finite-sized molecular clusters. The subject matter in this thesis is twofold: Mesoscopic solvation of anionic clusters and transition state dynamics of neutral organic molecules.

Solvation dynamics in the finite sized clusters were investigated at the molecular level of details. The main objective of the cluster study was to follow the evolution of cluster properties as function of cluster size. Ultrafast processes exhibited in the cluster systems were investigated by utilizing the femtosecond time-resolved anion photoelectron spectroscopy. The bond rupture and solvent evaporation of homogeneous and heterogeneous clusters were studied, and the correlation between the dissociation rates and the cluster size is obtained. Gas-phase analogues of solvated systems were studied, and the key steps involved in the solvation dynamics are highlighted.

Direct probing of the transition state dynamics in the ground state is studied with femtosecond time resolution. The transition state of the ring inversion reaction of cyclooctatetraene was directly accessed by the vertical detachment from the planar anion. The subsequent nuclear motion was then probed by ionization mass spectrometry. The oscillatory feature observed in the transients reflects trajectories of motion (resonance) along the reaction coordinate, and comparison with theory is reported. This work demonstrated the applicability of the charge reversal scheme to a complex organic system and suggests the possibility of studying ground-state thermal organic reactions with their transition states resolved in real time.

Table of Contents

Acknowledgments	iv
Abstract	v
Table of Contents	vi
Chapter 1. Introduction	1
1.1. Femtochemistry	2
1.2. Survey of Gas-Phase Anion Spectroscopy	3
1.3. Monomer Anion	3
1.4. Mesoscopic Clusters	8
1.4.1. Neutral Clusters	9
1.4.2. Ionic Clusters	10
1.4.3. Types of Anionic Clusters	11
1.4.3.1. Homogeneous Clusters	11
1.4.3.2. Heterogeneous Clusters	13
1.5. Methodology	13
1.5.1. Mass Spectrometry	14
1.5.2. Laser Spectroscopy	14
1.5.2.1. Fragmentation Study	14
1.5.2.2. Photoelectron Spectroscopy	16
1.6. Dynamics	17
1.7. Charge Reversal Experiment	19
1.8. Contents of the Thesis	21
References	24

Chapter 2. Experimental Apparatus	30
2.1. Introduction	31
2.2. Vacuum Chamber	31
2.3. Vacuum System	34
2.4. Ion Source	38
2.4.1. Thermionic Electron Emitter (Electron Gun)	40
2.4.2. Pulse Electron Gun	42
2.4.3. Continuous Electron Gun	44
2.4.4. Other Ion Sources	49
2.5. Tandem Mass Spectrometer	79
2.6. Primary Mass Spectrometer	79
2.6.1. Ion Accelerator	80
2.6.2. Deflectors	86
2.6.3. Einzel Lens	87
2.6.4. Mass Gate	88
2.6.5. MCP Detector	91
2.7. Reflectron Mass Spectrometer	111
2.7.1. MCP Detector in the Linear Reflectron Spectrometer	116
2.8. Photoelectron Spectrometer	118
2.8.1. Magnetic Bottle Photoelectron Spectrometer	120
2.8.2. Doppler Broadening and Ion Decelerator	123
2.8.3. Field-Free TOF Photoelectron Spectrometer	125
2.8.4. Data Processing: Conversion to eKE	126
2.8.5. MCP Detector for Photoelectron Detection	128
2.9. Femtosecond Laser System	161
2.10. Mode Quality and Stability of the Fs Laser System	161
2.10. Synchronization of the laser and the ion beam	162
2.11. Data Acquisition	163
2.12. Overview of Experimental Procedure	163
2.13. Reduction of Background Noise	

References	164
Chapter 3. Femtochemistry of Mass-Selected Negative-Ion Clusters of Dioxygen: Charge-Transfer and Solvation Dynamics	175
3.1. Introduction	176
3.2. Experimental	177
3.3. Results	179
3.4. Discussion	181
3.5. Conclusion	184
References	185
Chapter 4. Femtosecond Dynamics of Solvated Oxygen Anions: Bifurcated Electron Transfer Dynamics Probed by Photoelectron Spectroscopy	195
4.1. Introduction	196
4.2. Experimental	197
4.3. Results	198
4.4. Discussion	201
4.5. Conclusion	206
References	207
Chapter 5. Femtosecond Dynamics of Solvated Oxygen Anions: Nature of Dissociation and Caging in Finite-Sized Clusters	219
5.1. Introduction	220
5.2. Experimental	221
5.3. Results	222
5.4. Discussion	225

5.4.1. Electron Transfer and Solvation	226
5.4.2. From Clusters to Bulk	226
5.4.3. Evaporation and Solvation	229
5.4.4. Recombination and Caging	232
5.5. Conclusion	235
References	236
Chapter 6. Ultrafast Vectorial Dynamics of Anionic Clusters: Heterogeneous Clusters of Azobenzene Anion Solvated by Oxygen Molecules	256
6.1. Introduction	257
6.2. Experimental	258
6.3. Results	260
6.4. Discussion	264
6.5. Conclusion	270
References	271
Chapter 7. Femtosecond Dynamics of Hydrated Electrons in the Mesoscopic Water Clusters	284
7.1. Introduction	285
7.2. Experimental	286
7.3. Results	287
7.4. Discussion	289
7.5. Conclusion	291
References	293
Chapter 8. The Transition State of Thermal Organic Reactions: Direct Observation in Real Time	311
8.1. Introduction	312

8.2. Experimental	313
8.3. Results	315
8.4. Discussion	318
8.5. Conclusion	325
References	326
Appendix A. Interlock Unit in Vacuum System	343
Appendix B. Corona Discharge Source	344
Appendix C. Parallelization and Mirror Effect in the Magnetic Bottle Photoelectron Spectrometer	345

CHAPTER 1.

Introduction

1.1. Femtochemistry

Direct observation of atomic motions exhibited in various chemical reactions became possible since the birth of femtosecond spectroscopy.¹⁻⁴ The essence of femtosecond spectroscopy lies in the preparation of coherent wave packets and capability of capturing the snapshots of the wave packet motions. The wave packet motions represent the reaction trajectories in well-defined potential energy surfaces, which provide complete description of the chemical reactions at the molecular level of scrutiny. The subject of femtochemistry is literally unlimited, and new fields of femtosecond studies are constantly emerging as the scientific researches become more and more sophisticated. Over the last two decades, the scope of applications has been expanded from the isolated molecules in gas phase to complex biological systems in condense phase, and the femtosecond spectroscopic investigations have discovered new phenomena and provided better understanding of the fundamental processes.

This thesis work presents femtosecond studies of negatively charged systems, ranging from gas-phase organic molecule to mesoscopic clusters. The recent advances in laser technology and ion-beam methodology make it possible to conduct femtosecond pump-probe experiment on the isolated anions. The femtosecond anion spectroscopy is a relatively infant field but it has showed the potentials for exploring the solvation dynamics and wave packet dynamics of electronic ground state neutral reactions. The purpose of this chapter is to furnish the general overview of the negative ion chemistry. The chapter discusses the unique aspects of negative ion studies, and the recent accomplishments in the femtosecond anion spectroscopy are highlighted.

1.2. Survey of Gas-Phase Anion Spectroscopy

The subject matters in gas-phase anion spectroscopy can be categorized in two topics: First, the intrinsic properties of the isolated negative ions (monomer) have been the primary interest in ion chemistry. The excess electrons in negative ions alter the physical properties of the neutral molecule, and the negatively charged species have distinct structure, energetics and reactivity compared to the positively charged form as well as the neutral.⁵⁻⁷ Second, the ion-solvent interactions have been extensively studied by means of gas-phase cluster studies which provide nice models for studying the solute-solvent interaction in the bulk systems.⁸

1.3. Monomer Anion

The negative ion formation has been the primary concern in the gas-phase anion spectroscopy.⁶ Unlike the positive ion generation which can be achieved easily by ionization methods (photo-induced, collision-induced, electron impact, etc.), two considerably challenging steps are involved in the negative ion formation. First, the slow electrons with near-zero kinetic energy must be generated. Second, the zero kinetic energy electrons are attached to the neutral molecules via three body collision. Over last three decades, many ingenious methods have been developed for negative ion generation, which include plasma formation, secondary electron attachment, ion sputtering, laser ablation, electrospray ionization, matrix assisted laser desorption, electrospray ionization, etc.

The electron attachment is not only an important process for generating negative ions, but it also serves as a spectroscopic method which determines the energetics and

structures of negative ions. For example, Kondow group has implemented the electron attachment spectroscopy by inducing the collision with high-Rydberg atoms, which offer a brilliant way of preparing zero kinetic energy electron.^{9,10} Mark and his colleagues studied dissociative electron attachment, which involves two-body collision between the neutral molecules and the slow electrons with non-zero kinetic energy^{11,12}. More details of the electron attachment will be discussed in Chapter 2.

An excess electron can be attached to molecules or atoms by two different ways. Excess electrons can reside in the empty orbital (covalent binding), or it can attach to the positive end of the permanent dipole exhibited in molecules (dipole-binding). The covalent binding usually causes geometric deformation of the molecules by changing the bond order of the molecule or by inducing electrostatic interaction. For instance, when the excess electron occupies anti-bonding orbitals, bond length of the molecule becomes elongated. When a macromolecule possesses additional electron, the charge-dipole interaction within the molecule reduces the torsional degree of freedom and locks the geometry of molecule in a specific conformation. This type of geometric confinement imposed in the ionic compounds is an important subject in biochemistry. Many anionic systems including hydrocarbon chains, polypeptides and zwitter ions have been extensively studied to understand the intramolecular forces exhibited in the elementary processes of protein folding.^{13,14}

The dipole-bound anions are not common in nature because of the weak binding force between the molecule and the excess electron. Molecules with dipole moments greater than 1.625 D can possess the dipole-bound electrons, and the binding energy increases with increasing dipole moment. Since the dipole-bound electrons are diffused

at the surface of the molecule rather than occupying empty orbitals, structures of the dipole-bound anions are almost identical to the neutral forms. Hence, upon laser excitation, the 0-0 vertical transition is predominant, and the photoelectron spectrum of a dipole bound anion appears as a very narrow peak at low electron binding energy (a few millielectron volts).

Bowen and Schlag groups characterized the dipole-binding electron in the monomeric DNA bases and its hydrated clusters. They also studied the evolution of the dipole-bound state as the clusters grow in a stepwise fashion.^{15,16} Recently, *quadrupole*-bound metal anions have been observed by Wang and his coworkers.^{17,18} Researchers in chemical physics community continue to search for the ion-molecule complexes formed by higher order electric or magnetic moments, which will provide invaluable information about the electron-molecule interactions.

Double Rydberg dianion is another uncommon form of negatively charged species which was first proposed by Bowen and his coworkers. The term double Rydberg dianion describes the singly charged anion which is composed of a closed-shell positive ion and two Rydberg-type electrons orbiting around the nucleus.¹⁹ For example, Bowen claimed that NH_4^- has the form of NH_4^+ core and two electrons in the Rydberg like state based on their photoelectron analysis. So far the double Rydberg forms have been found in NH_4^- and its ammonia clusters only, and the concept hasn't been fully developed yet. However, the possibility of forming the double Rydberg anion could prevail in the condense phase, which provides a new way of approaching the properties of ionic solutions.

Multiply charged anions can be formed when the anions are large enough to

accommodate the Coulomb repulsions created by the extra charges. Wang's research group at Pacific Northwest National Laboratory has been most active in pursuing this field.²⁰ They prepared variety of multiply charged anions by utilizing electrospray ion source and characterized the electrostatic effect on the reactivity of multiply charged anions.^{18,21} The dynamic stability of multiply charged anion was understood by the concept of the repulsive Coulomb barrier which is defined by the superposition of the long range Coulomb repulsion and short range electron binding energy. He adopted this concept to explain the nature of *negative* electron affinity,²² and also suggested the idea of resonant tunneling through the repulsive Coulomb barrier.

Attachment of an excess electron to labile neutral species sometimes creates very stable anionic radicals which otherwise is susceptible to molecular rearrangement or self-dissociation. For instance, the neutral vinylidene radical undergoes rapid isomerization to form acetylene, while the vinylidene anion exists for hundreds of milliseconds in the gas phase. The stable radical anions can be used as the precursor to the short-lived neutral radicals, which provides a nice way of characterizing the properties of the labile neutral species. Neumark at the University of California at Berkeley utilized this concept to prepare the anions which are precursor to the neutral form at the transition state.²³ By using photoelectron spectroscopy, the energetics and the structure of the transition state complex were able to be investigated. Lineberger employed the same method to investigate the neutral cyclooctatetraene molecule at the transition state of the ring-inversion coordinate.²⁴

The reactivity of negative ions has been the central theme of the gas-phase ion chemistry. In many cases, the excess electron in the molecule or atoms changes their

reactivity. Negatively charged species often have a greater degree of nucleophilicity or basicity than their neutral forms. Since the pioneering works by Professor Brauman at Stanford^{25,26}, numerous anion-neutral bimolecular reactions have been studied. The reactive scattering of anion-neutral interaction has been studied by cross beam technique and the rate of bimolecular reactions have been measured by using the flow-tube method.

One of the representative works by Brauman is the investigations of S_N2 type organic reactions.²⁷ He has mainly concentrated on the reactions involved in the halogen anion which provided detailed descriptions of the elementary processes involved in the nucleophilic substitutions. His pioneering works have stimulated many scientists in the ion chemistry community, and until now persistent efforts have been devoted to study the fundamental organic reactions. Johnson at Yale University made significant contribution in determining the potential energy surface of S_N2 type reactions.²⁸ He used I⁻CH₃I as the model system to map out the double-well characters in the bimolecular substitution reaction and to study the nucleophilicity of negative ions. Recently, Neumark and his coworkers conducted the femtosecond spectroscopy on I⁻CH₃I and other derivatives to delineate the real-time dynamics of S_N2 reaction.

One of the most frequently studied anion-neutral bimolecular reaction is the hydrogen abstraction. Especially, the negatively charged atomic oxygen has been studied for many years because of its extraordinary reactivity in the organic and biochemical reactions. Lineberger reported its strong propensity for abstracting hydrogen atoms and protons from organic compounds.²⁹ The negatively charged atomic oxygen also has considerably high basicity which induces proton migration in the bimolecular reactions. The anionic oxygen atom often abstracts a hydrogen atom and a

proton simultaneously to form water molecule. Ellison group has studied the reactivity of the organic radicals and determined the electronic structures of the anionic radicals.³⁰⁻³² He utilized the anion photoelectron spectroscopy and reactive scattering to study the reaction mechanism involving organic radicals. The research area has been extended to complex bimolecular reactions in wide variety of biological systems.

1.4. Mesoscopic Clusters

Clusters are aggregates of atoms and molecules that are small in size such that the state of matter is distinct from the bulk liquid or solid. The main objective of cluster studies is to bridge the gap between the isolated gaseous molecules and the bulk continuum. The cluster reduces the inherent complexity exhibited in the condensed phase in which the many-body interaction cannot be described at the level of molecular scale. The key issues in the cluster studies can be narrowed down to a few fundamental questions: (1) What is the minimum number of solvent required to prepare the clusters in gas phase? (2) What is the smallest cluster that mimics bulk systems? (3) When does phase transition occur upon going from small to large clusters? (4) What is the motif that represents the solvent cavity? To answer these questions, one must come up with a systematic way of controlling the size and composition of clusters. The laser spectroscopy of anionic clusters has been recognized as the most promising approach for resolving the aforementioned issues. Before getting into the topics in anionic cluster studies, it is necessary to overview the spectroscopy of the neutral clusters in order to provide critical background elements for the upcoming discussions.

1.4.1. Neutral Clusters

For spectroscopic studies of neutral clusters, the size-dependent studies rely on the positive-ion mass spectrum generated by ionizing neutral clusters. The size distribution in the post-ionization of neutral clusters *may* provide useful information regarding the evolution of cluster properties. However, the subsequent dissociation of the positive ions often complicates the analyses. The correlation of cluster size can only be acquired when the mass selection is achieved prior to light interactions or collision-induced reactions. The precise mass selection cannot be achieved for the neutral clusters unless they exhibit permanent magnetic moment.³³

The neutral clusters formed in the supersonic jet have wide range of size distribution; hence, the spectroscopic studies of the gas-jet of clusters reflect the *averaged* properties of cluster mixture over broad range of size *distribution*. For most cases, the size of neutral clusters is controlled by varying the source condition such as stagnation pressure, nozzle temperature, types of carrier gas, and so forth; however, the manipulation of source condition provides limited control of the size distribution. Numerous instruments have been developed to execute mass-selection of neutral clusters. A few designs of neutral mass-filters have demonstrated promising ways to achieve precise mass-selection.

Buck and coworkers invented the helium beam filter which spreads the clusters by their mass.^{34,35} The filtration is executed by crossing the helium atoms with the cluster jet, and the degree of deflection depends on the magnitude of the momentum transfer between the helium beam and the clusters. The clusters will spread along the helium beam direction, and heavier cluster deflects less by the collision and *vice versa*.

Another popularly used *neutral* mass-filter is the molecular-beam chopper that discriminates the clusters by their expansion velocity. The operating mechanism relies on the assumption that heavier clusters move slower in the expansion region. These mass filters provide a nice way to skim the size distribution, but do not provide rigorous size-selection since the cluster packet selected contains significant amount of impurity (different sizes of clusters).

1.4.2. Ionic Clusters

The essence of cluster studies relies on the precise mass selection, which provides a systematic way to change the number and the composition of clusters. The ionic clusters can be sorted out by the well-defined mass-to-charge ratio, and a particular size of the clusters can be selected by creating electrostatic or magnetic field in the ion path. Many clever designs have been developed, but all the variations in the *ion* mass-filters are originated from the two representative devices: quadrupole ion guide and pulsed massgate.

The quadrupole mass guide controls the oscillatory motion of the ions by the rf field, and the cluster motion resonant with the rf frequency can be guided through the ion channel; otherwise deflected out of the channel. The pulsed massgate creates the electric gate with variable delay and width, which filter through the target ions while blocking unwanted clusters. The former is used in the slow ion-beam scheme while the latter is used in the fast ion-beam apparatus. Thanks to major progress in the ion mobility methods, the separation of conformational isomers became possible. Bowers group succeeded to separate polypeptide isomers in the ion mobility channel in which

ions with different shape drift with different velocity due to the frictions exerted on the ions.^{36,37}

1.4.3. Types of Anionic Clusters

Cluster anions can be categorized into two groups based on the composition of clusters: homogeneous and heterogeneous clusters.

1.4.3.1. Homogeneous Clusters

Homogeneous anionic clusters refer to weakly bound aggregates which consist of one type of constituent and an excess electron. The clusters can accommodate the excess electron in several different ways. First, it can be attached to the net dipole of the cluster aggregate. The cluster aggregates containing dipole-bound electron generally have a tendency to grow uniaxially and form chain-like structures. As the result, the net-dipole moments increase and electrons are more tightly bound to the clusters. In this case, electrons are diffused in the surface of clusters without forming the monomeric anion within the clusters. For instance, water, CO₂, ammonia, benzene, pyridine and naphthalene cluster anions, all of which are not stable as monomeric anion, can accommodate the extra electron as the molecular cluster.³⁸⁻⁴¹ As cluster size increases, phase transition may occur and the excess electron is likely to be encapsulated by solvent molecules. The electron situated in the solvent cavity is the gas-phase analogue of the solvated electron in bulk systems, which provides a nice system to study solvation dynamics.

Electrons can occupy one of the solvent constituents to form homogeneous

clusters having anionic solutes and neutral solvent molecules. In this case, electrons are covalently (occupying empty orbital) bound to the solutes and the neutral solvent are attached to the anionic solutes. One of the daunting tasks of studying homogeneous anionic clusters is to identify the true form of the anionic solute in the clusters. Especially when the core solute is not a monomer but a fused entity of multiple constituents, the core unit is hard to be defined from the solvent shell. For instance, some homogeneous clusters form dimeric cores by resonantly sharing the excess electron between two molecules.⁴²⁻⁴⁷ The two molecules are linked by pseudo-covalent bonding which has the bond length significantly shorter than van der Waals distance. In this case, one might easily make mistake to assign the excess electron as the solute of the clusters.

Homogeneous metal clusters have very different characteristics compared to the non-metallic clusters. The clusters are conglomerated by metal-metal bond, and the excess electron is delocalized throughout the clusters. Similar to other cluster studies, the main goal of the metal cluster studies is to provide atomic level of description of the bulk solid. Until now, the physical properties of bulk metals have been described by valence-conduction band theory which is limited to the macroscopic description bulk metal. For many decades, physicists have been intrigued by the evolution of metal properties such as ferromagnetism and electric conductance, and tremendous efforts have been devoted to study the insulator-to-metal transition. By implementing mass-selected spectroscopy, emergence of bulk behavior has been systematically studied by growing the metal clusters in atom-by-atom fashion.^{48,49}

1.4.3.2. Heterogeneous Clusters

Heterogeneous clusters refer to the finite-sized systems in which the solute is different from the surrounding solvent molecules. Wide varieties of heterogeneous clusters have been used for studying solvation dynamics. The heterogeneous systems have nice features that can be utilized in the spectroscopic studies. First, since the unsolvated solute exists in gas phase, the properties of solute (chromophore) can be well-characterized before studying the solvated form. Second, since the solute-solvent interaction is relatively weak, the solvated chromophore has similar properties as unsolvated solute. Third, solute and solvent can be easily distinguished; thus, solvation dynamics can be monitored by following the trajectory of the solute inside the solvent cavity.

The chemistry of metal-nonmetal complexes such as metal oxide, metal carbide, metal halide, and metal hydride draw great deal of attention from organometallic chemists because of their potential usage as the catalysts. The field of anionic metal-nonmetal clusters has been established thanks to the advances in ion source technology.^{47,50-54} Despite the rapid progress in organometallic syntheses, the mechanisms of the catalytic reactions are poorly understood.

1.5. Methodologies

Many ingenious techniques have been developed for studying anionic clusters. Most widely used methodologies are briefly outlined here.

1.5.1. Mass Spectrometry

The intensity profiles in negative ion mass spectra provide important information regarding the stability of clusters. For certain cases, “magic number” is the signature of a favored size of clusters, which often suggests the completion of solvent shell. Sudden steps or irregularities in intensity profile indicate the abnormal properties of the corresponding clusters, and the structure of these extraordinary clusters can be deduced with the assist of computational chemistry.

Ion cyclotron mass spectrometer has been recognized as the most powerful tool in mass spectrometry. The mass resolution and detection sensitivity are superb compared to other types of mass spectrometers. The operating principle relies on the resonant excitation of the uniform circular motion of the charged species in the strong magnetic field and the detection of image current induced by the gyroscopic motion of the charged particles. Various supramolecular ions have been prepared and studied by combining electrospray ionization source with the ion cyclotron mass spectrometer.

1.5.2. Laser Spectroscopy

Recent advances in the development of ion source made it possible to generate sufficient amount of ions to carry out laser spectroscopy of the size selected clusters. This giant stride in the cluster studies realizes the systematic studies of stepwise solvation. Most commonly used methodologies are reviewed in the following sections.

1.5.2.1. Fragmentation Study

Laser interaction with anionic clusters generates various photoproducts among

which fragment ion and photoelectrons can be detected and analyzed. Fragment mass spectrum can be obtained by employing *tandem* mass spectrometer which creates the second set of electric or magnetic fields to separate the fragment from the parent clusters. The intensity profile in the fragment mass spectra provides valuable information about the dissociation channel. By incorporating anisotropy measurement and kinetic energy release, energy partitioning can be determined and the structure of clusters can be deduced.

Johnson group has established the action spectroscopy of anionic species and applied this method to various anionic clusters, which is equivalent to the conventional absorption spectroscopy of the bulk.^{44,55} The method relies on the preparation of heterogeneous anionic clusters in which a few inert atoms (Ar or Ne) are attached to the chromophore (cluster of interest). When the inert gas-chromophore complex absorbs light, it acquires thermal energy to boil off the weakly bound inert gas. The absorption spectrum of the chromophore can be obtained by plotting the ion intensity of the chromophore as a function of wavelength.

Continetti at the University of California at San Diego has developed the coincident technique to conduct the simultaneous detection of electron-neutral and electron-ion, which provides a nice way of tagging conjugate particles. He demonstrated that three-body and four-body motions can be studied by the coincidence technique and the structure of the clusters can be determined from the kinetic energy of the photoproducts.⁵⁶⁻⁵⁹

1.5.2.2. Photoelectron Spectroscopy

The most versatile method used in the gas-phase anionic studies is the photodetachment spectroscopy. Photodetachment of anions can be easily accomplished by irradiating relatively weak laser beam. Typically, electron affinity of the anionic clusters is below 4 eV and the photodetachment cross section is on the order of 10^{-17} cm²; therefore, the detachment of the excess electrons can be achieved by the single-photon absorption of vis/UV light. The photodetachment spectrum contains vast amount of information regarding the energetics and structures of the cluster anions. The electron affinity can be estimated from the onset of the spectrum, and the solvent binding energy can be determined from the stabilization energy. Frank-Condon profile of the spectrum reflects the structure of anionic clusters.

The electron affinity (adiabatic and vertical) of the bulk can be extrapolated from the linear correlation of electron affinity vs. radius of the clusters.^{41,46,60} Jortner developed a simple model for describing the solvent cavity of the finite-sized clusters.⁶¹ He considered the finite-sized clusters as the spherical dielectric continuum which reflects the solvent cavity of bulk systems. The plot has been used as the criterion for judging the structure of the clusters. If the extrapolated values coincide with the actual bulk value, the solutes are likely to be inside the clusters and have similar structures as the core motif of the bulk system. When the solutes are located outside clusters, the values do usually not match. The deviation in the extrapolated value suggests that the cluster must grow further and undergo some type of phase-transition to mimic the bulk system. The surface-to-core transition has been the most intriguing subject in the gas-phase cluster chemistry, because this phenomenon is directly related to the fundamental issue of

“cluster-bulk similarity.”

1.6. Dynamics

For finite-sized clusters, which consist of countable number of solvent molecules, it is possible to describe the dynamics of the many-body system. The gas-phase cluster system reduces the enormity of the bulk phase, which makes it feasible to map out the potential energy surface and conduct the molecular dynamics simulations. Femtosecond dynamics of neutral clusters have been studied in this group^{62–66}, and the fundamental processes exhibited in the clusters (caging, charge transfer to solvent, solvent friction, etc.) are investigated.

The time-resolved pump-probe spectroscopy of mass-selected clusters was first accomplished by Lineberger and his colleagues.⁶⁷ They utilized the reflectron mass spectrometry to follow dissociation of I_2^- and the subsequent geminate recombination occurring in the argon clusters.⁶⁸ Later Lineberger group employed femtosecond time-resolved pump-probe scheme to follow the coherent nuclear motion of iodine molecule⁶⁹, and they also observed the evolution of dissociation and recombination dynamics as function of cluster size. Lineberger used this method to examine the dissociation of triatomic molecules, and followed the dissociation channels.^{70,71} The work by Lineberger group is significant in a sense that they showed that the pump-probe scheme can be applied to the low density of mass-selected ions and it also brings the possibility of studying positively charged clusters.

The femtosecond time-resolved photoelectron spectroscopy of anionic system was first conducted by Neumark and his coworkers. Neumark first implemented this

technique to follow the dissociation of diatomic iodine anion I_2^- and demonstrated the versatility and the reliability of the technique.⁷² Both depletion of I_2^- and emergence of I^- were followed in real time by recording the photoelectron signatures of I_2^- and I^- . The I_2^- system has been exhaustively used in the femtosecond time-resolved studies because of the following properties that facilitate the experimental execution. First, I_2^- exhibits a repulsive state lying below the neutral ground state which can be accessed by absorbing 800 nm light. Second, the photoelectron spectrum of I^- is distinct from the photoelectron spectrum of I_2^- , so the generation of nascent fragment can be differentiated from the parent depletion. Third, the photodetachment of the excess electron from both I^- and I_2^- can be easily achieved by single-photon absorption of uv light.

By using the well-characterized I_2^- anion as the solute of the solvated system, Neumark studied the dissociation and recombination dynamics of I_2^- caged by finite number of solvent molecules.^{73,74} The time-dependent photoelectron signals clearly illustrated the recombination and vibrational relaxation. He proposed anomalous charge shifting in the initial stage of dissociation. Neumark implemented the stimulated emission pumping to induce large amplitude vibration of I_2^- and studied the damped oscillatory motion caused by solvent friction.⁷⁵⁻⁷⁷

Neumark also studied solvation dynamics of small clusters. By exciting the system to the charge-transfer-to-solvent band, the electron recombination and subsequent relaxation dynamics was observed. The effective rates of solvent rearrangement and the

spin-orbit coupled relaxation were correlated with the cluster size.⁷⁸⁻⁸⁰ Neumark also applied the femtosecond anion photoelectron spectroscopy to study the excited state dynamics of small carbon clusters and dissociation channel of I_3^- .^{81,82}

Eberhardt and his coworkers have investigated the excited state dynamics of negatively charged metal clusters by employing the femtosecond time-resolved photoelectron spectroscopy. Eberhardt group has concentrated on the dynamics of small metallic clusters. They first studied the relaxation dynamics of optically excited Au_3^- , and followed both depletion of excited state and recovery of ground state by resolving, in energy and time the time-dependent photoelectron signature the photoelectron spectrum.⁸³ A number of different metal trimers have been studied by Eberhardt group, and their findings have contributed to new way of describing the conducting electrons.⁸⁴⁻⁸⁷

Recently, time-dependent rotational motion of negatively charged systems has been investigated by utilizing femtosecond imaging technique, which allows one to monitor femtosecond evolution of vectorial properties.⁸⁸⁻⁹⁰ This method is promising for the femtosecond time-resolved studies since it provides significantly improved collection efficiency and energy resolution. The method permits to implement the coaxial arrangement where the detection axis is collinear with the ion-beam trajectory. This configuration eliminates the inherent Doppler broadening in the time-of-flight photoelectron spectrometer (Chapter 2).

1.7. Charge Reversal Experiments

Combining the femtosecond pump-probe scheme and the negative ion beam technique provides a unique way to study the coherent nuclear motions of *neutral*

molecules occurring on the electronic *ground* state. Stable (positive electron affinity) negative ions prepared in the gas phase have the electronic states lying below the neutral. Thus, coherent wave packets can be launched on the upper-lying neutral states by photodetaching the anion with a femtosecond laser pulse. If the geometries of the anion and the neutral are significantly different, vertical transition induces significant nuclear motion toward the equilibrium geometry of the ground state neutral. This motion can be monitored in real time by irradiating the second femtosecond laser pulse with variable time delay. For instance, the Frank-Condon overlap for the photoionization might evolve with time as the wave packet moves on the potential energy surface of the neutral. By ionizing the nascent neutral, one can map out the positive ion intensity as a function of time delay between the two pulses.

Wöste and his coworkers introduced the NeNePo (acronym for Negative ion to Neutral to Positive ion) charge reversal scheme to study the dynamics of neutral silver trimer (Ag_3).⁹¹ The nuclear motion of Ag_3 was initiated by photodetaching the linear Ag_3^- and observed the bending motion occurring on the electronic ground state of Ag_3 . In their experiment, Wöste group employed the linear quadrupole ion trap to accumulate the Ag_3^- ion and helium gas cell to control the vibrational temperature of Ag_3^- , and demonstrated the influence of the internal energy of Ag_3^- on the femtosecond dynamics of Ag_3 .^{92 93 94}

The silver trimer experiment was repeated by Lineberger and his coworkers by using their fast ion beam apparatus, and they were able to compensate the ion beam fluctuation and laser instability by monitoring the ion current and flux of the fast neutral simultaneously.⁹⁵ Lineberger and coworkers thoroughly performed the wavelength-

dependent study of pump and probe light, and proposed possible involvement of intermediate electronic states during the multiphoton ionization process. Recently, the low-frequency oscillatory motions of the silver tetramer (Ag_4) was examined by Wöste group, and wave packet dephasing and rephasing was observed in the excited dark state of the neutral Ag_4 .^{96 92} Metal clusters are very good candidates for the NeNePo experiment since large amount of anion can be produced, and they usually have low ionization potential with relatively large ionization cross section. However, until now only Ag_3 and Ag_4 have been studied by the NeNePo technique due to the difficulty of detecting the small amount of time-dependent signal produced via the charge reversal process.

1.8. Contents of the Thesis

The femtosecond time-resolved photoelectron spectroscopy has been applied to only a few anionic systems. Previously, the main focus of the study was on the dissociation and recombination dynamics of solvated I_2^- or relaxation of excited state anionic clusters. In this thesis work, the scope of subject matter is expanded to wide variety of systems including homogeneous and heterogeneous oxygen clusters, azobenzen clusters, and hydrated electron clusters. The major achievement in this thesis work is the substantial improvement of signal to noise ratio in the femtosecond transients, which allows one to decompose the multiple exponential components embedded in the observed transients.

In Chapter 2, details of the experimental procedure are described. Major portion of the chapter is devoted to the discussion of the molecular beam apparatus. The

focus was primarily on the unique features in the design, which are distinct from the other apparatus. The operating principles of major constituents are highlighted and some quantitative descriptions are provided.

In Chapters 3 through 7, solvation dynamics in finite-sized clusters is discussed. The chapters are presented in chronological order to illustrate the maturation of experimental techniques and sophistication of subject matter. Chapter 3 presents femtosecond time-resolved photoelectron spectroscopy of O_6^- . The O_6^- anion is the simplest system studied in this laboratory; however, the investigation of the O_6^- dissociation conveys the essence of the experimental methodology. The dissociation dynamics is governed by the wave packet bifurcation involving electron transfer and electron recombination. Two dissociation pathways are followed separately by resolving, in time and energy the time-dependent photoelectron of nascent fragment.

In Chapters 4 and 5, the dissociation dynamics of O_6^- is elaborated. Chapter 4 presents the single-solvent effect on the dissociation rate and the energy partition. In this experiment, the composition of the solvent is systematically varied from monatomic (Xe) to triatomic (N_2O) molecules. The observed rate and dissociation pattern in this study consolidate the bifurcation mechanism proposed in Chapter 3. In Chapter 5, the number of oxygen solvent was varied from 3 to 20. The focus was on the evolution of dissociation dynamics in the stepwise solvation. For cluster larger than O_{16}^- , reformation of O_4^- core was observed and delay in the geminate recombination was attributed to the orientation effect in the *Molecular* recombination.

Cluster size effect on the rotational dynamics is discussed in Chapter 6. Time-

dependent vectorial dynamics was observed in the Azobenzene-oxygen dissociation. This experiment demonstrated the new experimental approach for deducing the structure of molecular clusters.

In Chapter 7, femtosecond dynamics of hydrated electron clusters, $(\text{H}_2\text{O})_n^-$ was discussed. With femtosecond resolution, the photoelectron signature of $(\text{H}_2\text{O})_n^-$ in the short-lived excited state was captured. The observed time-dependent photoelectron signal depicts the fast internal conversion of the excited state and subsequent vibrational relaxation. The effective rate constants for the ground state recovery was determined, which show striking resemblance to the bulk system.

Finally, Chapter 8 presents the coherent molecular motion of the *neutral* cyclooctatetraene occurring in the electronic ground state. Direct probing of the transition state dynamics was accomplished by implementing the charge reversal scheme described earlier. The observed transients reflect the thermal organic reaction occurring in the electronic ground state.

References

- ¹ A. H. Zewail, *Femtochemistry: Ultrafast Dynamics of the Chemical Bond*. (World Scientific, Singapore, 1994).
- ² J. Manz and L. Woste, *Femtosecond Chemistry*. (VCH, Weinheim, 1995).
- ³ A. H. Zewail, *Angew. Chem.* **39** (15), 2587 (2000).
- ⁴ M. Chergui, *Femtochemistry: Ultrafast Chemical and Physical Processes in Molecular Systems*. (World Scientific, Singapore).
- ⁵ M. T. Bowers, *Gas Phase Ion Chemistry: Ions and Light*. (Academic Press, Orlando, 1984).
- ⁶ J. M. Farrar and W. H. Saunders, Jr. *Techniques for the Study of Ion-Molecule Reactions*. (John Wiley & Sons, New York, 1988).
- ⁷ E. Illenberger and J. Momigny, *Gaseous Molecular Ions: An Introduction to Elementary Processes Induced by Ionization*. (Springer-Verlag, New York, 1992).
- ⁸ C. Y. Ng, T. Baer, I. Powis, *Cluster Ions*. (John Wiley & Sons, New York, 1993).
- ⁹ K. Mitsuke, T. Kondow, and K. Kuchitsu, *J. Phys. Chem.* **90** (8), 1505 (1986).
- ¹⁰ Tsukuda, A. Terasaki, T. Kondow, M. G. Scarton, C. E. Dessent, A. Bishea G, and M. A. Johnson, *Chem. Phys. Lett.* **201**, 351 (1993).
- ¹¹ G. Senn, J. D. Skalny, A. Stamatovic, N. Mason, J., P. Scheier, and T. D. Mark, *Phys. Rev. Lett.* **82** (25), 5028 (1999).
- ¹² S. Denifl, S. Ptasinska, G. Hanel, B. Gstir, M. Probst, P. Scheier, and T. D. Mark, *J. Chem. Phys.* **120** (14), 6557 (2004).
- ¹³ S. J. Xu, M. Nilles, and K. H. Bowen, *J. Chem. Phys.* **119** (20), 10696 (2003).
- ¹⁴ B. C. Dian, J. R. Clarkson, and T. S. Zwier, *Science* **303**, 1169 (2004).
- ¹⁵ J. H. Hendricks, S. A. Lyapustina, H. L. de Clercq, J. T. Snodgrass, and K. H. Bowen, *J. Chem. Phys.* **104** (19), 7788 (1996).
- ¹⁶ J. Schiedt, R. Weinkauff, D. M. Neumark, and E. W. Schlag, *Chem. Phys. Lett.* **239**, 511 (1998).
- ¹⁷ G. L. Gutsev, P. Jena, and R. J. Bartlett, *J. Chem. Phys.* **111** (2), 504 (1999).
- ¹⁸ M. Gutowski, P. Skurski, X. Li, and L. S. Wang, *Phys. Rev. Lett.* **85** (15), 3145 (2000).
- ¹⁹ S. J. Xu, J. M. Nilles, J. H. Hendricks, S. A. Lyapustina, and K. H. Bowen, *J. Chem.*

- Phys.* **117** (12), 5742 (2002).
- ²⁰ X. B. Wang and L. S. Wang, *Phys. Rev. Lett.* **83** (17), 3402 (1999).
- ²¹ X. B. Wang, J. E. Dacres, X. Yang, K. M. Broadus, L. Lis, L. S. Wang, and S. R. Kass, *J. Am. Chem. Soc.* **125** (1), 296 (2003).
- ²² X. B. Wang, K. Ferris, and L. S. Wang, *J. Phys. Chem. A* **104** (1), 25 (2000).
- ²³ D. M. Neumark, *Accounts Chem. Res.* **26** (2), 33 (1993).
- ²⁴ P. G. Wenthod, D. A. Hrovat, W. T. Borden, and W. C. Lineberger, *Science* **272**, 1456 (1996).
- ²⁵ M. L. Chabinye, S. L. Craig, C. K. Regan, and J. I. Brauman, *Science* **279**, 1882 (1998).
- ²⁶ C. K. Regan, S. L. Craig, and J. I. Brauman, *Science* **295**, 2245 (2002).
- ²⁷ B. D. Wladkowski, K. F. Lim, W. D. Allen, and J. I. Brauman, *J. Am. Chem. Soc.* **114** (23), 9136 (1992).
- ²⁸ C. E. H. Dessent, C. G. Bailey, and M. A. Johnson, *J. Chem. Phys.* **150** (23), 10416 (1996).
- ²⁹ P. G. Wenthod and W. C. Lineberger, *Accounts Chem. Res.* **32** (7), 597 (1999).
- ³⁰ J. M. Oakes and G. B. Ellison, *J. Am. Chem. Soc.* **106** (25), 7734 (1984).
- ³¹ E. P. Clifford, P. G. Wenthod, W. C. Lineberger, G. A. Petersson, K. M. Broadus, S. R. Kass, S. Kato, C. H. DePuy, V. M. Bierbaum, and G. B. Ellison, *J. Phys. Chem. A* **102** (36), 7100 (1998).
- ³² S. J. Blanksby, T. M. Ramond, G. E. Davico, M. R. Nimlos, S. Kato, V. M. Bierbaum, W. C. Lineberger, G. B. Ellison, and M. Okumura, *J. Am. Chem. Soc.* **123** (39), 9585 (2001).
- ³³ I. M. L. Billas, A. Chatelain, and W. A. DeHeer, *Science* **265**, 1682 (1994).
- ³⁴ U. Buck and I. Ettischer, *Faraday Discuss.* **97**, 215 (1994).
- ³⁵ U. Buck and F. Huisken, *Chem. Rev.* **100** (11), 3863 (2000).
- ³⁶ A. C. Gill, K. R. Jennings, T. Wyttenbach, and M. T. Bowers, *Int. J. Mass. Spectrom.* **195**, 685 (2000).
- ³⁷ J. Gidden and M. T. Bowers, in *J. Phys. Chem. B* (2003), Vol. 107, pp. 12829.
- ³⁸ G. H. Lee, S. T. Arnold, J. G. Eaton, H. W. Sarkas, K. H. Bowen, C. Ludewigt, and H. Harberland, *Z. Phys. D: Atom Mol. Clusters* **20**, 9 (1991).

- ³⁹ S. Y. Han, J. H. Kim, J. K. Song, and S. K. Kim, *J. Chem. Phys.* **109** (22), 9656 (1998).
- ⁴⁰ M. Gutowski, C. S. Hall, L. Adamowicz, J. H. Hendricks, H. L. de Clercq, S. A. Lyapustina, J. M. Nilles, S. J. Xu, and K. H. Bowen, *Phys. Rev. Lett.* **88** (14), 143001 (2002).
- ⁴¹ M. Mitsui, A. Nakajima, K. Kaya, and U. Even, *J. Chem. Phys.* **115** (13), 5707 (2001).
- ⁴² T. Maeyama, T. Oikawa, T. Tsumura, and N. Mikami, *J. Chem. Phys.* **108** (4), 1368 (1998).
- ⁴³ A. Sanov, W. C. Lineberger, and K. D. Jordan, *J. Phys. Chem. A* **102** (15), 2509 (1998).
- ⁴⁴ J. A. Kelley, W. H. Robertson, and M. A. Johnson, *Chem. Phys. Lett.* **362**, 255 (2002).
- ⁴⁵ R. Mabbs, E. Surber, and A. Sanov, *Chem. Phys. Lett.* **381**, 479 (2003).
- ⁴⁶ J. K. Song, N. K. Lee, J. H. Kim, S. Y. Han, and S. K. Kim, *J. Chem. Phys.* **119** (6), 3071 (2003).
- ⁴⁷ K. Tono, A. Terasaki, T. Ohta, and T. Kondow, *Phys. Rev. Lett.* **90** (13), 133402 (2003).
- ⁴⁸ A. W. Castleman, *Int. J. Mass. Spectrom.* **118**, 167 (1992).
- ⁴⁹ D. E. Bergeron and A. W. Castleman, *Chem. Phys. Lett.* **371**, 189 (2003).
- ⁵⁰ A. Pramann, K. Koyasu, A. Nakajima, and K. Kaya, *J. Chem. Phys.* **116** (15), 6521 (2002).
- ⁵¹ H. J. Zhai and L. S. Wang, *J. Chem. Phys.* **117** ((17):), 7882 (2002).
- ⁵² G. Meloni, M. J. Ferguson, and D. M. Neumark, *Phys. Chem. Chem. Phys.* **5** (19), 4073 (2003).
- ⁵³ D. R. Justes, N. A. Moore, and A. W. Castleman, *J. Chem. Phys. B* **108** (12), 3855 (2004).
- ⁵⁴ M. L. Kimble, A. W. Castleman, R. Mitric, C. Burgel, and V. Bonacic-Koutecky, *J. Am. Chem. Soc.* **126** (8), 2526 (2004).
- ⁵⁵ J. M. Weber, W. H. Robertson, and M. A. Johnson, *J. Chem. Phys.* **115** (23), 10718 (2001).
- ⁵⁶ T. G. Clements and R. E. Continetti, *Phys. Rev. Lett.* **89** (3), 033005 (2000).
- ⁵⁷ T. G. Clements and R. E. Continetti, *J. Chem. Phys.* **115** (12), 5345 (2001).
- ⁵⁸ L. S. Alconcel, H. J. Deyerl, M. DeClue, and R. E. Continetti, *J. Am. Chem. Soc.* **123** (16), 3125 (2001).
- ⁵⁹ R. E. Continetti, *Annu. Rev. Phys. Chem.* **52**, 165 (2001).

- ⁶⁰ H. W. Sarkas, S. T. Arnold, J. G. Eaton, G. H. Lee, and K. H. Bowen, *J. Chem. Phys.* **116** (13), 5731 (2002).
- ⁶¹ J. Jortner, *Z. Phys. D: Atom Mol. Clusters* **24** (3), 247 (1992).
- ⁶² Q. L. Liu, J. K. Wang, and A. H. Zewail, *Nature* **364** (6436), 427 (1993).
- ⁶³ A. A. Heikal, S. H. Chong, J. S. Baskin, and A. H. Zewail, *Chem. Phys. Lett.* **242**, 380 (1995).
- ⁶⁴ J. K. Wang, Q. L. Liu, and A. H. Zewail, *J. Phys. Chem.* **99** (29), 11309 (1995).
- ⁶⁵ Q. L. Liu, C. Z. Wan, and A. H. Zewail, *J. Chem. Phys.* **105** (12), 5294 (1996).
- ⁶⁶ C. Wan, M. Gupta, J. S. Baskin, Z. H. Kim, and A. H. Zewail, *J. Chem. Phys.* **106** (10), 4353 (1997).
- ⁶⁷ D. Ray, N. E. Levinger, J. M. Papanikolas, and W. C. Lineberger, *J. Chem. Phys.* **91** (10), 6533 (1989).
- ⁶⁸ J. M. Papanikolas, J. R. Gord, N. E. Levinger, D. Ray, V. Vorsa, and W. C. Lineberger, *J. Chem. Phys.* **95** (21), 8028 (1991).
- ⁶⁹ J. M. Papanikolas, V. Vorsa, M. E. Nadal, P. J. Campagnola, J. R. Gord, and W. C. Lineberger, *J. Chem. Phys.* **97** (9), 7002 (1992).
- ⁷⁰ V. Vorsa, S. Nandi, P. J. Campagnola, M. Larsson, and W. C. Lineberger, *J. Chem. Phys.* **106** (4), 1402 (1997).
- ⁷¹ A. Sanov, S. Nandi, and W. C. Lineberger, *J. Chem. Phys.* **108** (13), 5155 (1998).
- ⁷² B. J. Greenblatt, M. T. Zanni, and D. M. Neumark, *Chem. Phys. Lett.* **258**, 523 (1996).
- ⁷³ B. J. Greenblatt, M. T. Zanni, and D. M. Neumark, *Science* **276**, 1675 (1997).
- ⁷⁴ M. T. Zanni, B. J. Greenblatt, and D. M. Neumark, *J. Chem. Phys.* **109** (22), 9648 (1998).
- ⁷⁵ M. T. Zanni, A. V. Davis, C. Frischkorn, M. Elhanine, and D. M. Neumark, *J. Chem. Phys.* **112** (20), 8847 (2000).
- ⁷⁶ A. V. Davis, M. T. Zanni, C. Frischkorn, M. Elhanine, and D. M. Neumark, *J. Electron Spectrosc.* **112**, 221 (2000).
- ⁷⁷ A. V. Davis, R. Wester, A. E. Bragg, and D. M. Neumark, *J. Chem. Phys.* **117** (9), 4282 (2002).
- ⁷⁸ L. Lehr, M. T. Zanni, C. Frischkorn, R. Weinkauff, and D. M. Neumark, *Science* **284**, 635 (1999).

- ⁷⁹ A. V. Davis, M. T. Zanni, C. Frischkorn, and D. M. Neumark, *J. Electron Spectrosc.* **108**, 203 (2000).
- ⁸⁰ M. T. Zanni, C. Frischkorn, A. V. Davis, and D. M. Neumark, *J. Phys. Chem. A* **104** (12), 2527 (2000).
- ⁸¹ C. Frischkorn, A. E. Bragg, A. V. Davis, R. Wester, and D. M. Neumark, *J. Chem. Phys.* **115** (24), 11185 (2001).
- ⁸² M. T. Zanni, B. J. Greenblatt, A. V. Davis, and D. M. Neumark, *J. Chem. Phys.* **111** (7), 2991 (1999).
- ⁸³ G. Gantefor, S. Kraus, and W. Eberhardt, *J. Electron Spectrosc.* **88**, 35 (1998).
- ⁸⁴ N. Pontius, P. S. Bechthold, M. Neeb, and W. Eberhardt, *Appl. Phys. B* **71** (3), 351 (2000).
- ⁸⁵ N. Pontius, P. S. Bechthold, M. Neeb, and W. Eberhardt, *Phys. Rev. Lett.* **84** (6), 1132 (2000).
- ⁸⁶ N. Pontius, P. S. Bechthold, M. Neeb, and W. Eberhardt, *J. Electron Spectrosc.* **114**, 163 (2001).
- ⁸⁷ N. Pontius, M. Neeb, W. Eberhardt, G. Luttgens, and P. S. Bechthold, *Phys. Rev. B* **67** (3), 035425 (2003).
- ⁸⁸ A. E. Bragg, R. Wester, A. V. Davis, A. Kammrath, and D. M. Neumark, *Chem. Phys. Lett.* **376**, 767 (2003).
- ⁸⁹ A. V. Davis, R. Wester, A. E. Bragg, and D. M. Neumark, *J. Chem. Phys.* **118** (3), 999 (2003).
- ⁹⁰ R. Mabbs, K. Pichugin, E. Surber, and A. Sanov, *J. Chem. Phys.* **in press** (2004).
- ⁹¹ S. Wolf, G. Sommerer, S. Rutz, E. Schreiber, T. Leisner, L. Woste, and R. S. Berry, *Phys. Rev. Lett.* **74** (21), 4177 (1995).
- ⁹² T. Leisner, S. Vajda, S. Wolf, L. Woste, and R. S. Berry, *J. Chem. Phys.* **111** (3), 1017 (1999).
- ⁹³ H. Hess, K. R. Asmis, T. Leisner, and L. Woste, *Eur. Phys. J. D* **16** (1-3), 145 (2001).
- ⁹⁴ I. Andrianov, V. Bonacic-Koutecky, M. Hartmann, J. Manz, J. Pittner, and K. Sundermann, *Chem. Phys. Lett.* **318**, 256 (2000).
- ⁹⁵ D. W. Boo, Y. Ozaki, L. H. Andersen, and W. C. Lineberger, *J. Phys. Chem. A* **101** (36), 6688 (1997).

- ⁹⁶ E. Schreiber, *Femtosecond Real-Time Spectroscopy of Small Molecules and Clusters*. (1998).

2.1. Introduction

This chapter provides the detailed descriptions of the molecular beam apparatus constructed in this laboratory. The content is divided into four sections dedicated to vacuum chamber, primary mass spectrometer, and reflectron and photoelectron spectrometers, and experimental procedures. The first section describes the exterior of the mass spectrometer which serves as a vessel containing the necessary ion-optic components used for guiding and detecting ions. Later part of the first section delineates the vacuum devices used for evacuating the vacuum chamber, which includes vacuum pumps, the foreline network, valves and gauges. The designs of ion sources are described at the end of the first section. The tandem mass/photoelectron spectrometer is described in the second and third sections. In the last section, the general overview of the experimental procedure is described. In order to avoid lengthy description of components, abbreviated nomenclatures are used: The machined components are indicated by the AutoCad file name (.dwg), and the purchased items are referred by the vendors and their part numbers.

2.2. Vacuum Chambers

The molecular beam machine consists of four custom-made chambers which are connected by hybrid adapters and reducers (Fig. 2.1). The source (CHMB-SRCE) and buffer chambers (CHMB-BFF) were fixed on the aluminum plate which is elevated to 3 feet high. All the ports in both source and buffer chambers have ASA type connection for the vacuum seal. The ASA style vacuum-seal is suitable for the source and buffer chambers since the ASA type O-ring sealing can maintain high vacuum (1×10^{-8} torr) and can be backed to 200 °C. The ASA flanges are easy to assemble and disassemble, which

is desirable for replacing ion source components such as a poppet in the pulse nozzle and a tungsten filament in the electron gun.

The partition flange (CHMB-PRTN) with a center hole (R 0.5) was inserted in between the source and buffer chambers. The partition flange serves as the base plate for mounting various sizes of skimmers and apertures. (Fig. 2.1.2) The aperture size is critical for generating negative ion as well as achieving the differential pumping inside molecular beam apparatus. The appropriate size of the aperture is generally determined by the type of ion source used in the experiment as well as the backing pressure in the gas inlet line. For instance, a disk with 1.0 cm hole was installed for the continuous electron gun whereas the skimmer with 1.0 mm hole was used for the pulsed electron gun. For making large size clusters, smaller aperture size was chosen to maintain the high vacuum in the photoelectron and the reflectron spectrometers. Relation between the aperture size and the ion source will be discussed later in this chapter.

As illustrated in Fig. 2.1, the mass spectrometer chamber (CHMB-MSS) was connected to the buffer chamber by ASA4-CF600 hybrid adapter which allows the transition from ASA to CF seals. Even though all the experiments presented in this thesis have been carried out under high vacuum, the CF-type fitting is employed for future applications that require ultrahigh vacuum. The spectrometer chamber was situated perpendicular to the buffer chamber such that the time-of-flight (TOF) axis in the buffer chamber is extended from the ASA4 port near the partition plate. It is important to have a short distance between the TOF axis and molecular beam nozzle in order to allow more ions to enter the ion-accelerator. The four-way cross (CRSS-MSS), a gate valve and the CF600-CF800 nipple (NIP-C-B) were retrofitted in order to add a

turbomolecular pump in the mass spectrometer. The addition of the turbomolecular pump improved the pumping speed and maintain high vacuum in the laser interaction region.

The tandem photoelectron spectrometer is vertically placed on the top CF600 port of the mass spectrometer chamber (CHMB-MSS). The vacuum chamber for the photoelectron spectrometer consists of two 10" long nipples (4" O.D. tube) and two double-sided CF600 flanges (CF600-SLN, CF600-EFT), CF600 flange (CF600-MCP) and ASA4 flange (ASA4-MCP). This design permits to implement two different types of photoelectron (PE) spectrometers: μ -metal shielded field-free PE spectrometer and magnetic-bottle type PE spectrometer. The tube length for the field-free PE spectrometer is about half of the magnetic-bottle PE spectrometer, and the change can be easily done by removing one of the 10" tubes. Detail will be discussed later.

The reflectron chamber (CHMB-RFL) serves as the mounting platform for all the tandem mass spectrometer. Besides the source and buffer chambers, only the reflectron chamber is supported on the aluminum frame (Mini-Tech). Unlike the source and buffer chamber, however the reflectron chamber is secured on the aluminum base plate which can be translated along the TOF axis. This translating chamber platform was implemented by utilizing a set of two parallel linear rails (48" long: Thomson LPS-SS-60 Care Linear Race) and four ball bearing pillow blocks (Thomson). The linear race containing two ball bearing blocks is supported by the low shaft supports (Thomson), and the aluminum base plate is secured on top of the four pillow blocks. The sliding chamber on a rail-bearing assembly provides maximum access to the interior of the apparatus without altering the alignment of the mass spectrometer.

2.3. Vacuum System

In general, typical base pressure required for the gas-phase laser spectroscopy is in the high vacuum regime ($10^{-5} \sim 10^{-8}$ torr). At this pressure range, the mean free path (λ) reaches up to a few meters while the number density (ρ) decreases down to $10^{10} \sim 10^8$ cm^{-3} .¹ For ion detection, the pressure range in low 10^{-7} torr ($\lambda \sim 10^4$ cm, $\rho \sim 10^9$ cm^{-3}) is sufficient; on the other hand, chamber pressure down to 10^{-9} torr ($\lambda \sim 10^6$ cm, $\rho \sim 10^7$ cm^{-3}) or even less might be necessary for electron detection. Especially, when photoelectrons are collected by irradiating UV or VUV light, significant amount of background noise can be produced by ionizing the background gas. This problem has not been encountered in this laboratory since photodetachment experiments have been carried out at 800 or 400 nm. However, we do see background photoelectron noise when 266 nm light is illuminated into the chamber.

Figure 2.2 shows the schematic representation of the vacuum system including pumps, valves, vacuum gauges and foreline layout. The source chamber is pumped by the 6.0" diffusion pump (Varian, VHS-6) which is backed by the combined unit of Roots pump ((LEYBOLD, RUVAC WAU251) - mechanical pump (LEYBOLD, TRIVAC D65 BCS). The discharge flange of the Roots pump is directly connected to the intake of the mechanical pump by stacking the Roots pump on top of the mechanical pump. The WAU251 unit has the internal bypassing channel which prevents overheating of the impellers in the case of the backing pump failure. Nonetheless, electrical relay in the power switch of WAU2521 was installed, which automatically turns off WAU251 when the electrical power line of the backing pump shuts off involuntarily.

The high pumping speed (210 m^3/h) of the conjoined WAU251-D65 BCS unit

accommodated the large throughput in the source chamber. In particular, high stagnation pressure in the gas line is used for making large size clusters, which increases the pressure inside source chamber. The typical pressure of the source chamber is at low 10^{-4} torr under continuous operation (20 Hz), and the pressure in the foreline does not exceed 0.1 torr, which is well below the back-streaming limit (0.55 torr). We observed the ion intensity fluctuation as well as decrease in intensity when the chamber pressure is in high 10^{-4} range. Large throughput can be avoided by using a molecular beam nozzle with smaller orifice size or by adjusting the pulse valve opening time, however, such manipulations can affect the cluster generation. Details will be discussed in later when the ion sources are described.

High vacuum in the rest of chambers (CHMB-BFF, CHMB-MSS and CHMB-RFL) is achieved by a 6" diffusion pump (Varian, VHS-6), a 4.0" turbomolecular pump (PFEIFFER: Balzers, TPU 510) and a 4.0" diffusion pump (Varian, VHS-4) which are backed by a mechanical pump (LEYBOLD, D65 BCS). (Fig. 2.2) Turbomolecular pump was added to the vacuum system after the first design was completed. The retrofitting of the turbomolecular pump was accomplished by inserting four-way crosses (CF600 and O.D. 4.0" tube) in between the CF600-ASA4 hybrid adapter (NIP-C-T) and the mass spectrometer chamber (CHMB-MSS). The turbomolecular pump was attached to the cross with the horizontal configuration, and the remaining port was sealed by a blank CF600. The horizontal orientation is allowed for TPU 510, but the pumping speed is slightly diminished.

Since the molecular beam flux in the buffer and the spectrometer chambers is relatively small, one dual stage rotary vane pump is sufficient to back the two diffusion

pumps and a turbomolecular pump. The foreline pressure is maintained below 10^{-2} torr with molecular beam valve operation. For every diffusion pump, a liquid nitrogen trap (Varian, 0362 Cryo Baffle) was appended above the diffusion pumps to prevent the hydrocarbon vapor back-streaming.

As described above, two separate forelines are assembled for the source chamber and the spectrometer chambers. For designing the foreline network, the following two points are considered: conductance (flow rate) and vibration isolation. The pressure in the roughing line is in viscous flow regime ($1 \sim 10^{-3}$ torr), thus the flow rate depends on the length and the cross section of the tube and also the foreline network.² Cross sections of the roughing parts are 50 mm I.D. (NW50) except for the 40 mm I.D. flexible stainless steel hose (NW40) KF) used in the foreline of the VHS-4. The foreline of the VHS-4 which is attached to CHMB-RFL needs to be flexible in order to translate the mass spectrometer. The Kwik-ISO fittings are used in most of the roughing components for easy assembly. In order to increase the conductance in the roughing line, the foreline network was designed to have the maximum straightness and minimum tube length. The foreline trap containing the stainless steel sieve is attached to the intake of the mechanical pump (or Roots pump for source foreline) in order to prevent the contamination of the diffusion pump charge by the mechanical pump oil vapor.

For both source chamber and mass spectrometer forelines, 20" long thin wall bellows (NW50) were installed within the foreline network in order to isolate the vibration caused by the mechanical pump and the Roots pump. The foreline of the source chamber was bifurcated, and the second branch was connected directly to the source and buffer chambers for the detour roughing line.

The pressure of the molecular beam apparatus was measured by three iridium ion gauges (Granville-Phillips), a convectron gauge (Granville-Phillips) and a thermocouple gauge (Duniway Stockroom). The chamber pressure ranging from one atmosphere down to 10^{-3} torr is measured by the convectron and thermocouple gauges. Once high vacuum ($<10^{-5}$ torr) is achieved, the ion gauges were turned on to monitor the chamber pressure. The foreline pressure was measured near the output ports of the diffusion pumps by thermocouple gauges (Duniway Stockroom) and a convectron gauge (Granville-Phillips).

It is important to follow the protocol for evacuating chambers because an incorrect sequence of pump-down procedure may contaminate the vacuum chambers and possibly destroy the vacuum pumps. The diffusion pump should be operated below 10^{-2} torr to avoid burning the hydrocarbon pump charge. Thus, preliminary evacuation by the detour roughing is necessary if the chamber has been opened to atmosphere. When the mechanical pump is turned off, a pressure gradient can be built in the foreline (low pressure at the output of the diffusion pump and higher pressure at the intake of the mechanical pump), which can cause the backflow of the mechanical pump oil into the diffusion pump. To prevent the backflow, a vent hole was installed near the output port of the diffusion pump, and the vent hole was opened to atmosphere right before turning the mechanical pump off, which blocks back-stream by reversing the pressure gradient

The schematic representation of the interlock system is illustrated in Appendix A. The purpose of the interlock system is to protect contaminating chambers and to avoid burning the diffusion pump oil. In any type of vacuum component failure (including mechanical pump, diffusion pump, chiller, etc.), the interlock unit will automatically

close the pneumatic controlled gate valves (Temescal, 5030 and MDC) and angle valves (MDC), which isolates the chamber from the pumps and close the foreline-network at the diffusion pumps output.

The base pressure of low 10^{-8} torr was achieved by our vacuum system. The pump-down rate depends on the types of chemical system introduced in the system, but generally it takes ~ 8 hours to attain mid 10^{-8} torr from atmosphere pressure. The operating pressure is determined by a number of different factors such as the orifice size of the pulse nozzle, backing pressure, type of carrier gas, opening time and duty cycle of the pulse valve. Under our typical experimental condition (orifice size: 200 \sim 500 μm ; backing pressure: 1 \sim 4 atm of argon, helium or nitrogen gas; opening time: 200 \sim 500 μs at 20 Hz), the pressure inside the mass spectrometer and reflectron chambers are maintained down to $1 \sim 2 \times 10^{-6}$ and $2 \sim 5 \times 10^{-7}$ torr, respectively. At this pressure, all the high voltage devices including ion accelerator, massgate and multi-channel plate detectors were operated properly without causing any arcing.

2.4. Ion Source

The ion source is composed of three parts: gas inlet system, molecular beam valve, and thermionic electron emitter (electron gun). The entire source assembly is mounted on the 2.0" tubing which stems from the back flange of the source chamber (Fig. 2.3). The linear race-ball bearing setup (Thomson) is also adopted for mounting the back flange. Two parallel aluminum bars (2" x 1" x 9") is fixed to the back flange, and each bar is attached to an aluminum platform (2.5" x 4.5" x 1.5") which sits on a pair of ball bearing pillows. The rail extends 24" from the end of the source chamber, which

permits the entire assembly to be pulled out of the source chamber, which facilitates replacing the poppet used in the solenoid valve and the filament used in electron gun. Moreover, the rail-bearing setup retains the nozzle position with respect to the skimmer, which is crucial for maintaining the previous experimental conditions.

When the gas inlet system was designed, two factors were considered. First, the inlet system should have a fine tunability for mixing different types of gases or vapors. The composition of the gas mixture as well as the types of carrier gas is extremely critical for generating negatively charged species. For instance, the ion intensity of Azobenzene anion increases when small amount of oxygen gas was presented in the carrier gas (either argon or nitrogen gas). However, if the amount of oxygen exceeds the optimal mixing ratio, the ion intensity of Azobenzene anion decreases because the electrons are consumed for making oxygen anion instead. The fine adjustment of the mixing ratio was accomplished by utilizing a pair of mass flow controllers (MKS, 1179A) which have the flow-scale range of 10 and 100 sccm.

The second factor is the heating assembly in the high temperature inlet manifold. For many cases, sufficient amount of vapor can be prepared at 200 °C, which can be routinely achieved by wrapping the standard wire-heater around the sample oven and the inlet system. On the other hand, heating a sample above 200 °C is not trivial mainly due to degradation of vacuum seals and condensation of the sample. Proper thermal isolation is another important factor to achieve efficient heating. In our design, high temperature-rated materials were used in our inlet system. Ceramic blocks (macor or alumina) were used for thermal and electrical isolation. The plastic parts in the gas inlet system were replaced by the high temperature-rated polymers (Teflon or Vespel), and Buna-N o-ring

were replaced by viton O-ring or copper gasket.

It is critical to maintain the temperature gradient such that the nozzle outlet is higher than the sample reservoir in order to prevent the vapor from being condensed. It is ideal to put the sample reservoir as close to the nozzle as possible to achieve uniform heating. Figure 2.3 shows the high temperature sample oven and the inlet system used for generating adenine and thymine vapors. The sintered-filter (SS-316, 1 micron) assembly (Swagelok, Nuprofilter-F series) was used for the sample oven which is heated by the cable nozzle heater (Watlow). The high temperature inlet system is thermally isolated by inserting a macor disk in between the sample oven and the mounting tube. The temperature of the inlet system was measured by nickel based thermocouple wires.

In our experiment, molecular beam was pulsed by using the externally triggered solenoid valve (20 Hz). The commercially available solenoid valve (Parker, General Valve Series 9) was modified in order to use at high temperature (> 200 °C). The stainless-steel housing for the solenoid was reused, while the enamel coated solenoid coil was replaced by the high temperature rated Teflon coated wire (OMEGA, TFCP-005). The resistance of the modified coil assembly (~ 20 ohm) was slightly smaller than the original assembly (~ 27 ohm). Nonetheless, the same electrical pulse (240 V, 1.5 A) was applied to the modified solenoid, which was driven by the multi-channel high voltage pulse generator (Parker, IOTA One).

2.4.1. Thermionic Electron Emitter (Electron Gun)

Negatively charged ions are more difficult to generate than the positively charged ions since negative ions cannot be produced directly from the electron impact ionization

as can positive ions. The commonly accepted mechanism of producing negatively charged species is the *secondary* electron attachment by three-body collision, dissociative attachment and evaporative attachment.³



The secondary electron refers to the conjugate electron of the positive ion which is generated by impacting the primary electron to the parent neutral. Thus, the key to produce large amount of negative ions is to promote the secondary electron generation and electron-molecule collision. One commonly used method is crossing the high kinetic energy (~ 1 keV) electron beam with the molecular beam at the nozzle hole where the molecular density is highest.⁴ When a fast electron penetrates through the molecular beam, many ionization processes can occur by successive inelastic collisions, leaving a trail of low energy electrons. Thus, the secondary electron can be multiplied by injecting the high kinetic energy electron into the dense region of the molecular beam.

Over the last few decades, many variations of ingenious designs have been developed for generating large flux of thermionic electrons.^{3,5-10} In the course of developing ion optic components, the injection of high energy electron (~ 1 keV) has provided an innovative leap in the negative ion generation. Besides the aforementioned advantage, this method can surpass the coulomb-repulsion limit imposed on the low-energy electron injection, which increases the number density of the electron stream. Author must note that the electron gun is one of many methods for preparing negatively charged species in gas phase, and there is no widely-accepted universal method for

making negative ions. For many cases, a specific type of ion source is favored for making a particular ionic species. In order to expand the scope of the research subject, it is essential to equip with various kind of ion sources such as ion-sputtering source, laser ablation source, plasma-discharge source, electrospray source, etc.

This thesis provides detailed descriptions of the two different types of electron guns which have been most extensively used in this laboratory. The main difference of the two electron guns is that one operates in pulsed mode and the other generates continuous electron beam. Even though both electron guns can produce same ionic species, the properties of the ions can vary depending very much on the choice of electron gun. The operating mechanisms of the two ion sources are quite different, which can affect the size distribution of clusters and the vibrational temperature of negatively charged species. The influence of the ion source on the properties of the ions will be discussed later (Chapters 3-8). In addition to the electron guns, a pulsed plasma-discharge and a Corona discharge were also constructed, but only briefly used for specific applications.

2.4.2. Pulsed Electron Gun

The pulsed electron gun shown in Fig. 2.4 has been most extensively used in this laboratory because of its versatility and stability. The key feature of the pulsed electron gun is the capability of trapping the high energy electrons traveling outward and reusing the trapped electrons to induce electron-impact ionization. This feature is achieved by building a high voltage trapping cage around the filament. The electrons generated from the filament bounces around inside the trap as far as the electric field applied on the trap

is higher than the repelling voltage applied on the filament. The simulated electron trajectory is shown in Fig. 2.5. (SIMION 7.0)

The pulsed electron gun consists of three parts: filament, trapping cage and ion-guide. (Fig. 2.4) The thermionic electrons are generated from a thin tungsten wire (0.015" thickness) or a thoriated iridium (0.010" thickness) wire. The thoriated iridium wire is preferably used because the tungsten filament is not chemically inert and contaminates the electrodes. The trapping cage is constructed by sandwiching the trapping fence between two plates. The closed loop (2.0" O.D. and 0.4" long) made from a strip of the stainless steel mesh (40 x 40) was used as the trapping fence. The fence is attached to the bottom plate (EG-PL3) by utilizing three L-shaped posts (SS-316, 0.02" O.D.). The short edge of the post is spot-welded onto the bottom plate while the long edge is spot-welded onto the grid. (Fig. 2.4.1) The lid of the electron cage (EG-PL2) sits on top of the fence and three macor spacers (EG-SP-MC2). The spacer is made to be ~ 0.01" shorter than the height of fence in order to ensure the electrical contact between EG-PE2 and EG-PL3.

The ion guide corresponds to the inner tube connected to the top plate, which has the ground electric potential. The purpose of the ion guide is to create the ground electric potential inside the tube such that the ion stream can travel to the ion accelerator without experiencing the high electric field emanating from the filament and the electron cage. The tubing (1.0" O.D, 1.5 cm long) is fused to the top plate (EG-PL1), and EG-PL1 is placed on three macor spacers (EG-SP-MC1) to be electrically isolated from the electron cage.

The electrical connection is shown on left-hand side of Fig. 2.4. Two small

openings are carved out from the trapping fence in order to connect the current supply to the filament (not shown). The source can be operated in both continuous and pulsed modes by simply changing the high voltage supply, but the latter provides better shot-to-shot stability and also eliminates the long-term drift of the ion intensity. The physics is not well understood, but author speculates that stray charges might be accumulated on the electrodes and the ion guide, which perturbs the initial electric fields created in the assembly. In the pulse mode, these stray charges can be released since the trapping voltage is applied for short period of time (~ 1 ms). Another advantage of the pulse mode is that the high voltage supply can be electrically grounded through a high resistance since the average current drawn by the circuit is relatively small. (Fig. 2.4)

The high voltage pulse (-1 kV) was generated by the inverting-amplification of a square pulse (+10 V) of which width is about twice longer than the valve opening time. The square pulse produced by the function generator (Wavetek, Model 802) was bifurcated into two high voltage amplifier-inverters. Each output voltage was applied to the filament and the trapping cage, which determines the kinetic energy of the primary electron. In this setup, the delay between the two pulses is fixed and the width of the two pulses cannot be changed independently. It is ideal to apply two separate pulses with independent delay and width, thus it might be worth testing two separate high voltage supplies for future applications.

2.4.3. Continuous Electron Gun

The continuous electron gun is one of the most widely used ion sources by the researchers in the field of gas-phase ion chemistry.³ The electron gun assembly can be

divided into two parts: The electron source part which forms the beam of high energy electrons and the electron optic part which collimate and guide the electron beam. Two different methods were implemented to produce the high energy electron beam. The first method is based on the thermionic-electron generation, and the same operating principle as the pulsed electron gun applies here. The basic design of the source mimics the conventional cathode ray tube in which the electrons emanated from a glowing filament is extracted by the biased voltage between the cathode (filament) and the anode.

The electron flux coming out of the anode is extremely sensitive to the geometry and the position of the electrodes. Unlike the wire filament in the pulsed source which repels electrons in random directions, the cuspidate filament (Kimball Physics, ES-020) was used with the apex pointing toward the anode. The hole-size of the anode and the distance between electrodes affect the electron flux drastically. The following equation roughly describes the relationship between electron current, I and the geometric parameters:

$$I \sim \left(\frac{r_a}{d} \right)^2 V_a^{3/2} \quad (2.4)$$

where r_a , d and V_a correspond to the radius of the hole, the distance between the electrodes and the electric potential of the anode, respectively. Based on a number of experimentations, it is found that the two dimensions are tightly linked; hence when the hole-size is changed, the distance between the electrodes must be adjusted accordingly. In our experiments, about 1 mm separation and the hole-sized between 1 to 3 mm yield the most electron flux.

To accelerate the electrons up to 1keV, it is necessary to float the current supply

at -1.0 kV. To achieve this, an electrically isolated AC to DC converter was assembled by utilizing the step-down transformer (Stancor, P-6133) with a high voltage electric isolation (tested at 7500 V). The input AC was supplied by a variable transformer (Superior), and the stepped-down AC current is converted to DC by a simple electric circuit composed of a glass passivated rectifier (Multicomp) and a capacitor (Sangamo, 16,000 μ F and 15 VDC). (Fig. 2.6) The rectifier was mounted on an aluminum block which serves as a heat sink, and both voltage and current meters were connected for measuring the DC output. The entire circuit including the isolation transformer was built inside a fiberglass enclosure (NEMA) for maximum electric insulation.

The electron beam emitted from the anode is collimated and steered by the einzel lens and a set of vertical-horizontal deflector. Due to the space-charge effect, the electron beam spreads out as it propagates. The three-cylinder einzel lens compensates this spreading of the electron beam by creating a convex equipotential surface inside the cylinder. This subject will be discussed in the later section. Since electrons are very light, focusing and steering can be achieved by small size of electrode. The B-series Kimball Physics components were employed to construct the ion optics. (Fig. 2.6) Figure 2.7 shows the miniature coaxial cable used in the electric connection. The coaxial cable shields the electric field radiating from the wire connections, which is important for guiding electron beam.

The entire assembly of the continuous electron gun was mounted on an ASA4 flange (ASA4-eGUN) and encapsulated by a cylindrical mesh to block the stray electric field radiated from the ion optics. The volume of the entire assembly is small enough to fit inside the ASA4 port of the source chamber (CHMB-SRCE). ASA4-2GUN was

attached horizontally to the port near the partition flange (CHMB-PRTN), which makes the electron beam crosses perpendicularly to the gas jet. A Faraday cup was placed at the opposite side of the source chamber to measure the electron current. Our continuous electron gun produces the electron beam of $\sim 500 \mu\text{A}$ and about 1 mm in diameter.

The ion-formation mechanism of the continuous electron gun is quite different from the pulsed electron gun. Lineberger and his colleagues explained its mechanism in terms of the formation of *neutral* plasma. Crossing the electron beam with gas jet produces the electrically neutral plasma in which low energy electrons and positive ions are confined. Both charged and neutral species suffer many collisions during the plasma-drift time, which increase the secondary electron attachment. When the plasma enters the ion accelerator, ions can be extracted to the mass spectrometer by applying an electric pulse to the ion accelerator, and the charge type is determined by the polarity of the electric pulse applied to the ion accelerator. The key to deliver the maximum amount of ions to the mass spectrometer is to preserve the neutral plasma during the drift time. Since the neutral plasma is fragile, any obstacle along the drift path should be removed. When our continuous electron gun was used, the skimmer (small aperture) was removed from CHMB-PRTN. The electron beam trajectory is shown in Fig. 2.8.

Lineberger group demonstrated that larger clusters can be formed by extending the drift length.^{5,6} Our current setup does not permit the elongation of the drift length, which, author believes, imposes an upper limit for making large cluster. (Detail will be discussed in Chapter 8) In addition, Johnson and coworkers reported the enhancement of the ion flux achieved by counter-propagating the electron beam. We tested this configuration by placing the electron gun at the back flange (FLNG-BFF) of the buffer

chamber. However, no negative ion was detected in the mass spectrometer due to the far separation between the electron gun and the nozzle.

The second method of generating electrons relies on the photoelectric emission. Electrons can be ejected irradiating a laser pulse onto a cathode which is usually made out of a material with low work function. In our design, a multi-channel plate (MCP) was employed as the photocathode. Compared to the metallic cathodes, the MCP photocathode provides a number of advantages. First, it does not warm out by laser irradiation. Second, the photoelectric emission is much more efficient. Third, the photoelectrons can be multiplied by stacking up more MCPs.

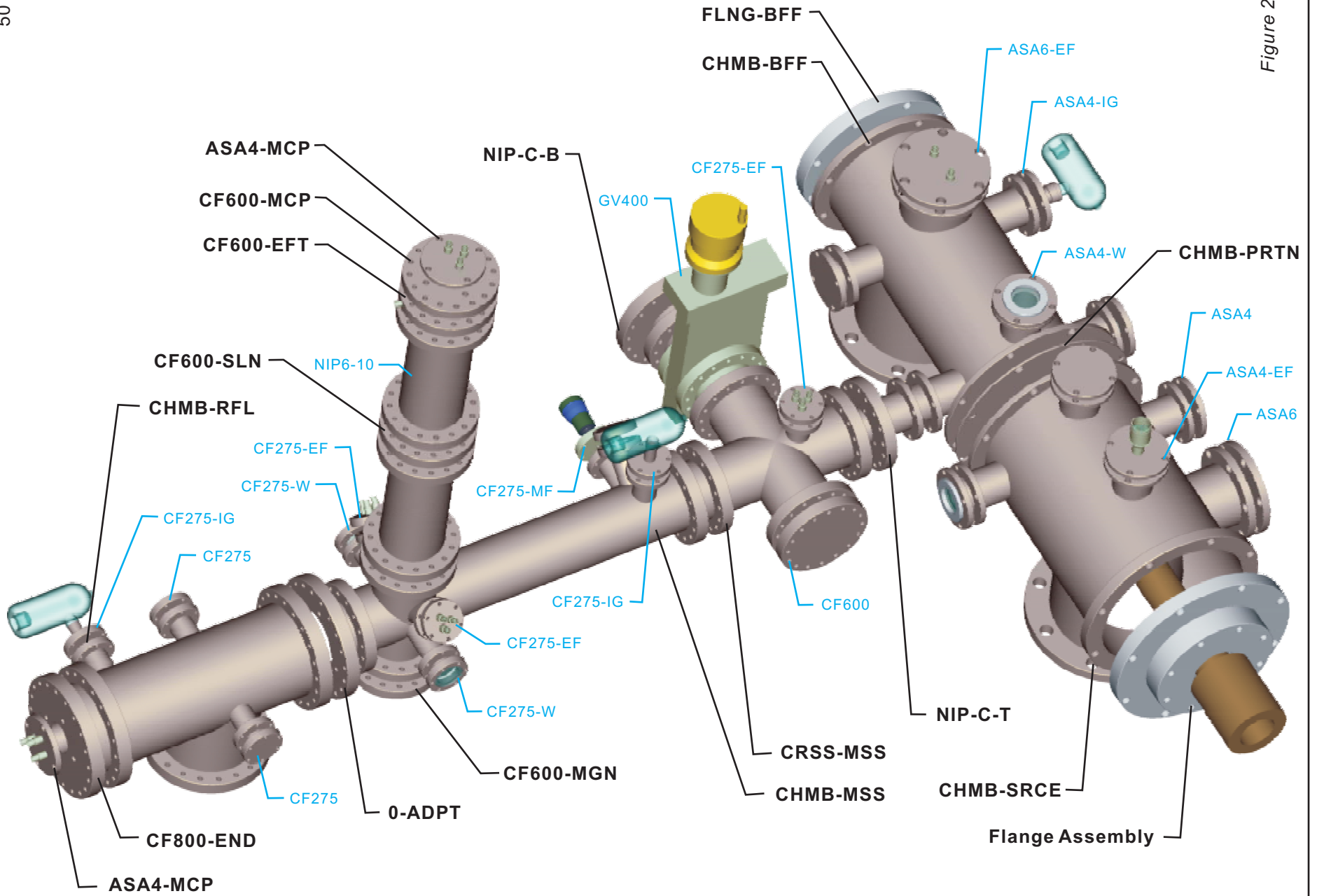
Our photocathode design is similar to the design proposed by Weinkauff and his colleagues. The electron source part consists of a stack of four MCPs and a voltage divider. As shown in Fig. 2.9 each MCP is sandwiched by a pair of stainless steel plates (Kimball Physics, SS-PL-C5X5), and a sheet of a donut-shaped copper shim is inserted inbetween the MCP and the stainless steel plate to ensure the electric contact. Four of these sandwiched MCP assemblies are stacked together with 0.05" spacing between them. A voltage divider was made out of series of resistors which provides three different biased voltages: 200 V across the MCP, 600 V between the MCPs, and 1000 V between the last MCP and the emitter plate (ground). The voltage divider was integrated together with the MCP stack and placed inside of the vacuum chamber due to the limited number of electric feedthroughs. The voltage divider was bent to form a square-spiral to fitted behind the MCP and create a path for the laser beam. (Fig. 2.9)

Converting the filament setup to the photocathode setup was easily done by the following procedures: (1) replace the filament housing by the fused silica window, (2)

remove the anode, (3) place the cathode assembly below the ion optic parts, (4) connect the 6.3 MW resistor in the voltage divider to the MHV feedthrough used for the anode, and (5) connect the other end of the voltage divider to the ground. Fourth harmonic of the nanosecond Nd:YAG laser (Spectra-Physics, Quanta-Ray) was used to induce the photoelectrons, which generated 50 ns electron pulse with the peak current of 1 mA.

2.4.4. Other Ion Sources

In addition to the electron guns described above, the corona discharge source and the pulsed discharge source were constructed. The corona discharge source was used for generating oxygen radical (O). Ozone anion (O_3^-) was produced by passing oxygen gas through the corona discharge source followed by the pulse electron gun produces. This combined source was briefly used for studying the photodissociation of the ozone anion. The pulsed discharge source was made for generating organic radical anions. However, the pulsed discharge source has not been fully tested because the high current-high voltage power supply was not available. The designs for both sources are appended at the end of the thesis (Appendix B).



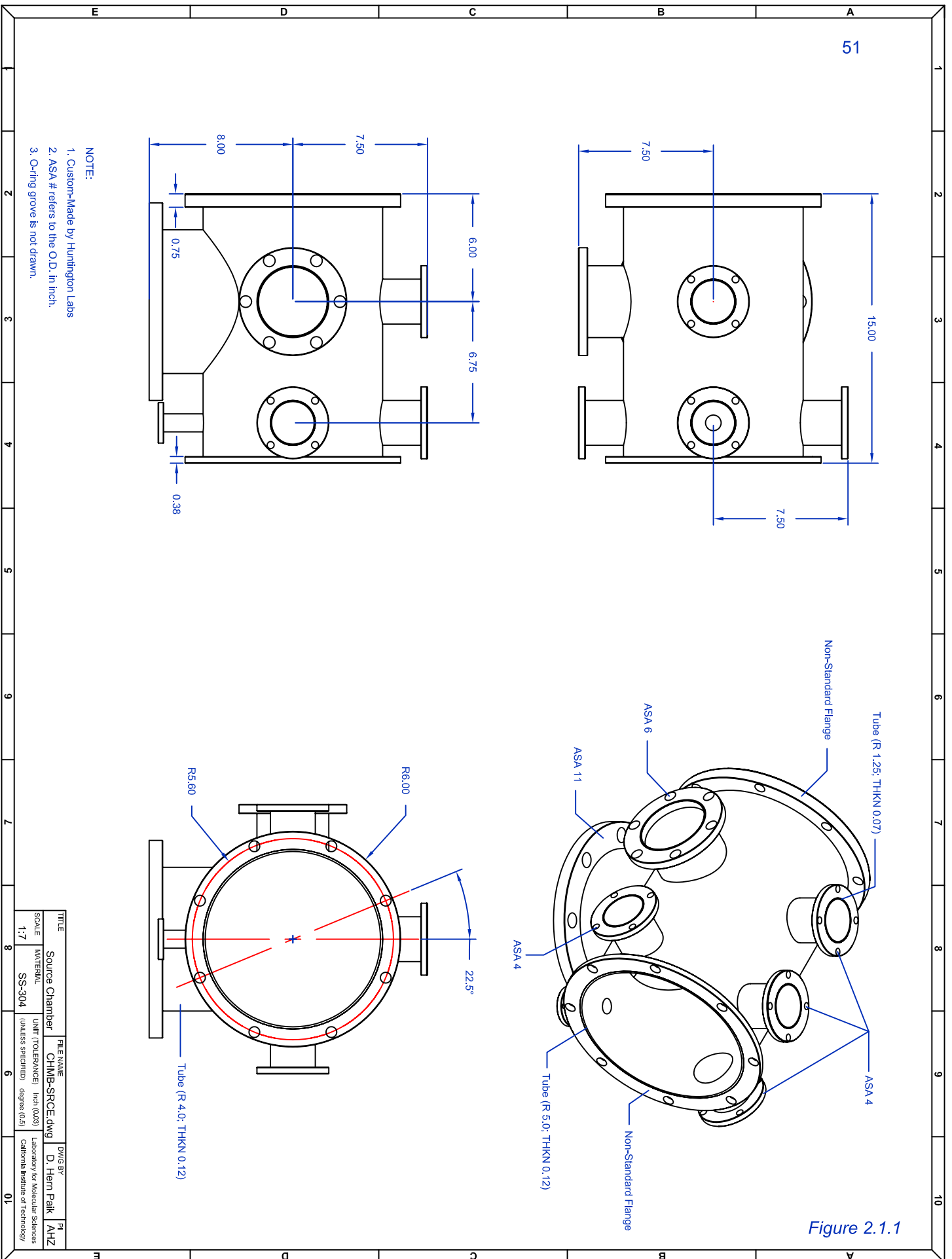
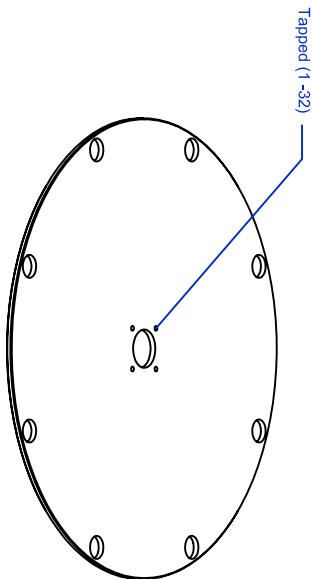
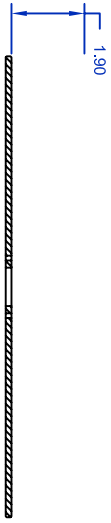
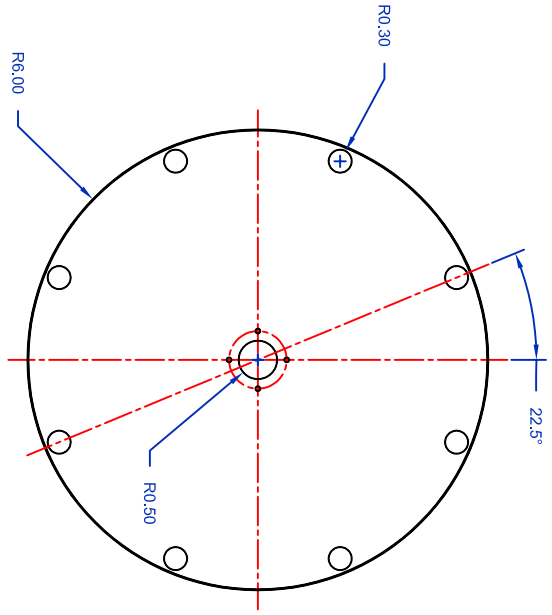


Figure 2.1.1

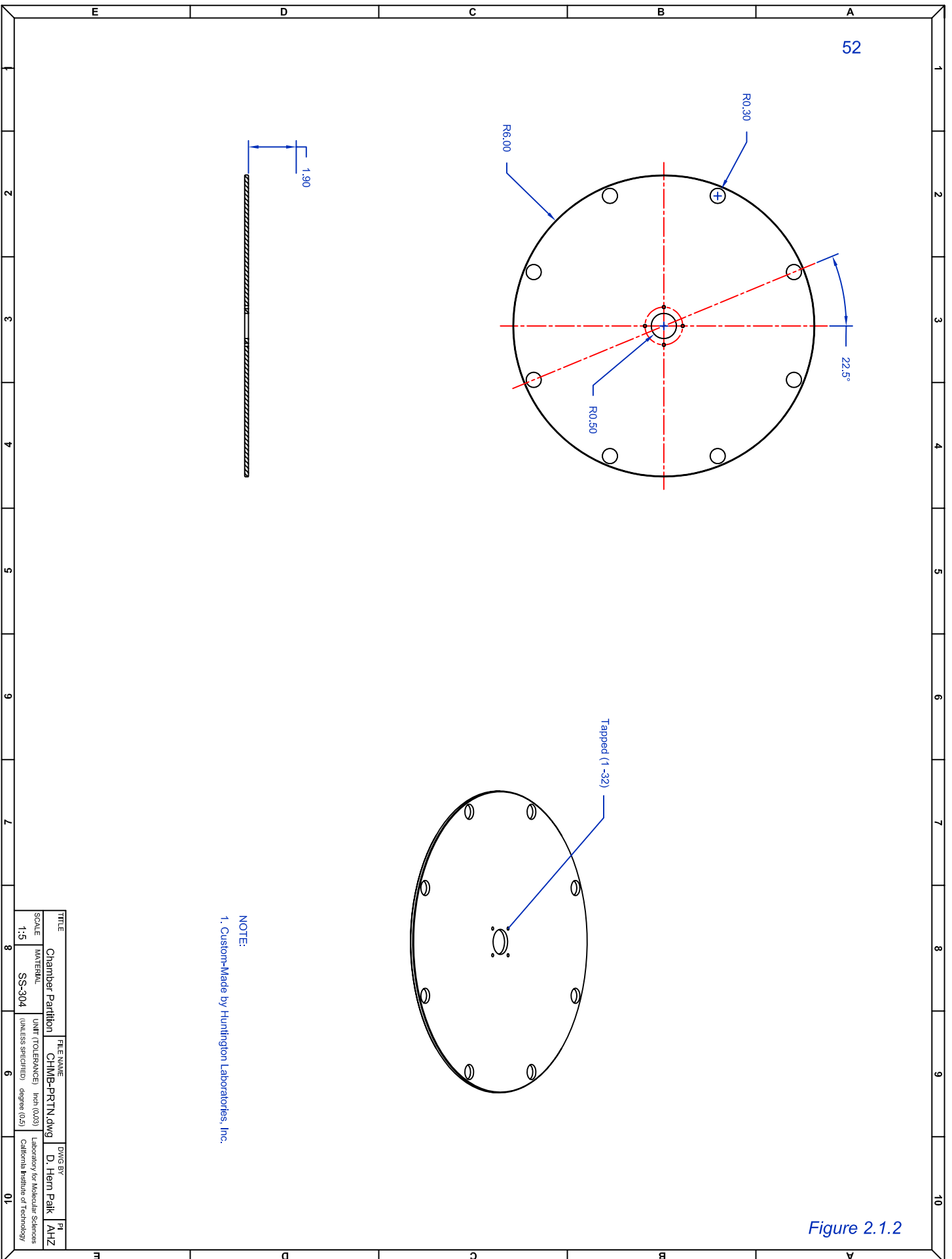
NOTE:
 1. Custom-Made by Huntington Labs
 2. ASA # refers to the O.D. in inch.
 3. O-ring groove is not drawn.

TITLE	FILE NAME	DWG BY	PI
Source Chamber	CHMB-SRCE.dwg	D. Hahn Park	AHZ
SCALE	UNIT (TOLERANCES)	LABORATORY FOR MOLECULAR SCIENCES CALIFORNIA INSTITUTE OF TECHNOLOGY	
1:7	(UNLESS SPECIFIED) degree (0.5)		



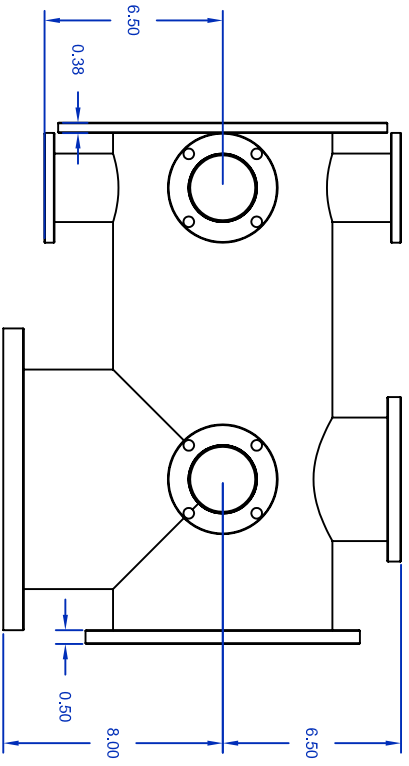
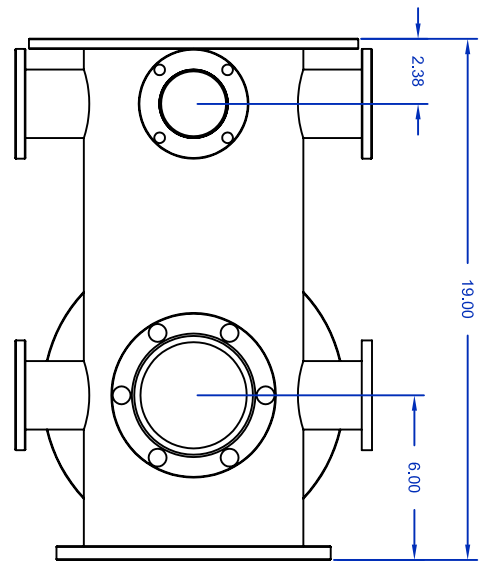
NOTE:
1. Custom-Made by Huntington Laboratories, Inc.

Figure 2.1.2



TITLE	CHamber Partition	FILE NAME	CHMB-PRTN.dwg	DWG BY	D. Hahn Park	PL	AHZ	
SCALE	1:5	MATERIAL	SS-304	UNIT TOLERANCES	inch (0.03) degree (0.5)			Laboratory for Molecular Sciences California Institute of Technology
							01	

53



- NOTE:
1. Custom-Made by Huntington Labs
 2. ASA # refers to the O. D. in inch.
 3. O-Ring groove is not drawn

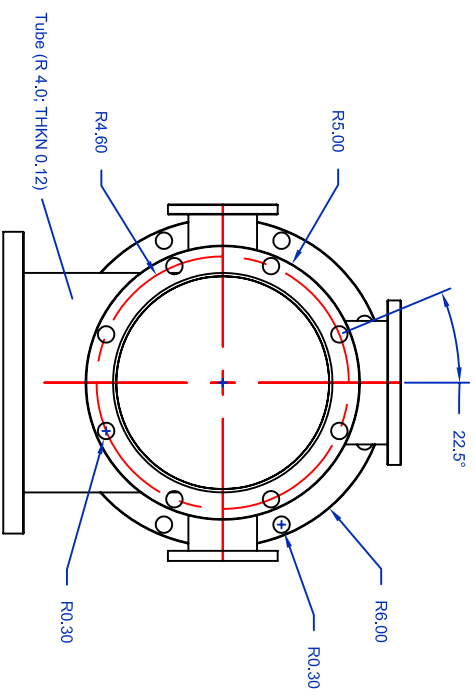
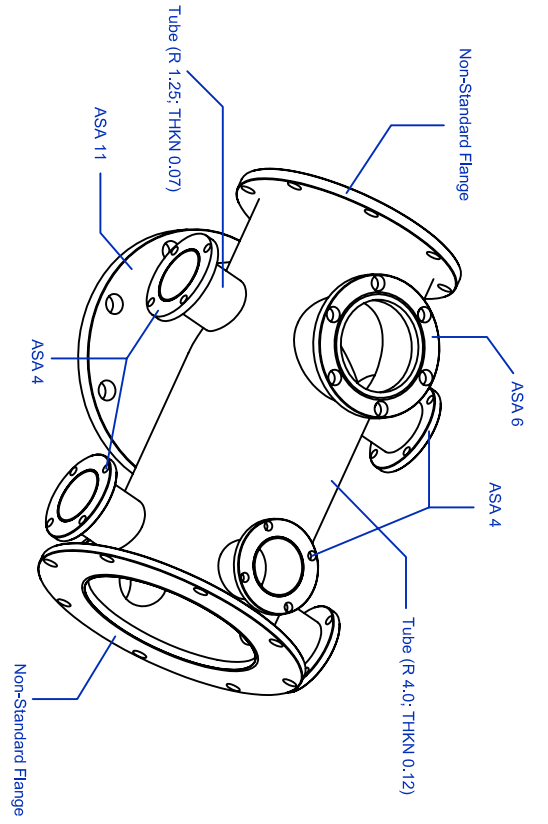


Figure 2.1.3

TITLE	Buffer Chamber	FILE NAME	CHMB-BFF.dwg	DWG BY	D. Hain Park	PL	AHZ
SCALE	1:7	MATERIAL	SS-304	UNIT TOLERANCES	inch (0.03)	Laboratory for Molecular Sciences California Institute of Technology	
				(UNLESS SPECIFIED)	degree (0.5)		

54

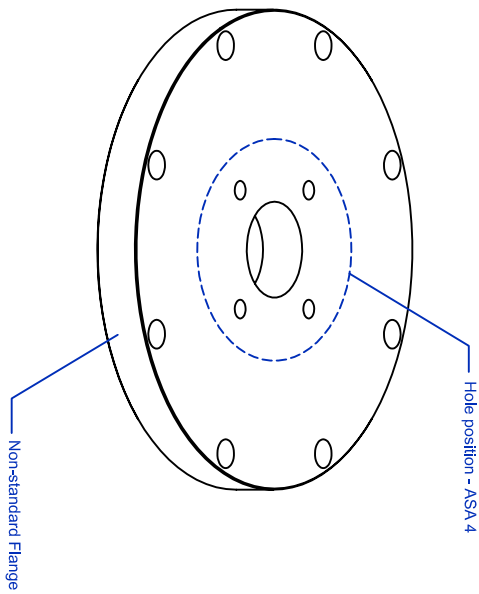
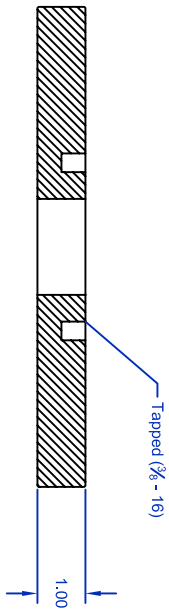
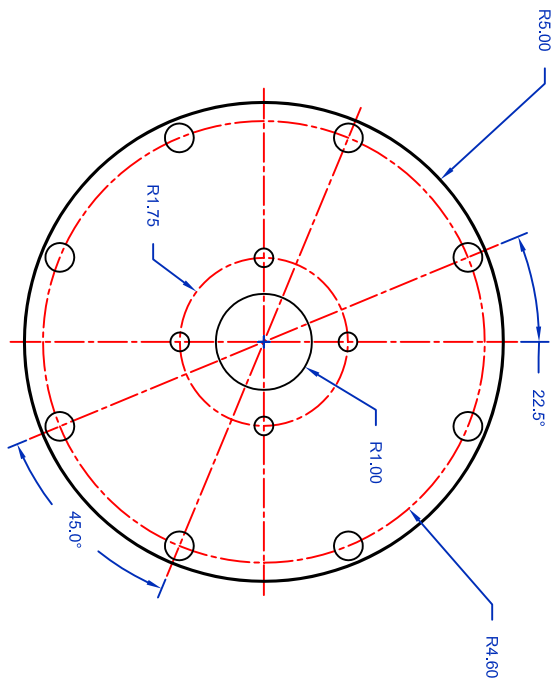


Figure 2.1.4

1	2	3	4	5	6	7	8	9	10																				
A	B	C	D	E						A																			
<table border="1"> <tr> <td>TITLE</td> <td>FILE NAME</td> <td>DWG BY</td> <td>PI</td> </tr> <tr> <td>Flange for Buffer CHMP</td> <td>FLNG-BFF.dwg</td> <td>D. Hain Park</td> <td>AHZ</td> </tr> <tr> <td>SCALE</td> <td>MATERIAL</td> <td>UNIT (TOLERANCES)</td> <td>(UNLESS SPECIFIED) degree (0.5)</td> </tr> <tr> <td>1:4</td> <td>AL 6061</td> <td>inch (0.03)</td> <td>Laboratory for Molecular Sciences California Institute of Technology</td> </tr> <tr> <td>8</td> <td>6</td> <td>01</td> <td></td> </tr> </table>										TITLE	FILE NAME	DWG BY	PI	Flange for Buffer CHMP	FLNG-BFF.dwg	D. Hain Park	AHZ	SCALE	MATERIAL	UNIT (TOLERANCES)	(UNLESS SPECIFIED) degree (0.5)	1:4	AL 6061	inch (0.03)	Laboratory for Molecular Sciences California Institute of Technology	8	6	01	
TITLE	FILE NAME	DWG BY	PI																										
Flange for Buffer CHMP	FLNG-BFF.dwg	D. Hain Park	AHZ																										
SCALE	MATERIAL	UNIT (TOLERANCES)	(UNLESS SPECIFIED) degree (0.5)																										
1:4	AL 6061	inch (0.03)	Laboratory for Molecular Sciences California Institute of Technology																										
8	6	01																											
E	D	C	B	A						E																			

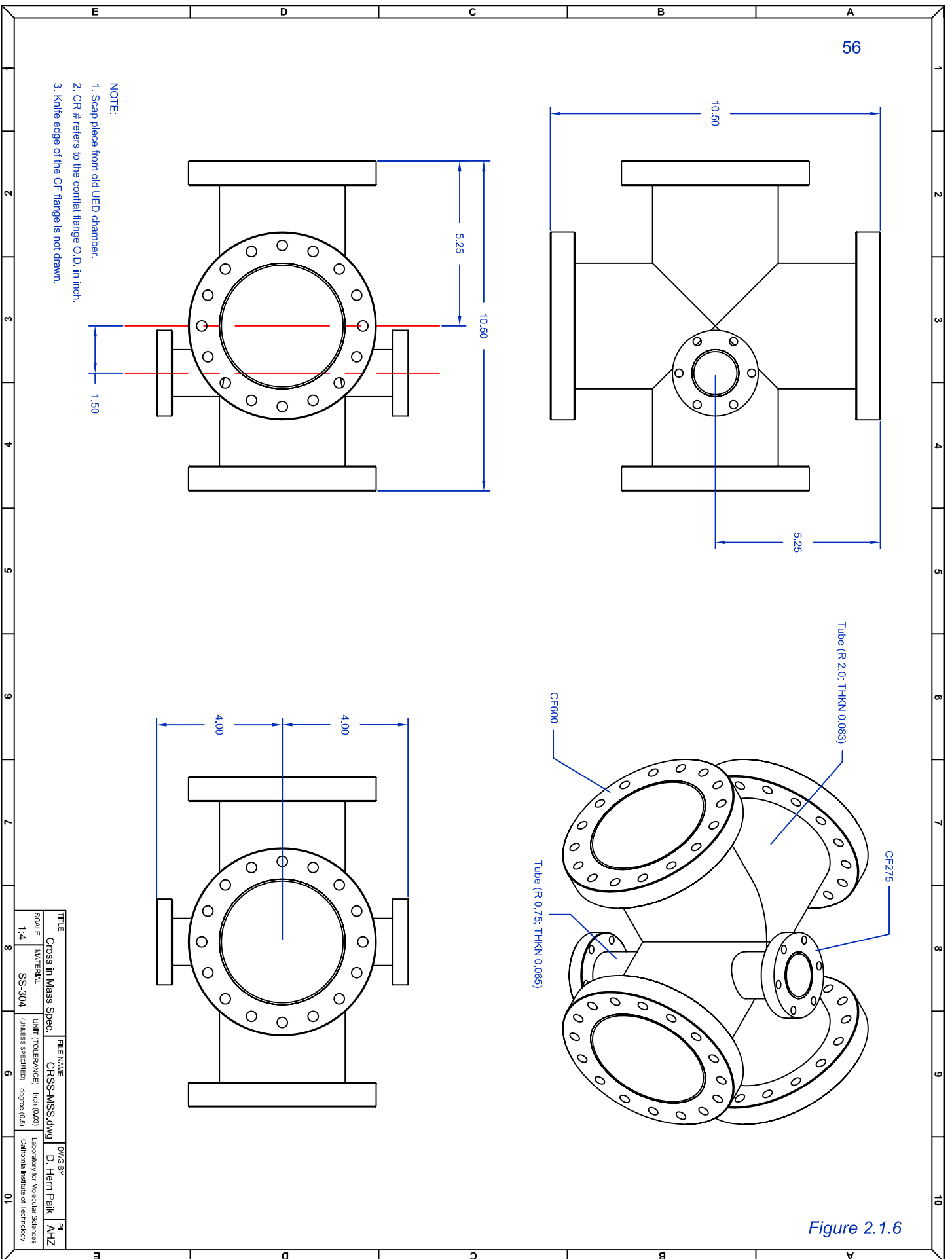
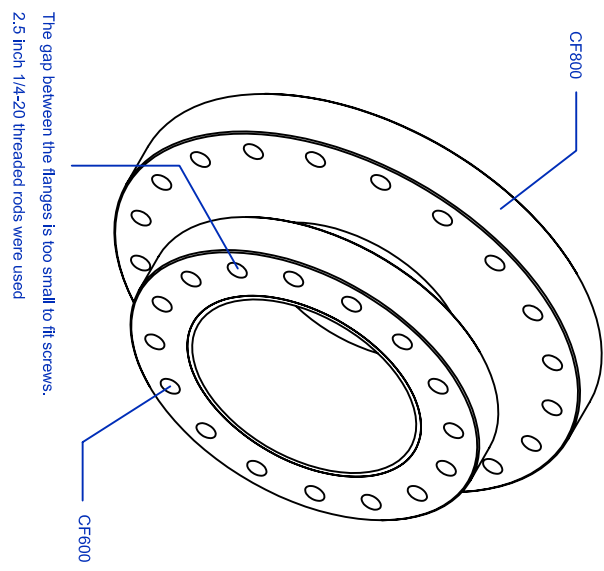
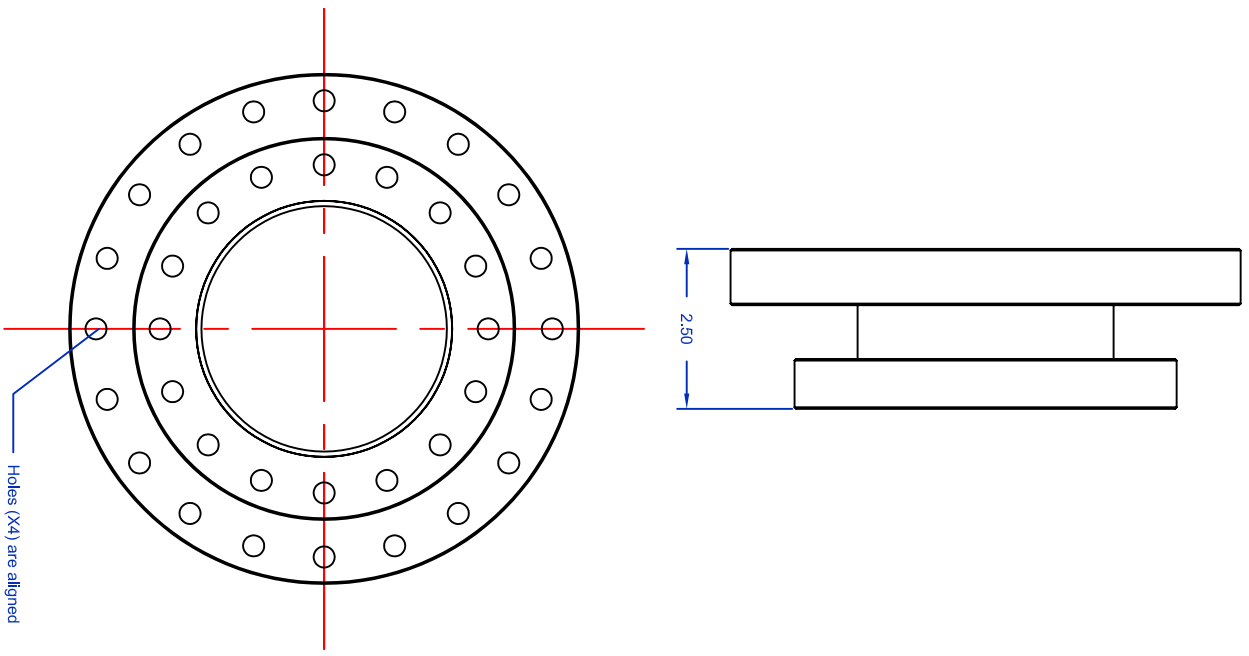


Figure 2.1.6

NOTE:
 1. Scap piece from old UED chamber.
 2. CR # refers to the conflat flange O.D. in inch.
 3. Knife edge of the CF flange is not drawn.

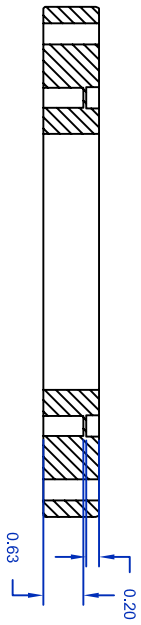
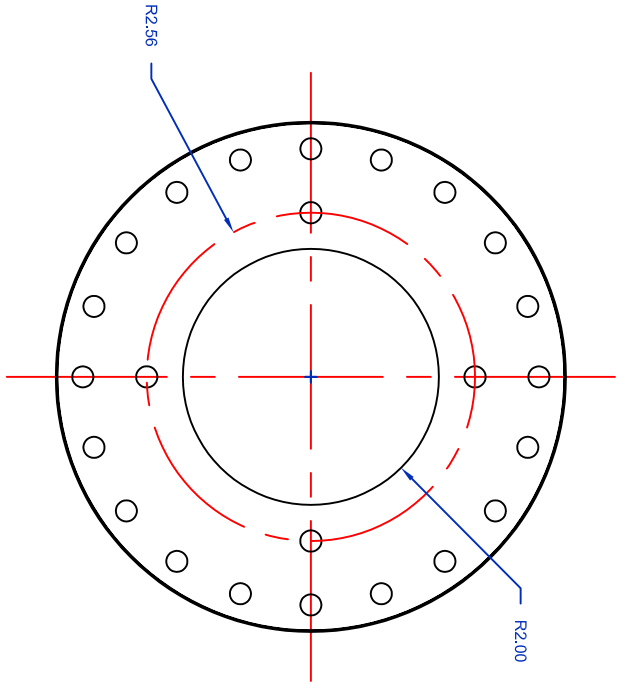
TITLE	FILE NAME	DWG BY	PI
Cross In Mass Spec.	CRSS-MSS.dwg	D. Hain Park	AHZ
SCALE	MATERIAL	UNIT TOLERANCES	(UNLESS SPECIFIED)
1:4	SS-304	inch (0.03)	degree (0.5)
8	6	01	



- NOTE:
1. The blank CF800 was machined. (R:3.0 hole)
 2. CF800 and CF600 were welded to the R:3.0 tubing.
 3. CR # refers to the conflat flange O.D. in inch.
 4. Knife edge of the CF flange is not drawn.

TITLE	FILE NAME	DWG BY	PI
Nipple CF800-CF600	NIP-C-T.dwg	D. Hahn Park	AHZ
SCALE	UNIT (TOLERANCES)	LABORATORY FOR MOLECULAR SCIENCES	
1:3	(UNLESS SPECIFIED) inch (0.03) degree (0.5)	CALIFORNIA INSTITUTE OF TECHNOLOGY	
MATERIAL		6	01
SS-304			

Figure 2.1.7



NOTE:
 1. 0-CF800-CF600 was purchased from MDC Vacuum Corp.
 2. Knife edge of the CF flange is not drawn.

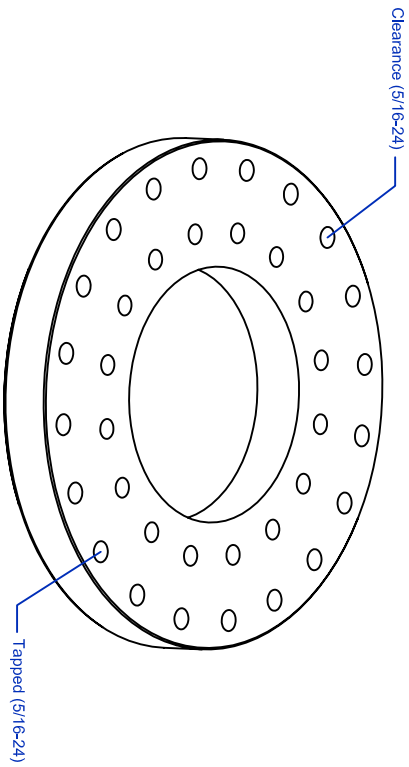
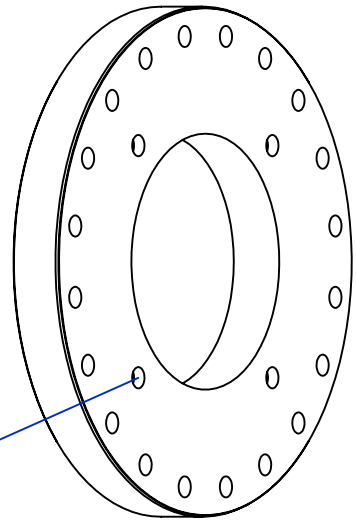


Figure 2.1.9

TITLE	0-Length Adapter Mod.	FILE NAME	0-ADPT.dwg	DWG BY	D. Hain Park	PI
SCALE	1:3	MATERIAL	SS-304	UNIT TOLERANCES (UNLESS SPECIFIED)	inch (0.03) Laboratory for Molecular Sciences degree (0.5) California Institute of Technology	
						01

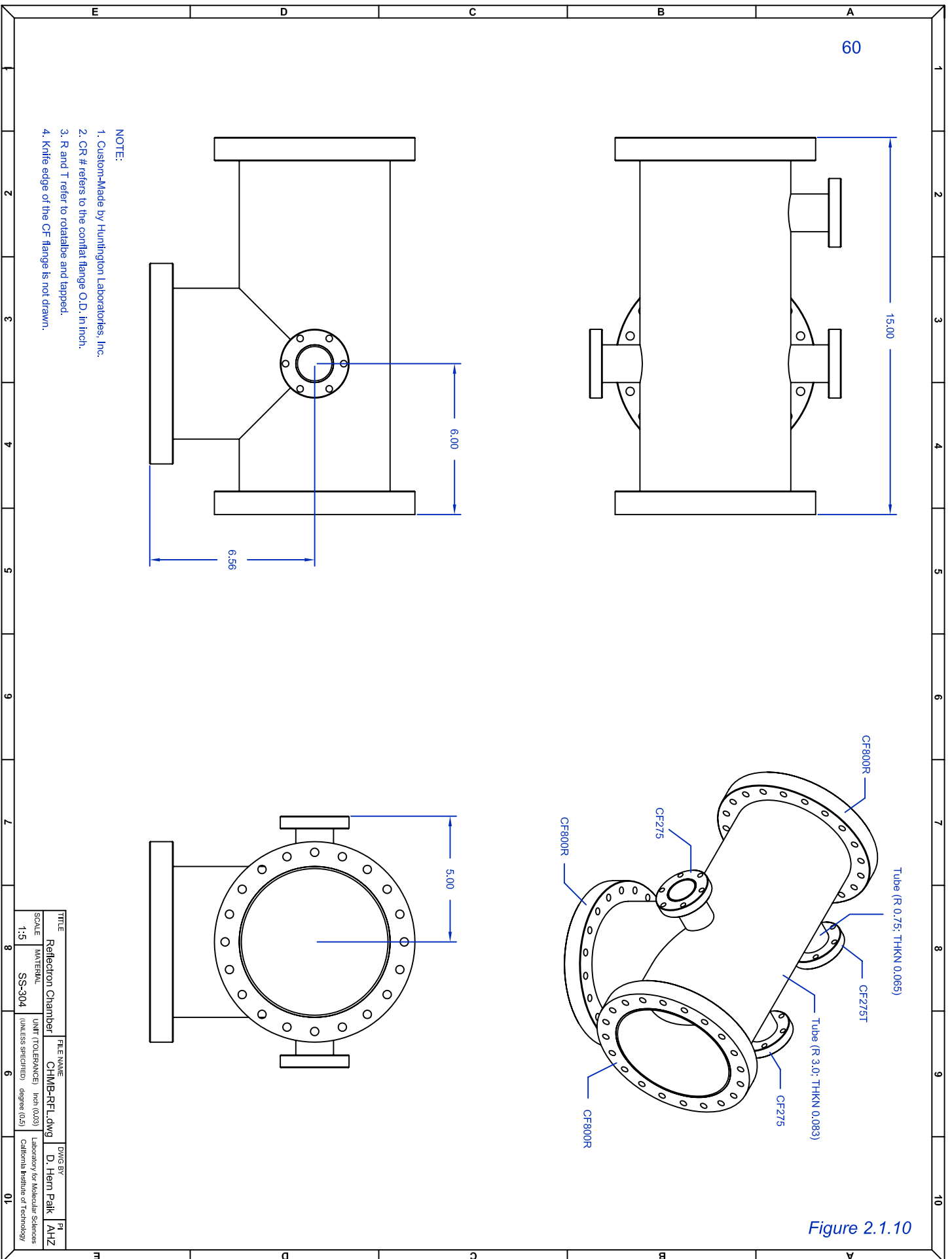
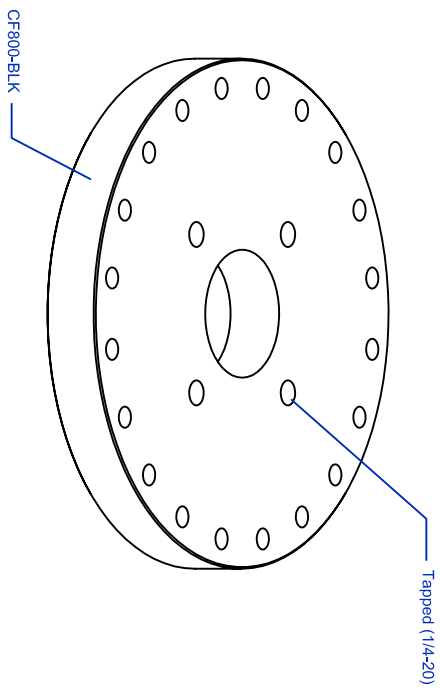
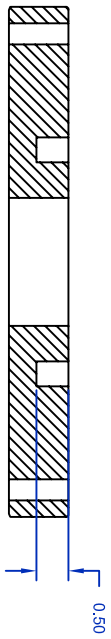
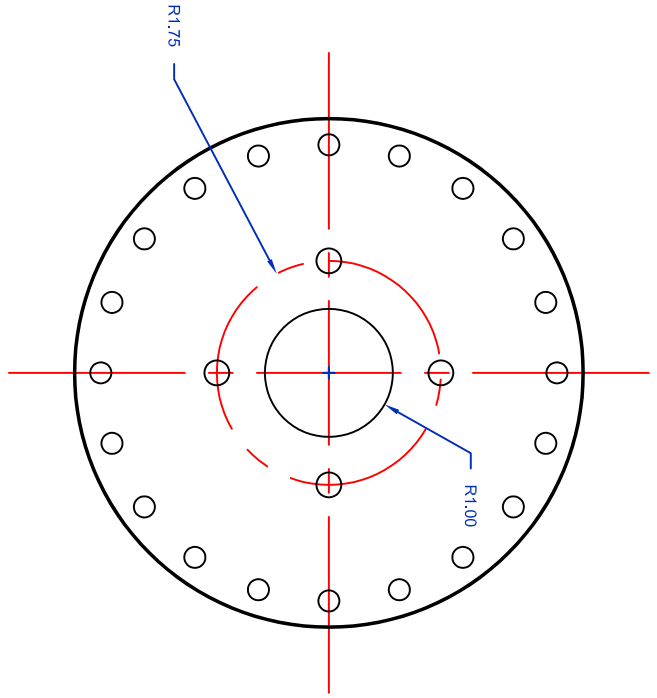


Figure 2.1.10

- NOTE:
1. Custom-Made by Huntington Laboratories, Inc.
 2. CR # refers to the conflat flange O.D. In Inch.
 3. Rand T refer to rotatable and tapped.
 4. Knife edge of the CF flange is not drawn.

TITLE	CHMB-RFL.dwg	FILE NAME	DWG BY	PI
SCALE	1:5	MATERIAL	SS-304	UNIT TOLERANCES (UNLESS SPECIFIED)
				inch (0.03)
				degree (0.5)
				Laboratory for Molecular Sciences
				California Institute of Technology
				01

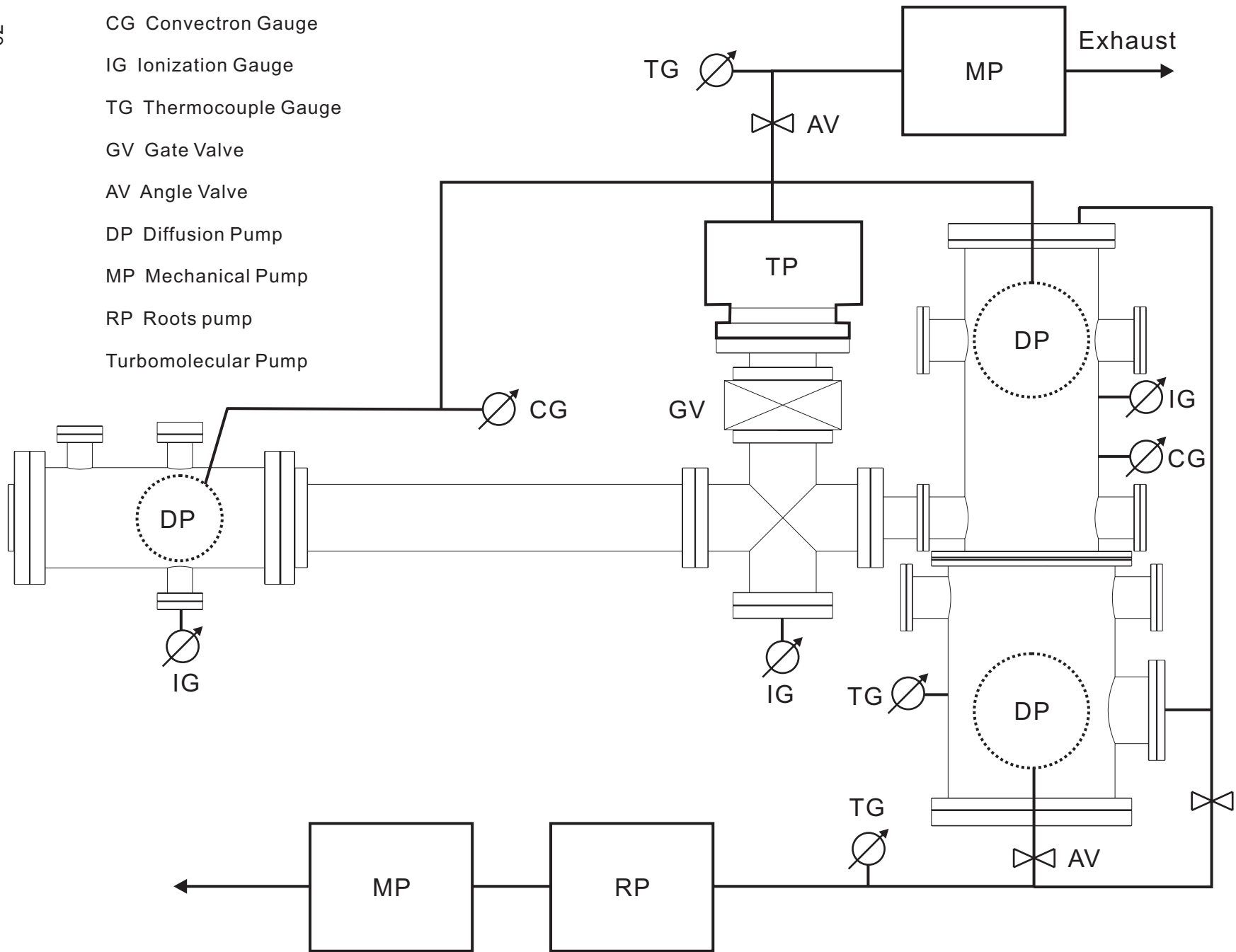


- NOTE:
1. CF800 was purchased from MDC Vacuum Corp.
 2. The blank CF800 was machined (R 1.0 hole)
 3. The tapped hole position matches the hole position of ASA 4
 4. Knife edge of the CF flange is not drawn.

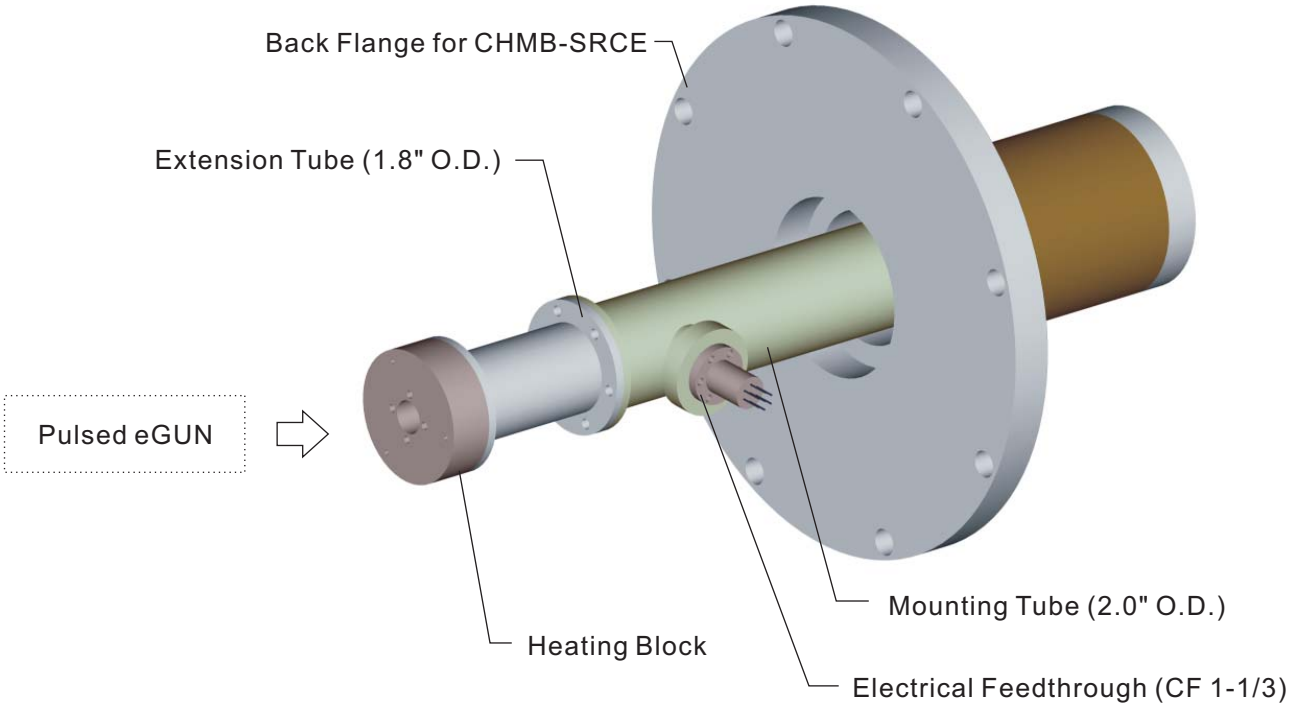
Figure 2.1.11

TITLE	FILE NAME	DWG BY	PI
CF800 modification	CF800-END.dwg	D. Hahn Park	AHZ
SCALE	UNIT (TOLERANCES)	LABORATORY for Molecular Sciences California Institute of Technology	
1:3	(UNLESS SPECIFIED) inch (0.03) degree (0.5)	6	01
MATERIAL		8	
SS-304			

CG Convectoron Gauge
 IG Ionization Gauge
 TG Thermocouple Gauge
 GV Gate Valve
 AV Angle Valve
 DP Diffusion Pump
 MP Mechanical Pump
 RP Roots pump
 Turbomolecular Pump



Back Flange Assembly



High Temperature Inlet System

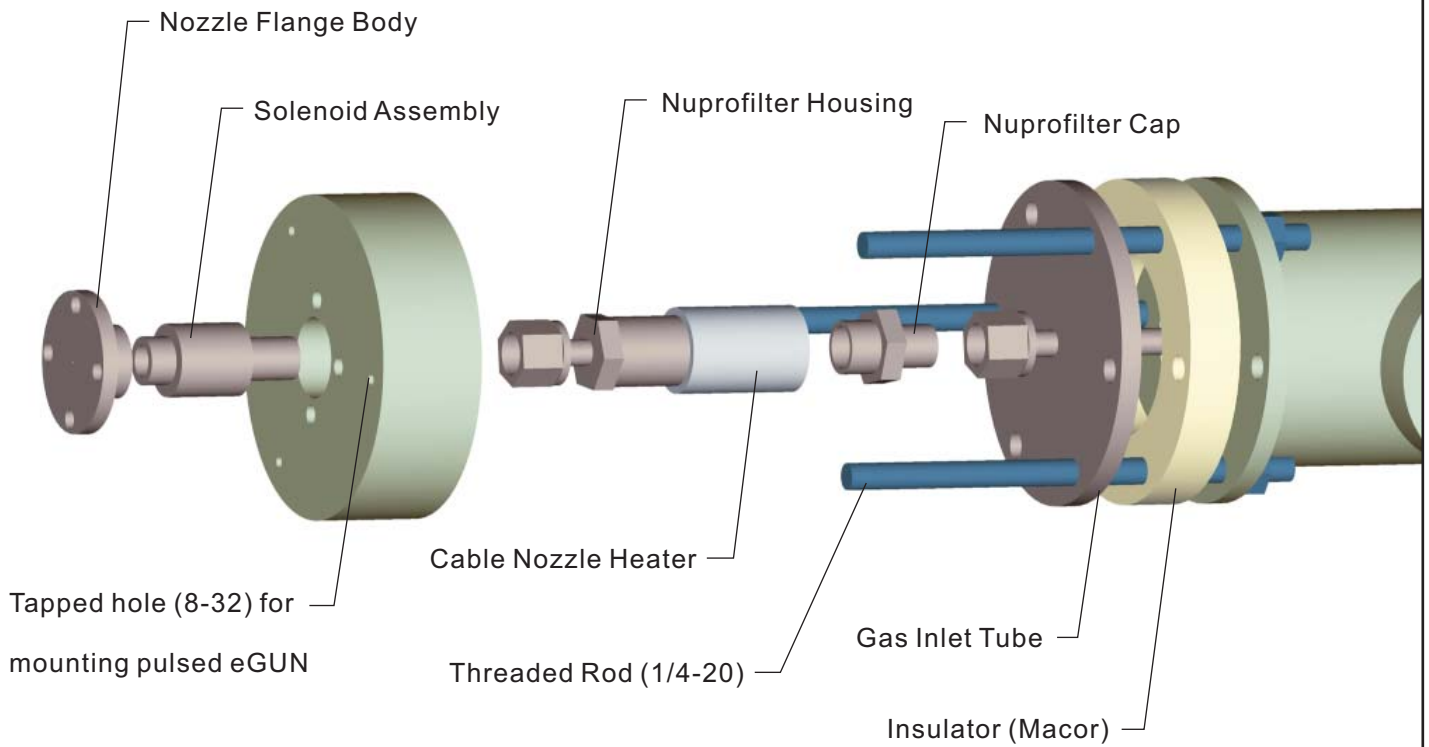


Figure 2.3

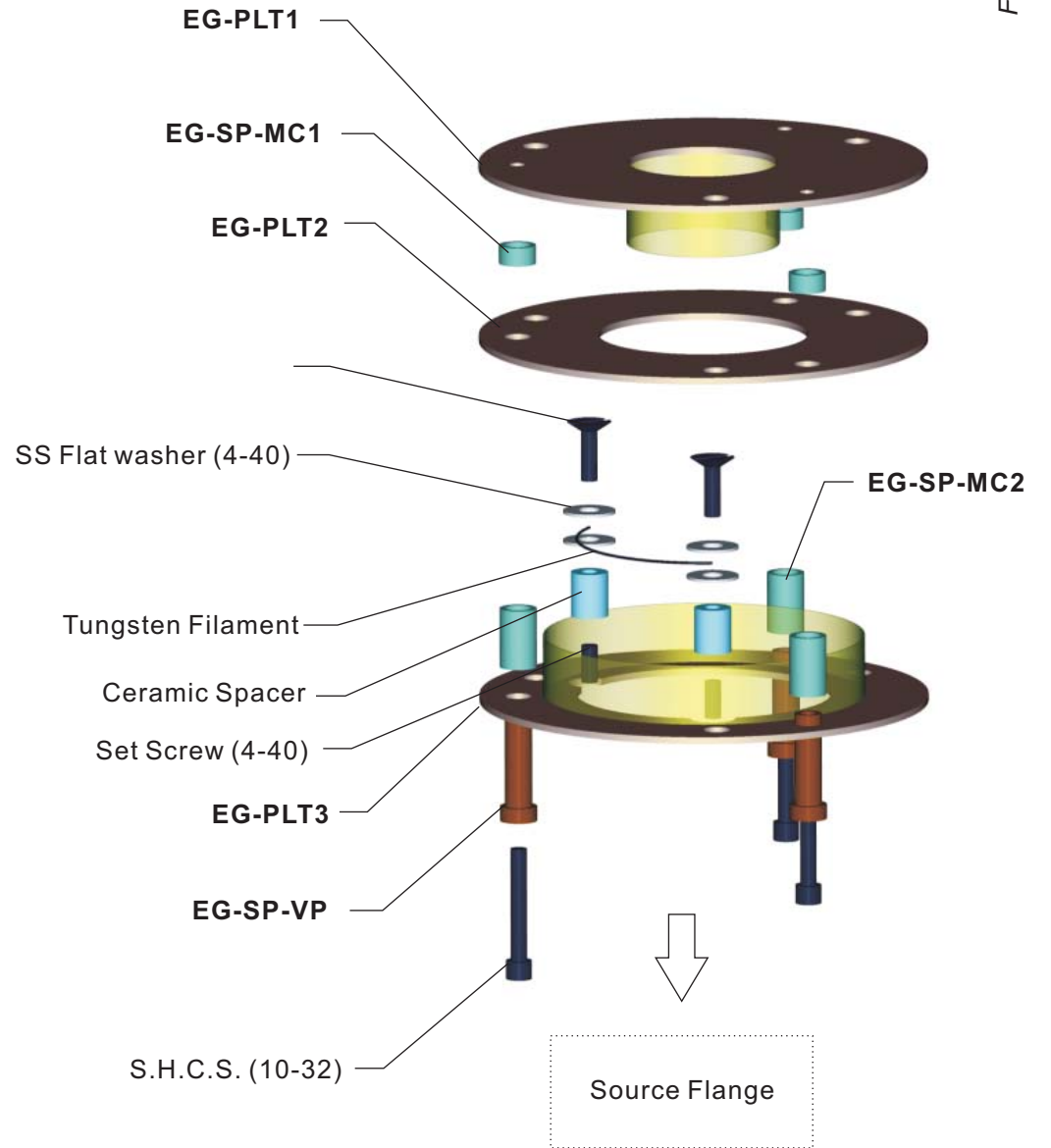
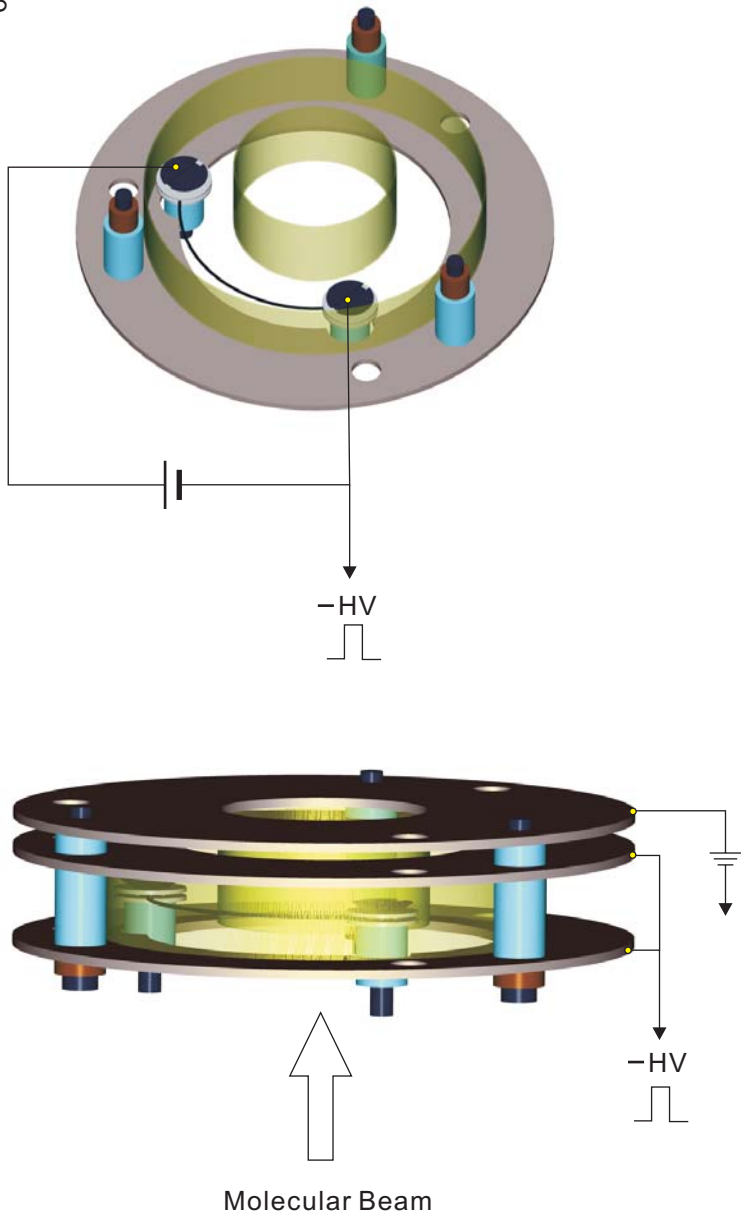


Figure 2.4

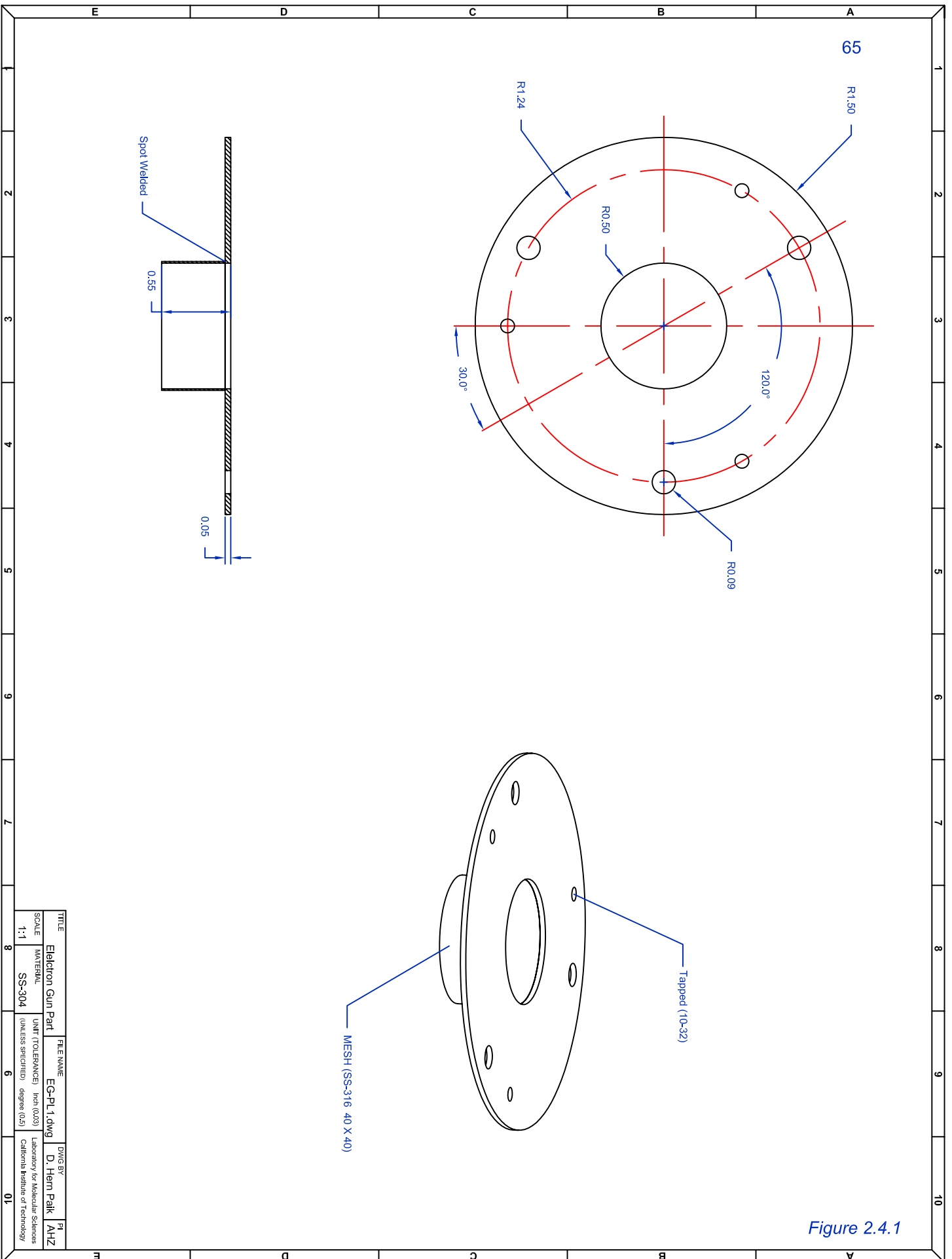


Figure 2.4.1

TITLE	EG-PL1.dwg	DWG BY	PI
FILE NAME	EG-PL1.dwg	DWG BY	D. Hahn Park AHZ
SCALE	1:1	UNIT (TOLERANCES)	inch (0.03)
MATERIAL	SS-304	(UNLESS SPECIFIED)	degree (0.5)
			Laboratory for Molecular Sciences California Institute of Technology

66

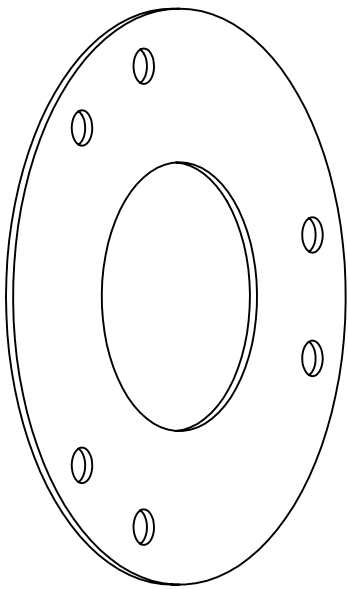
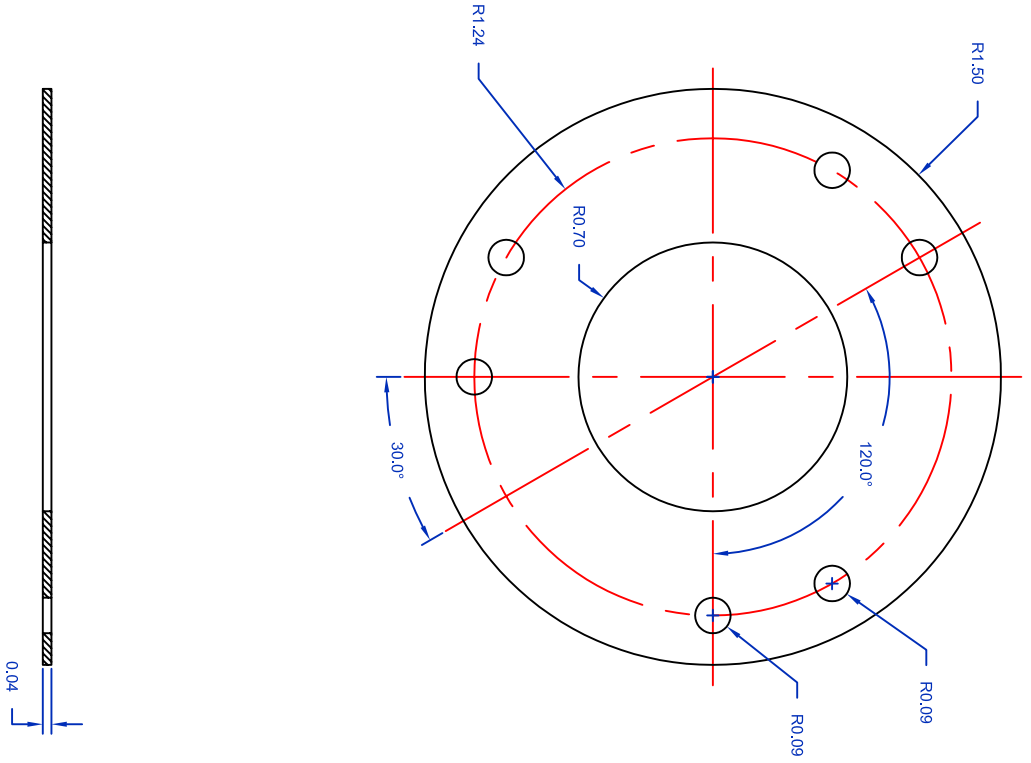


Figure 2.4.2

1	2	3	4	5	6	7	8	9	10
E	D	C	B	A					
1	2	3	4	5	6	7	8	9	10
E	D	C	B	A					

TITLE	EG-PL2.dwg	DWG BY	D. Hahn Park	PI
SCALE	1:1	UNIT TOLERANCES	inch (0.03)	Laboratory for Molecular Sciences
MATERIAL	SS-304	(UNLESS SPECIFIED)	degree (0.5)	California Institute of Technology

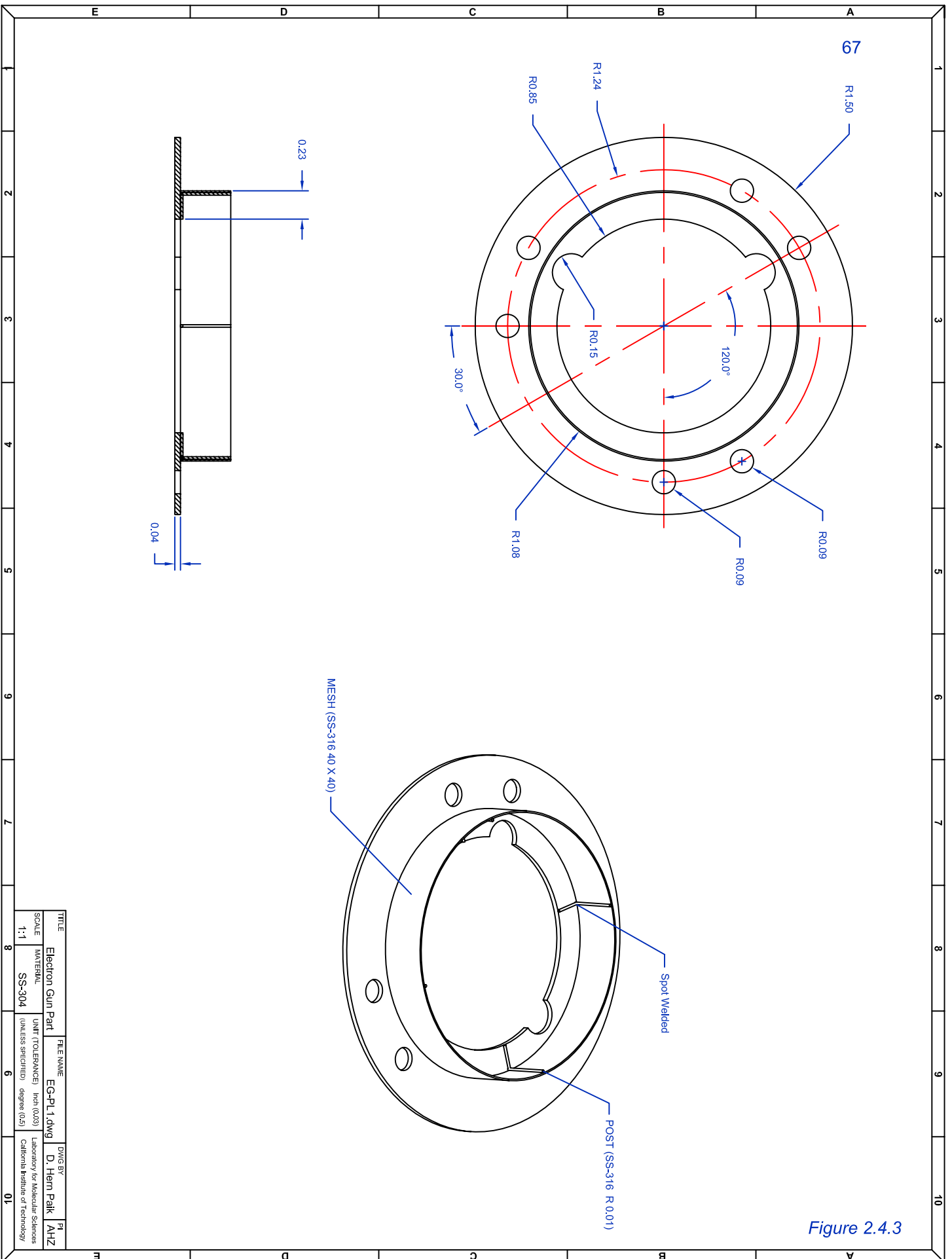
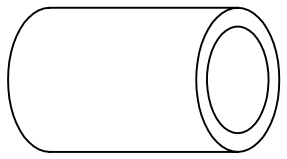
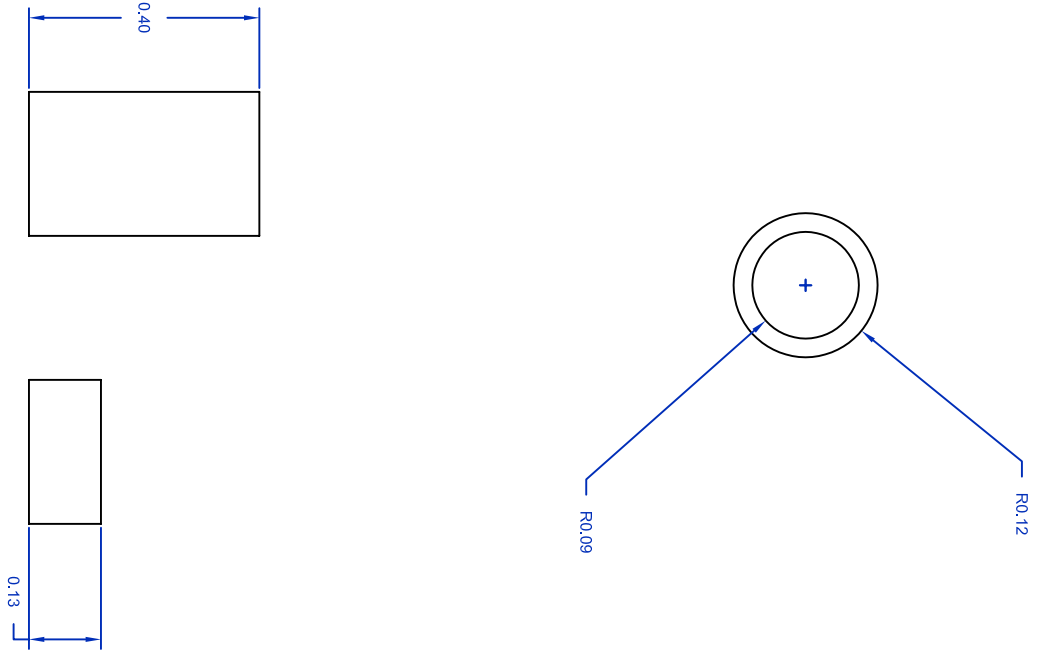
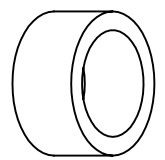


Figure 2.4.3

TITLE	EG-PL1.dwg	DWG BY	D. Hahn Park	PI
SCALE	1:1	MATERIAL	SS-304	
UNIT (TOLERANCES)	inch (0.03)	UNIT (TOLERANCES)	degree (0.5)	
Laboratory for Molecular Sciences		California Institute of Technology		

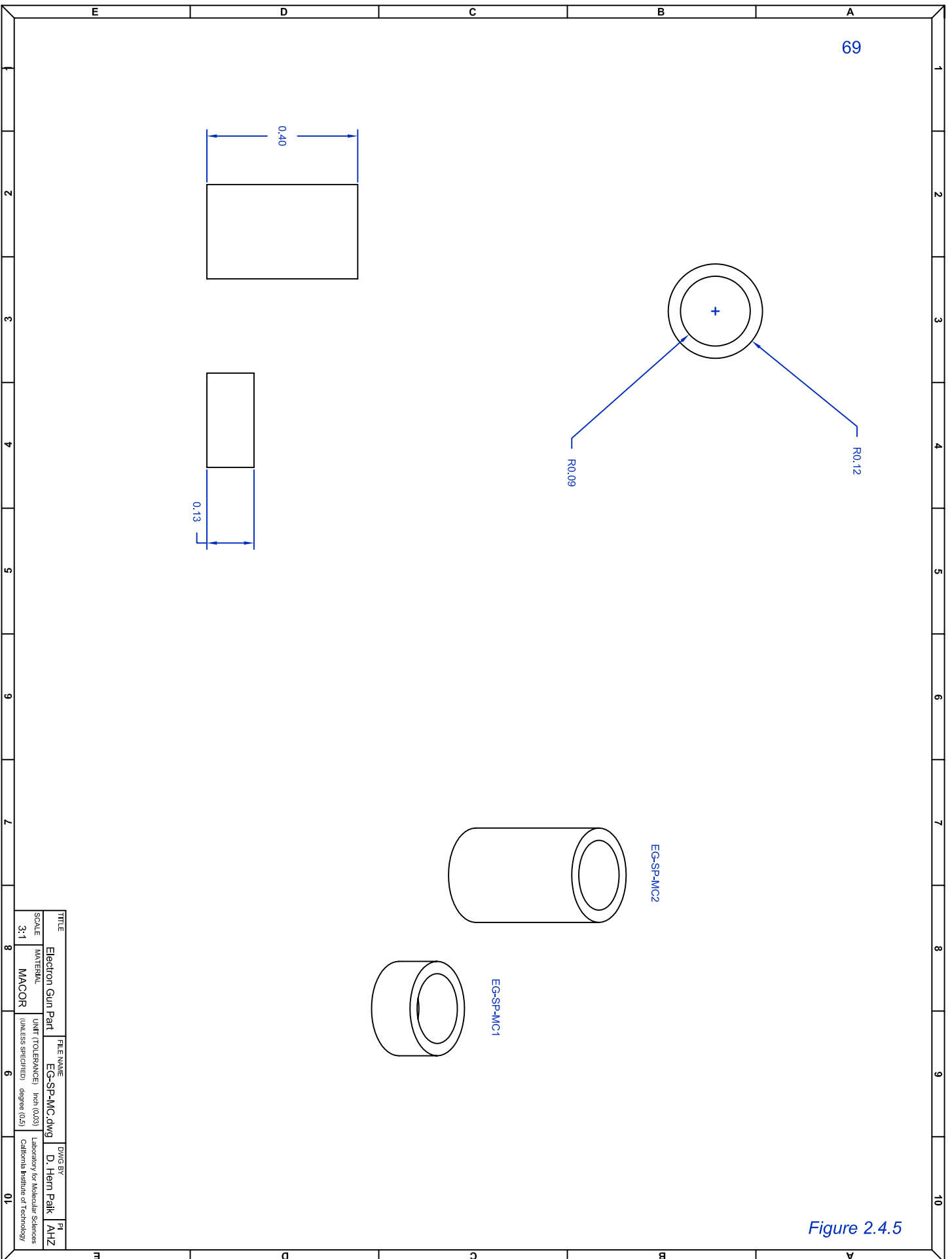


EG-SP-MC2



EG-SP-MC1

Figure 2.4.5



TITLE	EG-SP-MC.dwg	DWG BY	D. Hahn Park	PI
FILE NAME	EG-SP-MC.dwg			
UNIT (TOLERANCES)	inch (0.031)			
SCALE	3:1	LABORATORY FOR MOLECULAR SCIENCES		
MATERIAL	MACOR	(UNLESS SPECIFIED)	degree (0.5)	California Institute of Technology

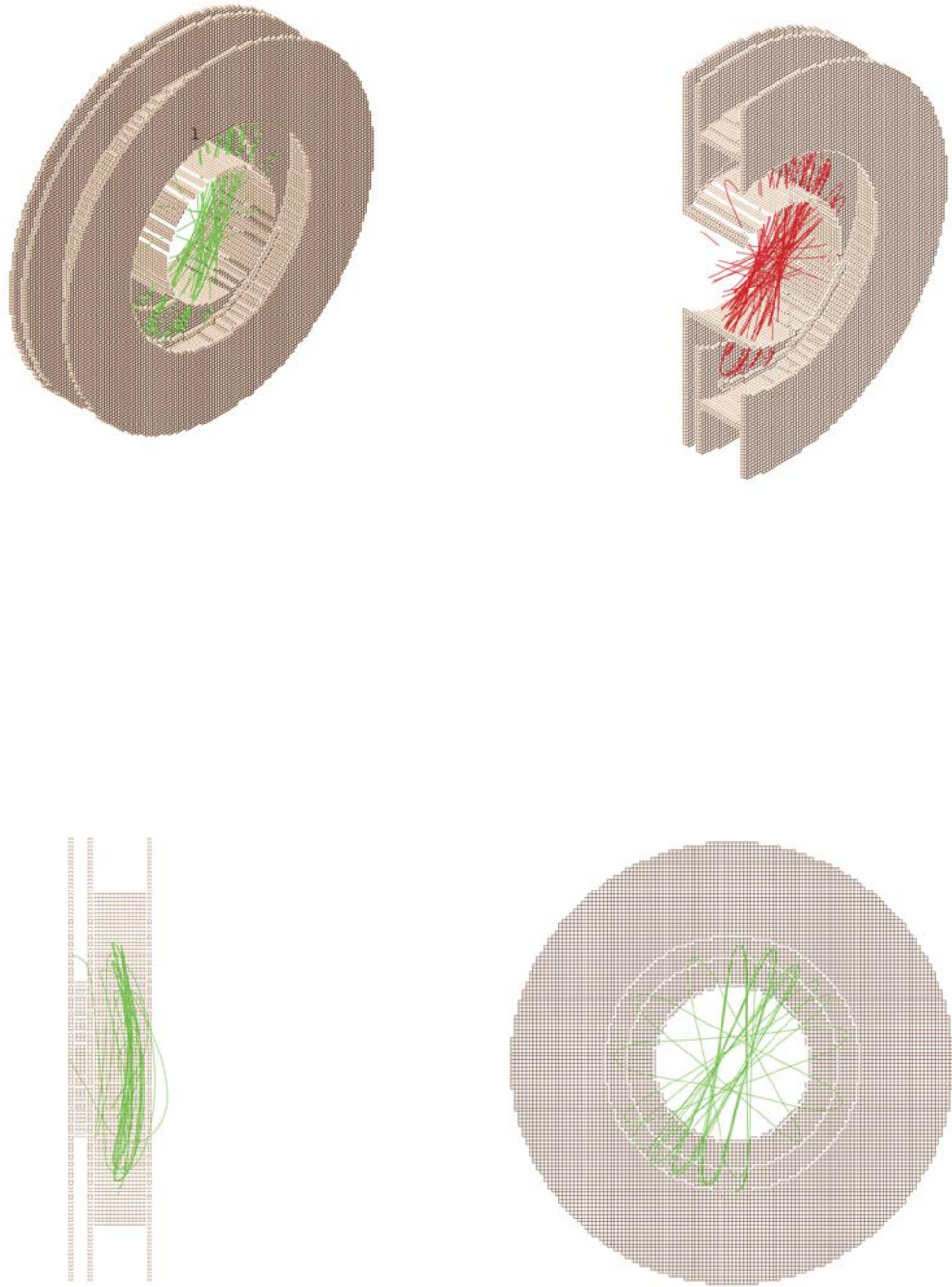


Figure 2.5

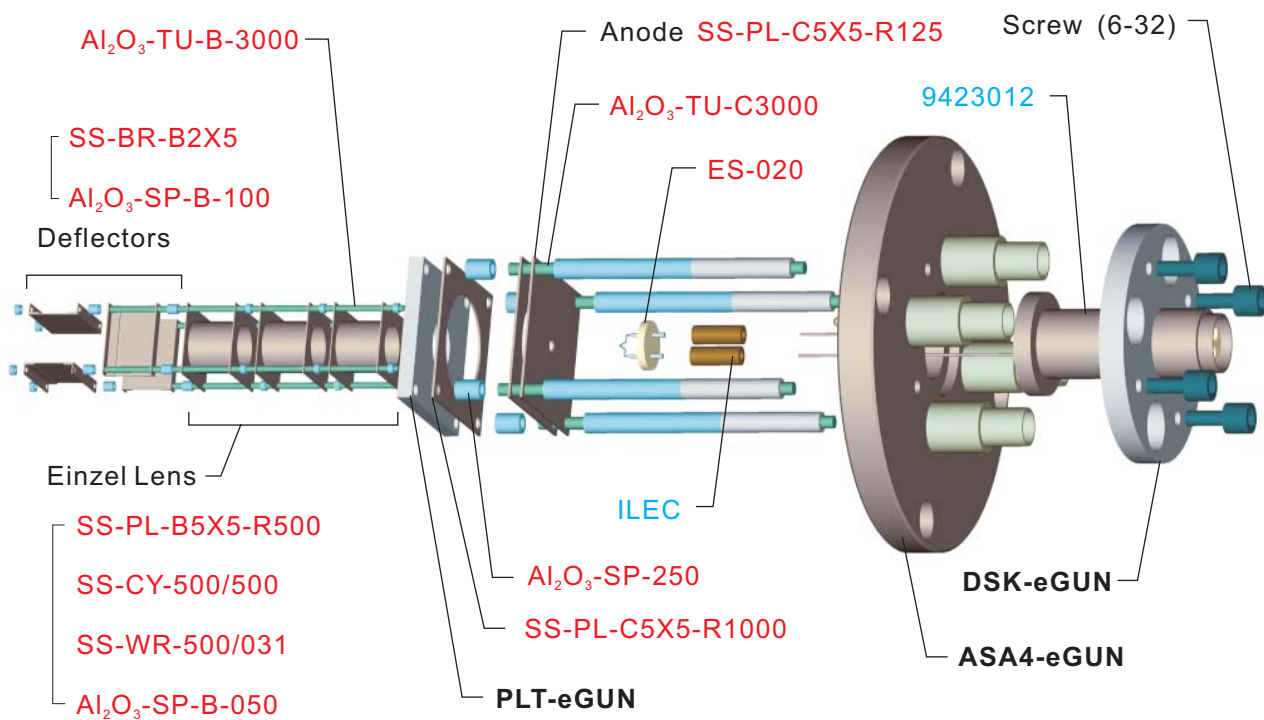
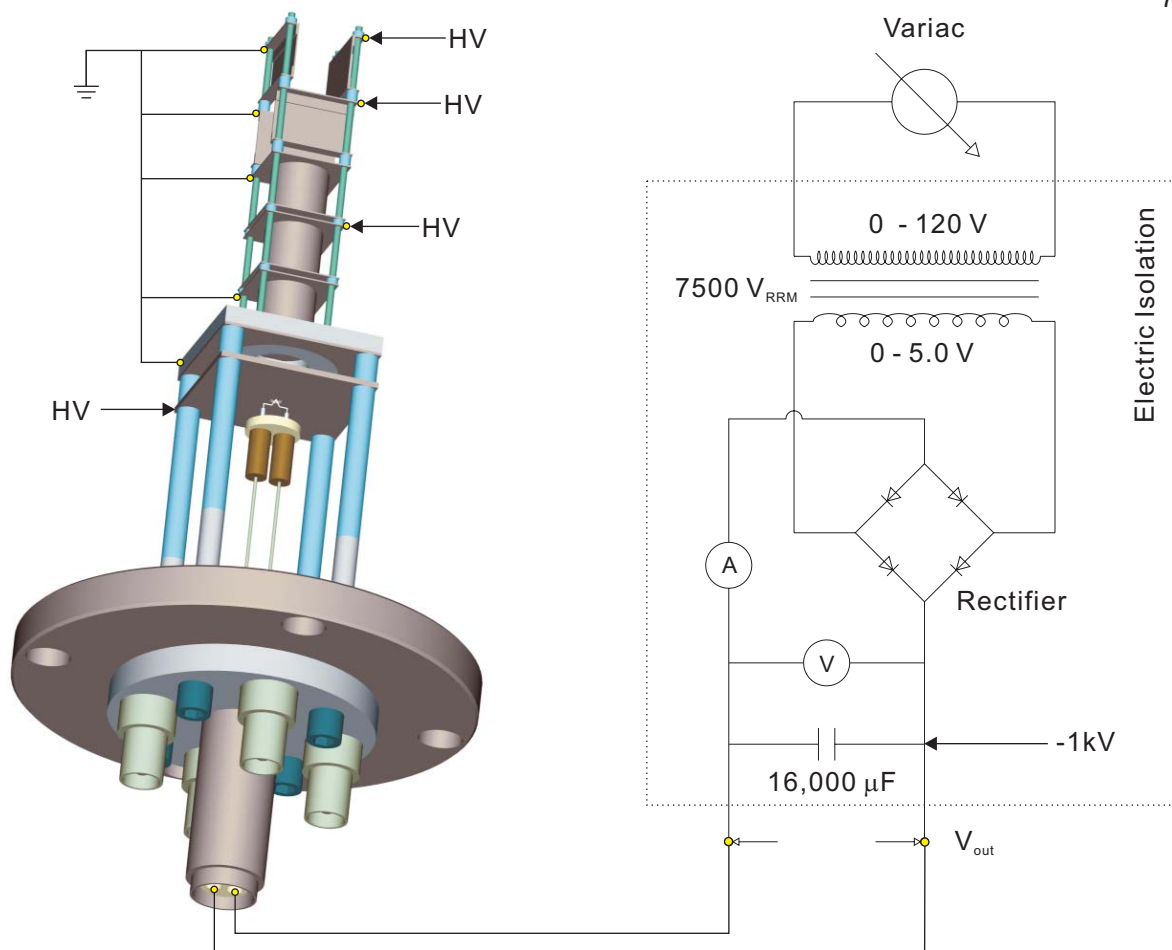


Figure 2.6

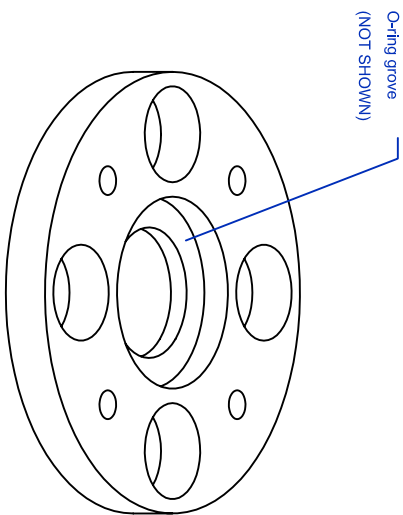
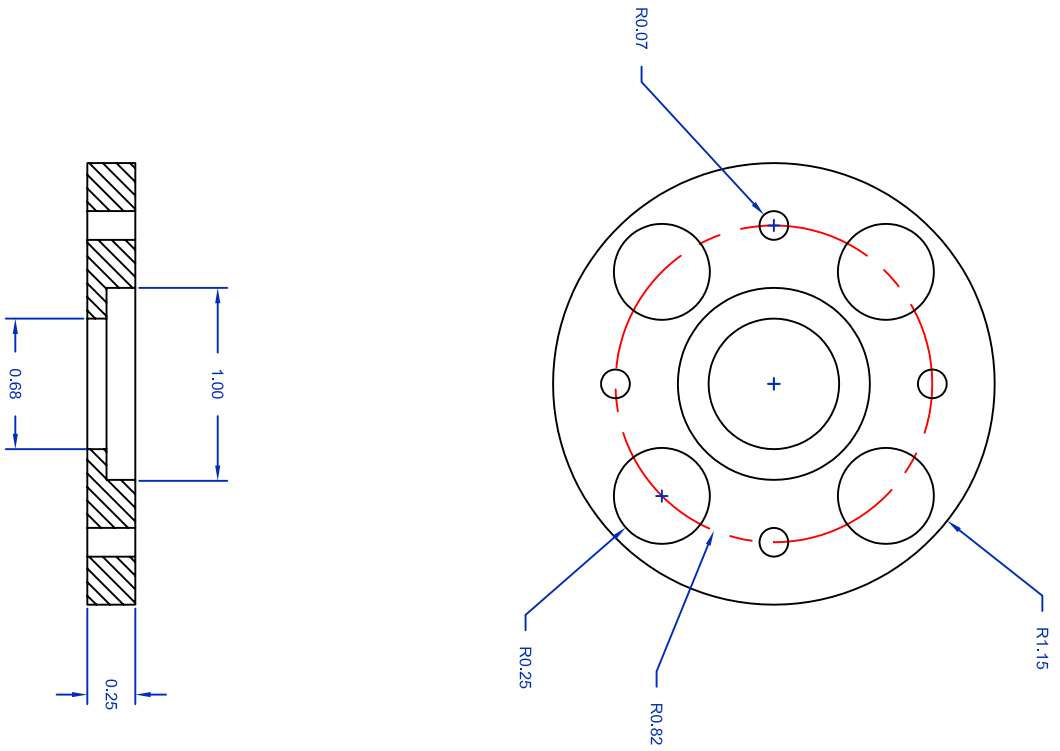


Figure 2.6.3

TITLE	DISK for Electron Gun	FILE NAME	DSK-EGUN.dwg	DWG BY	D. Hahn Park	PI	AHZ
SCALE	1:1	MATERIAL	AL 6061	UNIT (TOLERANCES)	inch (0.03)	Laboratory for Molecular Sciences California Institute of Technology	
				(UNLESS SPECIFIED)	degree (0.5)		

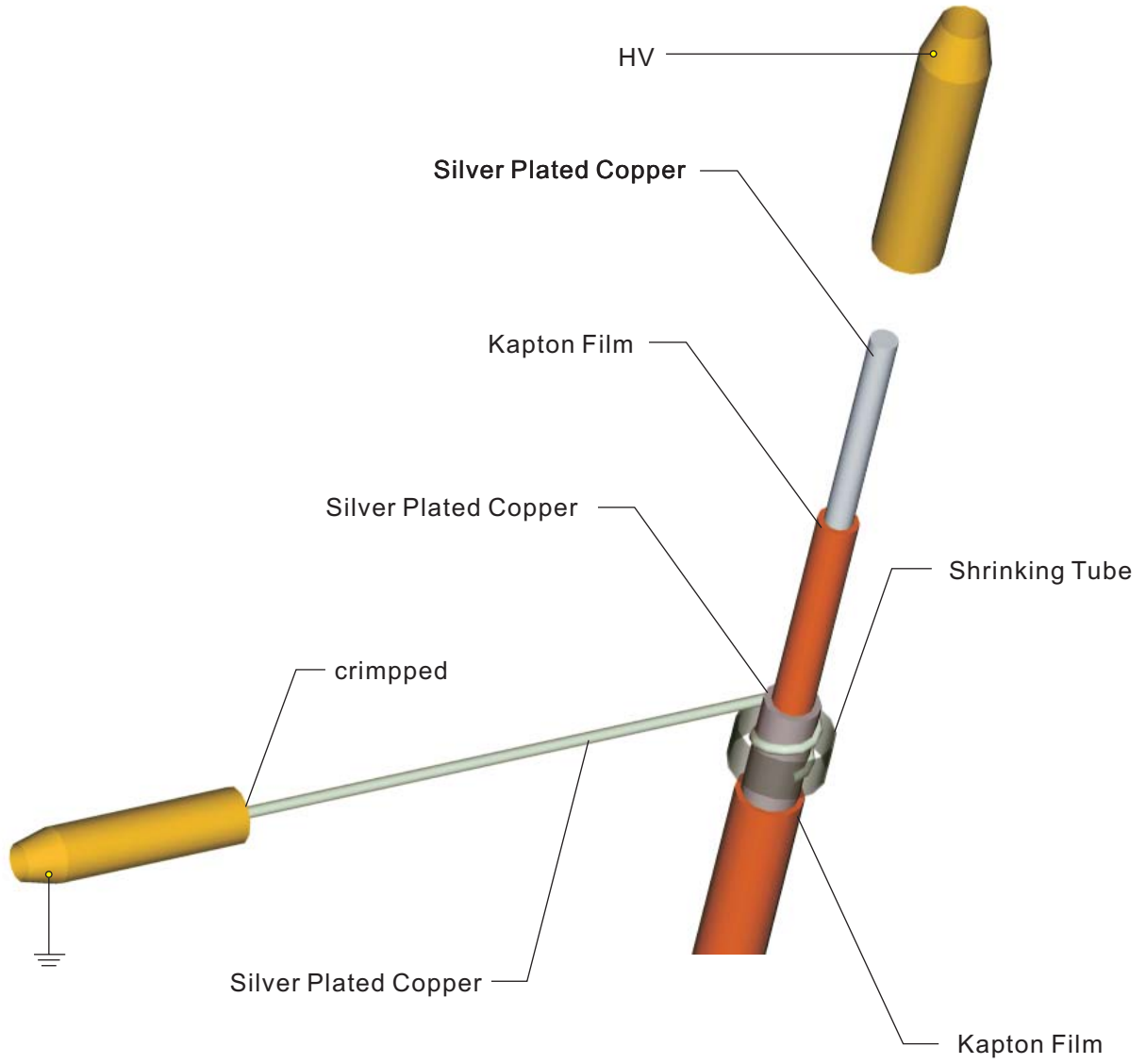


Figure 2.7

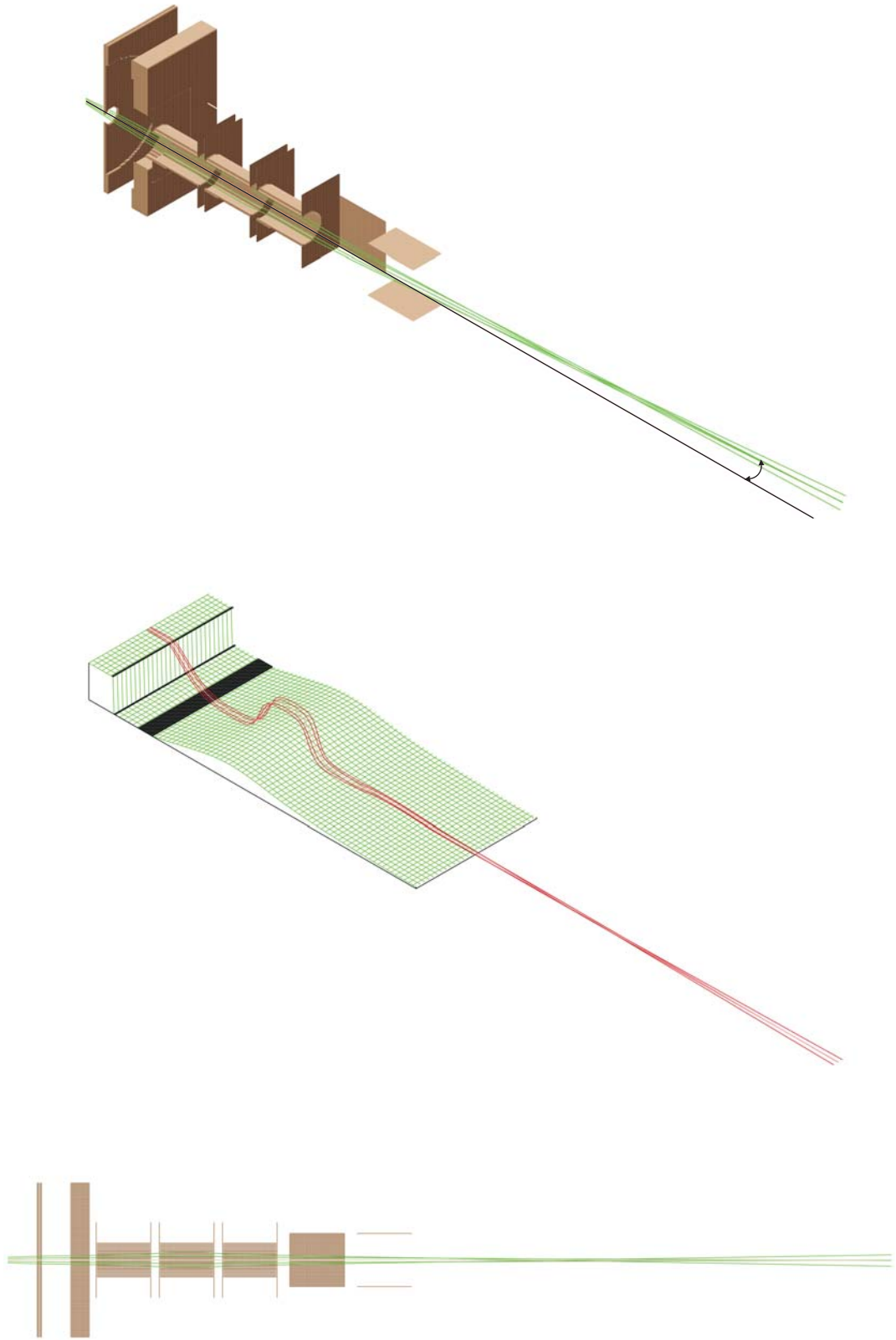


Figure 2.8

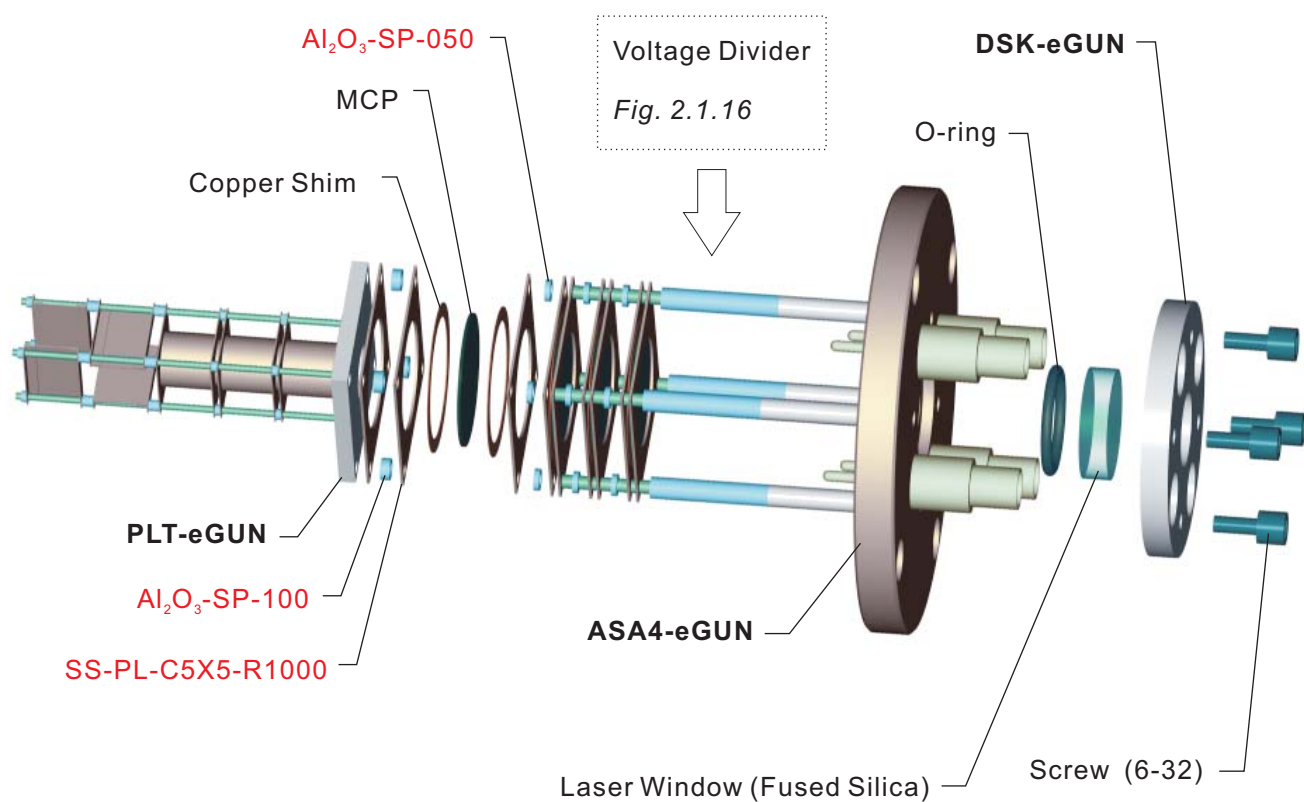
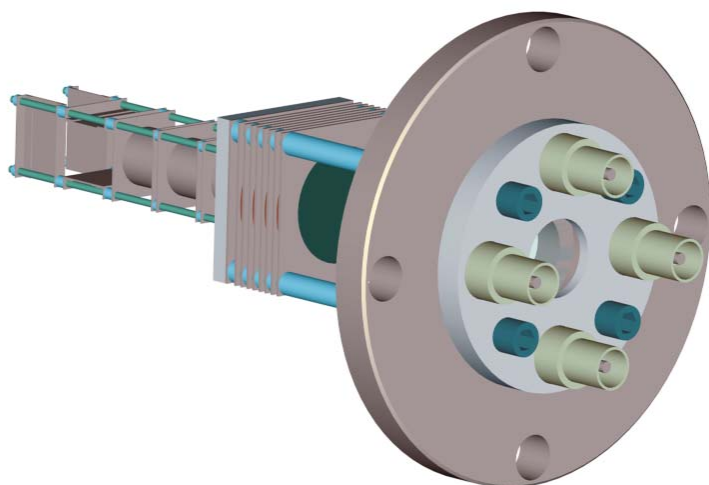
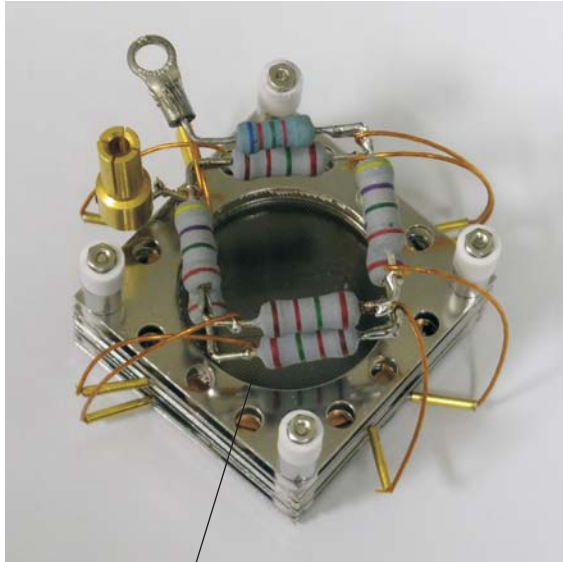


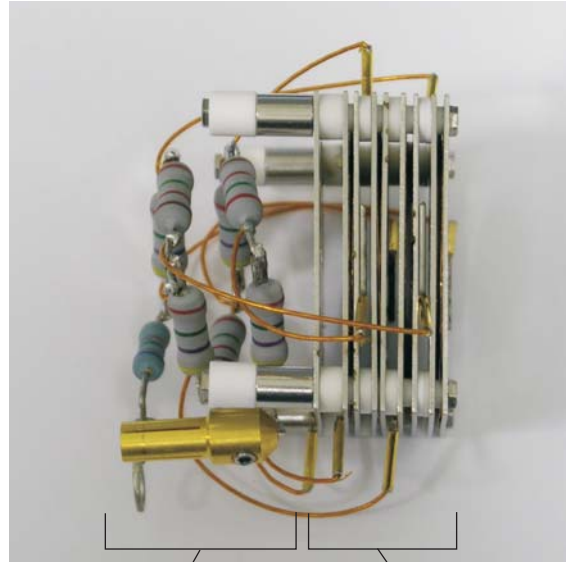
Figure 2.9

Bottom View



MCP

Side View



Voltage Divider

MCP Stack

R1 = 1.0 MΩ
R2 = 3.0 MΩ
R3 = 6.3 MΩ

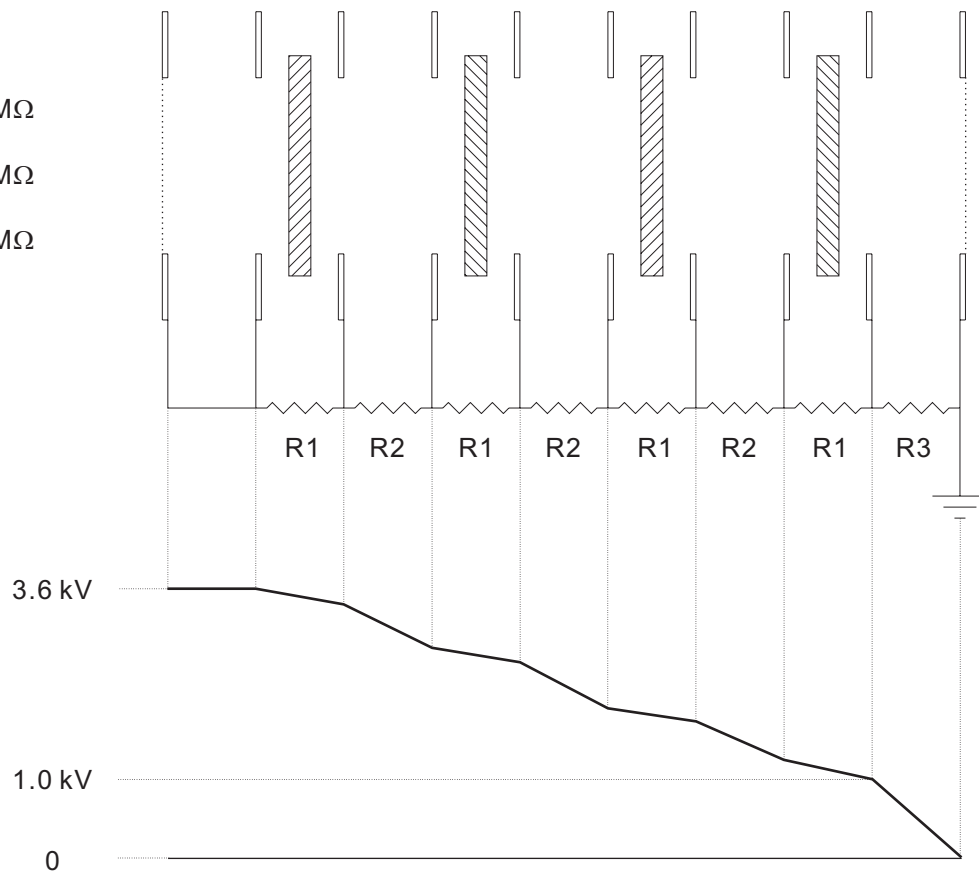


Figure 2.10

2.5. Tandem Mass Spectrometer

The main function of the tandem mass spectrometer is to guide mass-selected ions to the laser-interaction region and collect electrons and fragments generated from the photoreaction. Our tandem mass spectrometer incorporates three subunits of spectrometers: primary mass spectrometer, reflectron spectrometer and photoelectron spectrometer. The primary mass spectrometer refers to the uniaxial mass spectrometer, which serves as the framework for integrating the other spectrometers. The reflectron mass spectrometer is appended collinearly to the primary mass spectrometer, while the photoelectron spectrometer is attached perpendicular to the mass spectrometer.

The principal ion-optic components that constitute the tandem mass spectrometer are shown in Fig. 2.11 and they are labeled by the assembly numbers. The expanded illustration for each assembly will be provided when the component is discussed. In later discussion, the orientation of the spectrometers and the ion/electron trajectories are referred by the Cartesian coordinates defined as follow: x-axis is parallel to the gas jet expansion, y-axis is along the photoelectron TOF axis, and z-axis is along the TOF axis of the primary mass spectrometer.

2.6. Primary Mass Spectrometer

The primary mass spectrometer consists of a pulsed ion-accelerator, a pair of horizontal and vertical deflectors, an einzel lens, a massgate and a microchannel plate (MCP) detector. The pulsed ion-accelerator injects the ion beam into the field-free time-of-flight region where ions are separated by their mass and forms ion packets. The ion packet of interest can then be mass-filtered prior to light-interaction by utilizing a pulsed

massgate. The ions generated in the source are detected by an MCP detector and identified by their flight time.

2.6.1. Ion Accelerator

The ion accelerator of our mass spectrometer is designed based on the dual-stage extraction scheme proposed by Wiley and McLaren.^{11,12} The dual-stage accelerator compensates the time spread caused by the initial position and kinetic energy distribution of the ions in the acceleration region. Since our mass spectrometer is oriented perpendicular to the gas-jet expansion, the ionic species entering the accelerator are spread along the time-of-flight axis (TOF) and have the intrinsic velocity distribution originated from the supersonic expansion. These two factors affect the ion flight time (t) as described in the equation below:

$$t(U_0, s) = t_0 + t_1 + t_D, \quad (2.5)$$

$$t_0 = \frac{\sqrt{2m}}{eE_0} \left[\sqrt{U_0 + eE_0 s_0} \mp \sqrt{U_0} \right], \quad (2.6)$$

$$t_1 = \frac{\sqrt{2m}}{eE_1} \left[\sqrt{U_0 + eE_0 s_0 + eE_1 s_1} - \sqrt{U_0 + eE_0 s_0} \right], \quad (2.7)$$

$$t_D = \frac{\sqrt{2mD}}{2\sqrt{U_0 + eE_0 s_0 + eE_1 s_1}}, \quad (2.8)$$

where the total flight time t is the sum of t_0 , t_1 , and t_D which correspond to the time spent in the first extraction region, in the second extraction region and in the field free region, respectively. m and e are the mass and the charge of an ion. s_0 , s_1 and D are the distances between the electrodes and the distance of field-free region. E_1 and E_2

correspond to the electric field strengths applied in the first and the second extraction regions in the accelerator. U_0 and t_0 represents the initial energy distribution and the uncertainties in the time of ion formation, which correspond to the two factors causing the time spread.

The operation of the accelerator relies on the fact that an ion closer to the space-focal plane acquires less kinetic energy, thus is caught up by ions farther away from the focal plane. Compared to a single-stage accelerator, the dual-stage accelerator introduces two new parameters, s_1 and E_1/E_0 , which allows one to move the space-focal plane along the TOF-axis by two adjustable electric fields of the accelerator. For simplicity, consider the time spread caused by the initial position, *i.e.*, $U_0 = 0$. In typical operating condition, the field gradient in the second extraction region is very stiff, hence t_1 is relatively short. Consequently, the time spread in this Δt_1 is negligible compared to Δt_0 and Δt_D . Therefore, the spatial focus can be achieved when Δt_0 and Δt_D compensates each other. From Equations 2.6 and 2.8, Δt_0 and Δt_D can be deduced, and setting Δt_0 equal to $-\Delta t_D$ yields the following relationship:

$$D = \frac{2 \left(s_0 + \frac{E_1}{E_0} s_1 \right)^{3/2}}{\sqrt{s_0}} \quad (2.9)$$

As shown in equation 2.9, the space-focal plane (D) is independent of the mass to charge ratio and the total energy of the system, and the focal plane can be moved toward the detector by increasing the E_1/E_0 ratio and *vice versa*. The ability to adjust the space-focal plane is essential to our experiment. For mass-analysis, the focus was at the ion detector, but for laser-interaction, the focal point was moved to the laser beam path.

Because of the kinetic energy distribution (or second order spreading, $\Delta \frac{dz}{dt}$), the ion packet widens again after passing through the space-focal plane and it spreads more as the ion packet distances away from the plane. The space focusing (first order, Δz) exacerbates the post focal-plane broadening since the energy spread is increased when the first order is compensated by the extraction fields. The refocusing of the post focal-plane broadening and the second order focusing are achieved by the reflectron mass spectrometer. Detail will be discussed later (2.1.5.2).

The mass resolution ($M \equiv m/\Delta m$) is determined by the geometry of the mass spectrometer as well as the intrinsic spread due to the initial space and kinetic energy (velocity) distributions, as shown below:

$$\frac{1}{M} = \frac{1}{M_s} + \frac{1}{M_{U_0}}, \quad (2.10)$$

$$M_s \sim k \left(\frac{s_i}{\Delta s} \right)^2, \quad (2.11)$$

$$M_s \sim \sqrt{\frac{eE_0 s_i + eE_1 s_1}{U_0}} \left(\frac{k+1}{\sqrt{k}} - \frac{\sqrt{k}-1}{\sqrt{k}+k} \frac{D}{s_i} \right), \quad (2.12)$$

$$k = \frac{E_0 s_i + E_1 s_1}{E_0 s_i}, \quad (2.13)$$

where M_s and M_{U_0} are the mass resolutions related to the initial position and the kinetic energy of the ion, respectively. s_i and Δs correspond to the initial position of an ion and its spread respectively, and larger s_i means that the ion is farther away from the space-focal plane.

As shown in above equations, longer flight tube (D) and longer second extraction region (s_I), large value of $s_i/\Delta s$ increase the mass resolution. Note that k is also proportional to D as describe in equation 2.9. However, the main objective of the primary mass spectrometer is to guide maximum number of ions in the laser-interaction region, and the mass resolution is the secondary concern in our design. For practical purpose, shorter D is preferred for larger ion density, which minimizes the loss during the flight time. Therefore, the length of the flight tube must be compromised to achieve the most efficient ion-guide with a reasonable mass resolution. The primary spectrometer was made to be 60 inches long with the laser window positioned at 40 inches away from the accelerator, and the mass resolution of ~ 400 was achieved.

The geometry of the ion-accelerator is important for the ion-injection as well as the spatial focus.¹² The spacing of the first extraction region must be wide enough to accommodate the cross sectional area of the gas-jet; however, a large spacing decreases the mass resolution by elongating the ‘turn-around’ time. We carried out a number of experimentations to find the optimal configuration for the accelerator by changing the two parameters (s_0, s_I), and we constructed the accelerator with following configurations: The spacing of the first extraction region was made to be 11 mm, and the second extraction region (s_I) was about twice wider than the first extraction region (s_0). The accelerator is situated such that the gas-jet axis is 3 mm away from the end plate, which improves the mass resolution by increasing s_i . (equation 2.11) A small slit was occasionally placed near the end plate of the accelerator to decrease the initial position distribution (Δs), but the appendage reduces the ion intensity significantly.

The accelerator was constructed by utilizing the stainless steel plates and the alumina insulators manufactured by the Kimball Physics. The accelerator consists of an array of stainless plates (SS-PL-5X5) which are separated by the alumina spacers (Al_2O_3 -SP-C-150). The first and the second extraction regions are defined by the three electrodes: repeller (end plate), extractor (middle plate) and emitter (exit plate). The repeller and extractor are connected to the high voltage pulse switches while the emitter is electrically grounded. (Fig. 2.12) In order to create a uniform field gradient in the extraction regions, high transmittance (95%) electroformed nickel mesh (Buckbee-Mears) was attached to the extractor and the emitter.

For negative ion experiments, the ion accelerator should be operated in a pulsed mode. The continuous mode is suitable for accelerating the positive ions which are created inside the extraction region by ionizing neutral gas-jet. For accelerating negative ions which are generated outside the accelerator, the repeller and the extractor should be in the ground electric potential until the ions entered the extraction region. Once the ions are inside the extraction region, high voltage pulse can be applied to the accelerator to extract the ions to the field free region. Pulsation is achieved by utilizing the transistor switch (Behlke, HTS51-06), which takes a TTL gate and a DC high voltage inputs to generate a high voltage pulse.

The model HTS51-06 provides a pulse with fast turn-on time (1 kV/20 ns), and the turn-off time is determined by the auxiliary RC circuit appended to HTS51 ($\tau = RC$). It is critical to have a fast turn-on switch; otherwise mass resolution can be decreased by the finite rise time of the high voltage pulse. Fast turning-off is not necessary since ions will be departed from the extraction region within a few microseconds, and the decay tail

can be moderately long as far as the voltages on the electrodes to be completely terminated before the next cycle. In fact, an abrupt turning-off causes a ringing at the turn-on edge of the pulse. The TTL pulse controls the switching time and width of the high voltage pulse.

It must be pointed out that the primary mass spectrometer cannot separate the metastable species decomposed in the field free time-of-flight tube. Once the ion packet enters the field-free region, the metastable decay of ions, via either autodetachment or vibrational predissociation will not affect the velocity of nascent metastable species (both charged and neutral). The metastable species are retained inside the ion packets until they reach the space-focal plane. To filter out the metastable species, an additional electric field must be applied to the ion packet, which is accomplished by the reflectron mass spectrometer in our apparatus. However, the filtration is not achieved prior to the laser interaction. Either an ion-beam block or a multipole ion-guide type ion-selector must be incorporated to eliminate the metastable species from the ion packet.

Fragments generated in the extraction region can deteriorate the mass resolution depending on where and when the fragmentation takes place. If the fragments are generated in much shorter time than the extraction time ($t_0 + t_1$), the nascent fragment ion will gain the same kinetic energy as the parent ion and the flight time follows the same square root relation. Thus, prompt dissociation will not affect the mass resolution. On the other hand, slow fragmentation ($\sim t_0 + t_1$) is detrimental to the mass resolution. The kinetic energy of the intermediate species is between the parent and the fragment ions, which results in the tailing of the mass peak. Inversely, the shape of the tail might provide valuable clues regarding the properties of the ions generated in the source. For

instance, vibration temperature and strength of the intermolecular forces can be deduced from the broadening of the mass peak.

2.6.2 Deflectors

A pair of horizontal (x-axis) and vertical (y-axis) deflectors are placed after the exit plate of the accelerator. The ions entering the accelerator have velocity components in x and y directions, and these velocity components can be compensated by applying retarding voltages on the deflectors. The perpendicular configuration of ion-entering introduces a large velocity component in the gas-jet direction (x-axis) since the gases are supersonically (> 340 m/s) expanded in the source chamber. Strictly speaking, the ion trajectory in the primary spectrometer cannot be collinear with the time-of-flight axis, but the trajectory is rather skewed in x-direction. The ion trajectory in the primary mass spectrometer should be as straight as possible for the implementation of the *linear* reflectron mass spectrometer (2.1.5.2). To straighten the ion trajectory, a tiltable setup was integrated to the ion accelerator. Conover *et al.* reported that the tiltable accelerator in conjunction with the deflection provides effective way of directing the ion trajectory, and their illustration of ion trajectories is presented in Reference [ref#].

The tilting mechanism is accomplished by inserting a miniature hinge in between the accelerator and the x-deflector. (Fig. 2.13) One end of the hinge is connected to the exit plate such that the pivot is located near the entrance, and the other end is connected to the deflection plate with a high voltage connection. Tilting is executed by pulling the edge of the exit plate with a flexible stainless steel wire which is connected to a motion feedthrough. (Fig. 2.13.3) Two torsion springs (SS 302, deflection angle: 180°) are

inserted in the pivot, which restores the hinge to the original (straight) position. The design permits the maximum tilting of 30 °, but for most case, the accelerator was tilted less than 10 ° from the straight position.

2.6.3. Einzel Lens

The electrostatic lens focuses the ion beam in the x and y directions, and the xy-plane focusing is necessary for implementing the *linear* reflectron mass spectrometer. The xy-plane focusing not only permits the ion beam to pass through the entrance of the reflectron mass spectrometer, but it also determines the ion trajectories in the reflector region. The focal properties of an electrostatic lens depend of the equipotential surface created inside the cylindrical electrodes, which are determined by the diameter of the cylinder, spacing between cylinders, and electric potential applied to the electrodes. The design of the electrostatic lens is very simple; however, care must be taken when putting the components together. It is critical to create symmetric equipotential surface inside the cylinders; otherwise, the transmitted charges will deviate from the coaxial trajectory.

Creating symmetric equipotential surface requires uniform spacing between the cylinders and exact alignment of the cylinders along the center axis.¹ The precision was acquired by utilizing the Kimball Physics ion optic components (0.005” tolerance). The electrostatic lens used in this laboratory consists of three-cylinder electrodes. Each cylindrical electrode is composed of a 1.0” O.D. stainless steel cylinder (SS-CY-1000/1000) and two stainless steel mounting plates (SS-PL-C-5X5-R1000). The mounting plate is fixed at the edge of the cylinder by spot-welding a retaining ring (SS-

WR-1000/031) at the junction of the cylinder and the plate. Three cylindrical electrodes are stacked together with 0.1” separation between the electrodes. The commonly used 10:1 ratio (cylinder O.D. to spacing) was adopted in our design, which provides a moderate sensitivity for adjusting the focal position.

The *three-cylinder* lens can be operated as an asymmetric lens or an einzel lens (*unipotential* lens) depending on the electric potentials applied to the electrodes. In the asymmetric lens, two different voltages are applied to the terminal (entrance and exit) cylinders, whereas same potential is applied to the entrance and exit cylinders in the einzel lens. In our experiments, the two end cylinders are electrically grounded, and the focal point was changed by tuning the voltage of the middle cylinder. This configuration provides an effective way of focusing without changing the energy of the transmitted particles. There are two focusing schemes: accelerating mode ($V_{\text{middle}} > V_{\text{end}}$) and decelerating mode ($V_{\text{middle}} < V_{\text{end}}$).¹ The former is preferred to the latter because the latter causes expansion of the transmitted ion beams.

2.6.4. Massgate

The massgate is an essential ion optic component for carrying out fragmentation studies (Chapters 3 to 7) and charge reversal experiments (Chapter 8). It selects the ion of interest while filters out rest of ions prior to the laser interaction, which provides a unique opportunity to record a fragment ion spectrum generated from photodissociation or charge reversal scheme. The simplest and most widely used massgate is the pulsed deflector. It blocks (or bends) the ion beam by creating a high electric field between the plates, and opening and closing of the gate are achieved by turning the electric field off

and on. The pulsed deflector exhibits an intrinsic demerit in the ion-selection, and many modified versions of the pulsed deflector (*e.g.*, ion-lift and the magnetic field deflector) have been developed to improve its shortcoming.

The main drawback of the ‘deflector-type’ massgate is the low sensitivity in the ion-selection, which is due to the large dimension of the deflection plates. First, if the separation of the ion packets is smaller than the length of the deflection plate, rigorous mass selection cannot be achieved. In many cases, two or more sets of the deflectors are required to overcome this problem. Second, it is necessary to apply high voltages to the deflection plates in order to filter the unwanted ion packets which travel with high kinetic energies. Because of the large separation between the deflection plates, the electric field gradient between the plates is not steep, thus relatively high electric potential must be applied to acquire the field strength compatible to the acceleration field.

The ‘interleaved-comb type’ massgate eliminates the aforementioned demerits of the deflector massgate.¹³⁻¹⁵ The interleaved comb (ILC) massgate has a very thin gating plane formed by two alternating threads of thin stainless steel wires, and the distance between the alternating wires is in millimeter scale. The electric field gradient is created by connecting one thread to the plus voltage and the other to the minus voltage. The ultra-thin gating plane provides rigorous ion selectivity, and the small spacing between the alternating electrodes yields a steep electric field with relatively small electric potential applied to the electrodes. The usage of small electric potential suppresses the leaked electric-field coming from the massgate, which provides the following advantages: First, shorter pulse (off) can be applied to the ILC massgate

without perturbing the kinetic energy of the transmitted particles. Second, it can be placed near other ion optic components without affecting their operations.

The first design was proposed by Loeb and Lusk, and it was incorporated in their study as a high sensitivity electron filter. Many variations of the original design have been developed for various applications in high resolution mass spectroscopy. Schlag *et al.* applied the ILC massgate to their study of the photodissociation of benzene.¹⁴ The effective mass-filtration performed by the ILC massgate provided a more pronounced mass spectrum for the photo-fragmentation of the benzene molecule. Kappes and his coworkers demonstrated high resolution separation (mass resolution of 280 at $m/e = 559$) of ions achieved by the two sequential interleaved comb massgates.¹⁵ Enke and his coworkers reported unit mass resolution for selection to m/z 167 in their tandem reflectron mass spectrometer.¹³

Our interleaved comb massgate was constructed based on the design proposed by Enke and collaborators.¹³ The massgate consists of two vespel blocks (MSG-VSP), two posts, four electrodes, two threads of stainless steel wires. The gating plane was built by weaving two threads of ultra-thin (0.076 mm thickness) wires (California Fine Wire, SS 318 high temperature stress-relieved) through the vespel blocks which have a row of 26 predrilled holes (0.38 mm I.D.; 1.0 mm spacing). The two threads occupy every other hole, so that two threads alternate in the gating plane. Each end of the wire was anchored on the top and bottom electrodes (threaded rod, 2-56) by pinching the wire in between two flat washers. The top vespel block has two tapped holes (6-32) at the bottom side, while the bottom vespel piece has the clearance hole (6-32) instead. This is

intended for holding the two vespel blocks together by the tension on the wires. The tension in the wires can be increased by pulling the two vespel pieces apart by tightening the hex nuts in the posts, which provides wrinkleless gating plane with uniform spacing between the wires. The distance between the vespel block was adjusted to be 1.8" to match the hole position of dimension of a Kimball Physcis component (SS-PL-C7X7), and the effective area of the gating plane was 1.5" x 1.0".

The effective gating relies on the electric pulse applied to the massgate. In order to achieve high selectivity, the high voltage pulse should be short with fast fall (off) and rise (on) time. We used the module PVM-4201 manufactured by DEI as the high voltage pulser. The module contains a high voltage on/off switch with built-in bipolar DC supplies. It produces maximum voltages of ± 950 V with 15 ns fall and rise time, and the width can be reduced down to 40 ns. The reliable mass selection was achieved with ± 500 V (100 ns) at 3-kV acceleration. The pulse width shorter than 100 ns affects the kinetic energy of the transmitted charges due to the electric field leakage. It is ideal to place the massgate near the laser-interaction region where the ion packets are focused along the TOF axis. As mentioned above, the ILC massgate gives out stray electric field which is extremely defective to the photoelectron spectrometer. The massgate was positioned 3.5" before the laser interaction point.

2.6.5. MCP detector

Ion detection in the primary mass spectrometer is accomplished by using the home-built microchannel plate detector. Microchannel Plate (MCP) consists of millions

of very thin, semi-conductive glass capillaries (4 to 25 micrometers in diameter). Each capillary or channel works as an independent secondary-electron multiplier. A bias voltage (typically 1 kV) across the microchannel plate accelerates the electrons inside the channel and induces a collision between the electrons and the inner surface of the capillary. The secondary electrons become multiplied in the course of cascading down the channel, which results in electron-avalanche at the output.¹⁶ The electric response time in the amplification process is very fast and the overall resolution is greater than 100 MHz (10 ns), which makes an MCP detector suitable for recording a train of short ion-packets.

Our detector assembly consists of two microchannel plates (Burle Electro-Optics), four electrodes, a ground-mesh plate and a voltage divider. The entire assembly including the voltage divider was mounted on the ASA flange (ASA4-MCP) which has two SHV and one BNC high electric feedthroughs. The MCPs are stacked together in ‘Chevron’ configuration which refers to the 180° rotation of the front plate with respect to the rear plate. The MCP Chevron prevents the positive ion generated at the output of the front plate reaching the input of rear plate by creating a large directional change in the microchannel axis. Three stainless steel electrodes (SS-PL-C5X5-R1000) were placed at the top (entrance), inbetween and at the bottom (exit) of the Chevron assembly, and a donut-shaped copper shim is inserted in every junction between the MCP and the stainless plate to ensure the electric contact. The collecting plate (anode) was placed 0.25” from the exit electrode and a ground mesh was placed in front of the entrance plate to screen the electric-field emanating from the MCP plates.

The MCP assembly was operated in the AC mode which permits high frequency waveforms and blocks DC current, and the AC mode detection scheme can be easily implemented by appending an RC circuit in the anode output. The negative-ion detection necessitates the AC mode operation because of the following: For positive ion detection, the acceleration gradient is created by applying negative voltage to the entrance plate while grounding the anode. This scheme cannot be applied for negative-ion detection since the electric field on the entrance plate will repel the negative ions (or electrons). The electric potential gradient across the MCP must be created by lowering the anode potential while keeping the entrance plate at zero electric potential. Therefore, it is necessary to apply a positive DC voltage to the anode. The AC mode operation permits the high DC voltage on the anode since it prohibits the DC current from flowing to an oscilloscope or a boxcar integrator.

Unlike the conventional assembly of a MCP detector, two high voltage inputs (SHV) were employed in our design. Each SHV is connected to the entrance plate and the anode, which provides a great deal of operational ease for switching between negative-ion detection and positive-ion detection. For negative-ion detection, the DC voltage supply is connected to the anode SHV while the entrance SHV is connected to ground. With positive voltage on the anode, ‘pulling mechanism’ (as if the anode is pulling the electron from the MCPs) is implemented for the signal amplification. Conversion to the positive-ion detection can be effortlessly done by swapping the two connections and switching the polarity of the DC supply to negative voltage.

The supplementary RC circuit is integrated together with the voltage divider, and

the circuit diagram for RC circuit and the voltage divider is shown in Fig. 2.16. A series of three resistors (R_1 , R_2 and R_3) divides the input voltage into 1:1:1/4 ratio. Typically ± 2.0 kV is applied to the high voltage end, which provides ± 900 V across each microchannel plate and ± 250 V between the exit plate and the anode. Relatively large current ($220 \mu\text{A}$) was drawn in the voltage divider in order to minimize the precision uncertainty caused by the current fluctuation. The capacitors C_1 and C_2 are connected in parallel to the voltage divider, which eliminates high frequency noises generated from the DC supply and the electrodes. The resistor R_4 is the current stopper which works in both directions. First, it stops the signal flow to the SHV inputs and directs the entire signal to the BNC output. R_4 must have larger impedance than C_3 which has impedance of $\chi_C = (2\pi \cdot f \cdot C)^{-1} \sim 100 \Omega$, in order to suppress the current flow to the SHV connector. Second, it prohibits dark current generated in the MCPs from reaching the BNC output. The R_5 - C_3 corresponds to the supplementary high frequency pass filter used in the AC mode operation. To match the input impedance of the oscilloscope and the boxcar integrator, $50\text{-}\Omega$ resistor was used for R_5 . The size of capacitance is important since it determines the lower limit of the signal (or noise) frequency that can pass through the RC circuit. We chose 150 pF for C_3 to give the lower limit of $\sim 20 \text{ MHz}$ [$f = (2\pi \cdot R \cdot C)^{-1}$], which is sufficiently smaller than the MCP resolution (2 GHz) and the signal of interest ($> 100 \text{ MHz}$). The overall resolution of the assembly was about 2.5 ns , and the output waveform corresponding to the single ion event is shown in Fig 2.17. The negative and positive ion mass spectra are shown in Fig. 2.17.

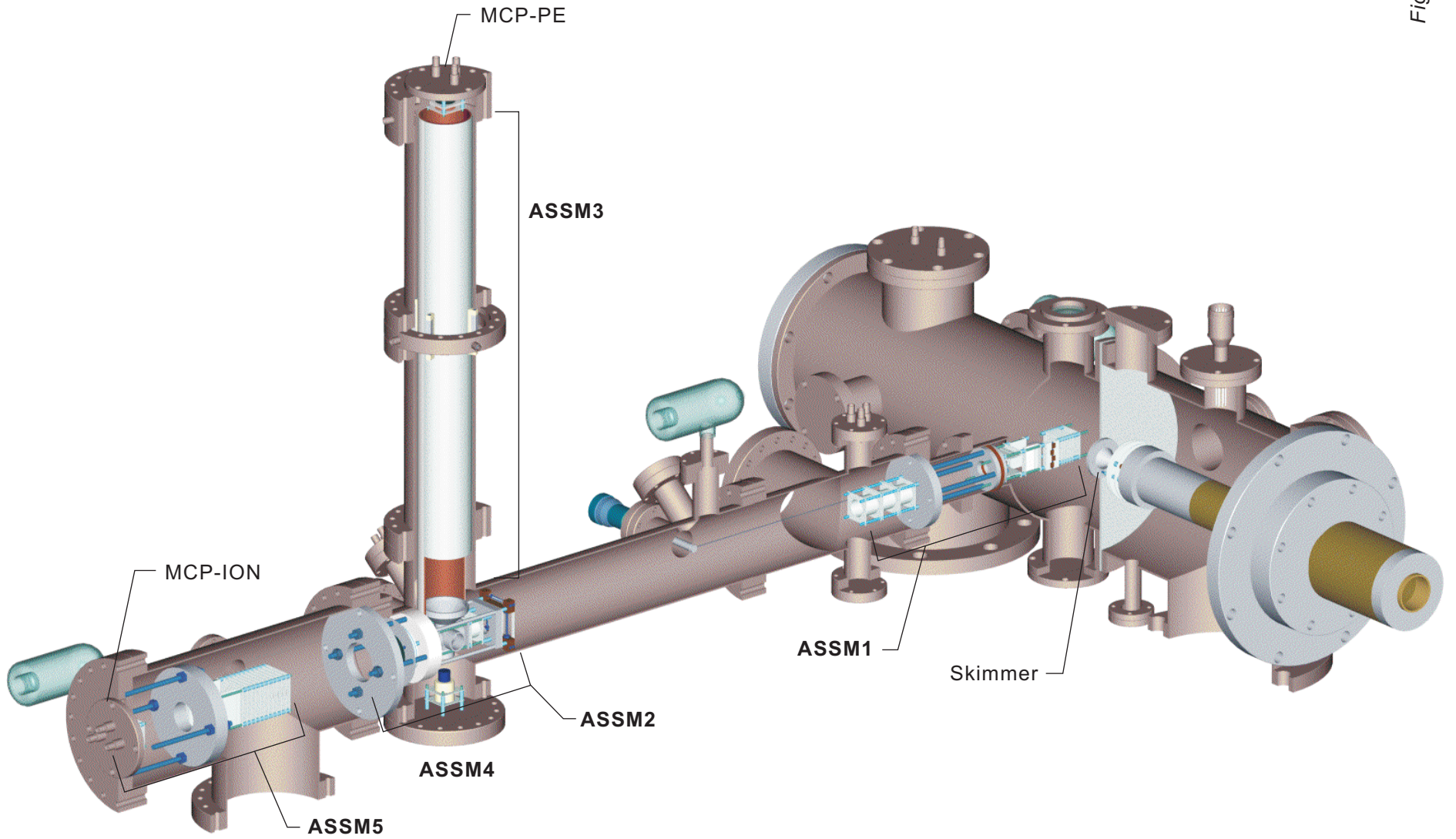
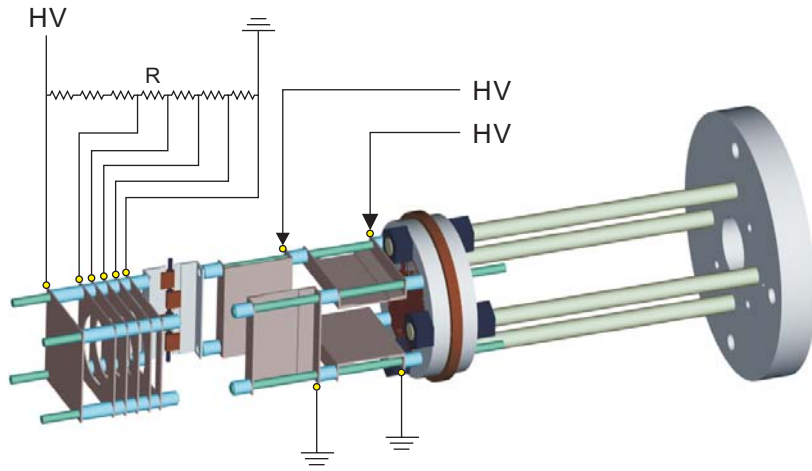


Figure 2.11

96



$R = 2.2 \text{ k}\Omega$

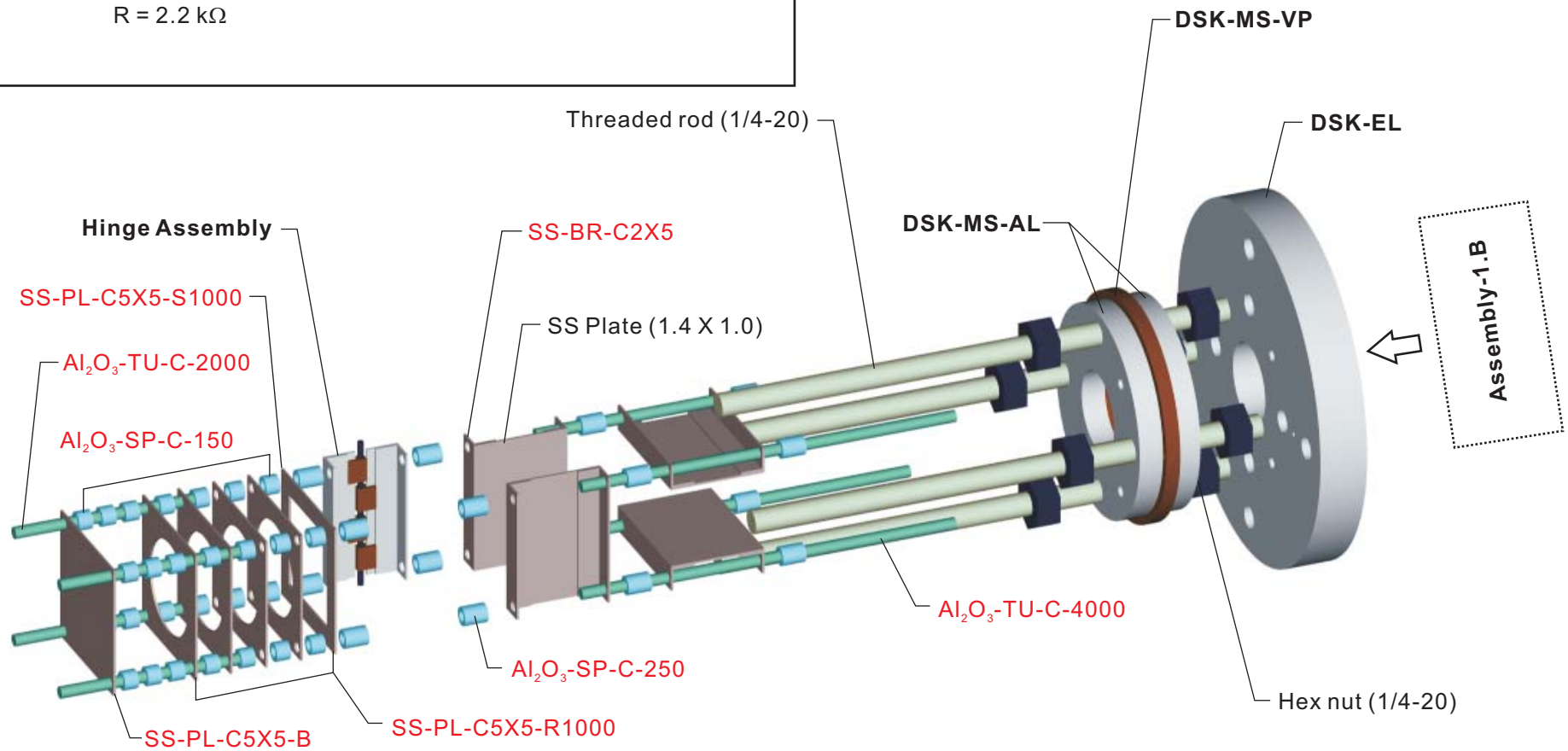
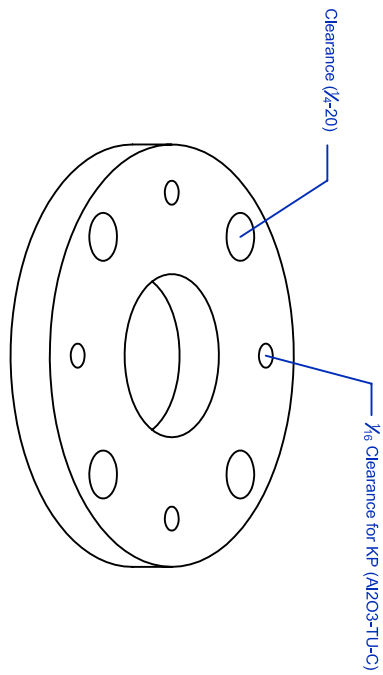
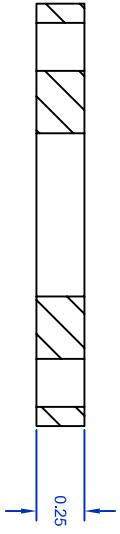
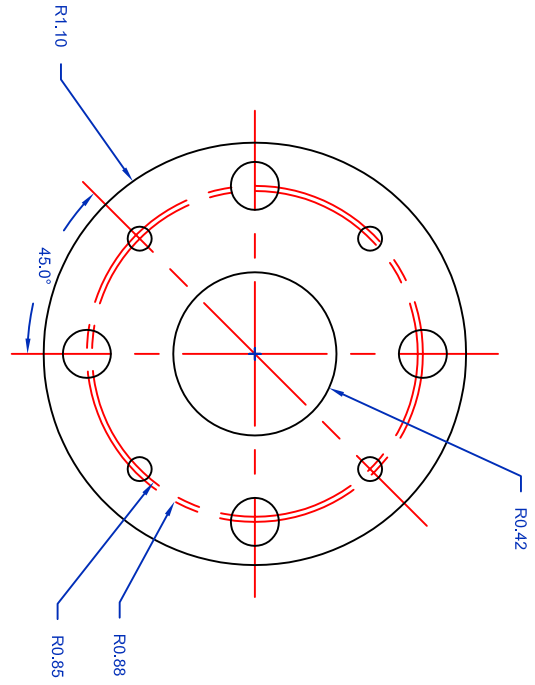


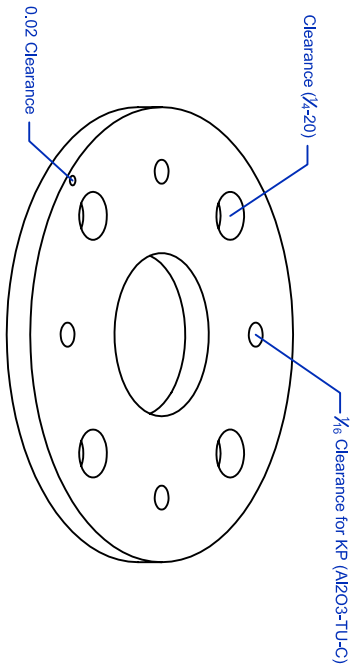
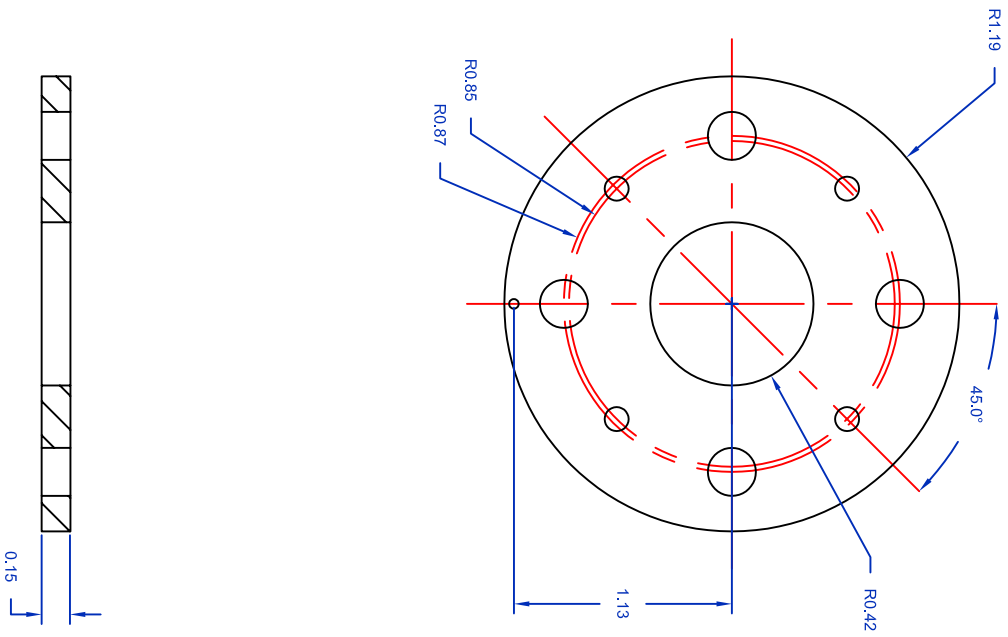
Figure 2.12



NOTE:
1. KP stands for Kimball Physcis, Inc.

Figure 2.12.1

TITLE	FILE NAME	DWG BY	PI
DISK for Ion Optics	DSK-MS-AL.dwg	D. Hahn Park	AHZ
SCALE	MATERIAL	UNIT TOLERANCES	(UNLESS SPECIFIED)
1:1	AL 6061	inch (0.001)	degree (0.5)
		Laboratory for Molecular Sciences California Institute of Technology	
		6	01



NOTE:
1. KP stands for Kimball Physics, Inc.

Figure 2.12.2

TITLE	DISK for Ion Optics	FILE NAME	DSK-MS-VIP.dwg	DWG BY	D. Hahn Park	PI
SCALE	1:1	MATERIAL	VESPEL	UNIT TOLERANCES	(UNLESS SPECIFIED) inch (0.03)	Laboratory for Molecular Sciences
					degree (0.5)	California Institute of Technology
						01

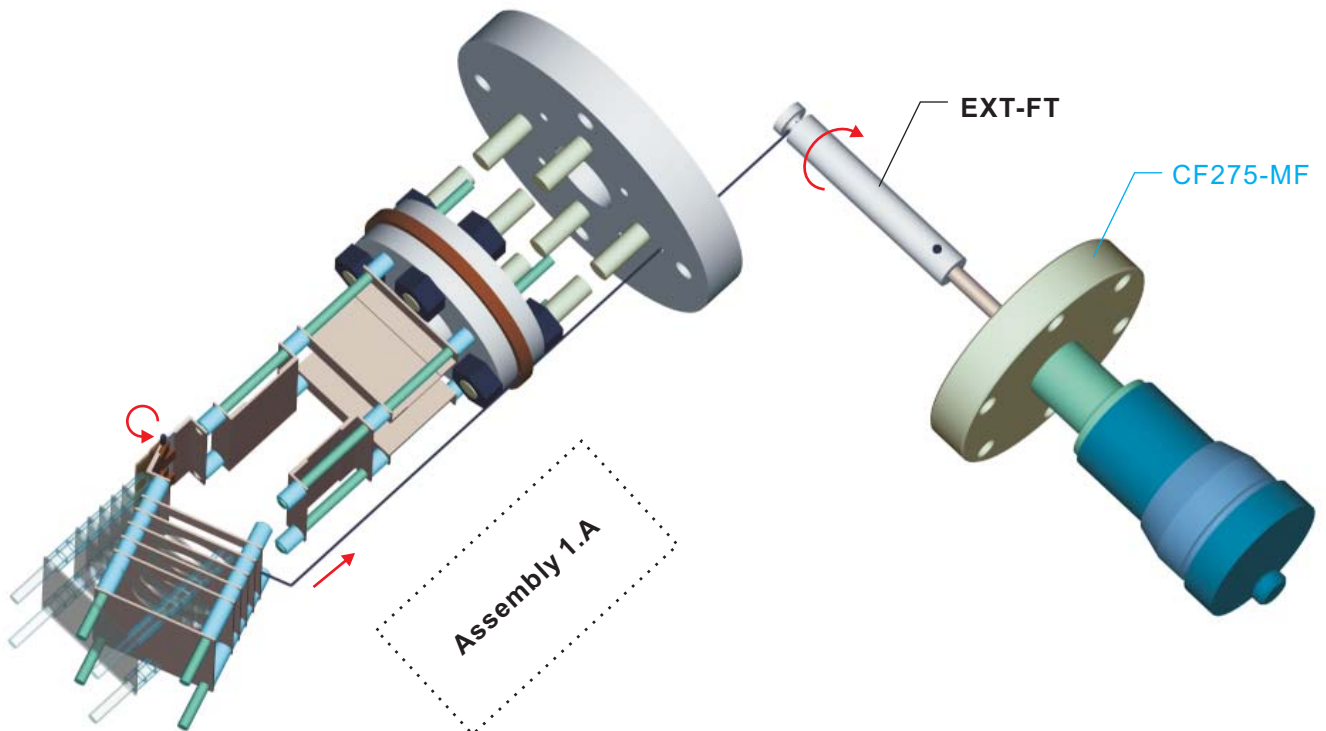
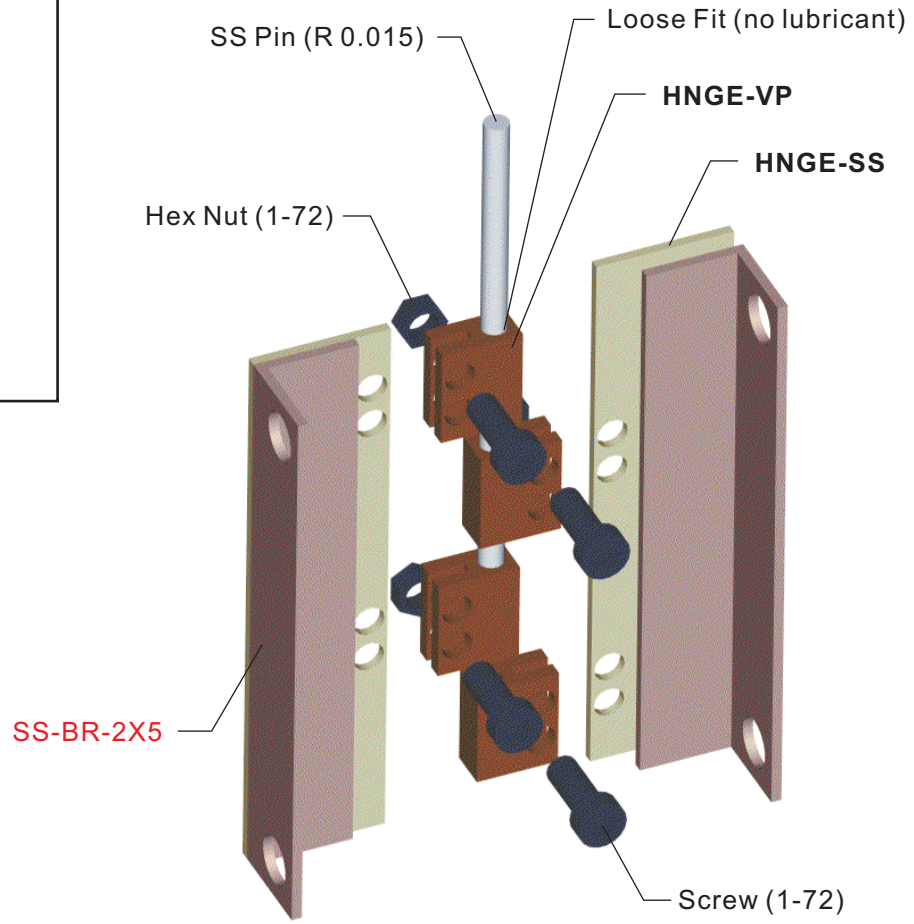
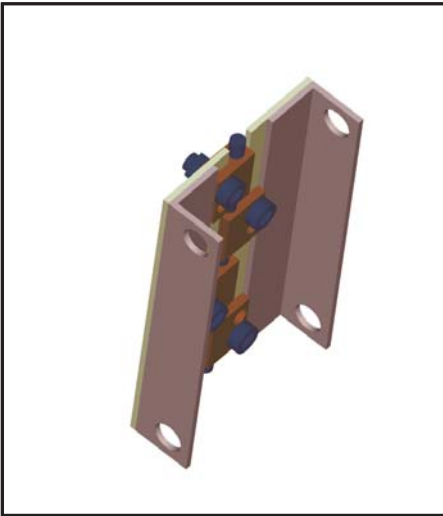


Figure 2.13

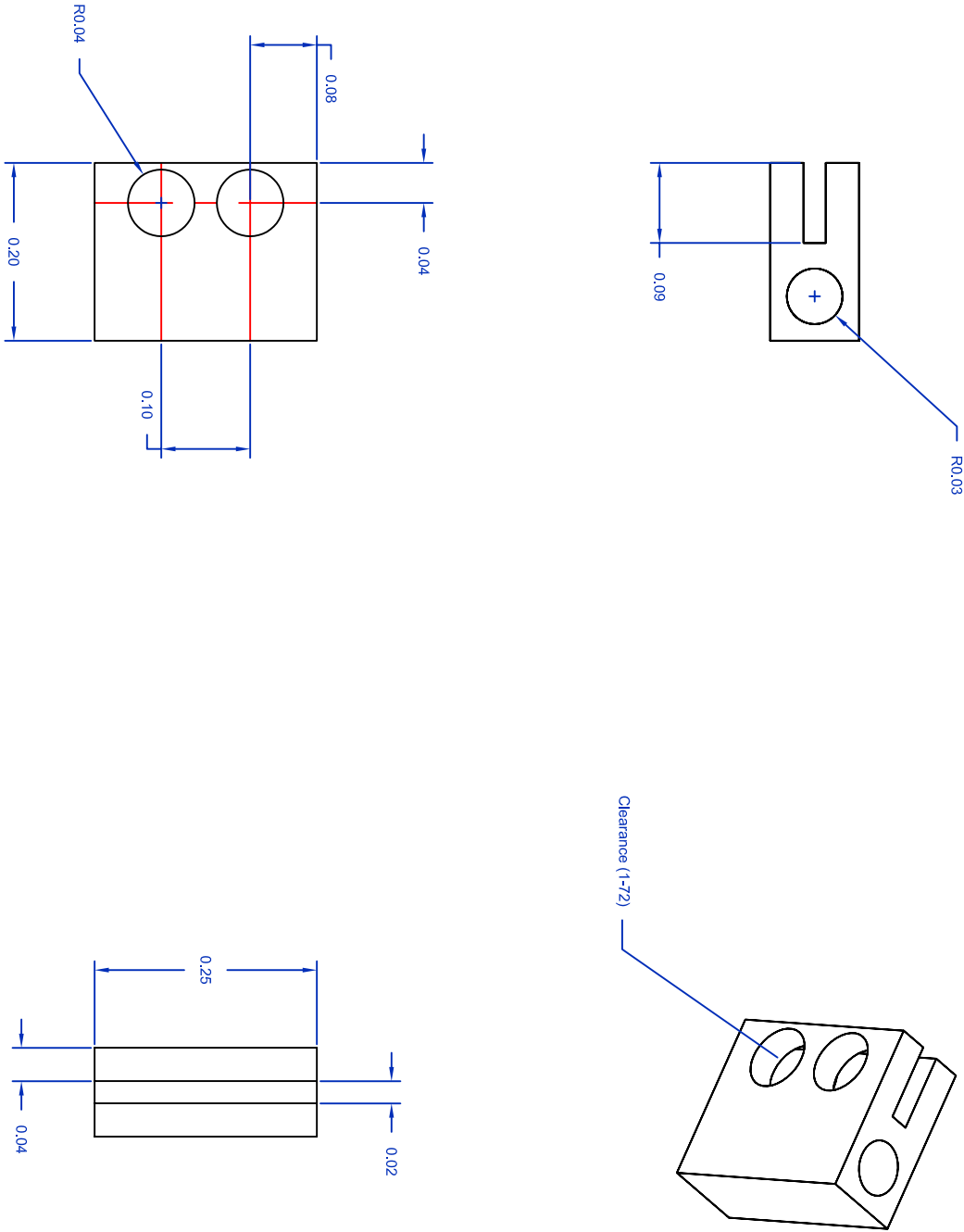


Figure 2.13.1

TITLE	HINGE-V/VP.dwg	FILE NAME	DWG BY	PI
SCALE	5:1	MATERIAL	D. Hahn Park	AHZ
	VESPEL	UNIT (TOLERANCES)	Laboratory for Molecular Sciences (UNLESS SPECIFIED) inch (0.03) degree (0.5) California Institute of Technology	
			6	01

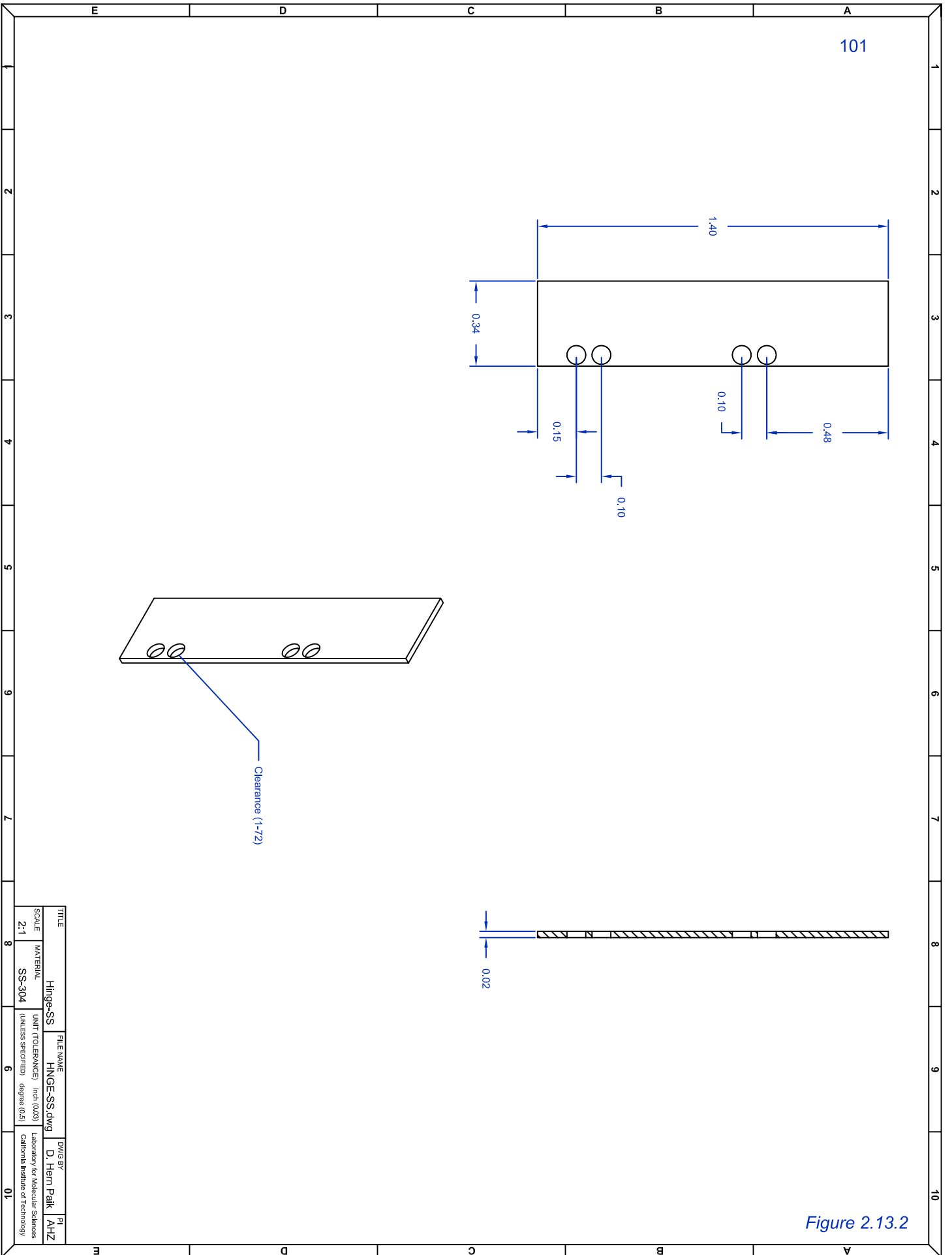
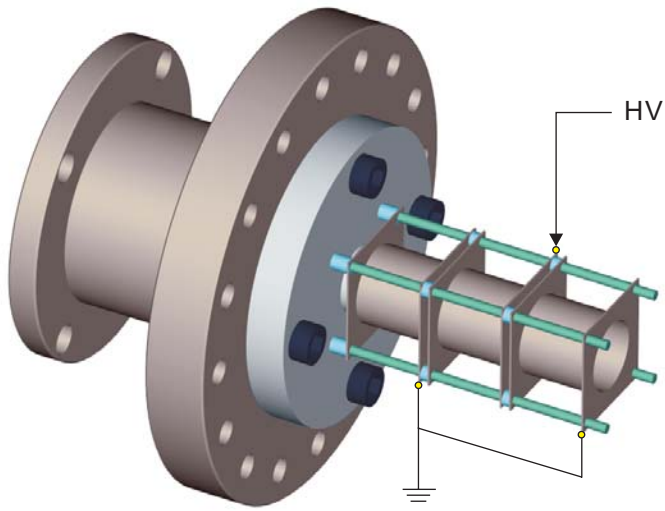


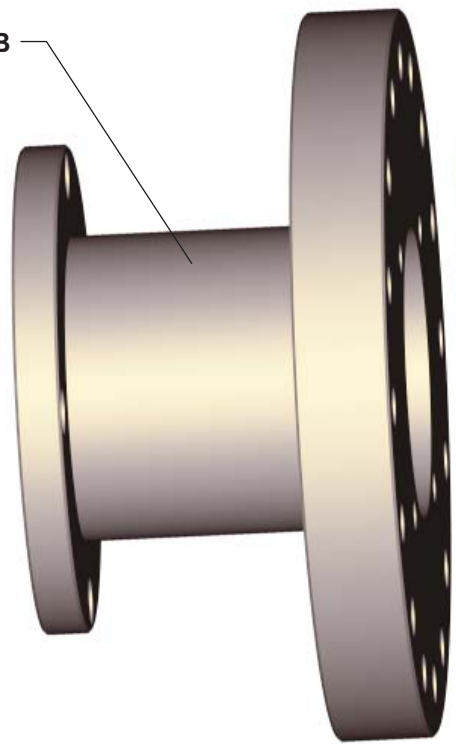
Figure 2.13.2

103



Assembly-1.A

NIP-C-B



DSK-EL



SS-PL-C5X5-R1000

SS-CY-1000/1000

Al₂O₃-SP-C-100

Al₂O₃-TU-C-4000

Al₂O₃-SP-C-250

Screw (1/4-20)

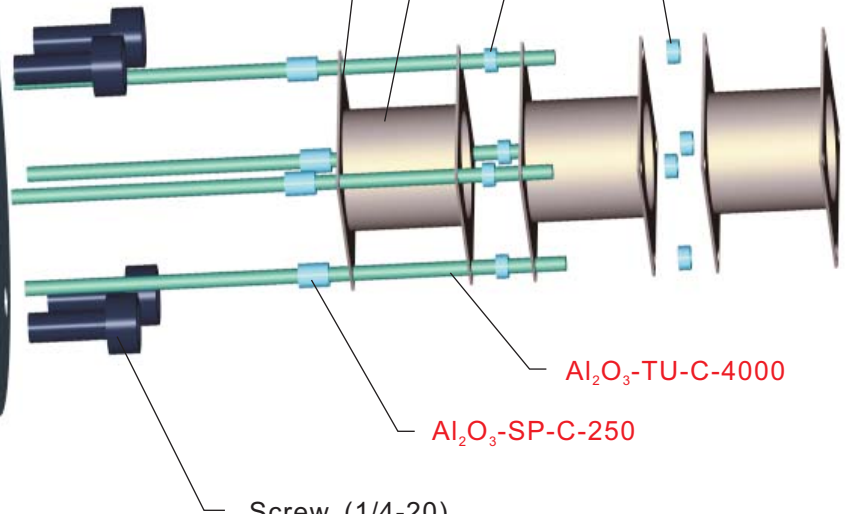
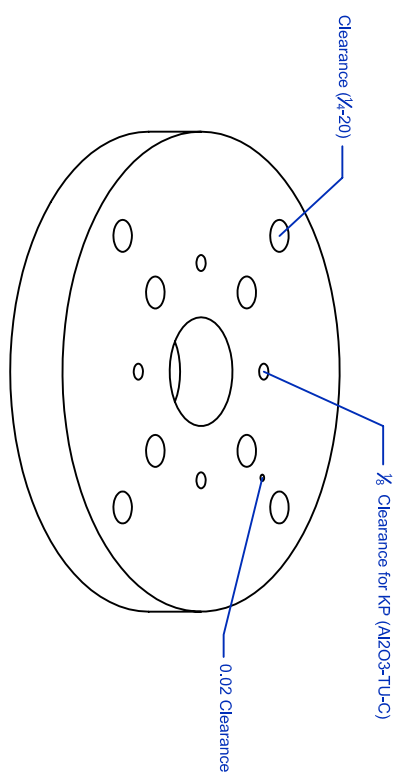
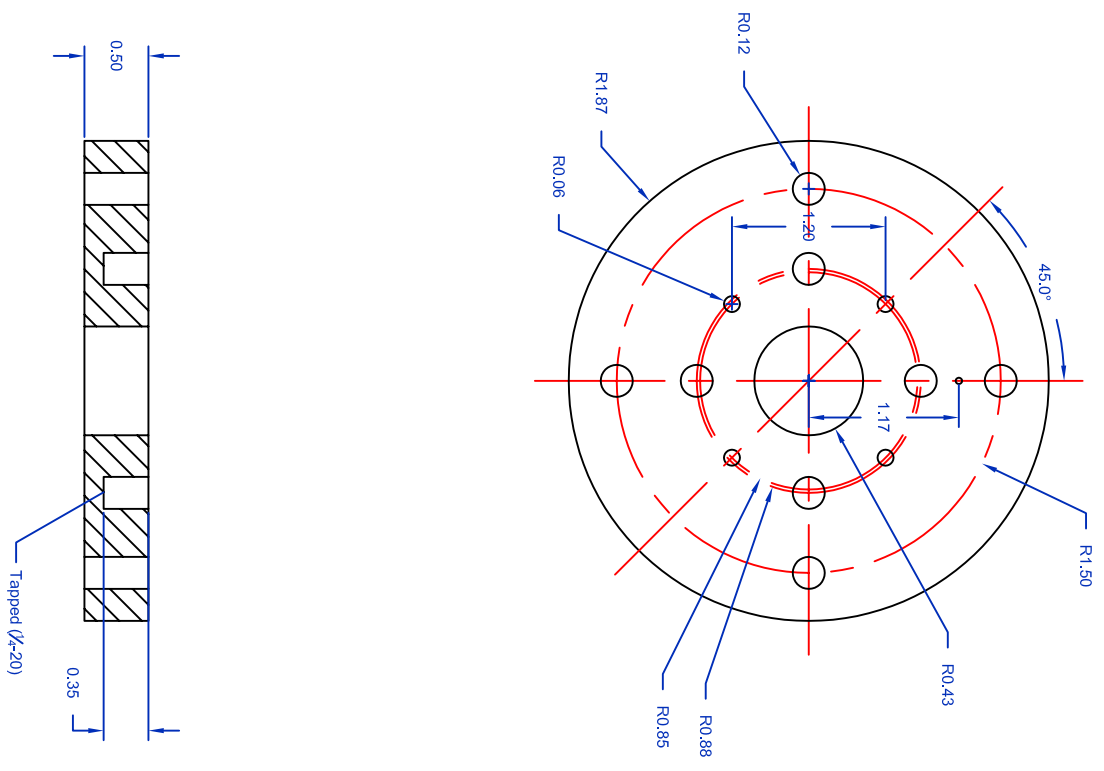


Figure 2.14



NOTE:
1. KP stands for Kimball Physcids, Inc.

Figure 2.14.1

TITLE	DSK-EL.dwg	FILE NAME	DWG BY	PI
SCALE	2:3	MATERIAL	D. Hahn Park	AHZ
	AL 6061	UNIT (TOLERANCES)	Laboratory for Molecular Sciences	
		(UNLESS SPECIFIED)	California Institute of Technology	
			6	01

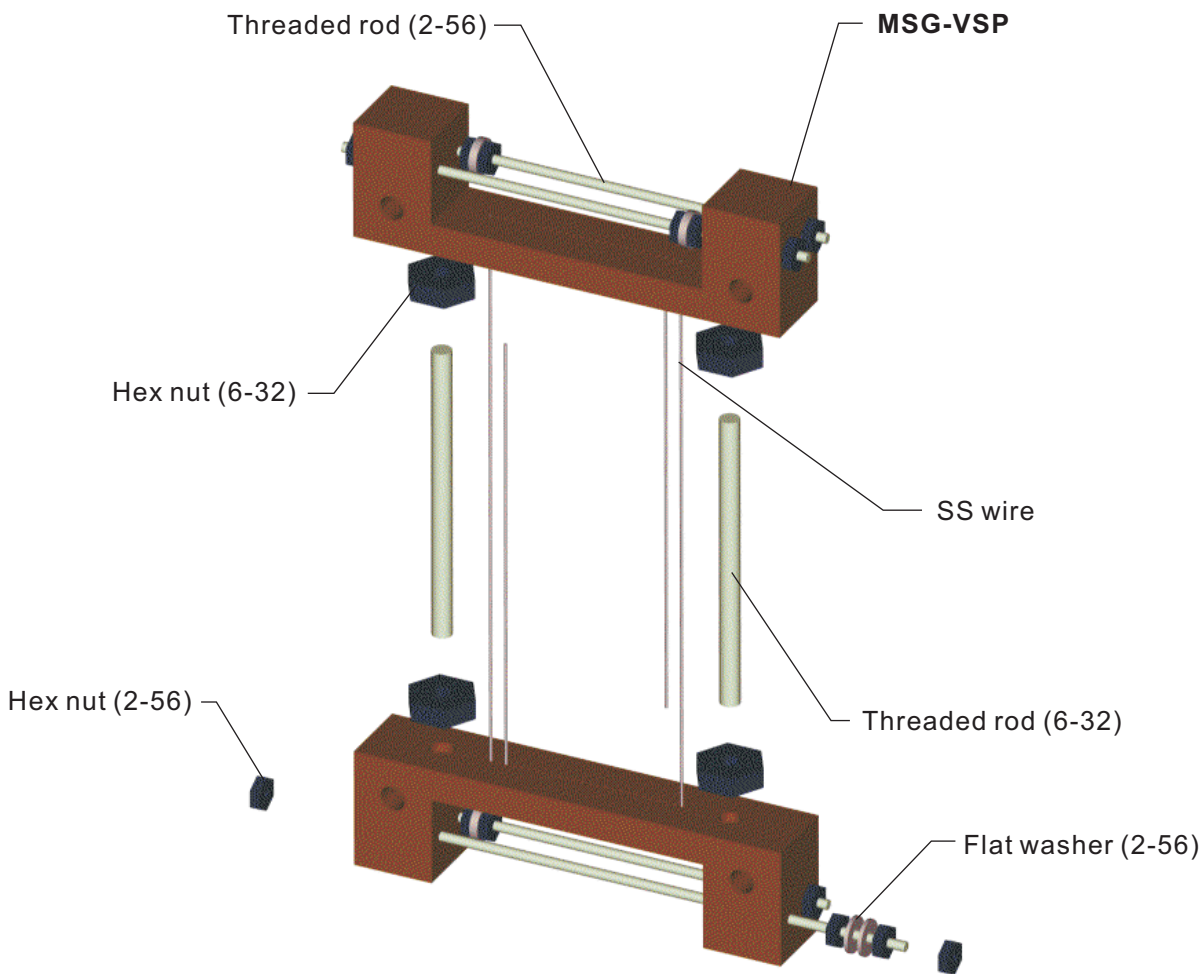
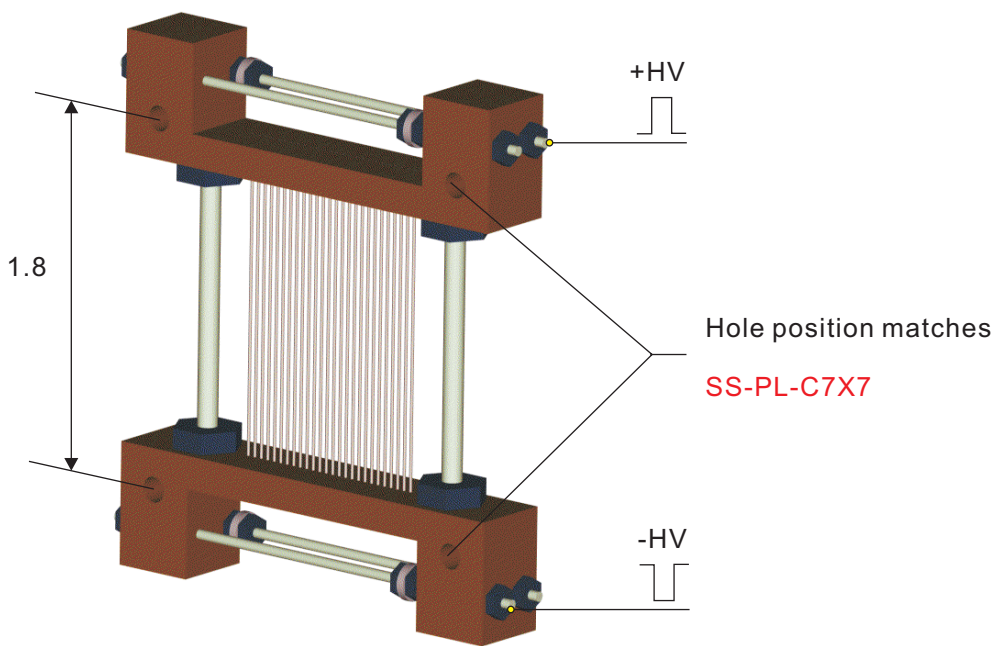
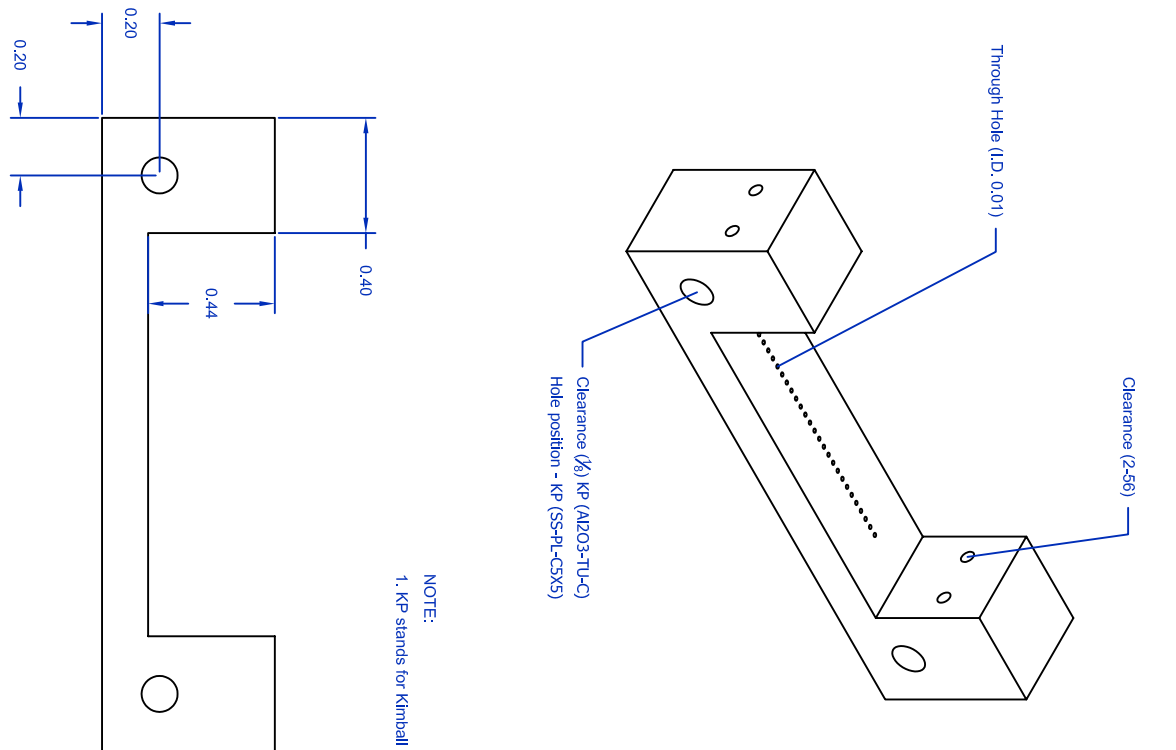
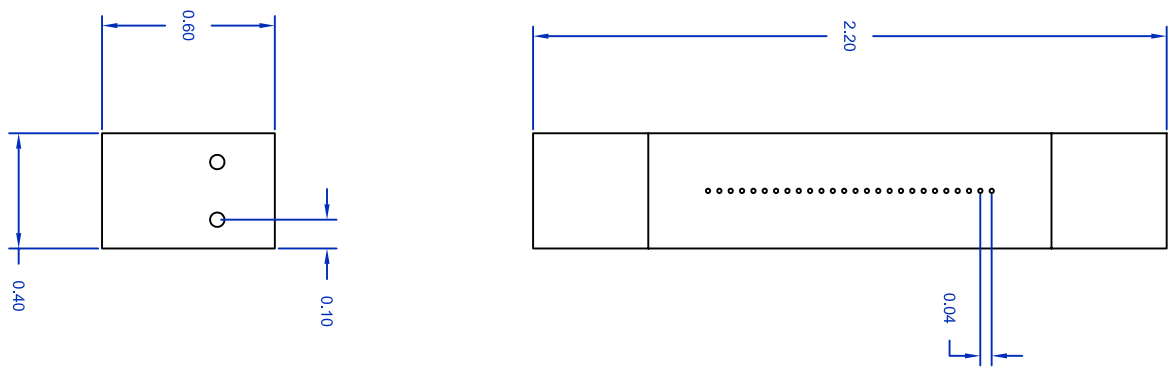
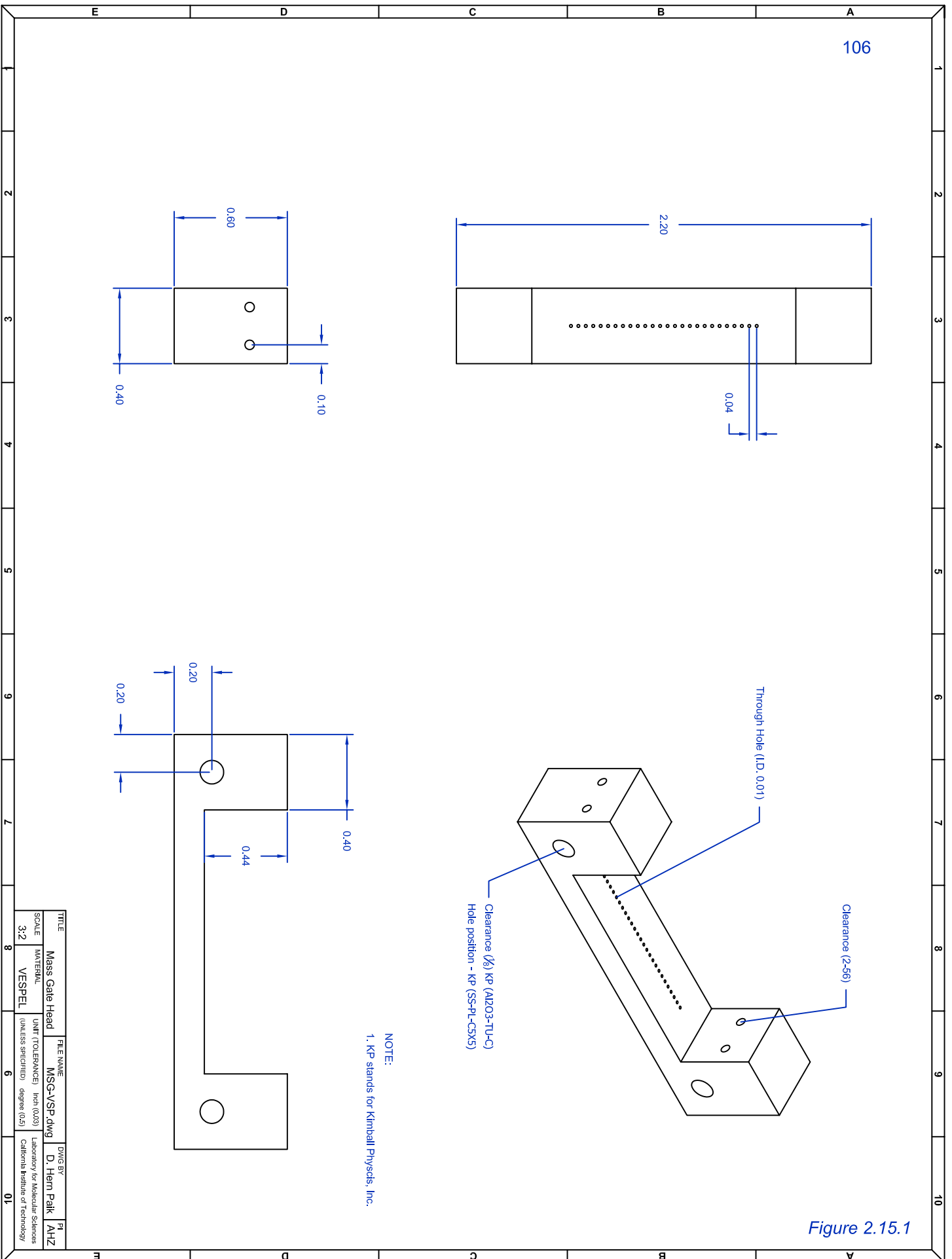


Figure 2.15



NOTE:
1. KP stands for Kimball Physcids, Inc.

Figure 2.15.1



TITLE	MSG-VSP.dwg	DWG BY	D. Hahn	PI	AHZ
SCALE	3:2	MATERIAL	VESPEL	UNIT (TOLERANCES)	inch (0.001)
				(UNLESS SPECIFIED)	degree (0.5)
					Laboratory for Molecular Sciences
					California Institute of Technology
					01

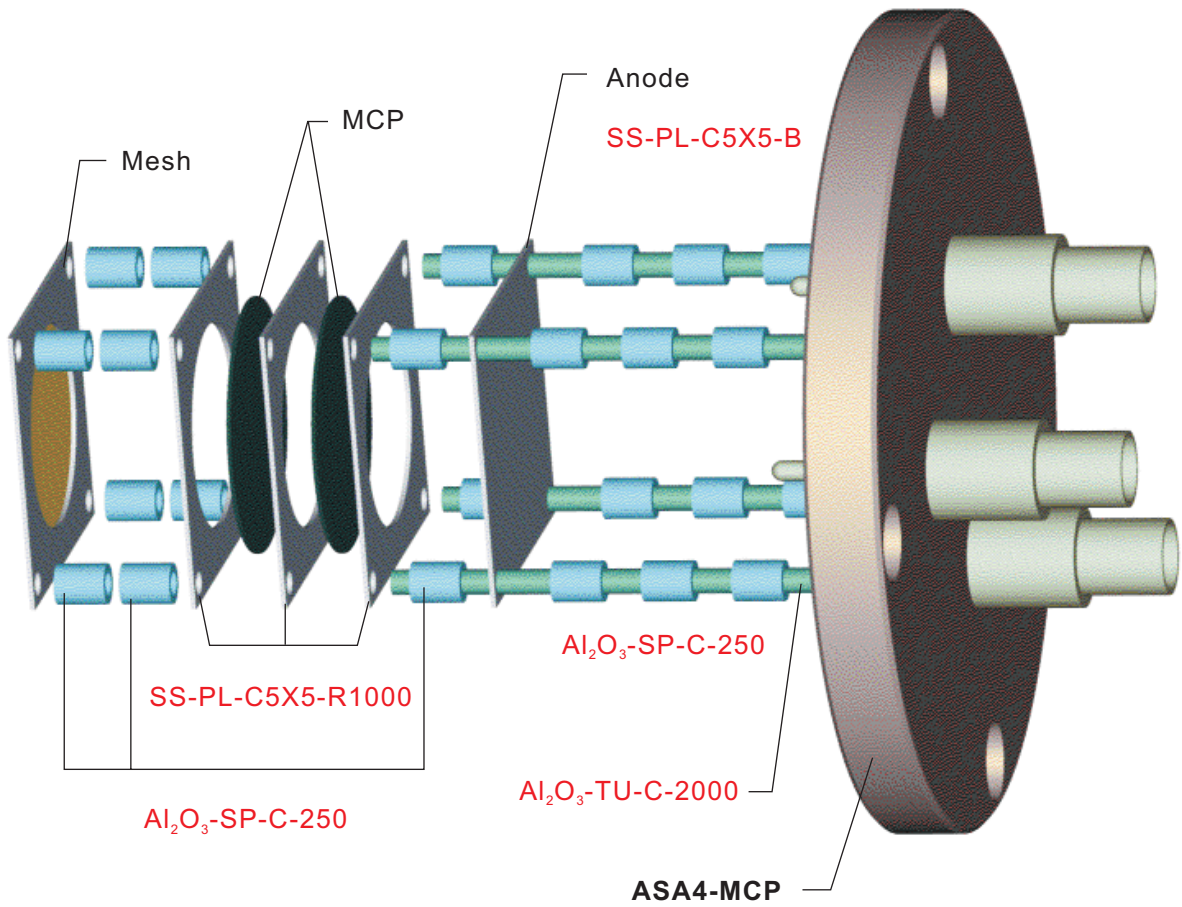
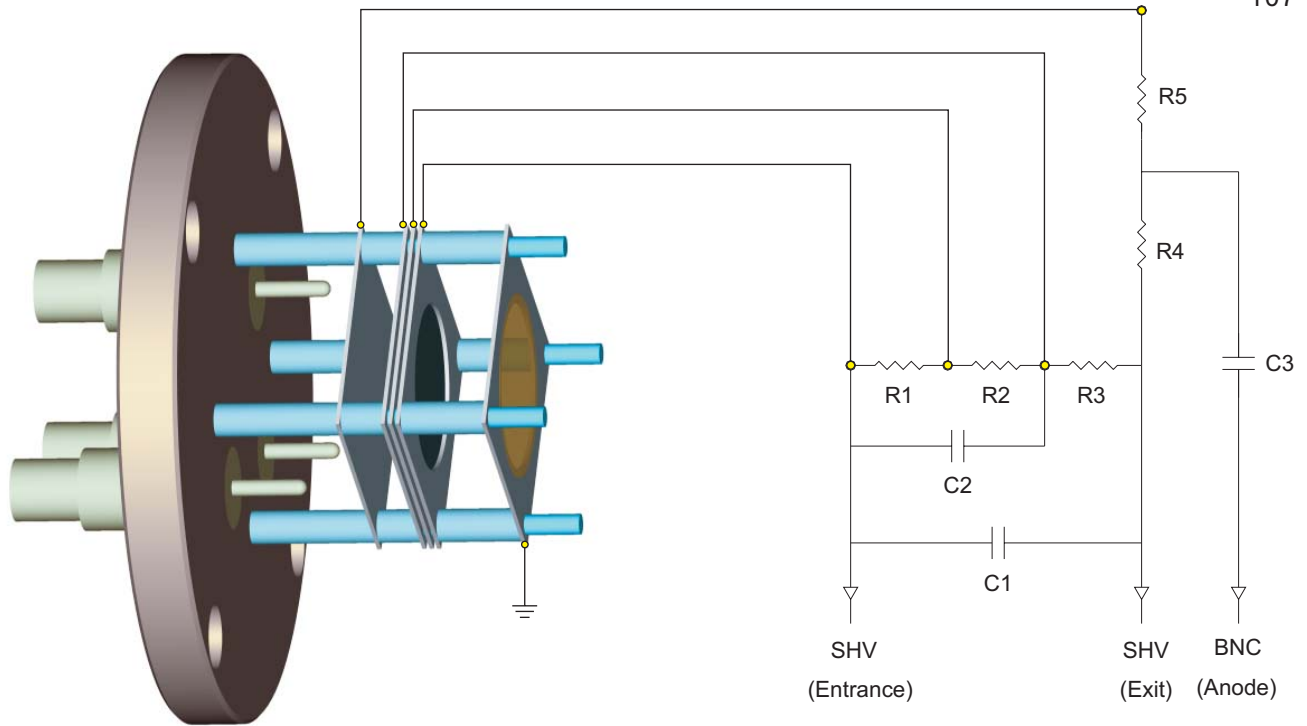
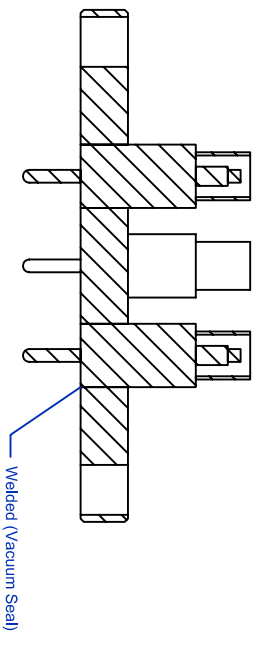
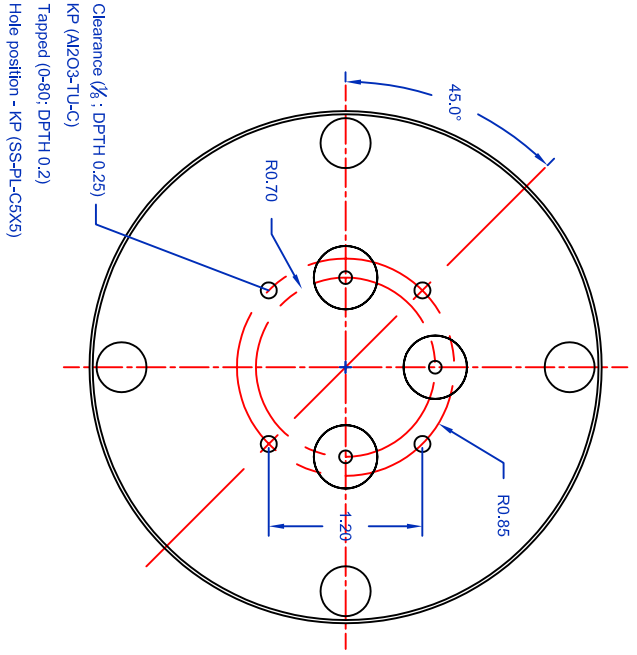


Figure 2.16



- NOTE:
1. AS44 was purchased from Huntington Laboratories, Inc.
 2. No O-ring groove on the flange.
 3. KP stands for Kimball Physods, Inc.
 4. SHV 5 and BNC were purchased from ISI.

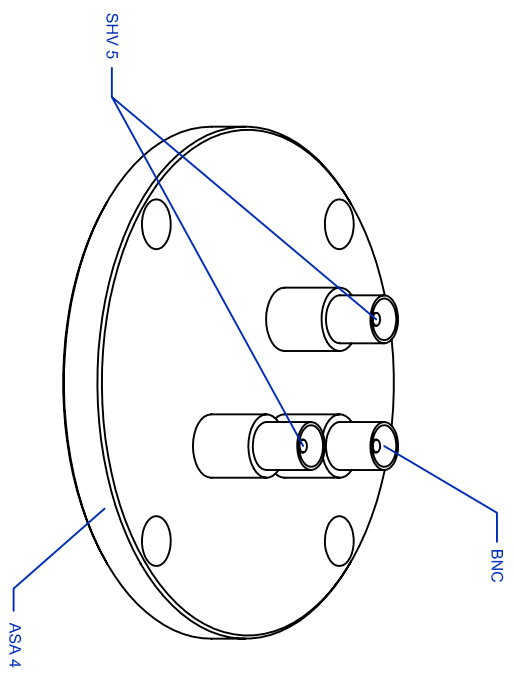


Figure 2.16.1

TITLE		FILE NAME		DWG BY		PI	
AS44 Modification		AS44-MCP.dwg		D. Hain Park		AHZ	
SCALE		UNIT (TOLERANCES)		MATERIAL		Laboratory for Molecular Sciences	
2:3		inch (0.03)		SS-304		California Institute of Technology	
		UNLESS SPECIFIED degree (0.5)		6		01	

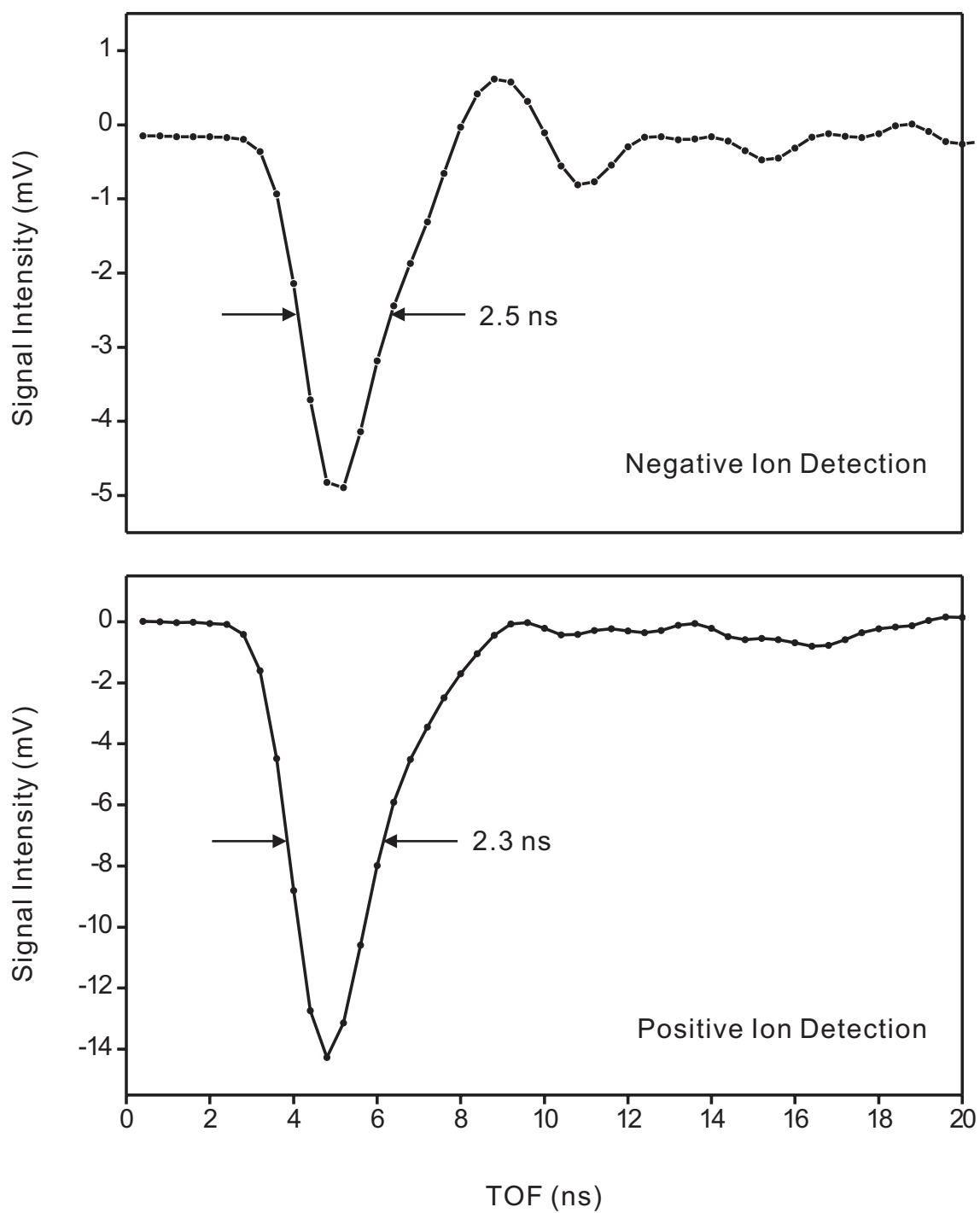


Figure 2.17

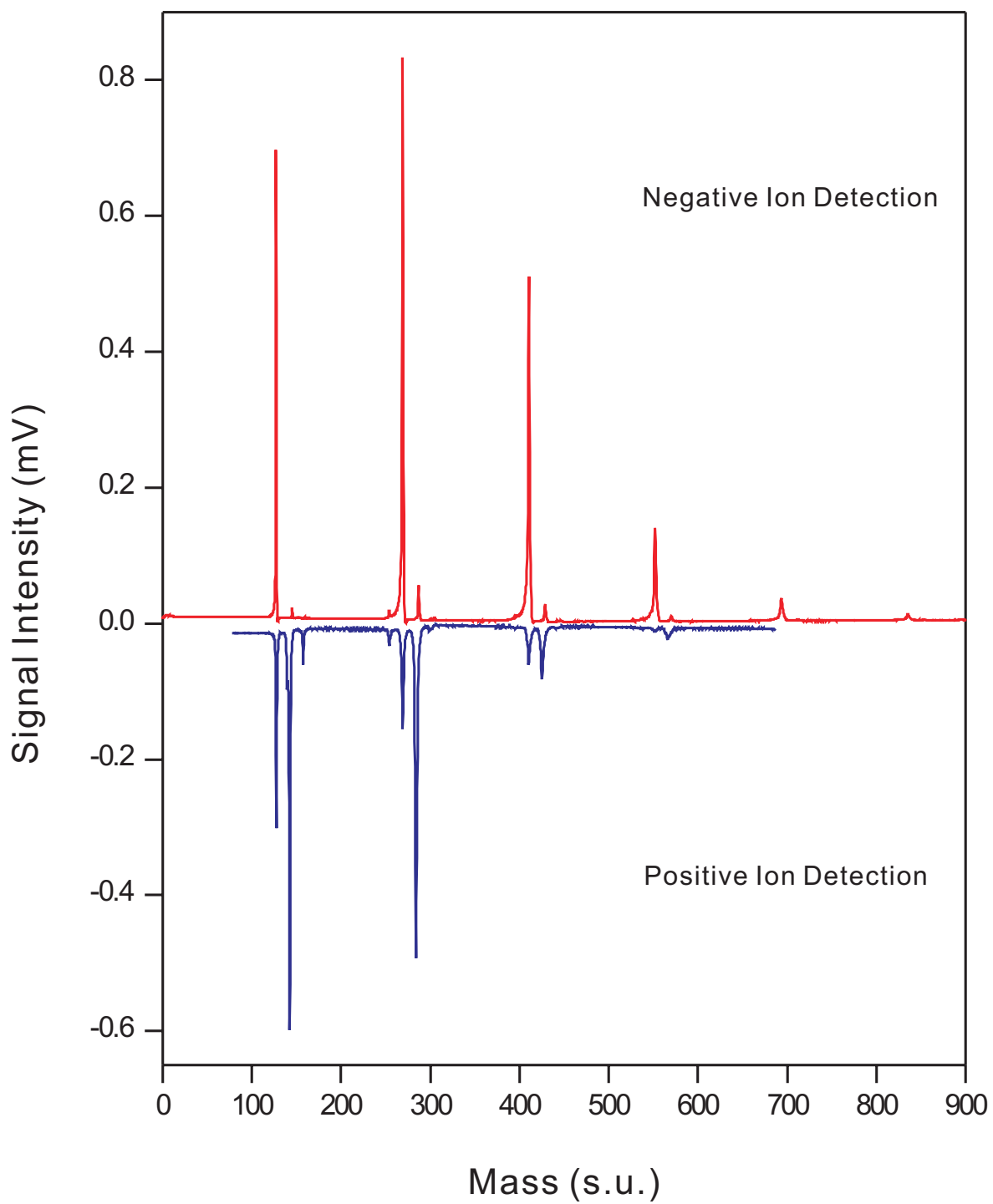


Figure 2.18

2.7. Reflectron Mass Spectrometer

The reflectron mass spectrometer is the secondary mass spectrometer which serves two main roles: First, it collects fragment ions and charge-reversed cations. As a result of laser interaction, a negatively charged species can undergo the following processes: (1) It can be dissociated into a negatively charged fragment and neutral fragments. (2) It can be neutralized by removing the excess electron. (3) In the presence of strong electromagnetic field, it can also undergo sequential photoreactions of neutralization followed by photoionization.^{5,6} It can also discriminate the metastable species from the parent ion, which is not possible in the uniaxial primary mass spectrometer. Second, the reflectron mass spectrometer compensates the second-order spatial (dz/dt) broadening originated from the initial energy distribution. As discussed before, it can refocus the post focal-plane broadening caused by the space-focusing action.

The reflectron consists of a series of ring electrodes in which the retarding electrostatic field is formed. It decelerates, reflects, then reaccelerates the ions climbing the 'uphill' created inside the reflectron. By tuning the gradient of the retarding voltage, the penetration depth (distance at which the ions turn around) can be adjusted. The energy focusing is based on the fact that the penetration depth varies with ion kinetic energy. The high energy ion penetrates further into the reflectron and spends longer turn-around time, but it traverses the field-free drift region more quickly. Incorporating the reflectron into the primary mass spectrometer gives an immensely improved mass resolution.¹⁷⁻¹⁹ The primary mass spectrometer focuses an ion packet at the entrance of the reflectron, which eliminates the initial position distribution of the ions entering the

reflectron. By doing so, the initial position spread is converted to the kinetic energy distribution which is compensated by the reflectron mass spectrometer.

The concept of the reflectron can be understood by considering the reflection of a charged particle with a kinetic energy of eE by a *single-stage* reflectron.^{3,12} The time spent in the accelerator is disregarded for simplicity. The total flight time of the particle with mass, m is

$$t = \sqrt{\frac{m}{2eE}}(L_1 + L_2 + 4d), \quad (2.14)$$

where L_1 denotes the distance from the exit plate of the accelerator to the entrance grid of the reflectron while L_2 is the distance from the entrance grid of the reflectron to the focal plane (detector), and d is the penetration depth. Then, the time spread (Δt) due to the excess kinetic energy (U_0) can be written below:

$$\Delta t \cong \frac{\sqrt{m} \cdot U_0}{(2eE)^{\frac{3}{2}}}(L_1 + L_2 - 4d), \quad (2.15)$$

and $\Delta t = 0$ when $4d = L_1 + L_2$. Hence, to achieve the energy focus by the *single-stage* reflectron, the length of the reflectron must be long enough to accommodate the required penetration depth.

The *dual-stage* reflectron does not bear the geometric constraints which are imposed on the *single-stage* reflectron. It decelerates the incoming ions in a relatively short distance by adding a steep electric field gradient before the reflection region. The ions enter the reflection region with considerably smaller kinetic energy, thus the penetration depth is now compatible to the scaled-down energy spread. The general rule of thumb is that the total tube length of the field free regions ($L_1 + L_2$) should be about 8

times the length of the reflectron if ions lose about two-third of their kinetic energy in the first one tenth of the reflectron depth. In addition, the second-order energy focusing can be achieved by the dual-stage reflectron. The basic principle is analogous to the operation of the dual-stage accelerator. See references 12 and 18 for details.

The dual-stage reflectron can operate in four different reflecting schemes, depending on the field strength of the deceleration and reflection regions. First, the transmittance of the reflection (totality of the reflection) can be controlled by the electric potential of the end plate, which provides a rigorous way of filtering various sizes of ions contained in an ion packet. Remember that fragmentation of an ion in the field-free region will not affect the velocity of the nascent fragments; therefore, the kinetic energy of the nascent fragments will be proportional to their mass. If the potential of the end plate is higher than the acceleration voltage, then all ions in the ion packet will be reflected (total reflection). If the potential energy (PE) of the end plate is lowered below the potential energy of the accelerator, then only the small fragment ions with $\frac{1}{2}mv^2 < PE$ will be reflected and the fragments with $\frac{1}{2}mv^2 > PE$ will penetrate through the reflectron (partial reflection).

If the electric potential of the reflectron (both deceleration and reflection regions) is scaled down proportional to the mass ratio, then the fragment will be detected at the same arrival time as the parent ion.

$$PE_F = \frac{m_F}{m_P} PE_P \quad (2.16)$$

$$\frac{1}{2}m_F v_F^2 = \frac{m_F}{m_P} \left(\frac{1}{2}m_P v_P^2 \right) \Rightarrow v_F = v_P, \quad (2.17)$$

where PE_F is the scaled down electric potential applied for collecting the fragment (m_F) and PE_P denote the original electric potential applied for parent ion (m_P) detection. v_F and v_P correspond to the average velocities of fragment and parent ions inside the reflectron. Since the velocity in the field free region ($L_1 + L_2$) is same, the total flight time of the fragment will be identical to that of the parent. The partial reflection scheme is especially useful for studying the fragmentation of weakly bound clusters which produces various sizes of fragments.

Second, the stiffness of the reflecting plane can be controlled by the electric field gradient in the reflectron, which determines the separations among the reflected ions.³ The soft reflecting plane refers to the slow rise (on average) of the field gradient, which permits relatively large penetration depth (soft reflection). The soft reflection is mainly used in the fragmentation study because this scheme separates the ions in an ion packet by their mass. The hard plane refers to a vertical slope which bounces off the incoming ions with no penetration depth (hard reflection), which results in the deflection of the ion trajectory with no separation of ions. The vertical slope can be created by applying a repulsive potential on the entrance grid which is usually connected to the electric ground. Alternatively, pseudo vertical plane can be obtained by applying a considerably high voltage on the decelerating plate.

Hard reflection is sometimes necessary when the photoproduct of interest undergoes a subsequent dissociation before detection. For instance, consider the following photodissociation and subsequent decay:



If one wants to integrate the entire intensity of AB^- , both A^- and B^- should be detected simultaneously and the detection sensitivity must be calibrated with respect to the arrival time. If hard reflection of AB^- (*i.e.*, $PE_{AB} < PE < PE_{ABC}$) is employed, then all the fragments including AB^- , A^- and B^- will be arrive at the detector as one ion packet. The four reflecting schemes and their combinations (e.g., soft-partial, *etc.*) provide a powerful method for studying fragmentations.

Our dual-stage reflectron consists of twelve evenly space stainless steel electrodes which has the total length of 3.0 inch and the inner diameter of 1.5 inch. The two stages of the reflectron are defined by three electrodes (first, second and last), and the remaining plates works as a guiding electrodes. The first electrode is the entrance plate which is electrically grounded. The second and the last electrodes correspond to the deceleration and the reflection plates, which are connected to two separate DC voltage supplies. A uniform electrostatic field was created inside the reflectron by (1) attaching a sheet of electroform mesh to the entrance, deceleration and reflection electrodes and (2) creating an equal voltage drop between the guiding electrodes. The electroform mesh was not attached to the guiding electrodes in order to achieve the maximum ion-transmittance. The input bias voltage was equally divided by a series of eleven 1.0 MW resistors. A set of deflection plates was mounted next to the reflectron for differentiating the neutral species from the charged particles, which is important in charge reversal experiments. A ground mesh was placed between the reflectron and the deflector to shield the electric fields between them. The reflectron assembly was mounted on an aluminum disk (DSK-RFL) which can be translated along four threaded

rod screwed onto the end flange (CF800-END), which facilitate the distance adjustment between the reflectron and the detector (Fig. 2.19).

A linear configuration was adopted to incorporate the dual-stage reflectron to the primary mass spectrometer. The main advantage of the linear reflectron is that the ion path is independent of the kinetic energy of the fragments. In the folded (V-shaped) configuration, the ion trajectory exhibits a parallel shift along the folding axis due to the difference in penetration depth. A deeper penetration results in a greater separation between the incoming and the outgoing paths, and *vice versa*. The ions with different kinetic energy impinge on different sections of the MCP detector, and some ions might miss the detector if its kinetic energy is significantly different from others. Therefore, the V-shaped reflectron spectrometer will always exhibit an intrinsic difficulty of executing the total reflection mode. The problem becomes more exacerbated with increasing folding angle, thus the parallel shift can be removed by combining the reflectron and the primary mass spectrometers with zero folding angle. The linear reflectron mass spectrometer minimizes the deviation of the daughter-ion trajectories from the parent ion, which makes it possible to obtain a quantitative analysis based on the intensity profile of the fragment ion spectrum.

2.7.1 MCP Detector in the Linear Reflectron Mass Spectrometer

To implement the linear configuration for the reflectron mass spectrometer, the annular MCP detector was utilized in the apparatus.^{20,21} The MCP detector was placed near the laser interaction region with the center hole located on the TOF axis and the

entrance plate facing the reflectron. In this setup, the xy focal point of the ions lies at the center hole of the MCP, which results in ‘inverted-W’ shape ion-trajectories in the reflectron mass spectrometer. After passing through the center hole, the ions will be diverged as propagating through the reflectron. The ions will enter the reflectron with a finite incident angle hence the outgoing ions will be spread out on the detection plane. (Fig. 2.23) The pre-assembled annular MCP (Burle Electro-Optics) with a large active detection area was employed to accommodate the wide spread of reflected ions. The assembly consists of a set of annular MCP Chevron (active area: 12 cm²; center hole: 6.14 cm I.D), three stainless-steel ring electrodes and a ceramic housing. (Fig. 2.21)

The center hole in the Burle MCP was not electrically isolated, thus a supplementary shielding was provided to allow charged particles to transmit the center hole. A stainless steel tube with 4 mm I.D. (TB-MCP) was inserted in the center hole with uniform spacing (~0.5 mm) around the tube, and a ground mesh (DSK-MSH) was placed in front of the entrance plate to shield the electric field emanating from the MCP. The length of TB-MCP was about 0.25 inch longer than the thickness of the MCP assembly such that DSK-MSH sits on TB-MCP with electric contact. This complete electric shielding creates zero electric field in the ion path, which is crucial for achieving the maximum detection efficiency. An einzel lens can focus an ion packet containing 10⁵ charges down to 0.5 cm², so if the focal point is at the middle of TB-MCP, ions can transmit through the tubing without collision. However, small fraction of ion packet was dissociated due to the collision. The MCP assembly and the electric-field shielding components were mounted on the stainless steel disk (DSK-LSR) which can be translated along the TOF axis.

The reflectron detector should be capable of detecting both negative and positive ions for carrying out the fragmentation and the charge reversal experiments. To achieve this, the AC-mode detection scheme was implemented by appending a supplementary circuit similar to the MCP detector used in the primary mass spectrometer. The supplementary circuit of the reflectron detector (Fig. 2.20) is about the same as the circuit previously illustrated in Fig. 2.16, except the following: First, 2.0 kV bias voltage was applied directly across the MCP Chevron without a partitioning plate. Second, the extra high frequency pass filter across the MCP Chevron (C_2 in Fig. 2.16) was removed. The detection sensitivity of the reflectron MCP is much greater than the detector used in the primary mass spectrometer because the former has larger active area and greater amplification efficiency than the latter. The ion-signal profile recorded by using the reflectron detector is presented in Fig 2.24. The overall mass resolution of reflectron mass spectrometer was about 1500.

2.8. Photoelectron Spectrometer

Photoelectron spectrometer analyzes the kinetic energy of the photoelectrons ejected from atoms and molecules as a result of laser interaction. To eject an electron, the photon energy must exceed the threshold energy of the electric continuum. For a negatively charged species, the electric continuum corresponds to the neutral state, and the photoelectron corresponds to the excess electron attached to the neutral form of the species. The photodetachment process occurs instantaneously via vertical transition which involves two sequential processes: promotion of the electrons to a virtual state

followed by vertical relaxation to neutral states. As depicted in Fig. 2.25, the vibronic manifolds of the neutral state can be accessed via the vertical relaxation, and excess photon energy is carried by the released electrons. The envelope of the photoelectron spectrum represents the transition probability between the negative ion state(s) and the vibronic manifolds of the neutral, which is determined by Frank-Condon factors as well as overlap of the electronic wavefunctions.

Since electrons are detached by the *fixed* frequency laser light, the kinetic energy of photoelectron can be converted to the electron binding energy (*eBE*) of anions which provides valuable information regarding the energetics of anions:

$$eBE = h\nu - eKE, \quad (2.21)$$

where $h\nu$ represents the monochromatic light of the laser and *eKE* is an abbreviation for electron kinetic energy. The onset and the peak values in *eBE* correspond to the adiabatic electron affinity (AEA) and the vertical detachment energy (VDE), respectively. AEA and VDE are spectroscopic signatures that can be used to identify negative ions. The temperature of anions can be deduced from the onset shift and the intensity profile of the vibration-level progressions.³

The key factors associated with the performance of a photoelectron spectrometer are the collection efficiency and the energy resolution. The two factors often conflict and must be compromised when designing and constructing a photoelectron spectrometer. In our apparatus, a magnetic bottle and a field free TOF photoelectron spectrometer were incorporated, and the vacuum chamber was designed to accommodate the two spectrometers without extensive modifications. The former has high collection

efficiency with low energy resolution, whereas the latter has low collection efficiency with high energy resolution.

2.8.1. Magnetic Bottle Photoelectron Spectrometer

The magnetic bottle photoelectron spectrometer creates highly non-uniform magnetic field in the laser interaction region between a strong magnet and a solenoid.²²⁻²⁷

The non-uniform magnetic field parallelizes the electrons ejected in all directions and guides them toward the weak field created inside solenoid. The parallelization effect is dictated by the adiabatic magnetic field gradient.²² The adiabatic variation of the magnetic field means that electrons do not experience the change of magnetic field during the course of parallelization. Under this condition, angular momentum of electrons should be conserved at any point along their gyroscopic trajectory, which yields the following relationship:

$$\frac{\sin \theta_f}{\sin \theta_i} = \sqrt{\frac{B_f}{B_i}}, \quad (2.22)$$

where θ corresponds to the angle between the velocity of the emitted electron and the detection axis (y-axis) and B denotes the magnetic field strength. The subscript i and f refer to the strong (initial) and the weak (final) magnetic field regions, respectively. For isotropic electron emission, the initial angle θ_i ranges from 0 to 90°. Thus, the maximum angle in the weak magnetic field is

$$\theta_{f,\max} = \sin^{-1} \sqrt{\frac{B_f}{B_i}} \quad (2.23)$$

When B_i is much larger than B_f , $\theta_{f,\max}$ becomes small and parallelization can be accomplished (e.g. $\theta_{f,\max} \sim 1.8^\circ$ when $B_f / B_i = 10^{-3}$). The mathematical derivation for the magnetic-field parallelization is provided in Appendix C.

If the drift region is much larger than to the non-uniform magnetic field region, then the time of flight can be expressed as follows:

$$t = \frac{D}{v_\perp} \sim \frac{D}{v} \left(1 + \frac{B_f \sin^2 \theta_i}{2B_i} \right) \quad (2.24)$$

When B_i is much greater than B_f , the time-of-flight is virtually independent of the initial direction of the emission, and only depends on the velocity (kinetic energy) of the photoelectron.

Our magnetic bottle spectrometer is composed of a solenoid and a permanent magnet. The solenoid was made by winding the non-magnetic copper wire (JCH Wire, 14 AWG) around the O.F.H. copper tube (Thyssen-TMX Division, 2.5" O.D. and 26" long). Relatively thick wire (1.65 mm) was used to have low resistance in the helical winding, which helps to suppress heat generation in the copper coil. Repetitive heating and cooling of the solenoid disintegrates the polymer coating of the copper coil and causes electric short to the ground potential. To ensure the electric insulation, the polyamide coated copper wire was used for high temperature endurance, and a shrinking Teflon tube (McMaster-Carr) was put over the copper tube before winding the wire.

The high temperature rated electric resin (3M, Scotchcase 5) was utilized to glue the coil onto the copper tube.

The helical winding was double layered to increase the number of turns per unit length. The μ -metal sheet (Mm-Metal, 0.015" thickness) with high permeability was wrapped over the second layer of the coil to shield earth magnetic field. Both copper tube and μ -metal sheet were electrically grounded, and the aerosol graphite (Aerodag G) was applied to the inner wall of the copper tube for adsorbing stray electrons inside the solenoid. Another Teflon sheet (McMaster-Carr) was placed between the coil and the μ -metal for electrical insulation. The cross section of the solenoid layers is shown in the middle of Fig. 2.26.

The solenoid was held by four T-shaped clamps stemming from the middle flange (CF600-SNL). Each clamp consists of an aluminum T and a Teflon cover which has the curvature matching the outer diameter of the solenoid (Fig. 2.26.2). The Teflon cover can be bulged by screwing in two set-screws located each end of the aluminum T, and the clamping action was achieved by pressing the Teflon cover against the solenoid. The electric current was provided through the high voltage electric feedthrough welded on the conflate flange (CF600-EFT). Magnetic field of 1 mT was created inside the solenoid when electric current of 0.91 A was provided to the coil. Solenoid and the permanent magnet were situated equal distance from the laser path. Fig. 2.28 shows the equipotential field line at the edge of the solenoid and the plot of magnetic field strength as a function of distance.

2.8.2. Doppler Broadening and Ion Decelerator

Since electrons are ejected from moving objects, the photoelectrons exhibit the Doppler Effect. The velocity of the electron in the lab frame is the vector sum of the center-of-mass velocity and the anion velocity ($\vec{v}_e = \vec{v}_{c.m.} + \vec{v}_{ion}$). Electrons have their maximum and the minimum velocities when the electrons are ejected parallel and anti-parallel to the anion velocity:

$$|\vec{v}_e|_{\max} = |\vec{v}_{c.m.}| + |\vec{v}_{ion}| \quad (2.25)$$

$$|\vec{v}_e|_{\min} = |\vec{v}_{c.m.}| - |\vec{v}_{ion}| \quad (2.26)$$

Thus, the Doppler broadening of the electron velocity (Δv_e) equals to twice the ion velocity ($\Delta v_e = 2 \cdot |\vec{v}_{ion}|$), and the energy broadening due to the Doppler Effect becomes:

$$\Delta E = m_e v_e \cdot \Delta v_e = 2 \cdot m_e v_{c.m.} v_{ion} \quad (2.27)$$

Equation 2.25 indicates that the energy resolution depends on the velocity of the electrons as well as the velocity of anion. For example, photoelectrons with a kinetic energy of 1 eV ($v_e = 590$ km/s) detached from anions moving with a velocity of 100 km/sec yields energy broadening of 560 meV.

To eliminate the Doppler broadening, the kinetic energy of anions must be reduced down to a few millielectron volts prior to photodetachment. An ion-lift potential switch was *tentatively* employed in the laser interaction for the ion deceleration. Our ion lift decelerator is similar to the ‘cylindrical-lens type’ design proposed by Handschuh *et al.* The concept of the Handschuh design is based on the deceleration

mode implemented in an electrostatic lens, which provides both deceleration and spatial focusing. Negative ions are decelerated by the electric field generated in the small gap between two cylindrical electrodes. Ions can be completely stopped by turning off the front electrode before the ions reverse the direction.

Our decelerator consisted of a cylindrical electrode and a six-way cross machined out of a non-magnetic aluminum block (SHLD-CRSS). The center of SHLD-CRSS was positioned at the laser interception point such that three orthogonal axes of SHLD-CRSS coincide with the x , y and z axes of the mass spectrometer. The cylindrical electrode was identical to the electrode of the einzel lens, and it was placed 0.25 inch before SHLD-CRSS. The cylindrical electrode and SHLD-CRSS were mounted on the aluminum block (PLT-DCL) which had predrilled holes for Al_2O_3 -TU-C, and the hole location matched the patterns of SS-PL-C5X5 and SS-PL-C7X7. (Fig. 2.29) PLT-DCL and the mass gate were mounted on DSK-LSR at the opposite side from the annular MCP. (Fig. 2.20.3)

The front cylinder was connected to an SHV connector while SHLD-CRSS was electrically grounded. The potential switch should be operated by a fast push-pull high voltage pulser because of the following: The front electrode should be switched from ground to a positive potential while anions are inside the cylinder, and it should be rapidly switched off to ground when the ions are at the turn-around point. The ion-lift decelerator has not been tested because the push-pull switch was not available in this laboratory. The photoelectron spectra presented in this thesis were obtained without deceleration. The spectra exhibit excessive Doppler broadening, and the energy

resolution of our magnetic bottle spectrometer was ~ 250 meV for detecting 1 eV electrons emitted from ions with 10 km/sec.

2.8.3. Field-Free TOF Photoelectron Spectrometer

The field-free TOF spectrometer collects the small solid angle of the electrons emitted in all directions, which provides decent energy resolution but with very low detection efficiency. Since only the electrons emitted along the TOF axis will arrive at the detector, velocity spread due to the Doppler Effect will be considerably small (eqs. 2.25–27). For a spectrometer with length of 30 cm and a detector with detection area of 10 cm^2 , the collection efficiency is about 0.25% for isotropic electron emission; hence, counting method must be employed to record a photoelectron spectrum. In our femtosecond pump-probe experiments, the field free TOF spectrometer was not able to be implemented due to the low collection efficiency. The time-dependent photoelectron signals produced by pump-probe scheme are generally a few orders of magnitude smaller than the photoelectron signals generated by the nanosecond laser pulse.

Another advantage of the field-free TOF spectrometer is the ability to resolve the angular distribution of the photoelectron emission. The photoelectron projected on the detector reflects the vectorial characteristic of the emitted electrons. By rotating the polarization of the laser light with respect to detection axis, it is possible to map out the contour of the electron emission. Author must point out that the magnetic bottle spectrometer can resolve the angular dependence in some extent if the anisotropy of the photoemission is sufficiently large. Detail will be discussed in Chapter 6.

Since electrons can be easily swayed by the ambient electric or magnetic field, it is important to achieve reliable shielding along the flight path. A custom-made double-layer μ -metal tube (M μ -Metal, 50 cm long) was used to block the ambient magnetic field. The double layer was prepared by inserting the port-less μ -metal tube (Mu-SHLD2) into the 6-way μ -metal cross (Mu-SHLD1), which reduced the base magnetic field down to 10^{-4} G. The field free photoelectron spectrometer can be easily installed by replacing the solenoid and the permanent magnet by the μ -metal tube. As shown in Fig.2.30, upright orientation of the tube was assisted by two Kimball plates (SS-PL-C5X5-R1000). The bottom part of the tube was inserted into the Kimball plate mounted on the magnet holder, while the upper part of the μ -metal tube was held by another Kimball plate which is extended from the MCP assembly.

2.8.4. Data Processing: Conversion to eKE

Unlike the energy analyzers such as hemispherical sector and cylindrical electrostatic mirror, the time-of-flight photoelectron spectrometers (both magnetic bottle and field-free spectrometers) measure the arrival time of the ejected electron. The arrival time should be converted to the electron kinetic energy and later to electron binding energy to construct the photoelectron spectrum which illustrates meaningful physical quantities. The time-of-flight was converted to the electron kinetic energy (*eKE*) by using the two equations below

$$eKE = \frac{1}{2} m_e D^2 \cdot \frac{1}{t^2} + E_0 \quad (2.28)$$

E_0 is the energy correction term which reflects the ambient surface potential inside apparatus.

$$eKE = \frac{1}{2} m_e \left(\frac{D}{t - t_0} \right)^2 \quad (2.29)$$

In most cases, equation 2.29 was used to take into account the time offset (t_0) originated from the initial position distribution in the laser interaction region. Note that equation 2.29 has an additional correction term t_0^{-1} and the second order term t_0^{-2} is equivalent to the energy correction term, E_0 in equation 2.28. By rearranging equation 2.29, a linear equation of $eKE^{-1/2}$ as a function of t can be obtained as below:

$$\frac{1}{\sqrt{eKE}} = \sqrt{\frac{2}{m_e}} \frac{1}{D} \cdot t - \sqrt{\frac{2}{m_e}} \frac{t_0}{D} \quad (2.30)$$

The slope and the y-intercept of the above equation can be considered as the calibration parameters of the spectrometer, which are determined by the magnetic field strength and the kinetic energy of the ions. A preliminary experiment must be carried out by using systems with known eKE s to obtain the calibration parameters.

When the abscissa is converted from TOF to eKE , the photoelectron intensity must be scaled accordingly. The total number of electrons must be conserved in the coordinate transformation, which suggests that the photoelectron count in the infinitesimal variation must be conserved as well:

$$N(E)dE = N(t)dt \quad (2.31)$$

From equation 2.28,

$$E = \frac{1}{2} m_e \left(\frac{D}{t} \right)^2 + E_0 \Rightarrow \frac{dE}{dt} = -\frac{m_e D^2}{t^3} \quad (2.32)$$

$$N(E) = N(t) \frac{dt}{dE} = -\frac{1}{m_e D^2} \cdot N(t) \cdot t^3 \quad (2.33)$$

Therefore, the raw intensity recorded by an oscilloscope must be multiplied by t^3 , in order to correct the intensity profile with respect to eKE or eBE . If equation 2.29 was used, t_0 must be included for scaling the photoelectron intensity.

$$N(E) = -\frac{1}{m_e D^2} \cdot N(t) \cdot (t - t_0)^3 \quad (2.34)$$

2.8.5. MCP Detector for Photoelectron Detection

When the microchannel plate is used for detecting low kinetic energy electrons, the electrons must be accelerated up to 500 eV before the impingement on the microchannel plate. Low kinetic energy impact will not induce satisfying scale of the secondary-electron multiplication. The MCP assembly used for electron detection is similar to the ion detector described earlier (2.1.5.2.5) except for a few modifications. First, an auxiliary acceleration region was created by placing two ring electrodes (Kimball Physics, SS-PL-C5X5-R1000) before the entrance of the MCP Chevron. The accelerator was placed 0.25" in front of the entrance plate, and the spacing in the acceleration region was 0.5". The first and the second electrodes are connected to the electric ground and the high voltage input, respectively. An electroform mesh was attached to both electrodes for uniform electric field in the acceleration region.

Wiza reported that the amplification efficiency of the Chevron falls off with increasing distance between the microchannel plates and the optimal distance between the plates is 150 μm . To increase the amplification efficiency, the partitioning plate inserted inbetween MCPs was removed, instead MCPs were stacked together (Burle Electro-Optics) with direct contact. Since the microchannel plates are slightly concaved, it was necessary to compress the Chevron stack in order to achieve *surface* contact. On the other hand, since the microchannel plates are extremely brittle excessive pressure might disintegrate the MCP. The proper compression was achieved by placing the Chevron stack in a vespel housing (HSNG-MCP) of which height is equal to twice the MCP thickness.

The supplementary circuit was modified according to the change made in the electrode arrangement. (Fig. 2.31) The series of two 4.0 MW resistors in the voltage divider were replaced by a 8.0 M Ω resistor, and auxiliary high frequency pass filter (C_1) was removed from the circuit. A 2.0 M Ω resistor was added in between the entrance SHV connector and the 8.0 MW resistor, in order to provide a bias voltage across the acceleration region. The signal profile of the photoelectron detector is about the same as the ion detector used in the primary mass spectrometer. The entire MCP assembly was mounted on ASA4 flange (ASA4-MCP). The radius of MCP assembly was smaller than I.D. of the copper tube, so front part of the MCP assembly was placed inside solenoid.

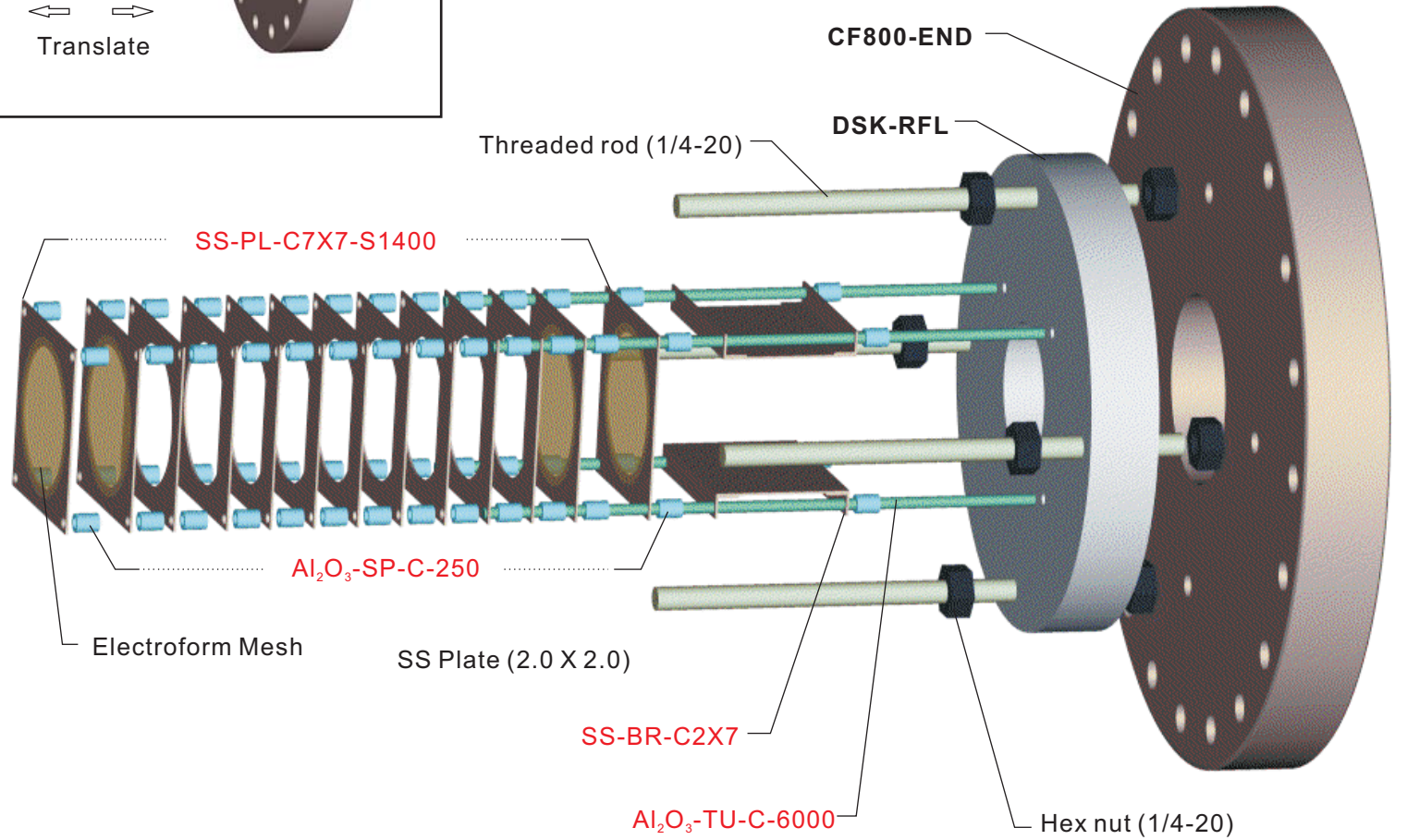
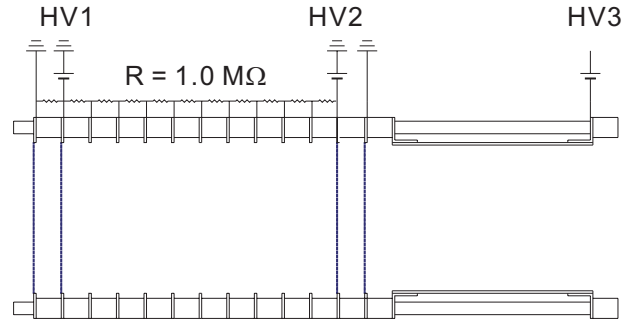
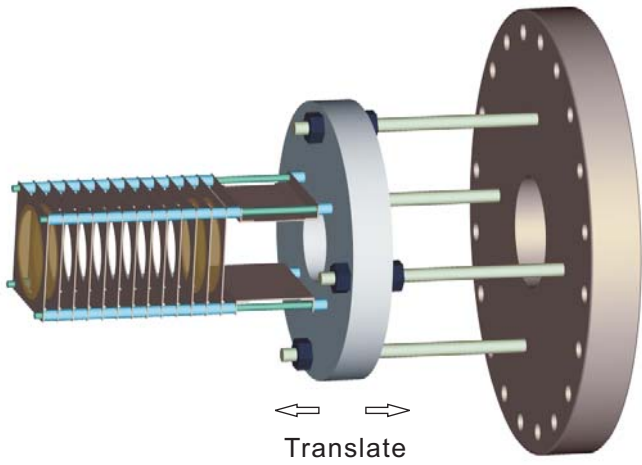
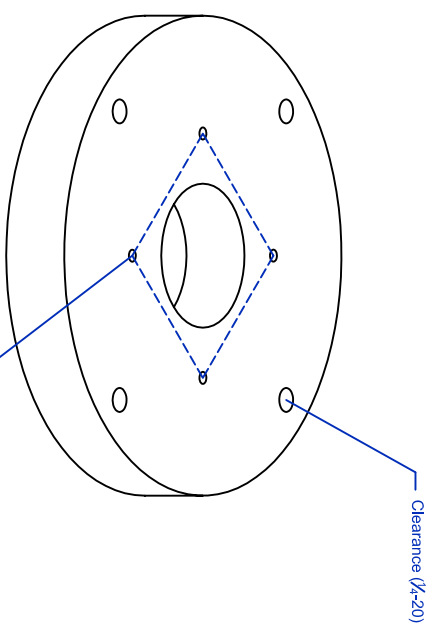
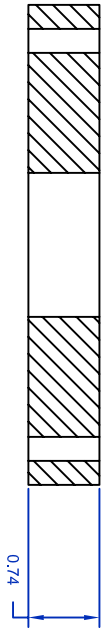
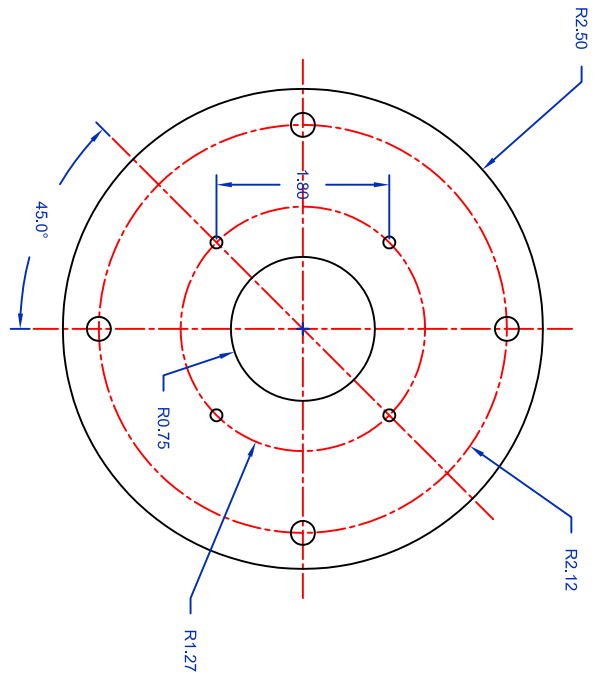


Figure 2.19



NOTE:
1. KP stands for Kimball Physics, Inc.

Figure 2.19.1

TITLE	DSK-RFL.dwg	DWG BY	PI
SCALE	1:2	DRAWN BY	AHZ
MATERIAL	AL 6061	DATE	01
UNIT (TOLERANCE)	inch (0.03)	LABORATORY	Laboratory for Molecular Sciences
(UNLESS SPECIFIED)	degree (0.5)	INSTITUTE	California Institute of Technology

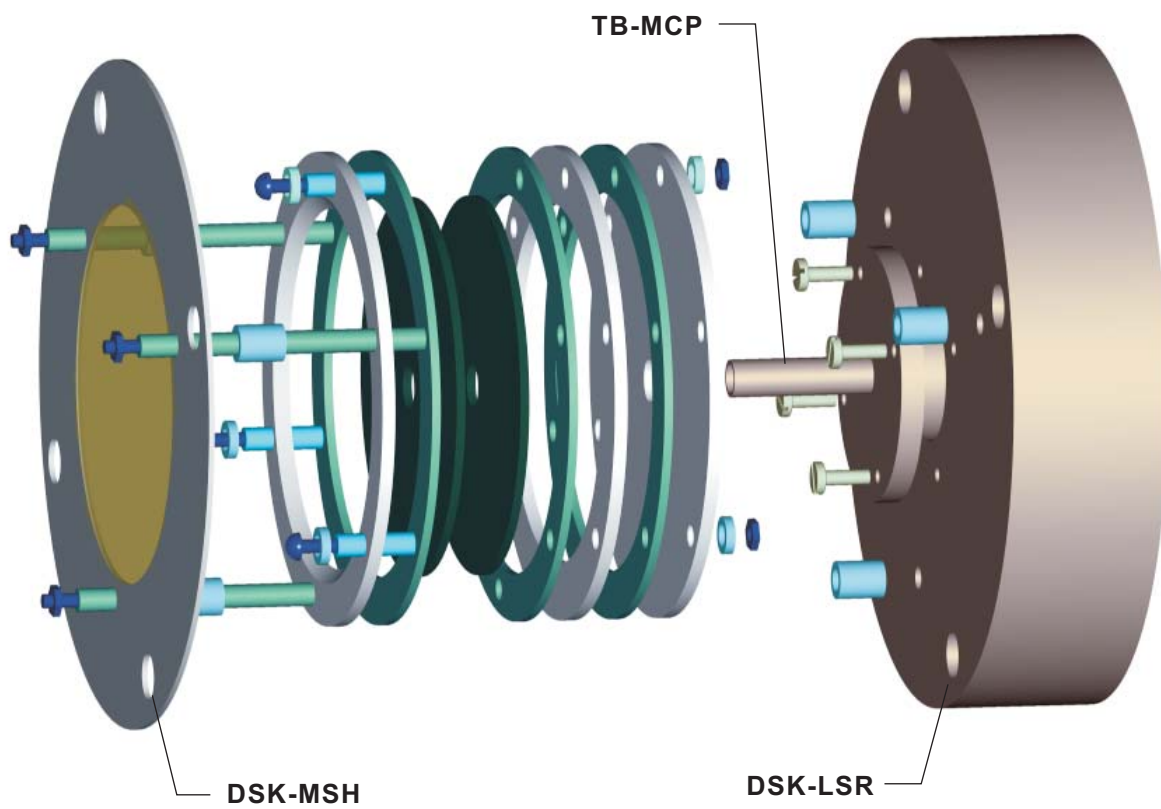
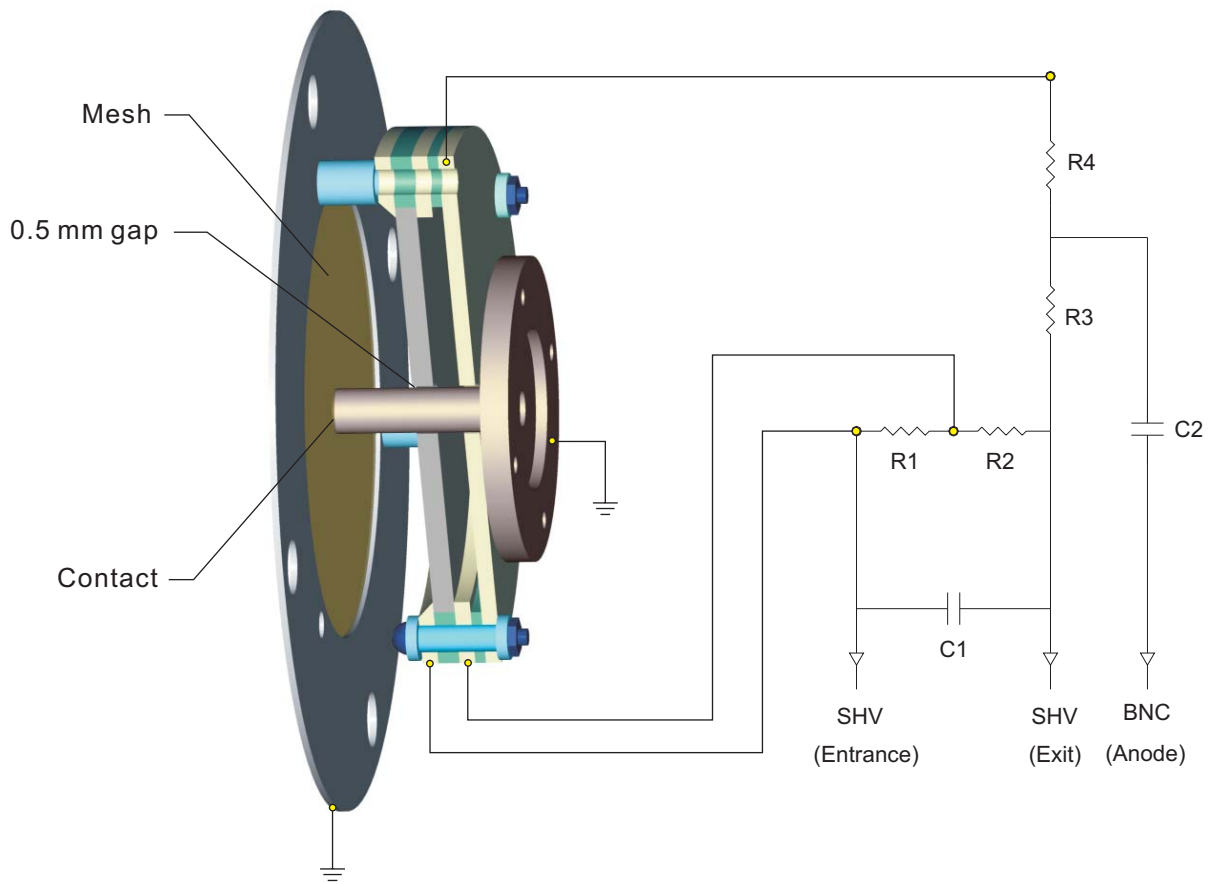
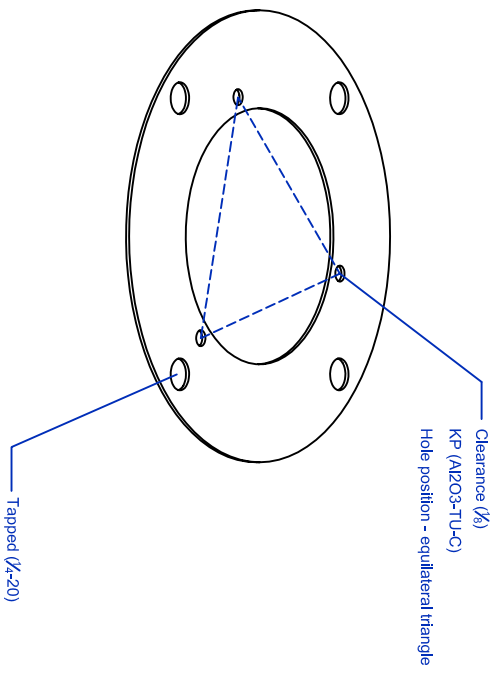
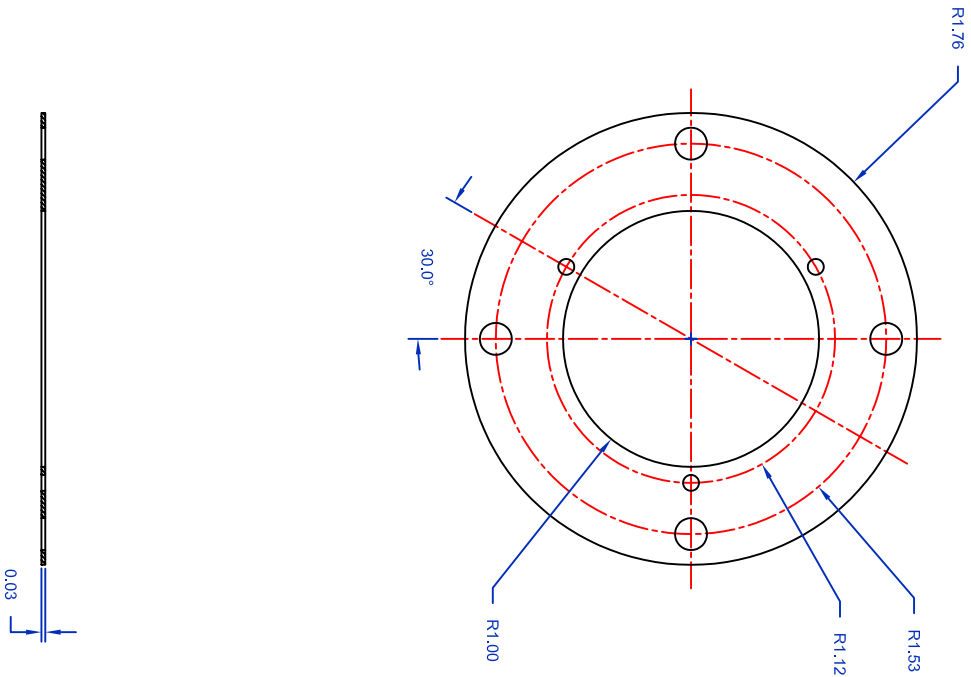


Figure 2.20



NOTE:
1. KP stands for Kimball Physcis, Inc.

Figure 2.20.1

TITLE		FILE NAME		DWG BY		PI	
DISK for Mesh		DSK-MSH		D. Hahn Park		AHZ	
SCALE		MATERIAL		UNIT TOLERANCES		UNLESS SPECIFIED	
2:3		AL 6061		Inch (0.03)		degree (0.5)	
Laboratory for Molecular Sciences				California Institute of Technology			
8		6		01			

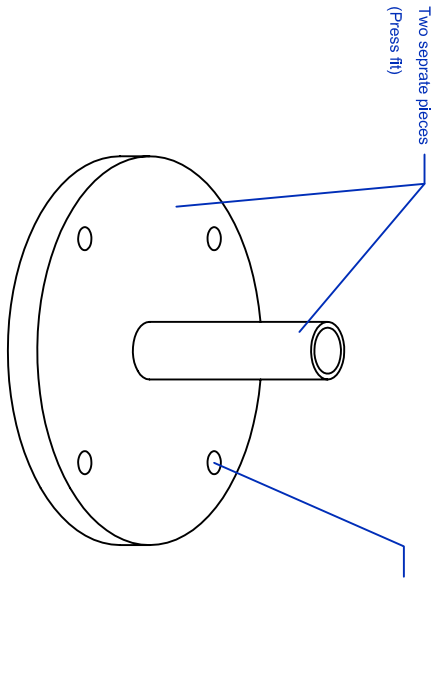
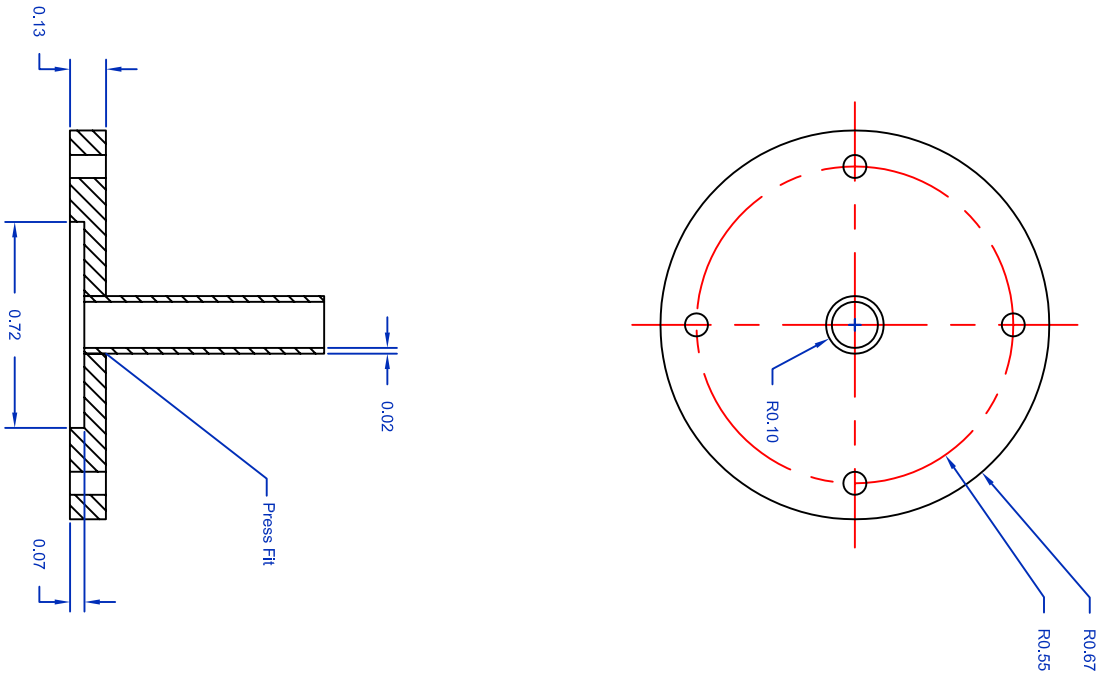
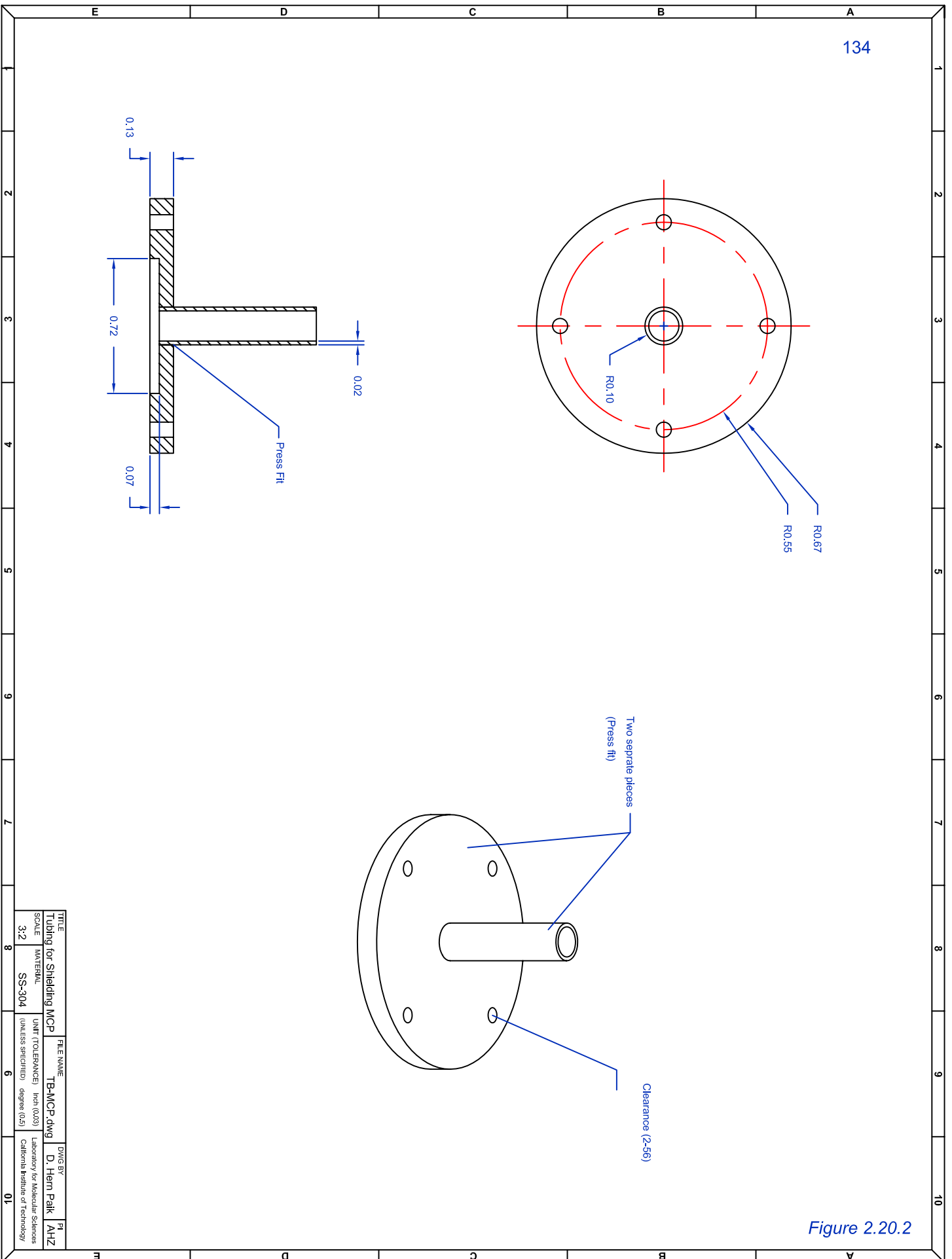
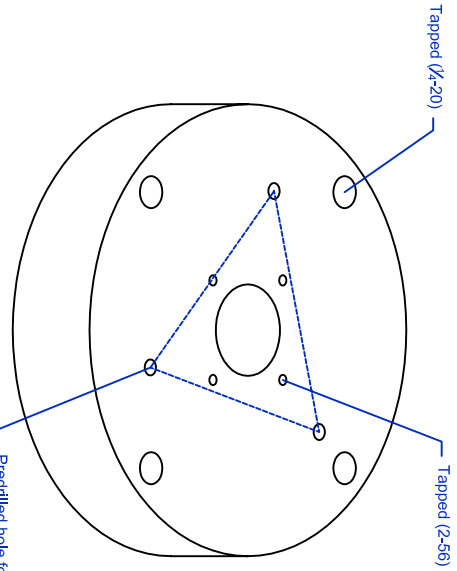
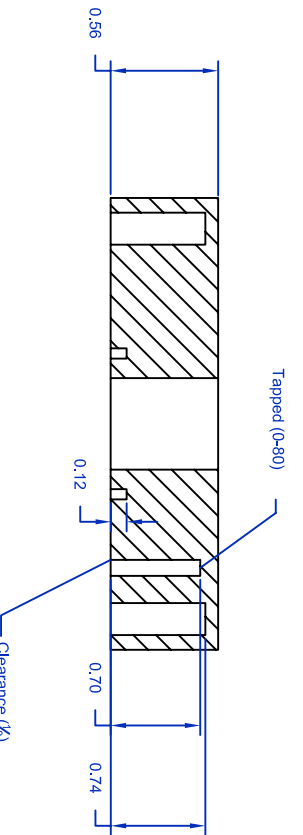
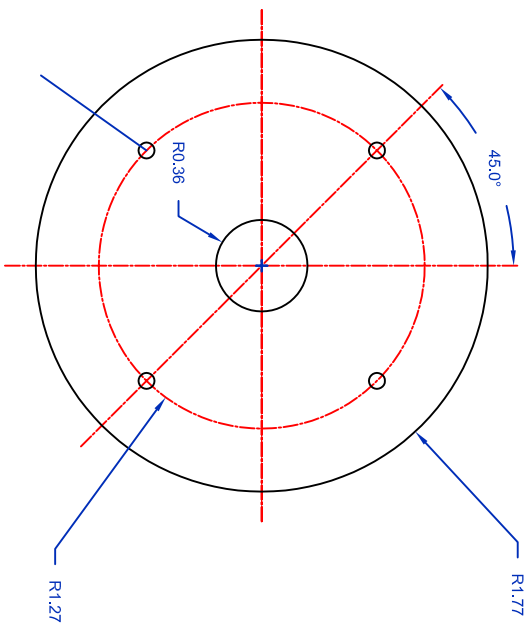
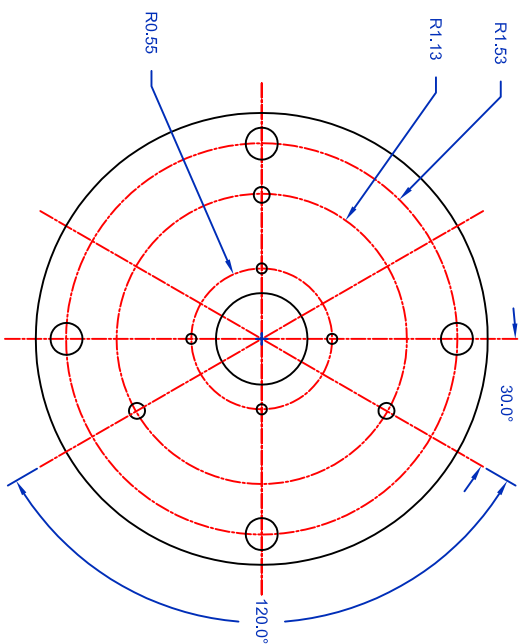


Figure 2.20.2

TITLE	FILE NAME	DWG BY	PI
Tubing for Shielding MCP	TB-MCP.dwg	D. Hahn Park	AHZ
SCALE	MATERIAL	UNIT (TOLERANCES)	(UNLESS SPECIFIED) degree (0.5)
3:2	SS-304	inch (0.03)	Laboratory for Molecular Sciences California Institute of Technology



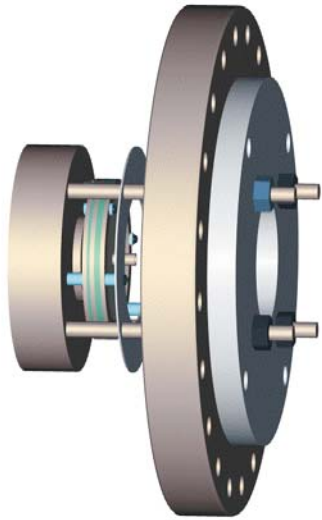


NOTE:
1. KP stands for Kimball Physyds, Inc.

Predrilled hole for mounting MCP
Hole position - equilateral triangle
(See Section Drawing for hole dimensions)

TITLE	FILE NAME	DWG BY	PI
DISK for Ion Optics	DSK-L-SR.dwg	D. Hain Park	AHZ
SCALE	UNIT TOLERANCES	LABORATORY FOR MOLECULAR SCIENCES	
2:3	(UNLESS SPECIFIED) inch (0.03)	California Institute of Technology	
MATERIAL	DEGREE (0.5)	01	
SS-304			

Figure 2.20.3



Assembly-2.A

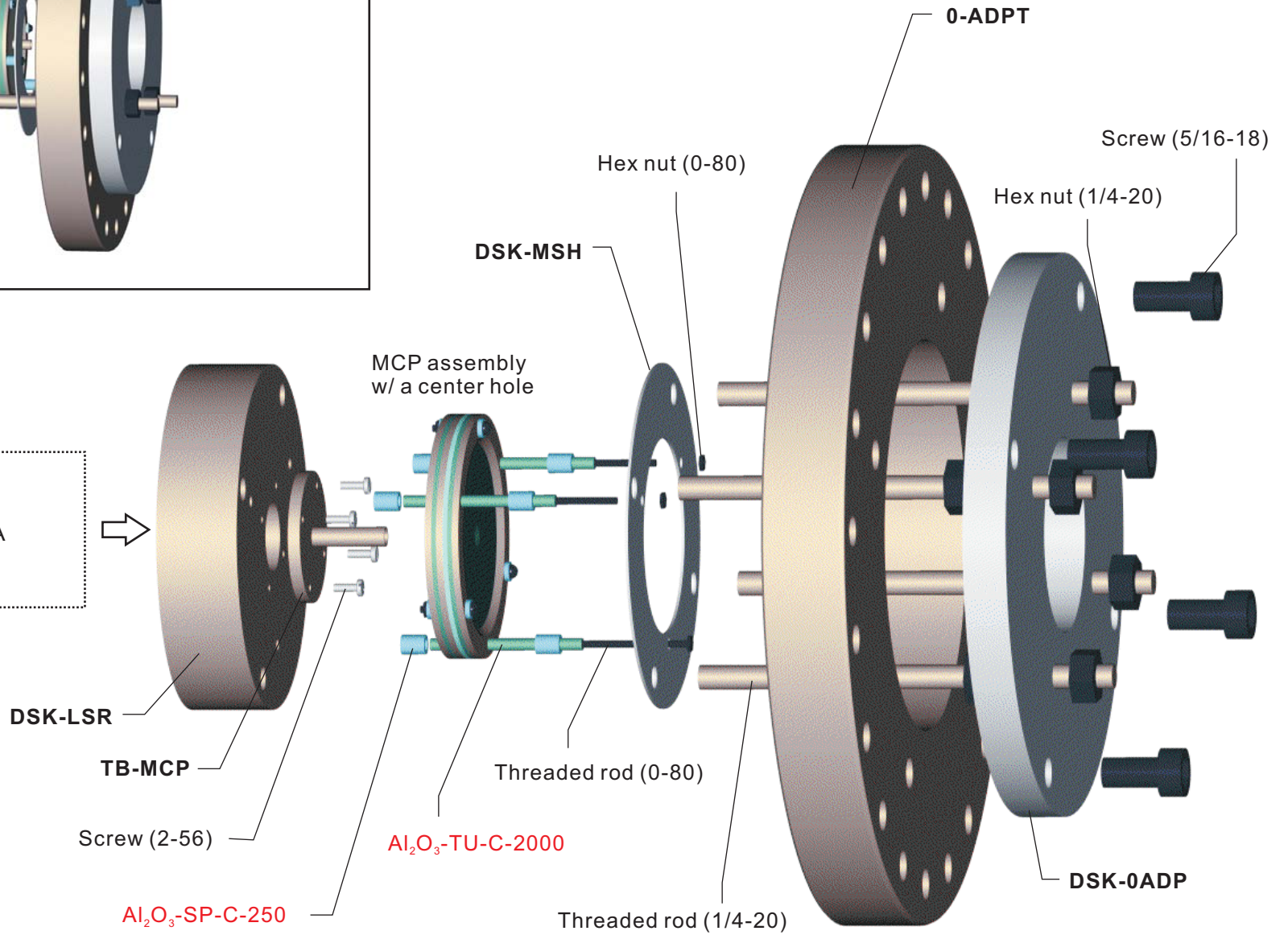


Figure 2.21

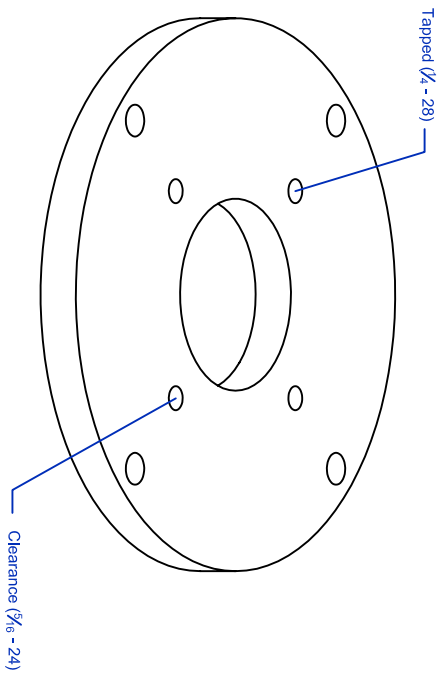
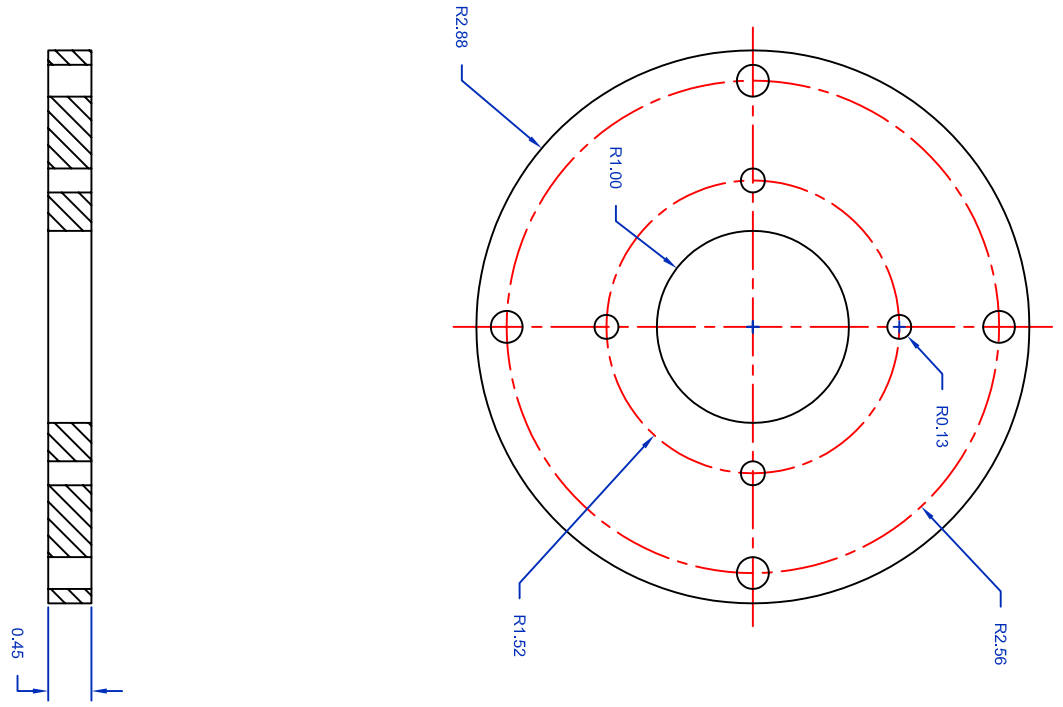


Figure 2.21.1

TITLE	FILE NAME	DWG BY	PI
DISK for Ion Optics	DSK-QADP.dwg	D. Hain Park	AHZ
SCALE	UNIT (TOLERANCES)	UNLESS SPECIFIED degree (0.5)	
1:2	AL 6061	Laboratory for Molecular Sciences California Institute of Technology	
8	6	01	

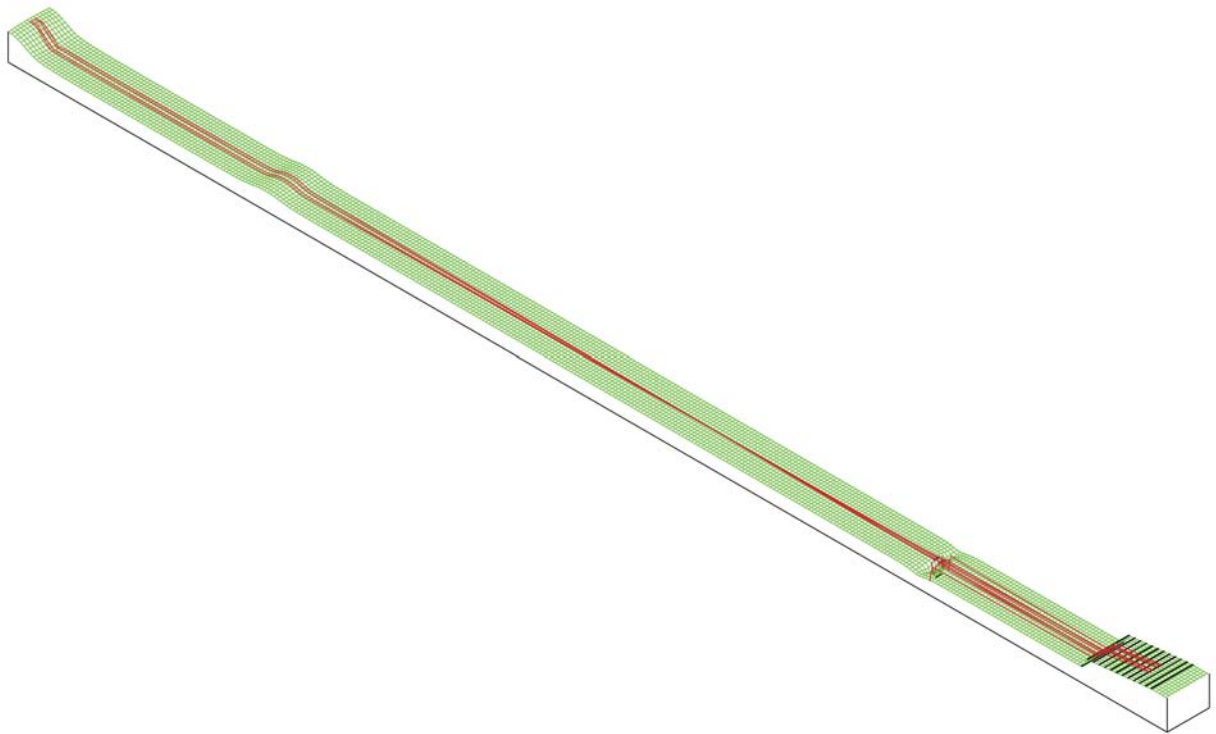
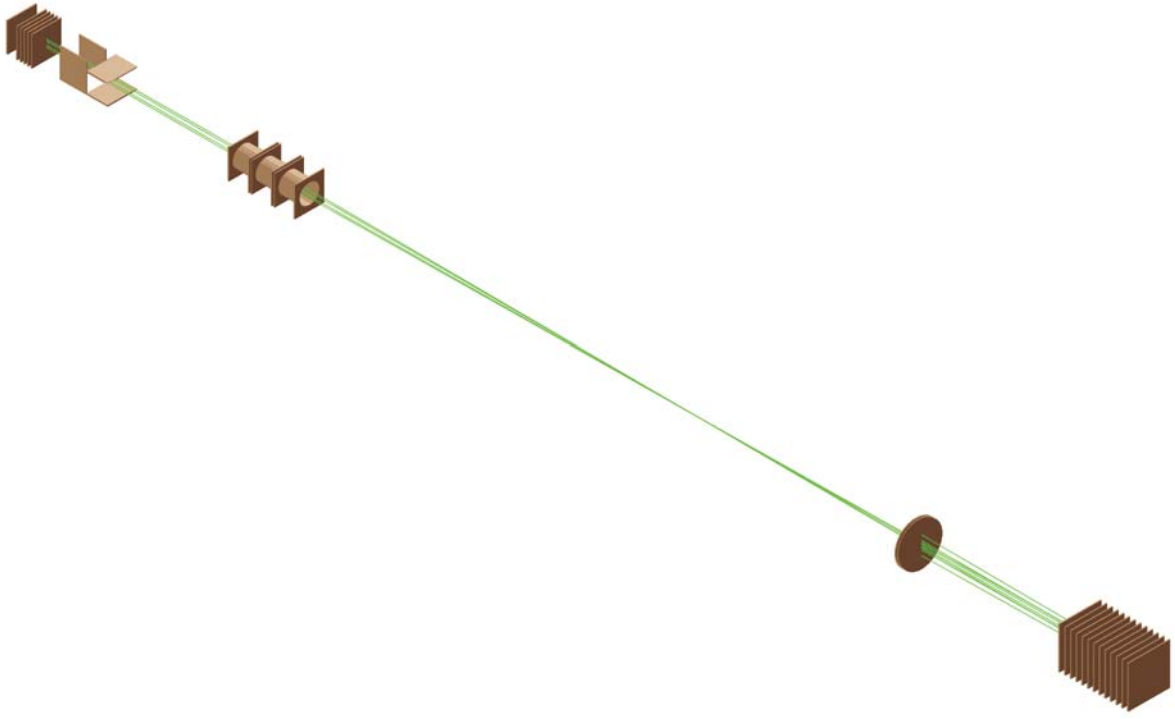


Figure 2.22

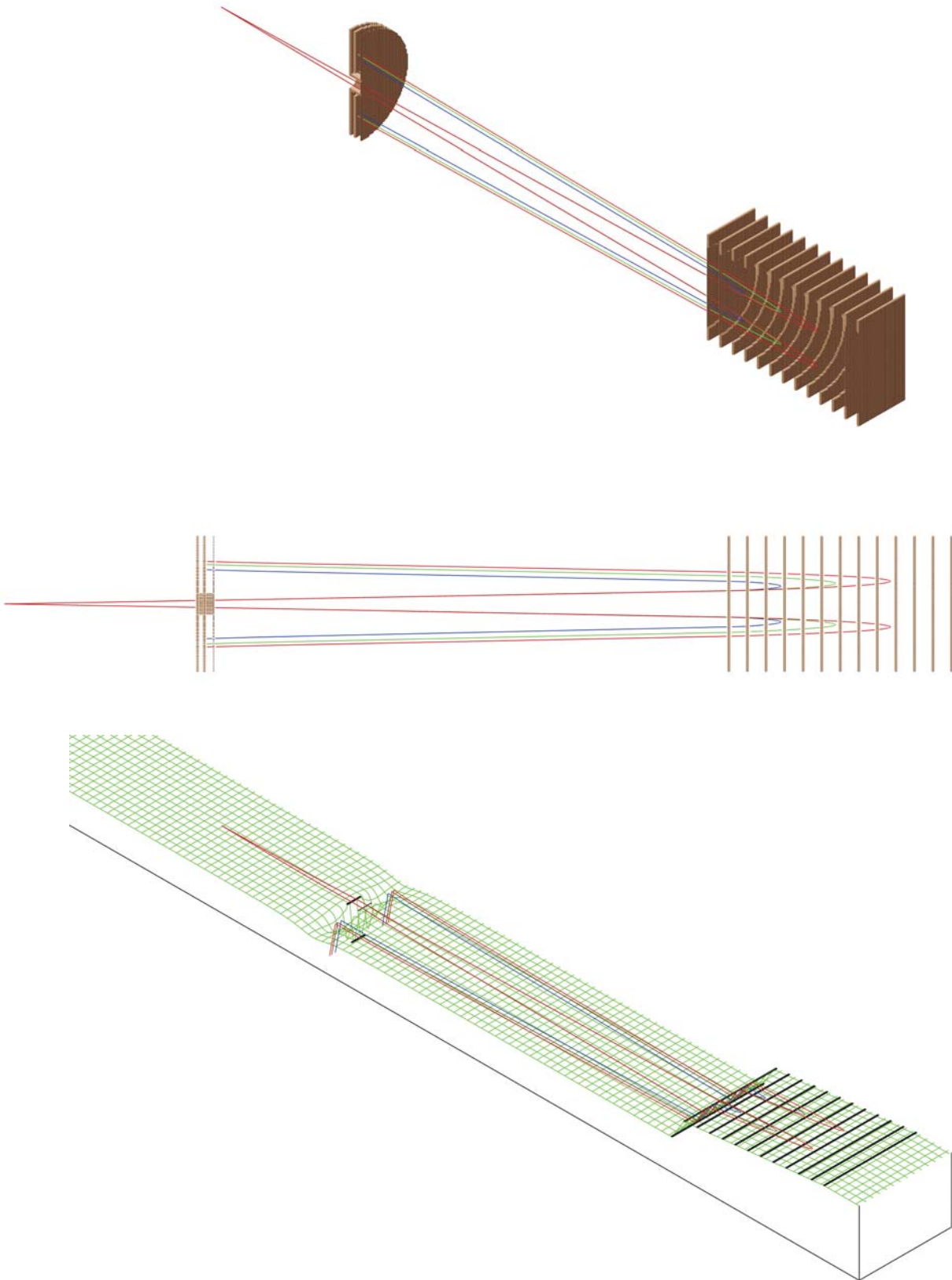


Figure 2.23

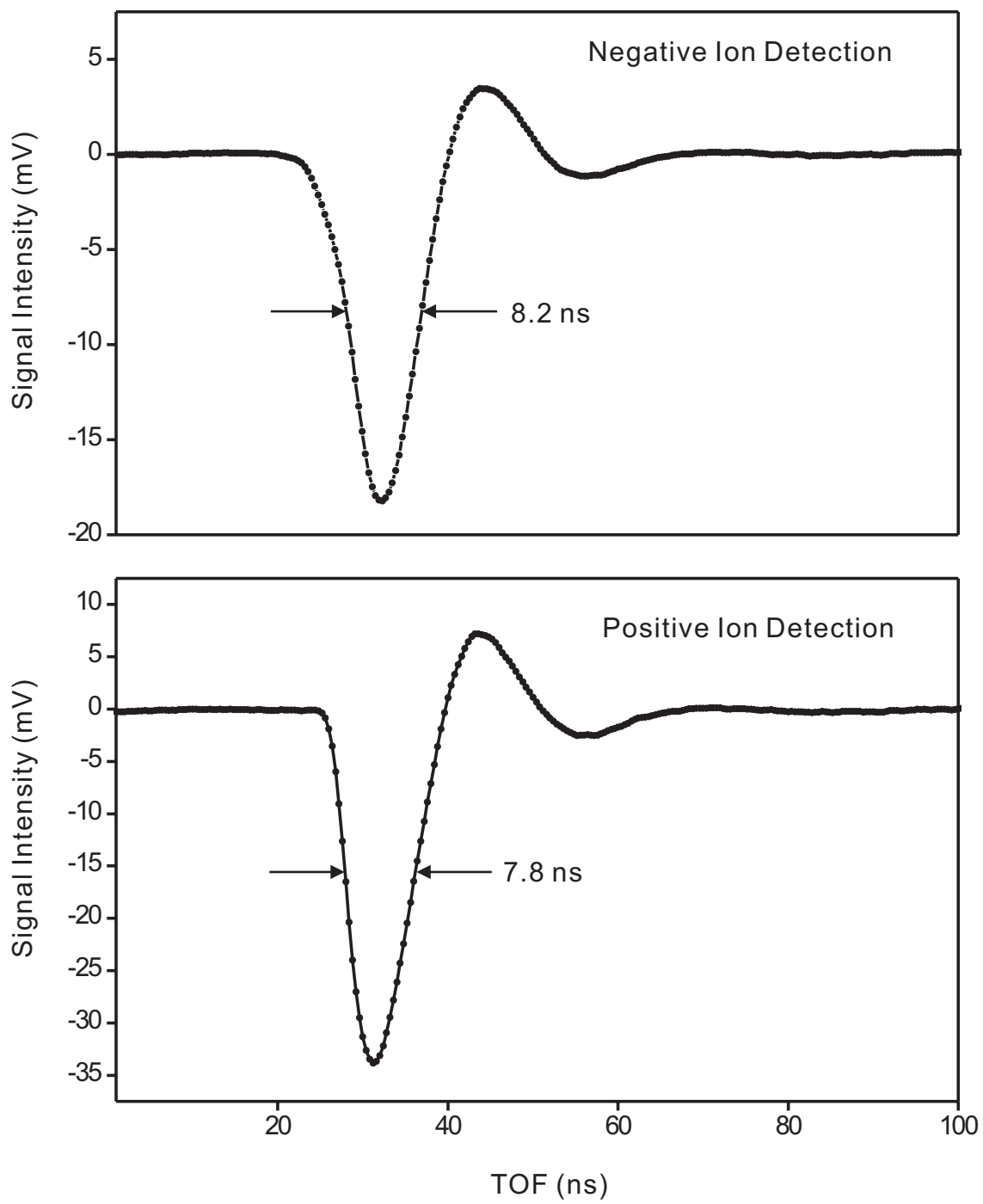


Figure 2.24

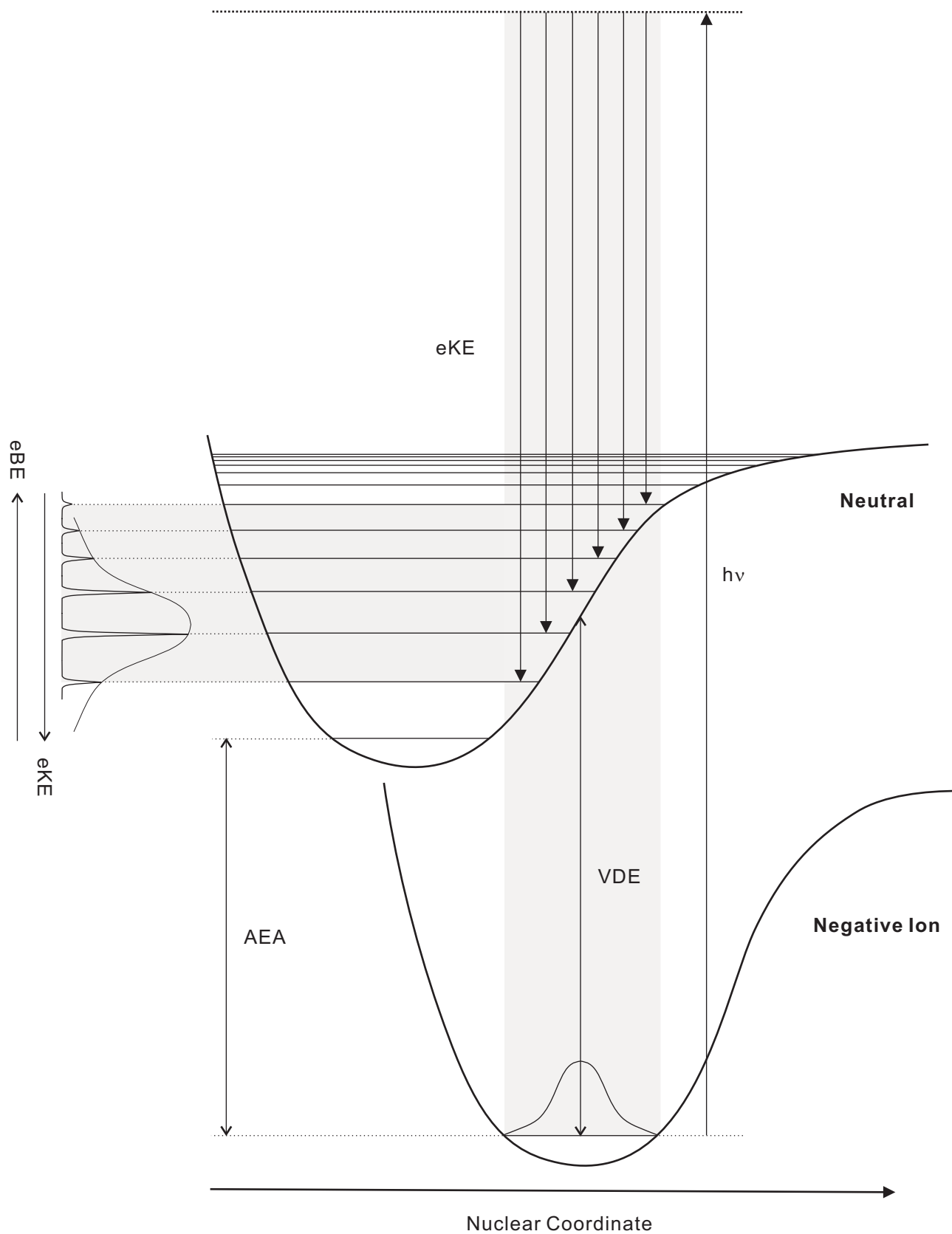


Figure 2.25

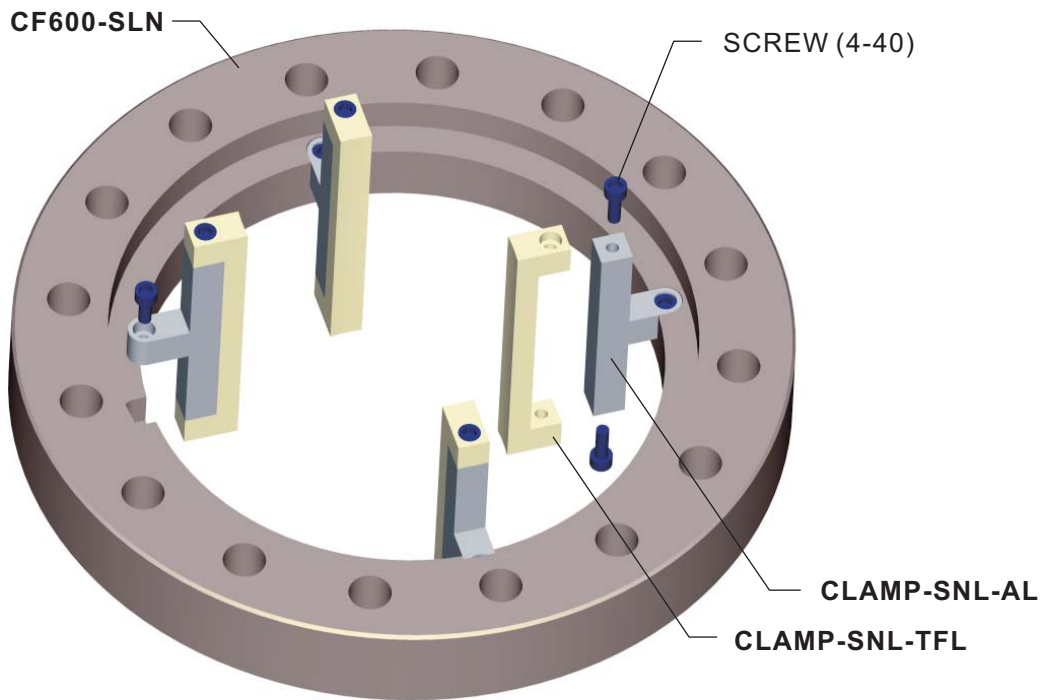
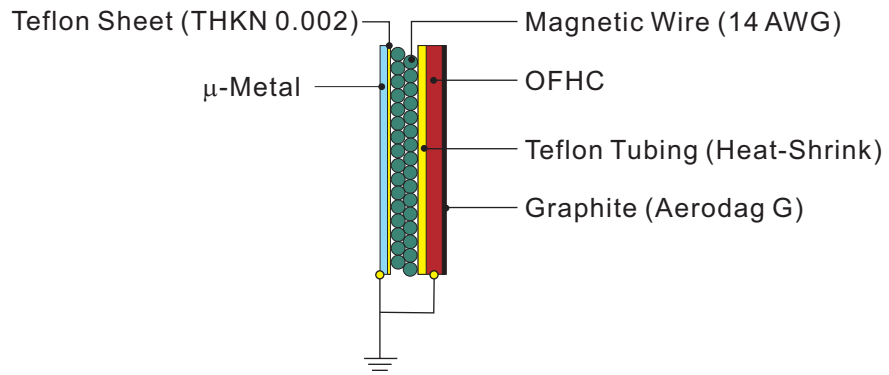
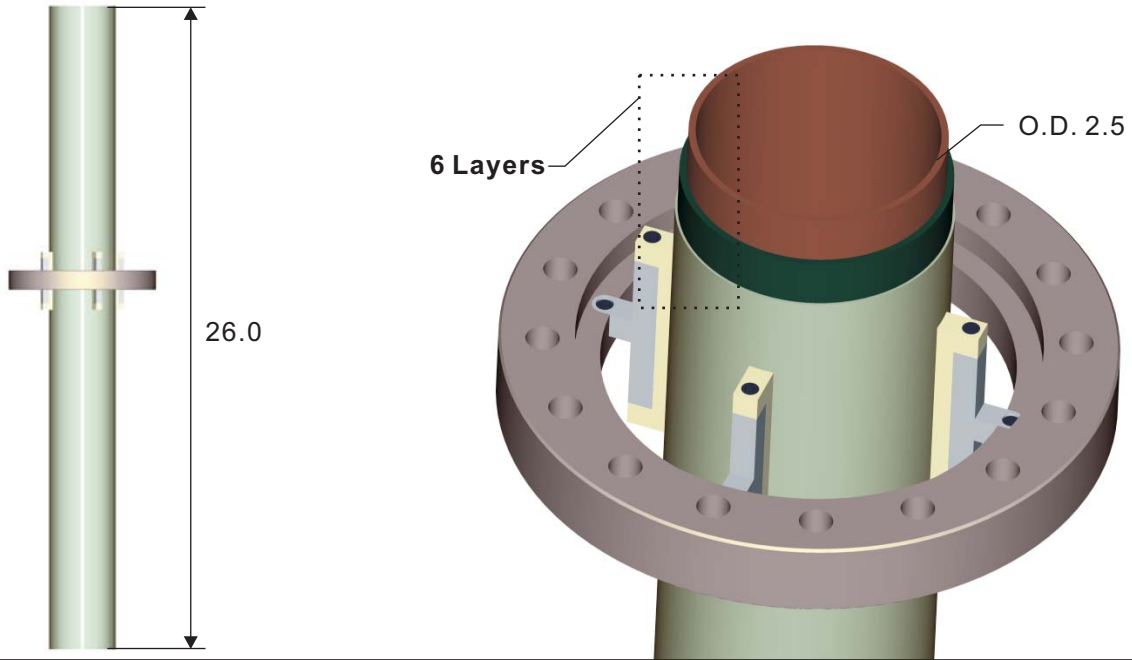
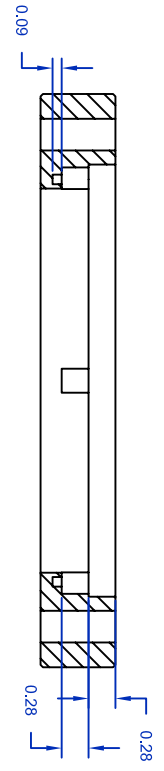
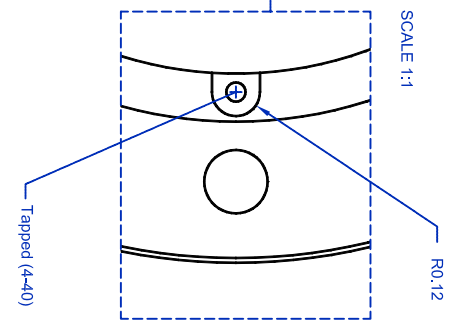
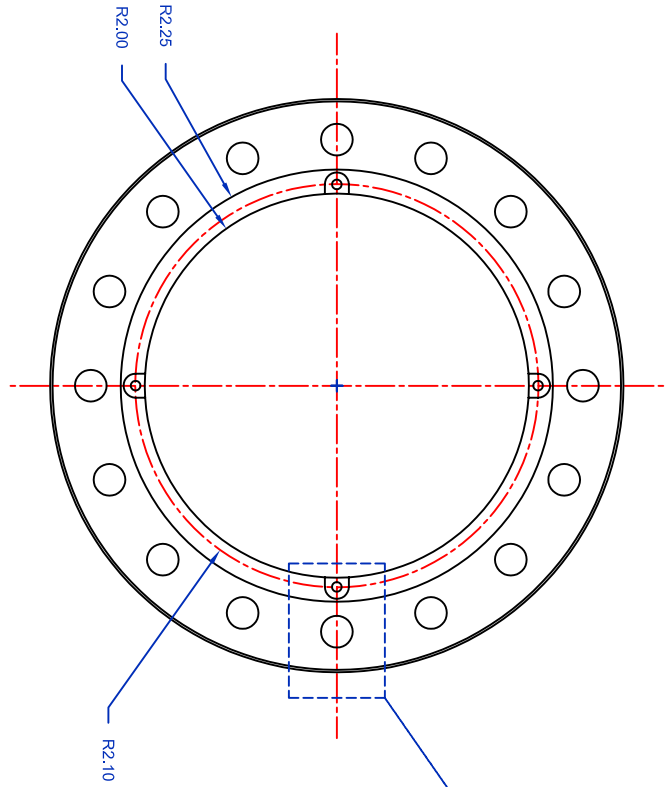
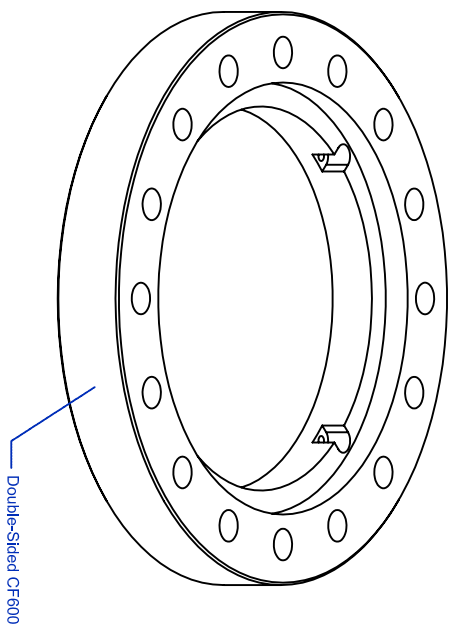


Figure 2.26



NOTE:
 1. DS-CF600 was purchased from MDC Vacuum Corp.
 2. Knife edge of the CF flange is not drawn.



TITLE	CF600 Modification	FILE NAME	CF600-SLN.dwg	DWG BY	D. Hain Park	PL	AHZ
SCALE	1:2	MATERIAL	SS-304	UNIT (TOLERANCES)	inch (0.03)	Laboratory for Molecular Sciences California Institute of Technology	
					degree (0.5)		

Figure 2.26.1

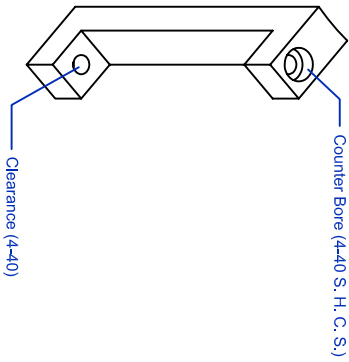
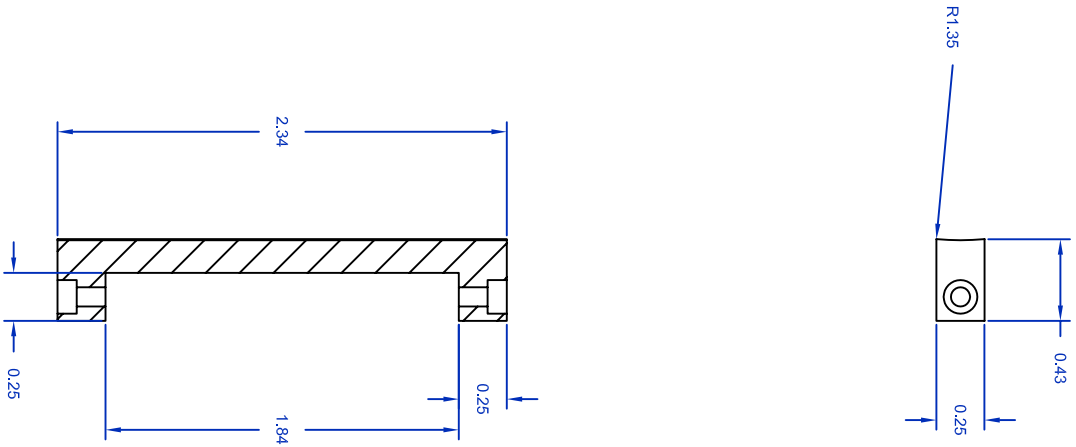


Figure 2.26.2

1	2	3	4	5	6	7	8	9	10
E	D	C	B	A					
1	2	3	4	5	6	7	8	9	10
E	D	C	B	A					
TITLE Clamp for Holding SLN		FILE NAME CLAMP-SLN-TFL.dwg		DWG BY D. Hahn Park		PI AHZ			
SCALE 1:1		MATERIAL TEFLON		UNIT TOLERANCES (UNLESS SPECIFIED)		Laboratory for Molecular Sciences California Institute of Technology			
				inch (0.03)		degree (0.5)			
				6		01			

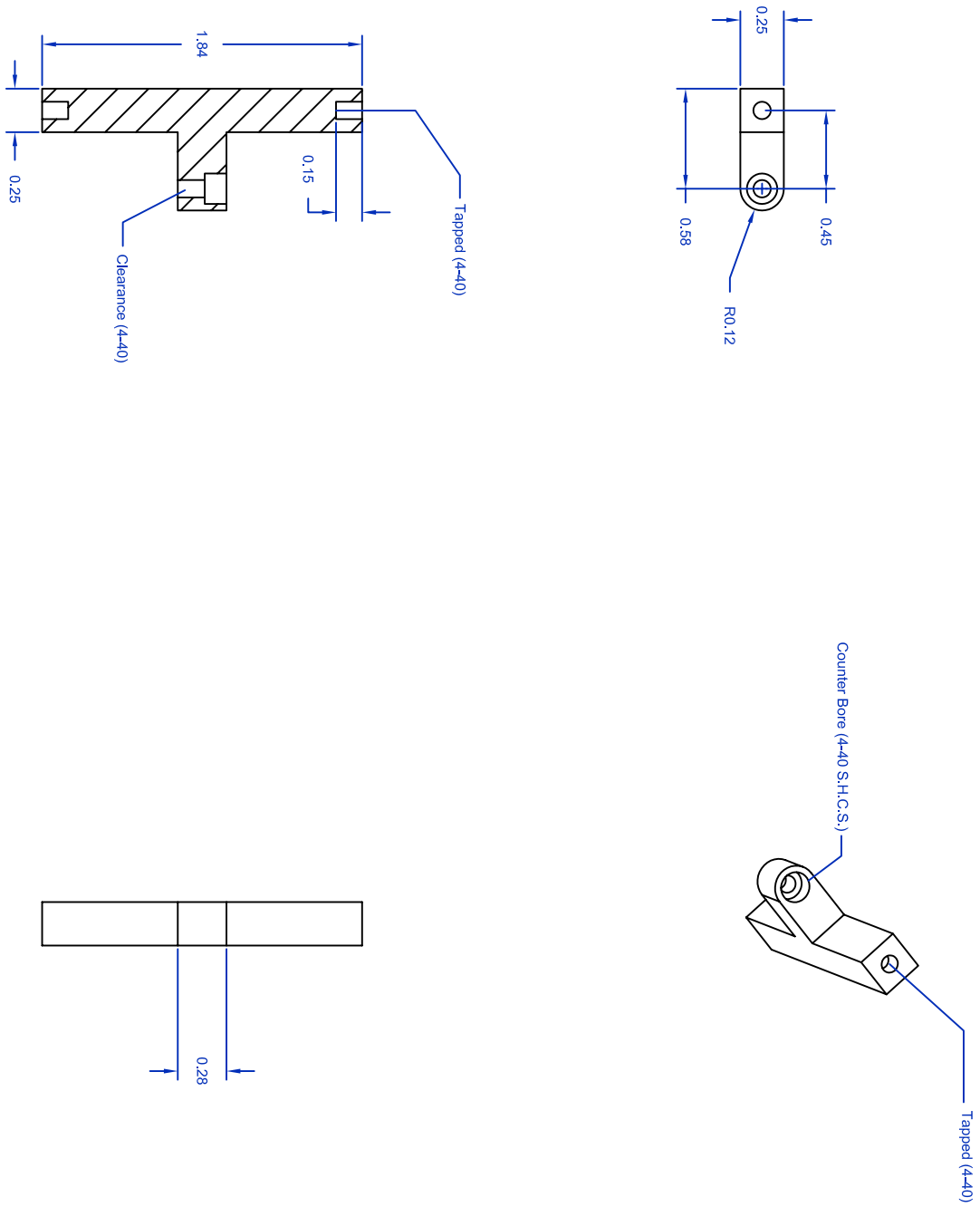
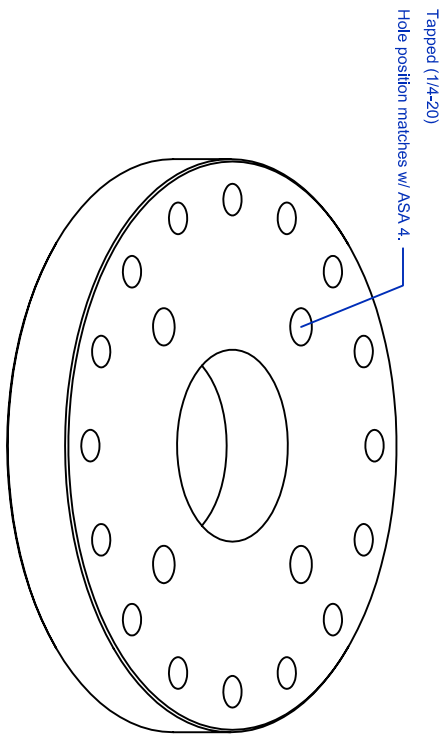
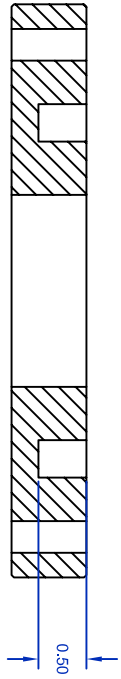
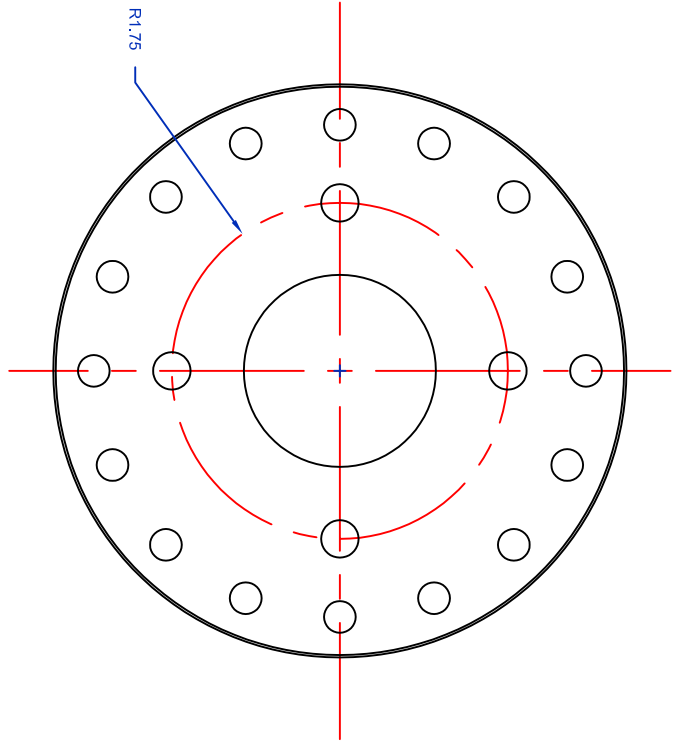


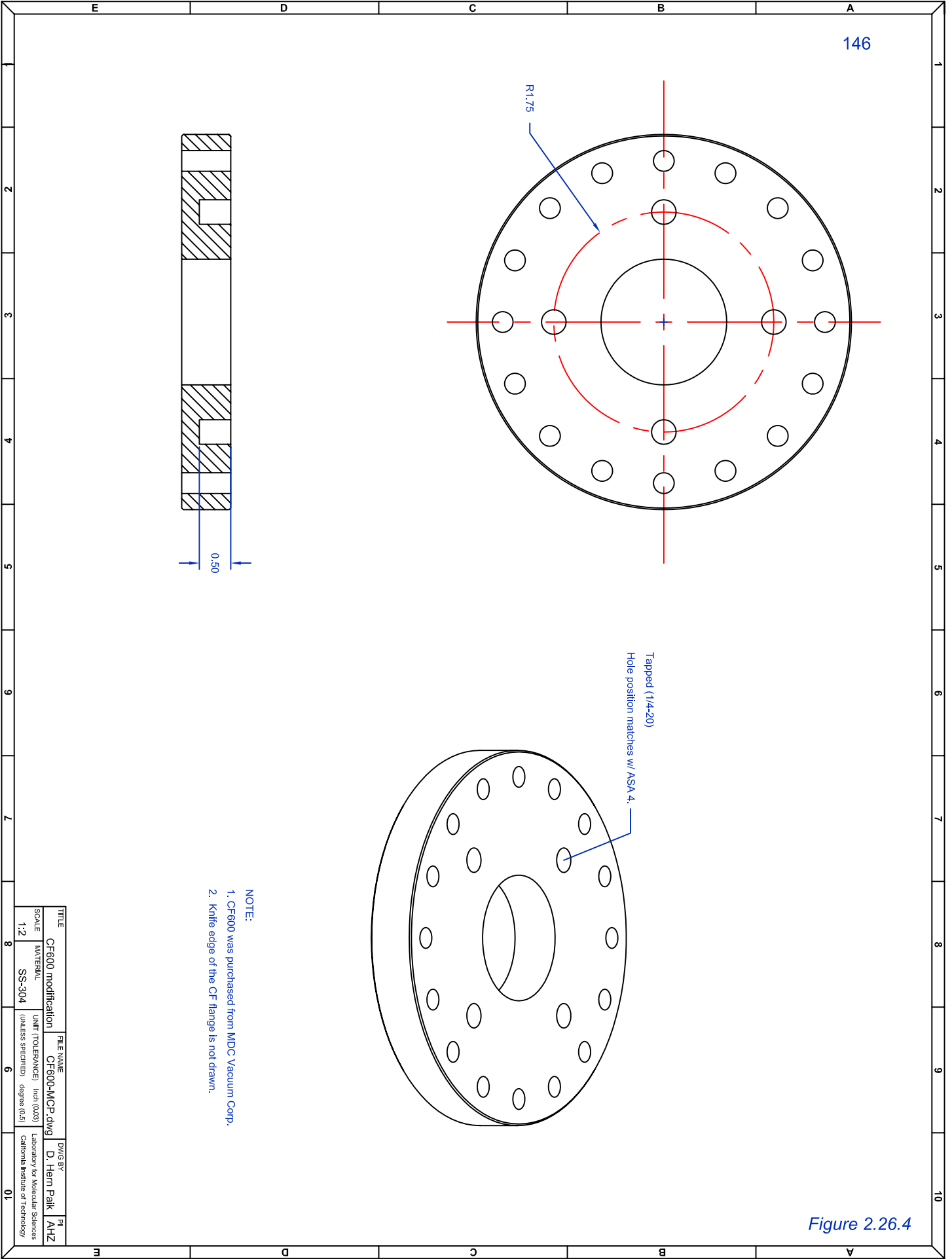
Figure 2.26.3

TITLE	CLAMP FOR HOLDING SLN	FILE NAME	CLAMP-SLN-AL.dwg	DWG BY	D. HERN PAK	PI	AHZ
SCALE	1:1	MATERIAL	AL 6061	UNIT (TOLERANCES)	inch (0.03)	Laboratory for Molecular Sciences California Institute of Technology	
				(UNLESS SPECIFIED)	degree (0.5)		



- NOTE:
1. CF600 was purchased from MDC Vacuum Corp.
 2. Knife edge of the CF flange is not drawn.

Figure 2.26.4



TITLE	CF600 modification	FILE NAME	CF600-MCP.dwg	DWG BY	D. Hahn Park	PI	AHZ
SCALE	1:2	MATERIAL	SS-304	UNIT TOLERANCES	(UNLESS SPECIFIED) inch (0.03) degree (0.5)		
				Laboratory for Molecular Sciences		California Institute of Technology	
				6	01		

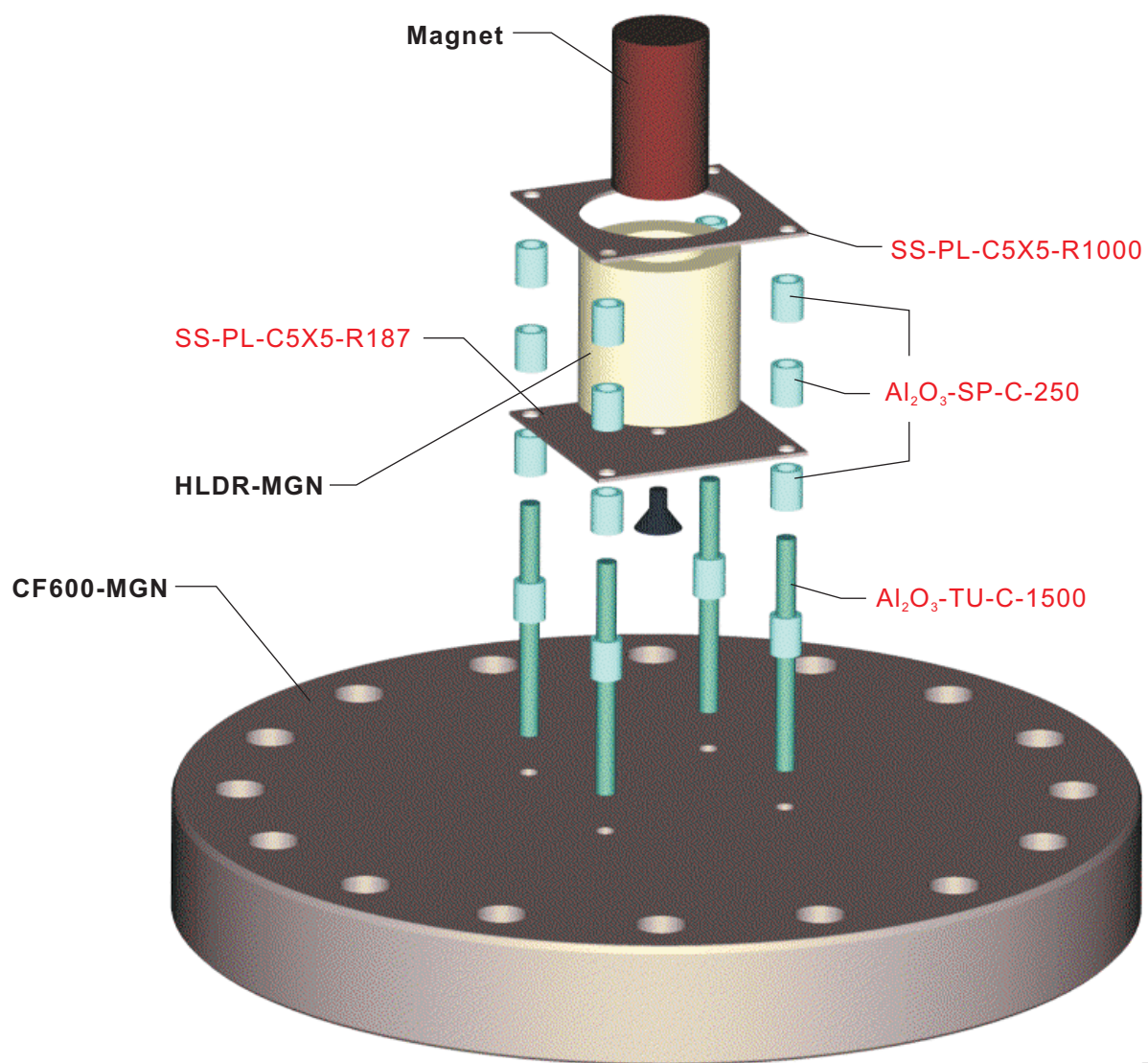
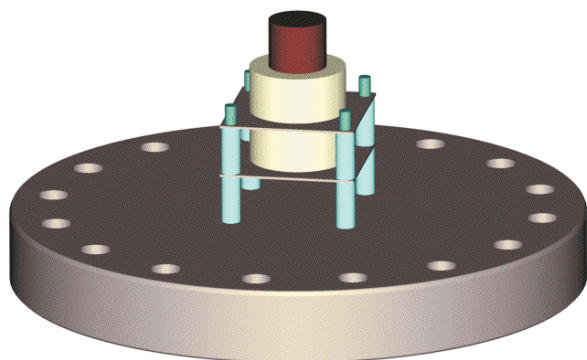
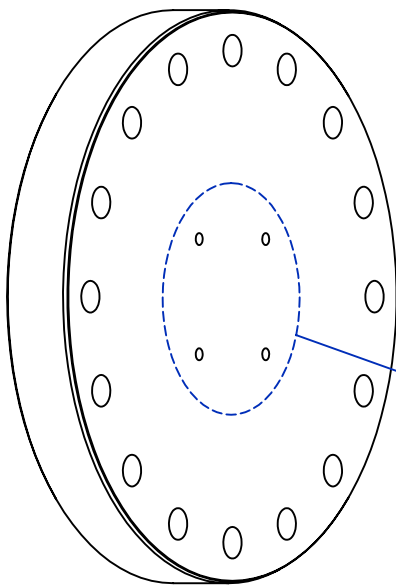
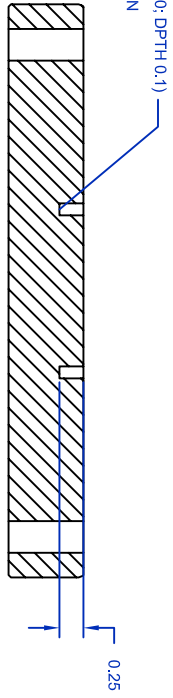
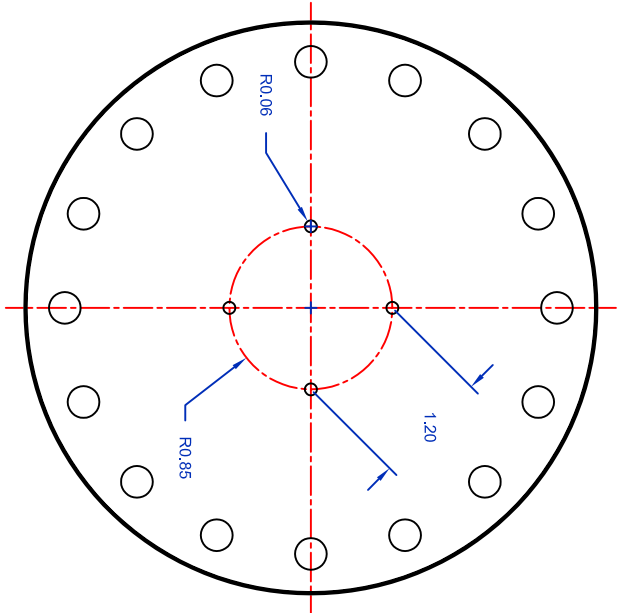


Figure 2.27



The hole position matches with Kimball Phys. Part (SS-PL-G5X5)

NOTE:

1. CF600 was purchased from MDC Vacuum Corp.
2. Knife edge of the CF flange is not drawn.

TITLE	FILE NAME	DWG BY	PI
CF600 modification	CF600-MGN.dwg	D. Hahn Park	AHZ
SCALE	MATERIAL	UNIT TOLERANCES	(UNLESS SPECIFIED) inch (0.03) degree (0.5)
1:2	SS-304		Laboratory for Molecular Sciences California Institute of Technology
8	6	01	

Figure 2.27.1

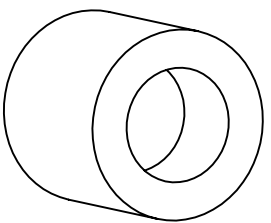
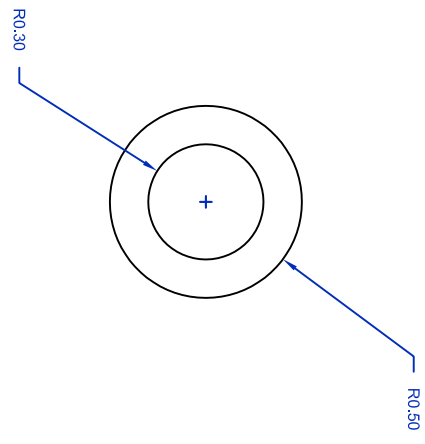
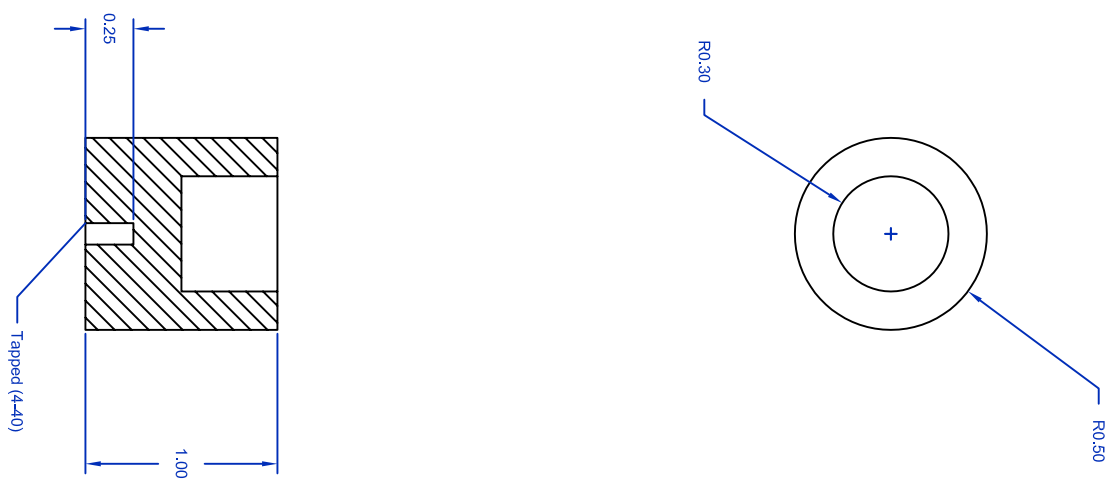


Figure 2.27.2

1	2	3	4	5	6	7	8	9	10
E	D	C	B	A					
1	2	3	4	5	6	7	8	9	10
E	D	C	B	A					

TITLE	FILE NAME	DWG BY	PI
Magnet Holder	HLDH-MGN.dwg	D. Hahn Park	AHZ
SCALE	UNIT (TOLERANCES)	Laboratory for Molecular Sciences California Institute of Technology	
1:1	(UNLESS SPECIFIED) inch (0.03) degree (0.5)	6	01
MATERIAL			
TEFLON			

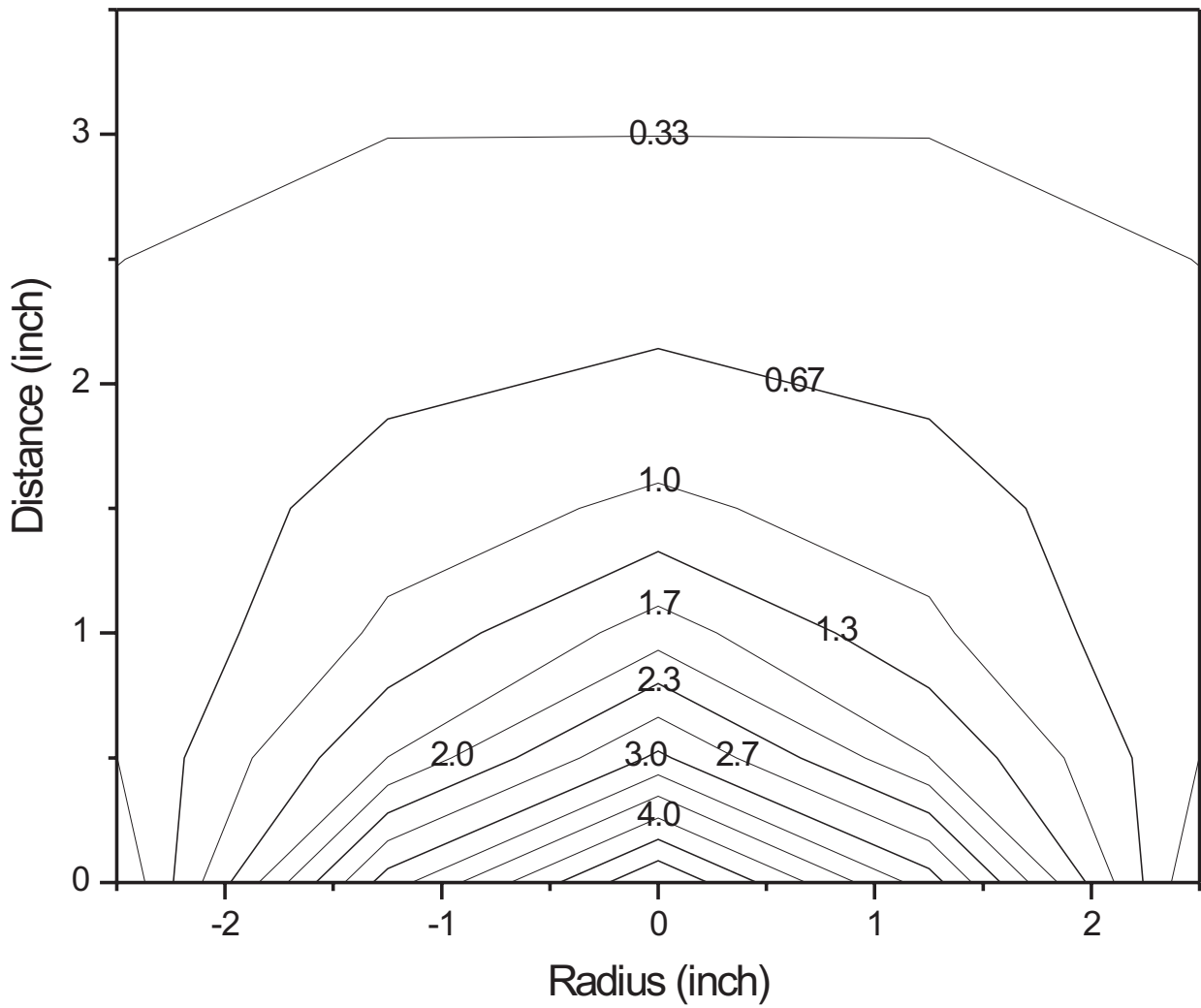
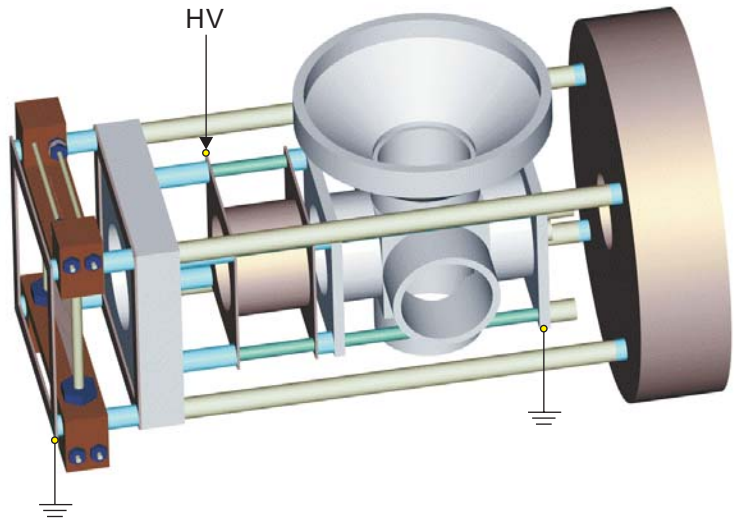


Figure 2.28



SS-PL-C7X7-S1400
Al₂O₃-SP-C-050

PLT-DCL

SS-PL-C5X5-R1000

SHLD-FNL

SHLD-CRSS

SS-SP-C-250

Al₂O₃-SP-C-100

DSK-LSR

Assembly-2.B

Mass Gate Assembly

Al₂O₃-SP-C-150

SS-CY-1000/1000

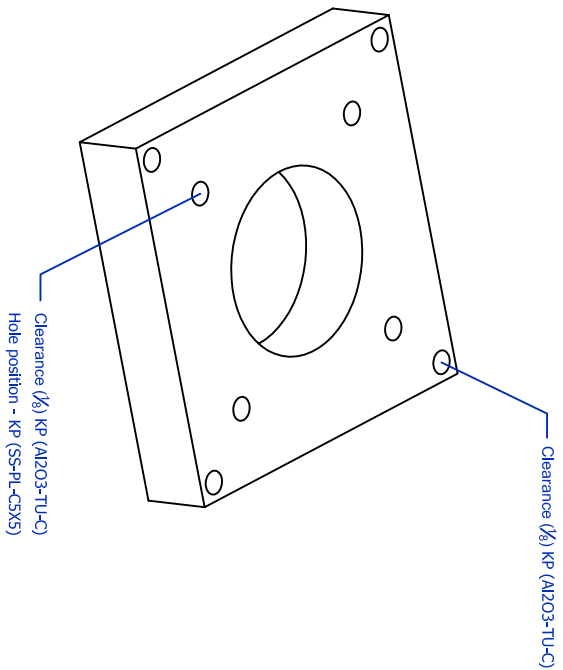
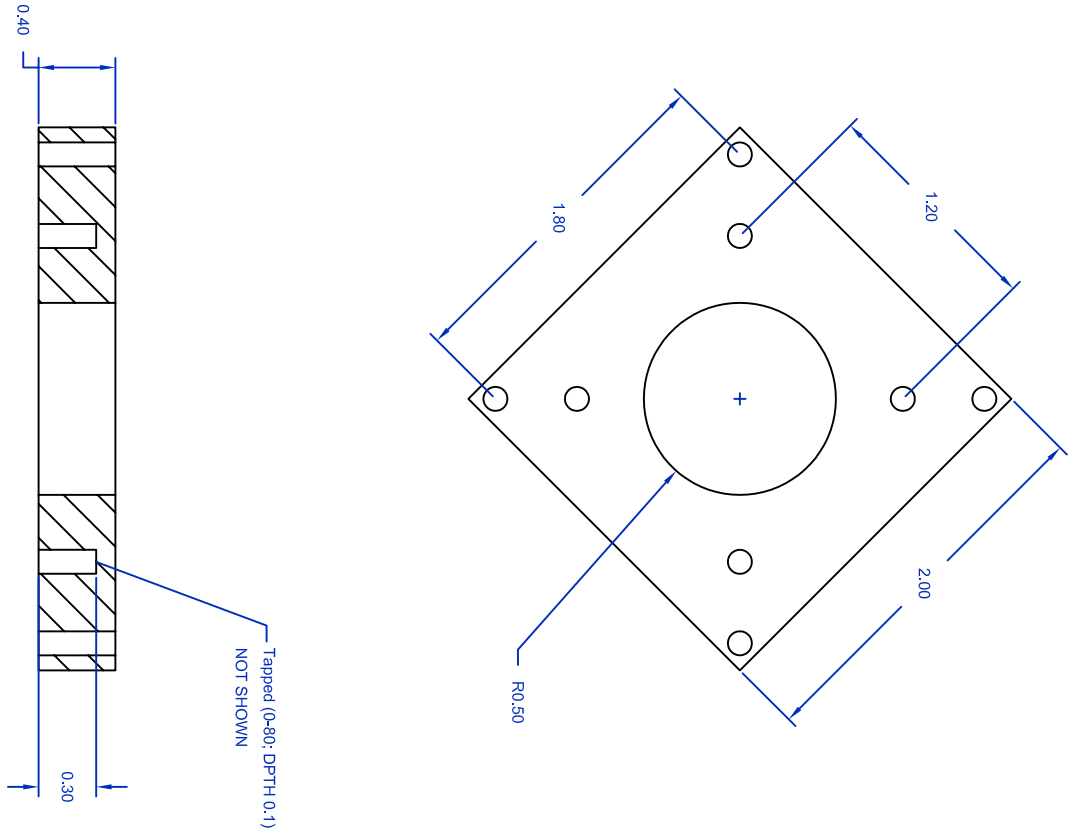
Al₂O₃-SP-C-250

SS-SP-C-2000

Al₂O₃-TU-C-6000

Al₂O₃-TU-C-4000

Figure 2.29



NOTE:
1. KP stands for Kinball Physyeds, Inc.

Figure 2.29.1

TITLE		FILE NAME		DWG BY		PI	
Plate for Ion Optics		PL-I-DCL.dwg		D. Hahn Park		AHZ	
SCALE		UNIT (TOLERANCE)		UNLESS SPECIFIED		degree (0.5)	
1:1		AL 6061		inch (0.03)		California Institute of Technology	
8		6		01			

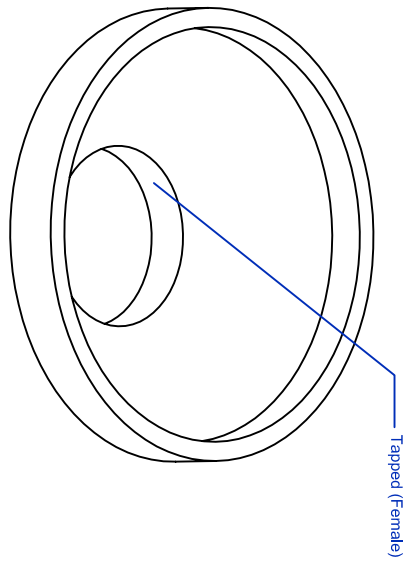
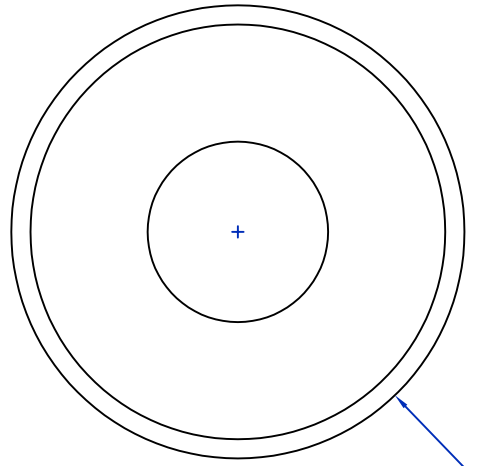
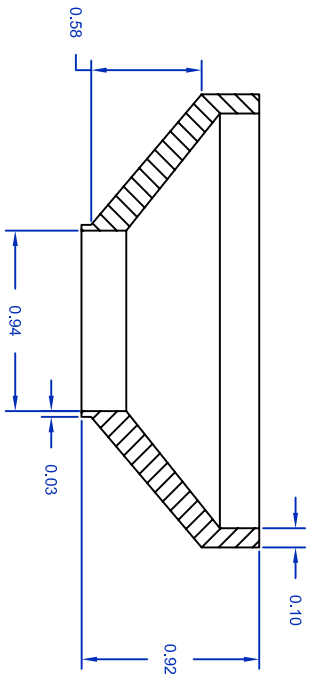


Figure 2.29.3

TITLE	FILE NAME	DWG BY	PI
Shield-Funnel	SHLD-FNL.dwg	D. Hain Park	AHZ
SCALE	UNIT (TOLERANCES)	Laboratory for Molecular Sciences California Institute of Technology	
1:1	(UNLESS SPECIFIED) inch (0.03) degree (0.5)		
MATERIAL			
AL 6061			

Mu-SHLD2

Mu-SHLD1

ASSM4



Figure 2.30

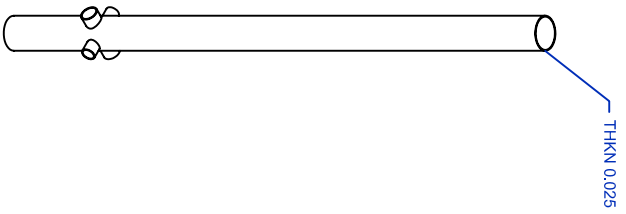
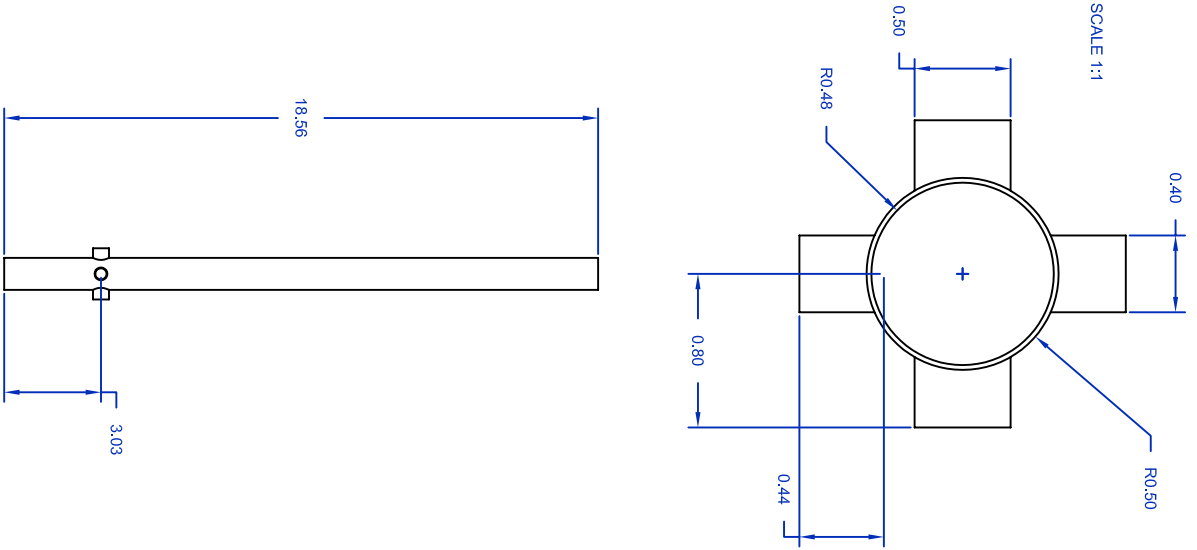


Figure 2.30.1

1	2	3	4	5	6	7	8	9	10	
A	B	C	D	E						A
157										
SCALE 1:1										
0.40										
0.50										
R0.48										
R0.50										
0.80										
0.44										
18.56										
3.03										
THKN 0.025										
TITLE: μ -metal Tube										
FILE NAME: mu-SHLD1.dwg										
DRAWN BY: D. Hahn Park										
P1: AHZ										
SCALE: 1:6										
MATERIAL: μ -metal										
UNIT (TOLERANCES): inch (0.03)										
UNLESS SPECIFIED: degree (0.5)										
Laboratory for Molecular Sciences										
California Institute of Technology										
01										
A	B	C	D	E						A

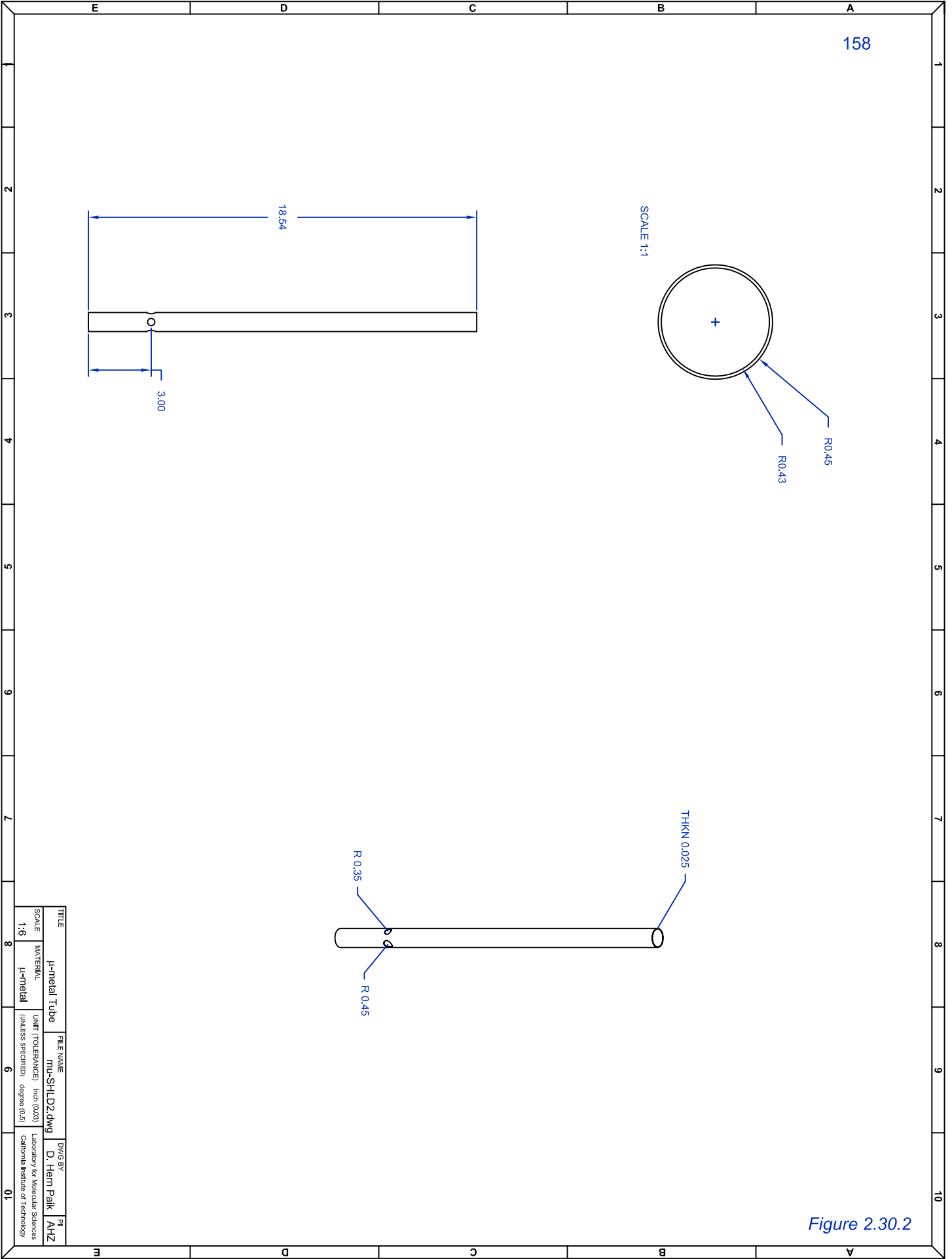
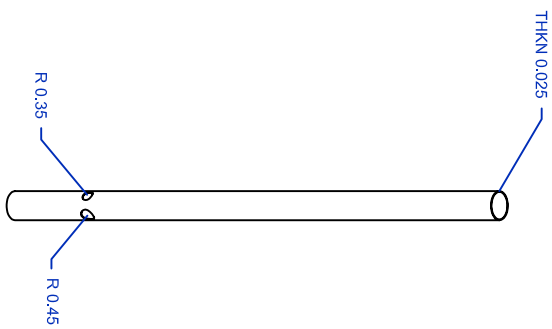
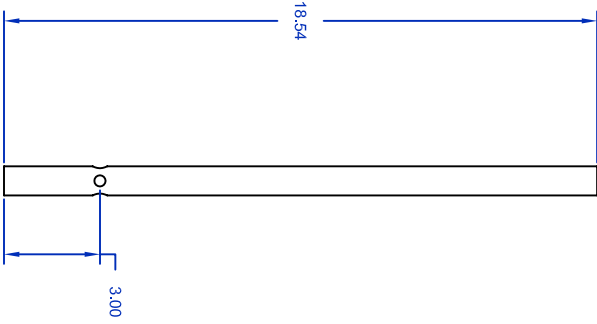
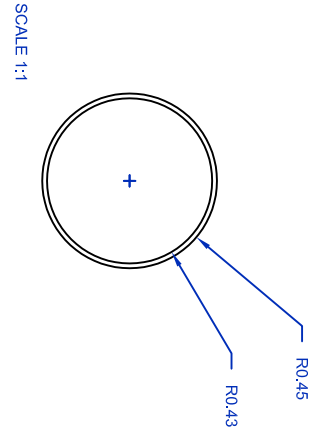


Figure 2.30.2

TITLE	FILE NAME	DWG BY	PI
μ -metal Tube	mu-SHLD2.dwg	D. Hahn Park	AHZ
SCALE	UNIT (TOLERANCES)	Laboratory for Molecular Sciences California Institute of Technology	
1:6	(UNLESS SPECIFIED) inch (0.03) degree (0.5)	6	01
MATERIAL			
μ -metal			

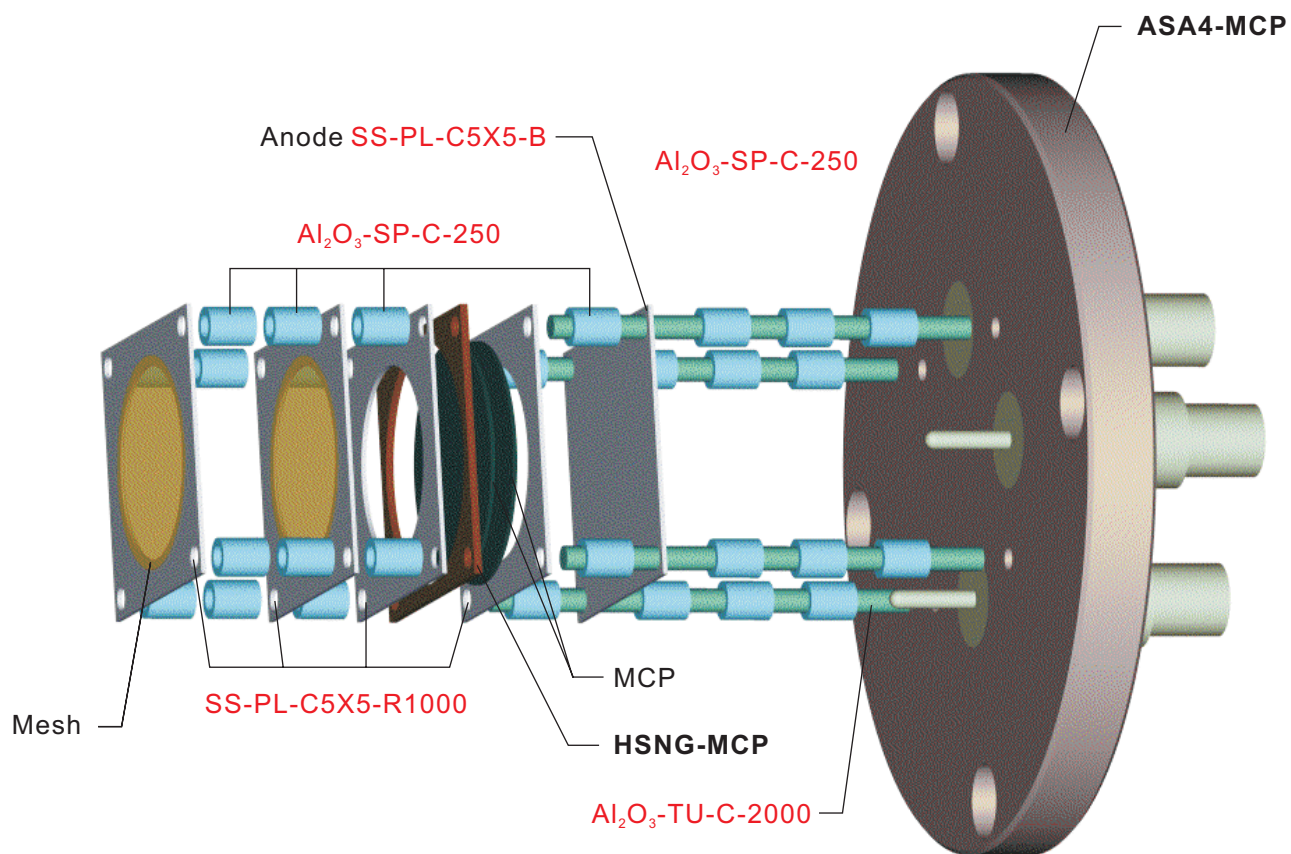
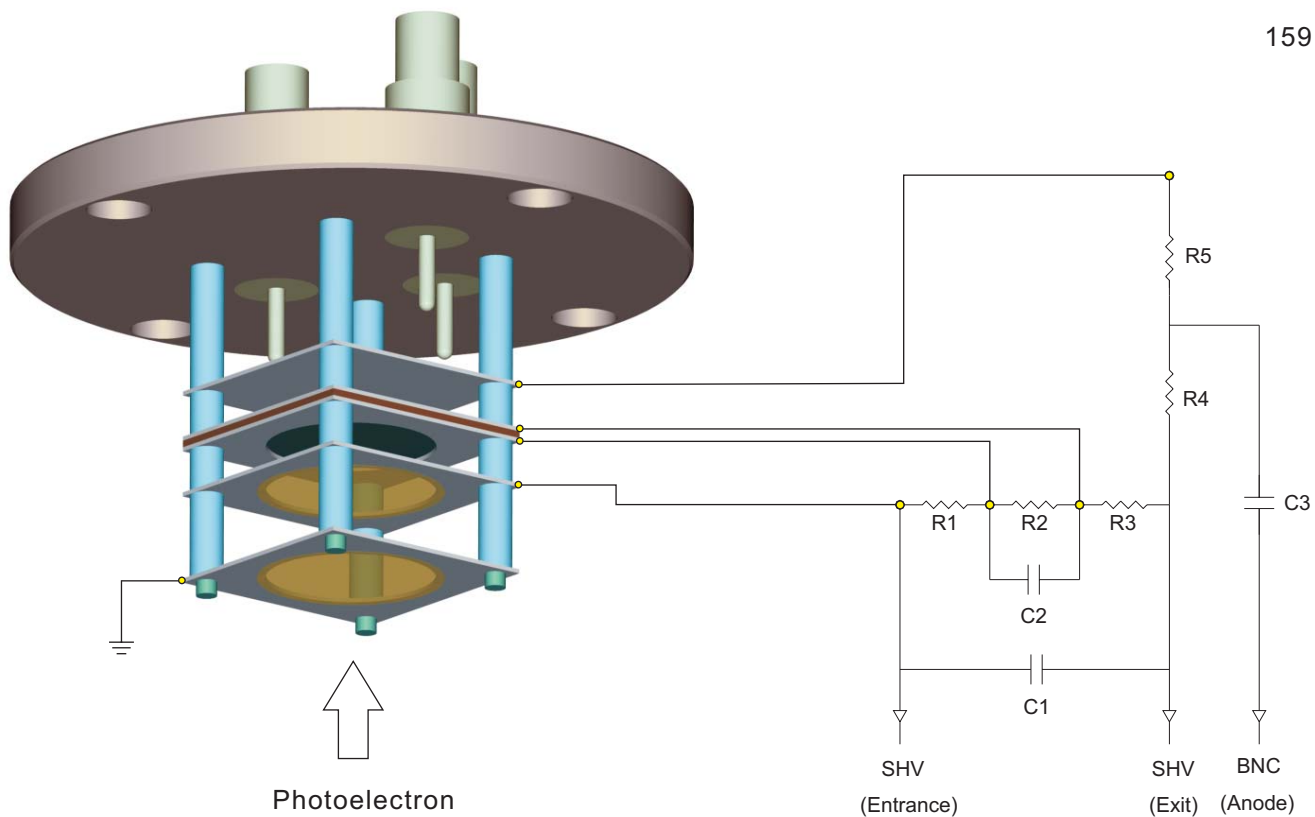
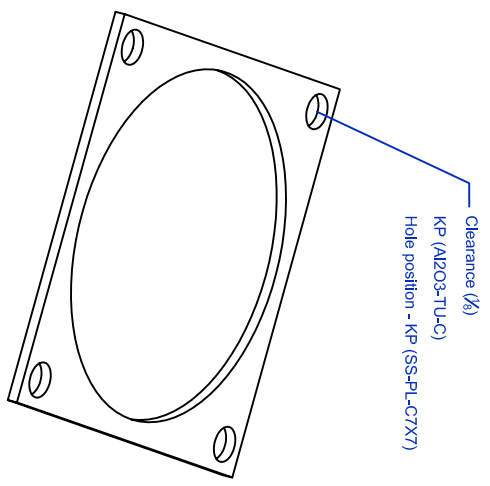
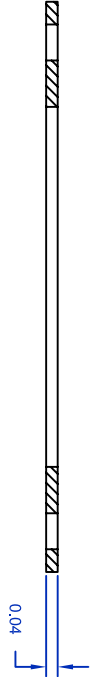
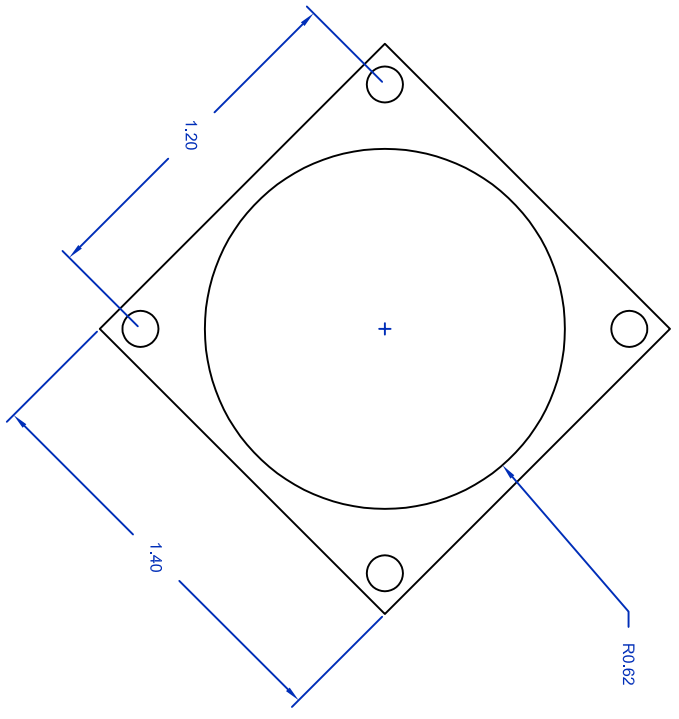
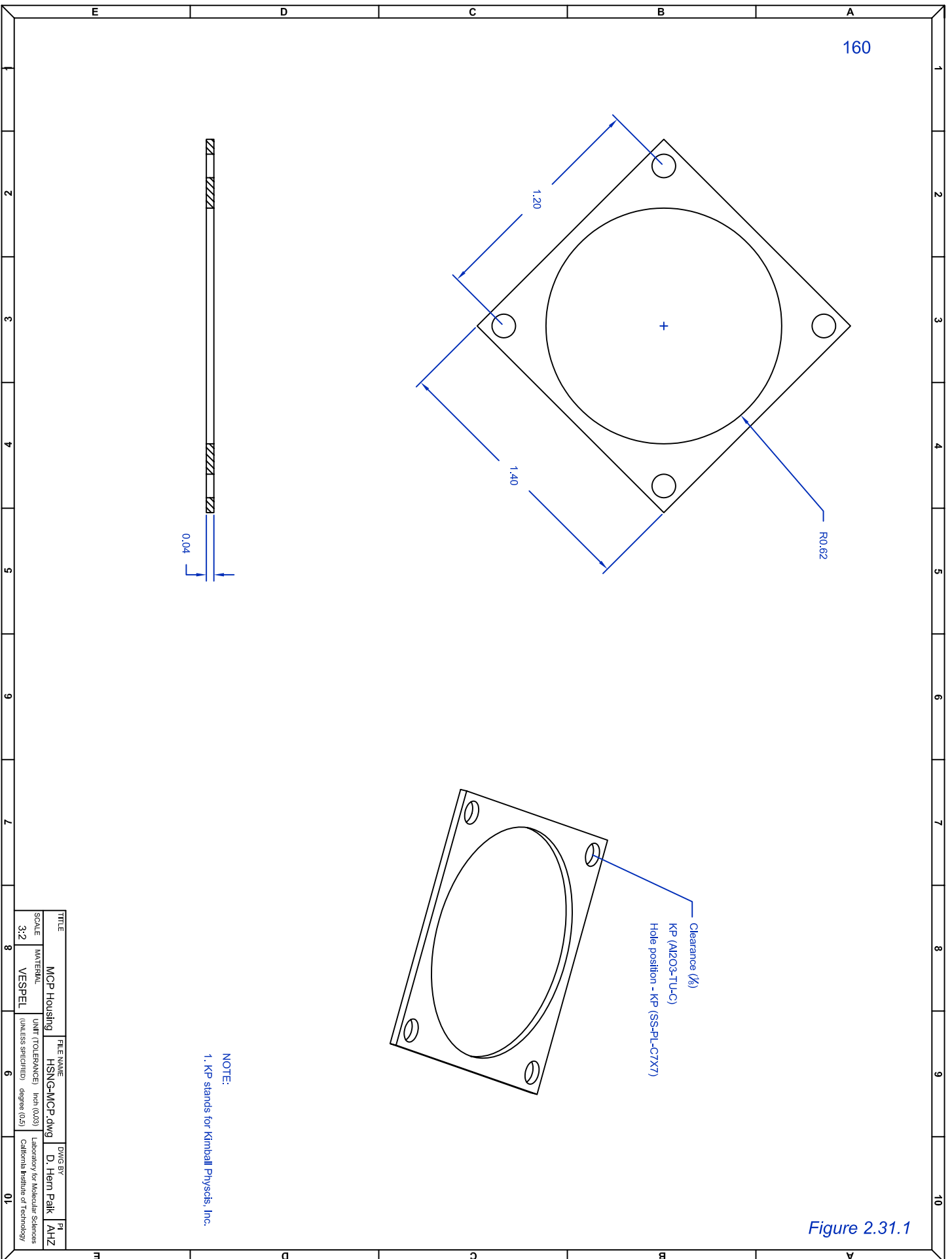


Figure 2.31



NOTE:
1. KP stands for Kimball Physics, Inc.

Figure 2.31.1



TITLE	MCP Housing	FILE NAME	HSNG-MCP.dwg	DWG BY	D. Hahn Park	PI	AHZ
SCALE	3:2	MATERIAL	VESPEL	UNIT TOLERANCES	inch (0.03)	Laboratory for Molecular Sciences California Institute of Technology	
					degree (0.5)		

2.9. Femtosecond Laser System

The femtosecond laser system used in this laboratory consists of Ti:Sapphire oscillator and amplifier which were manufactured by Spectra Physics Laser. The layout of the laser system is shown in Fig. 2.32 and 2.33. In this section, the post-installation modifications are briefly discussed. For operational procedure refer to the instruction manuals provided by Spectra Physics Laser.

Intense femtosecond laser pulse (100 fs, 800 nm, 25 mJ/pulse, 20 Hz) was generated from our laser system. The oscillator output (Tsunami, Spectra-Physics) was amplified by the Ti:Sapphire regenerative amplifier (TSA 25, Spectra-Physics) which was pumped by the second harmonic (532 nm) of two Nd:YAG lasers (LAB 130 and LAB 150, Spectra-Physics). Twenty percent of the output power was sufficient for most experiments which can produce 1.5 mJ pump pulse (800 nm) and 0.8 mJ of probe pulse (400 nm). The probe beam is generated by the doubling by the BBO crystal, which is optically delayed by the Michaelson Interferometer type translational stage. Pump and probe pulses were collinearly irradiated into the molecular beam chamber by utilizing a harmonic separator. Both pump and probe pulses were collimated down to 5 mm in order to achieve optimal overlap with the ion beam without causing multiphoton processes.

2.9.1 Mode Quality and Stability of the Femtosecond Laser System

The stability and mode quality of the output laser beam are predominantly dependent on the alignment and fine tuning of the TSA 25 amplifier. Unlike the 1 kHz Spittfier System, the Ti:Sapphire rods in the TSA 25 are pumped by the Nd:YAG Laser

operating at 20 Hz. The stability of Quanta-Ray series is not as good as other pump lasers used in the 1 kHz system. In addition, the spatial mode of the Quanta-Ray is 'donut' like shape rather than Gaussian type profile. These two inherent features of the Quanta-Ray Nd:YAG laser depreciate the stability and mode quality of the femtosecond laser output. These two drawbacks must be improved for carrying out transient, and the mode quality is critical for the OPA operation.

The key mind-set for improving the two qualities is not to hesitate to sacrifice the output power. The laser beam alignment must be changed significantly from the beam path suggested for acquiring the maximum output generation in order to achieve a good mode quality. For optimizing the mode quality, the beam size in the regenerative (regen) amplifier must be carefully adjusted since the mode quality improves when the pump beam is tightly focused in the regen rod. Distortion of the mode quality is most likely to occur in the multipass amplifiers since the beam path of the seed beam is 'V-shape', the spatial overlap between the pump and seed beams are not ideal. In addition, it is quite difficult to overlap the Gaussian mode profile of the seed beam and the donut shape mode profile of the pump (Nd:YAG) laser. Thus, the alignment of multipass amplifier is the key step for improving the mode quality and the stability.

2.10. Synchronization of the laser and the ion beam

The most critical is the synchronization of the femtosecond laser system and the molecular beam apparatus. The cable connections for the TTL transmission are shown in Fig. 2.33, and the pulse sequences used in the ion packet-laser pulse synchronization are shown in Fig. 2.34.

2.11. Data Acquisition

The mass and photoelectron spectra are recorded the LeCroy Digital Oscilloscope and transferred to the computer by using the software provided by LeCroy. The data acquisition program for recording transient is programmed by I-Ren Lee. For the detailed programming, refer to the source code written by I-Ren Lee.

2.12. Overview of Experimental Procedure

The schematic of experimental method is shown in Fig. 2.35. The negative ion beam is prepared by injecting the electron beam to the pulsed supersonic jet expansion.

2.13. Reduction of Background Noise

Appendix D.

References

- ¹ J. H. Moore, C. C. Davis, and M. A. Coplan, *Building Scientific Apparatus: A Practical Guide to Design and Construction*, 2 ed. (Perseus Books, Cambridge, 1991).
- ² A. Chambers, R. K. Fitch, and B. S. Halliday, *Basic Vacuum Technology*. (IOP Publishing Ltd., New York, 1989).
- ³ J. M. Farrar and W. H. Saunders, *Techniques of Chemistry: Techniques for the Study of Ion-Molecule Reactions*. (Wiley-Interscience Publication, New York, 1988).
- ⁴ R. Campargue, *J. Phys. Chem.* **88**, 4466 (1984).
- ⁵ M. A. Johnson, M. L. Alexander, and W. C. Lineberger, **112**, 285 (1984).
- ⁶ M. L. Alexander, N. E. Levinger, M. A. Johnson, D. Ray, and W. C. Lineberger, *J. Chem. Phys.* **88** (10), 6200 (1988).
- ⁷ C.-Y. Cha, G. Gantefor, and W. Eberhardt, *Rev. Sci. Instrum.* **63** (12), 5661 (1992).
- ⁸ O. Cheshnovsky, S. H. Yang, C. L. Pettiette, M. J. Craycraft, and R. E. Smalley, *Rev. Sci. Instrum.* **55** (11), 2131 (1987).
- ⁹ O. Cheshnovsky, S. H. Yang, C. L. Pettiette, M. J. Craycraft, Y. Liu, and R. E. Smalley, *Chem. Phys. Lett.* **138** (2,3), 119 (1987).
- ¹⁰ A. Nakajima, T. Taguwa, K. Hoshino, T. Sugioka, T. Naganuma, F. Ono, K. Watanabe, K. Nakao, Y. Konishi, R. Kishi, and K. Kaya, *Chem. Phys. Lett.* **214** (1), 22 (1993).
- ¹¹ W. C. Wiley and I. H. McLaren, *Rev. Sci. Instrum.* **26** (12), 1150 (1955).
- ¹² R. J. Cotter, *Time-of-Flight Mass Spectrometry: Instrumentation and Application in Biological Research*. (American Chemical Society, Washington, DC, 1997).
- ¹³ P. R. Vlasak, D. J. Beussman, M. R. Davenport, and C. G. Enke, *Rev. Sci. Instrum.* **67** (1), 68 (1996).
- ¹⁴ R. Weinkauff, K. Walter, C. Weickhardt, U. Boesl, and E. W. Schlag, *Z. Naturforsch.* **44a**, 1219 (1989).
- ¹⁵ C. W. Stoermer, S. Gilb, J. Friedrich, D. Schooss, and M. M. Kappes, *Rev. Sci. Instrum.* **69** (4), 1661 (1998).
- ¹⁶ J. L. Wiza, *Nuclear Instrument and Methods* **162**, 587 (1979).
- ¹⁷ B. A. Mamyryn, V. I. Karataev, D. V. Shmikk, and V. A. Zagulin, *Sov. Phys. JETP* **37**,
- ¹⁸ D. V. Shmikk, *Sov. Phys. Tech. Phys.* **26** (5), 615 (1981).

- ¹⁹ R. B. Opsal, K. G. Owens, and J. P. Reilly, *Anal. Chem.* **57**, 1884 (1985).
- ²⁰ B. Ernstberger, A. H. Krause, A. Kiermeier, and H. J. Neusser, *J. Chem. Phys.* **92** (9), 5285 (1990).
- ²¹ B. A. Mamyrin and D. V. Shmikk, *Sov. Phys. JETP* **49** (5), 762 (1979).
- ²² P. Kruit and F. H. Read, *J. Phys. E: Sci. Instrum.* **16**, 313 (1983).
- ²³ B. J. Greenblatt, M. T. Zanni, and D. M. Neumark, *Chem. Phys. Lett.* **258**, 523 (1996).
- ²⁴ H. Handschuh, G. Gantefor, and W. Eberhardt, *Rev. Sci. Instrum.* **66** (7), 3838 (1995).
- ²⁵ K. Rademann, T. Rech, B. Kaiser, U. Even, and F. Hensel, *Rev. Sci. Instrum.* **62** (8), 1932 (1991).
- ²⁶ G. Markovich, S. Pollack, R. Giniger, and O. Cheshnovsky, *J. Chem. Phys.* **101** (11), 9344 (1994).
- ²⁷ L. S. Wang, H. S. Cheng, and J. Fan, *J. Chem. Phys.* **102** (24), 9480 (1995).
- ²⁸ C. W. Conover, Y. J. Twu, Y. A. Yang, and L. A. Bloomfield, *Rev. Sci. Instrum.* **60** (6), 1065 (1989).
- ²⁹ S. Della Negra and Y. Le Beyec, *Int. J. Mass Spectrom. Ion Proc.* **61**, 21 (1984).
- ³⁰ O. F. Hagen and W. Obert, *J. Chem. Phys.* **56** (5), 1793 (1972).
- ³¹ D. M. Lubman, W. E. Bell, and M. N. Kronick, *Anal. Chem.* **55**, 1437 (1983).
- ³² D. M. Lubman and R. M. Jordan, *Rev. Sci. Instrum.* **56** (3), 373 (1985).
45 (1973).

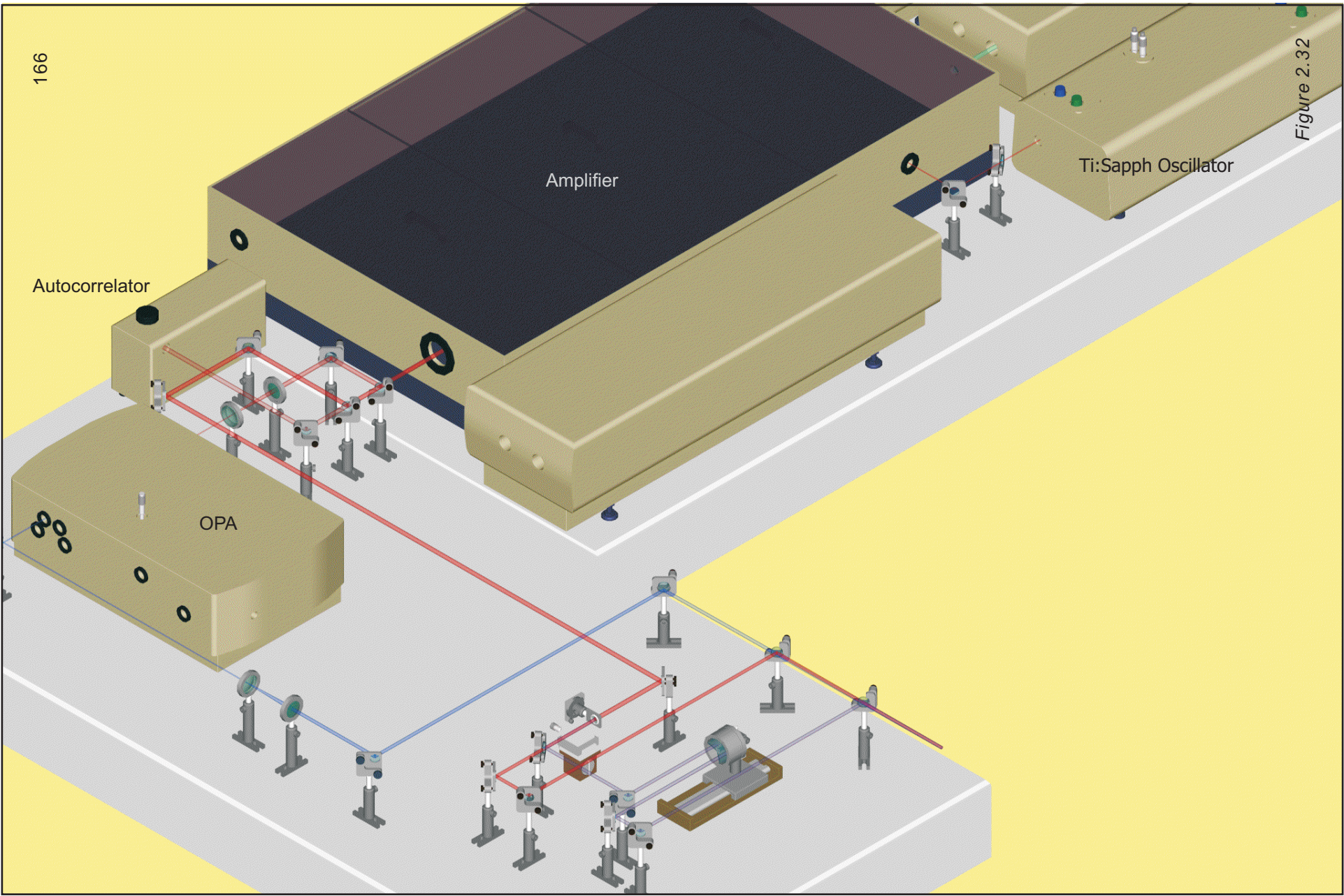


Figure 2.32

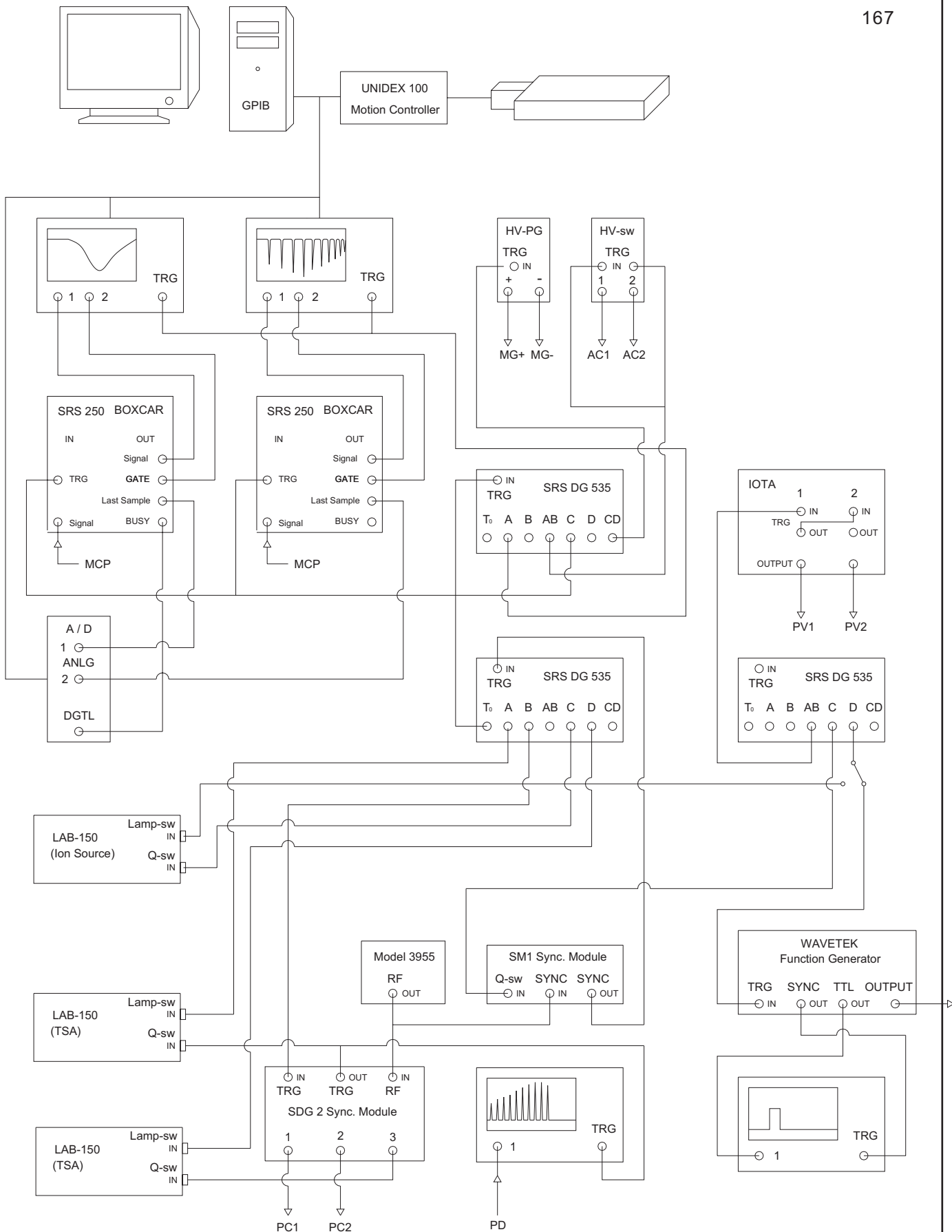


Figure 2.33

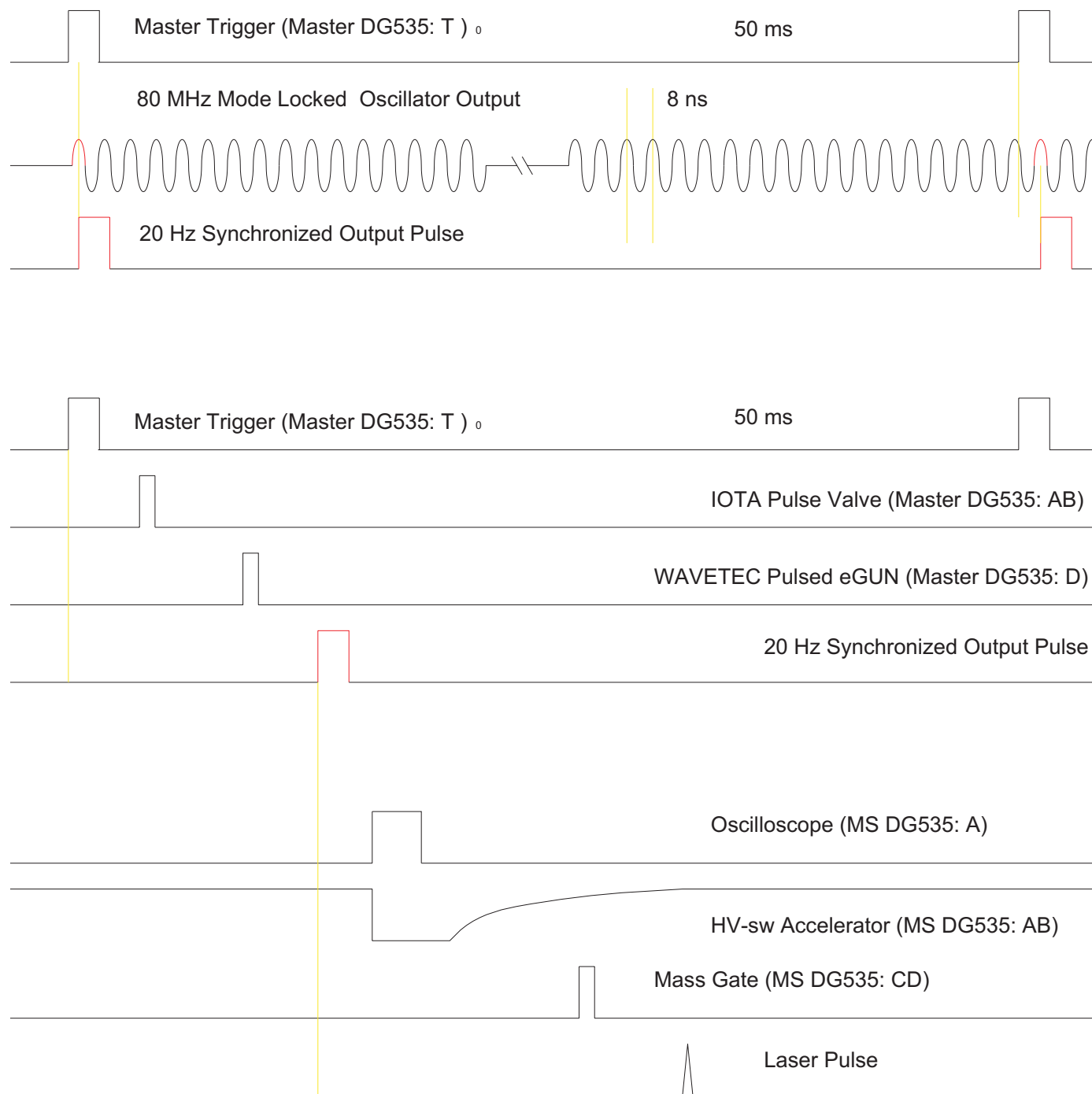


Figure 2.34

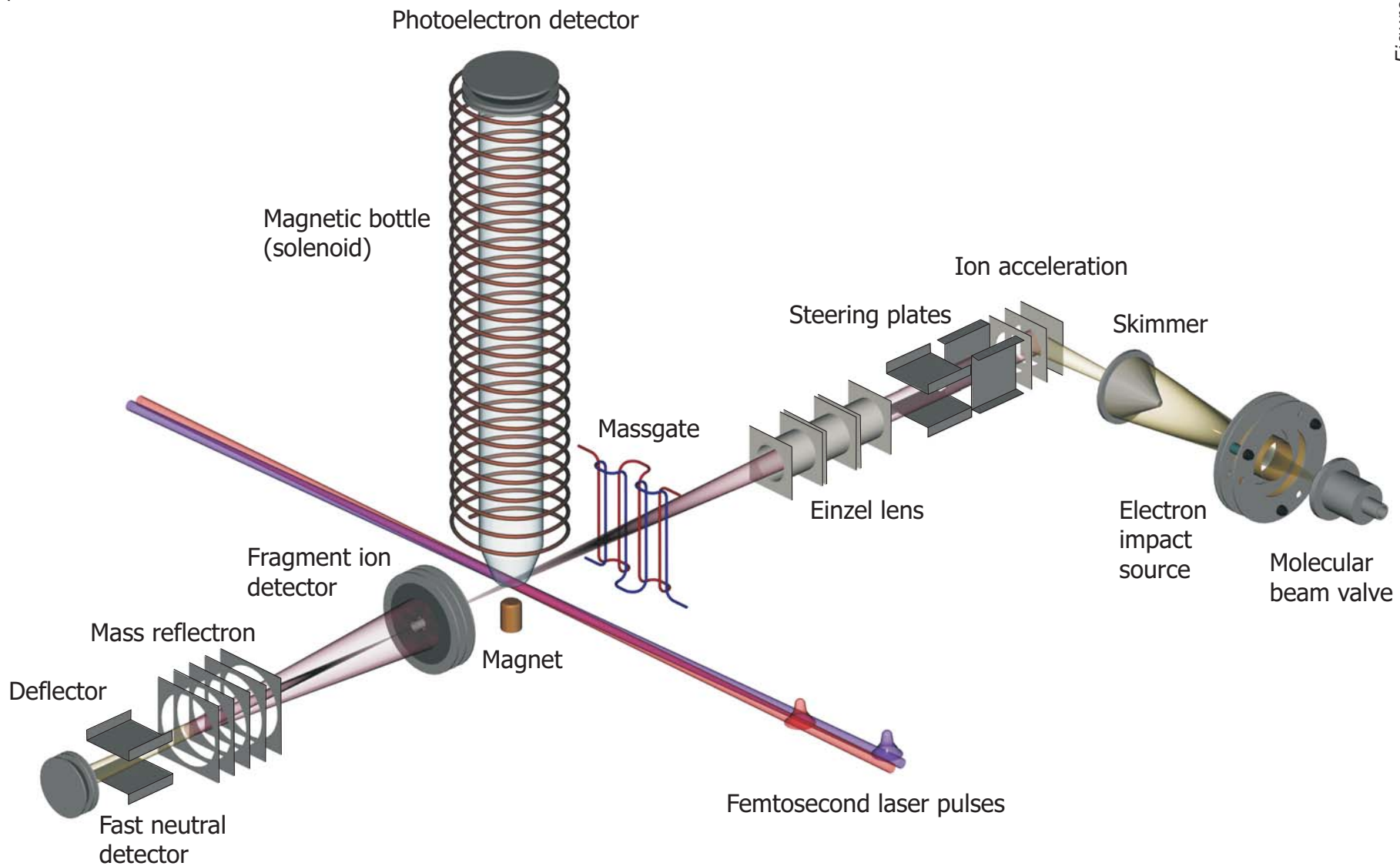


Figure Captions

Figure 2.1 Labels for the individual vacuum chambers. The components in the bolded label correspond to custom-made or home-built parts.

Figure 2.1.1 Drawing of the source chamber.

Figure 2.1.2 Drawing of partitioning plates utilized for mounting various sizes of skimmers and apertures.

Figure 2.1.3 Drawing of the buffer chamber.

Figure 2.1.4 Drawing of the home-built aluminum flanges covering the backend of the buffer chamber.

Figure 2.1.5 Drawing of the reducing nipple used for coupling CF600 and ASA400 fittings.

Figure 2.1.6 Drawing of the CF600 cross used for mounting the turbo-molecular pump.

Figure 2.1.7 Drawing of the reducing nipple used for coupling CF800 and CF600 fittings.

Figure 2.1.8 Drawing of the mass spectrometer chamber.

Figure 2.1.9 Drawing of the modified zero-length adapter.

Figure 2.1.10 Drawing of the reflectron chamber.

Figure 2.1.11 Drawing of the modified CF800 flange used for covering the reflectron chamber.

Figure 2.2 Schematic of vacuum lines.

Figure 2.3 Top: Back flange assembly. Bottom: High temperature Inlet System.

Figure 2.4 Drawing of the pulsed electron gun assembly.

Figure 2.4.1 Drawing of the top plate and the ground mesh used in the pulse electron gun

Figure 2.4.2 Drawing of the middle plate used in the pulse electron gun.

Figure 2.4.3 Drawing of the bottom plate and the trapping mesh used in the pulse electron gun.

Figure 2.4.4 Drawing of the vespel spacer used in the pulse electron gun.

Figure 2.4.5 Drawing of the macor spacers used in the pulse electron gun.

Figure 2.5 The simulated trajectory of the electrons trapped in the pulse electron gun.

Figure 2.6 Drawing of the continuous electron gun used in the thermionic mode.

Figure 2.6.1 Drawing of the aluminum base plate used in the continuous electron gun.

Figure 2.6.2 Drawing of the modified ASA400 flange which was used for mounting the entire assembly of the continuous electron gun.

Figure 2.6.3 Drawing of the aluminum disk used in the continuous electron gun.

Figure 2.7 Miniature coaxial cable used in the ion optic components

Figure 2.8 The simulated trajectory of the electron beam ejected from the continuous electron gun.

Figure 2.9 The continuous electron gun used in the photocathode mode.

Figure 2.10 Picture of the voltage divider used for the photocathode mode.

Figure 2.11 Cross section of the vacuum chamber showing the major constituents of the spectrometer.

Figure 2.12 Assembly of the two-stage ion accelerator.

Figure 2.12.1 Drawing of the aluminum disk used for extending the accelerator.

Figure 2.12.2 Drawing of the vespel disk used for extending the accelerator.

Figure 2.13 Hinge assembly and the tilting mechanism.

Figure 2.13.1 Drawing of the vespel piece used for holding the pivot in the hinge assembly.

Figure 2.13.2 Drawing of the stainless-steel plate extension used in the hinge assembly.

Figure 2.13.3 Drawing of the aluminum cylinder used for extending the motion feedthrough.

Figure 2.14 Assembly of the einzel lens.

Figure 2.14.1 Drawing of the aluminum disk used for mounting the einzel lens.

Figure 2.15 Assembly of the interleaved-comb mass gate.

Figure 2.15.1 Drawing of the vespel frame in the interleaved-comb mass gate.

Figure 2.16 MCP assembly used in the primary mass spectrometer.

Figure 2.16.1 Drawing of the modified ASA400 flange used for mounting the MCP assembly.

Figure 2.17 The electrical response time of the MCP assembly used in the primary mass spectrometer.

Figure 2.18 Mass spectra of negative and positive ions generated by using the pulsed electron gun.

Figure 2.19 The reflectron assembly.

Figure 2.19.1 Drawing of the aluminum disk used for mounting the reflectron

Figure 2.20 The annular MCP assembly and the schematic of subsidiary electronics used in the MCP assembly.

Figure 2.20.1 Drawing of the aluminum disk used in the annular MCP assembly The electroformed mesh is attached to the disk for electric shielding.

Figure 2.20.2 Drawing of the stainless-steel tube inserted in the center hole of the annular MCP, which shield electric field emanating from the electrodes.

Figure 2.20.3 Drawing of the stainless-steel block used for mounting the annular MCP and assembly 2A (Fig. 2.29).

Figure 2.21 Assembly 2B

Figure 2.21.1 Drawing of the aluminum disk for mounting assembly 2B.

Figure 2.22 Simulated ion trajectory in the tandem mass spectrometer. The relative scale is close to the actual dimension.

Figure 2.23 Simulated ion trajectory in the reflectron. The middle panel illustrates the kinetic energy dependence on the penetration depth.

Figure 2.24 The electrical response time of the annular MCP used in the reflectron mass spectrometer.

Figure 2.25 Schematic illustration of photodetachment process and the resulting photoelectron spectrum.

Figure 2.26 The solenoid assembly used in the magnetic bottle photoelectron spectrometer. The drawing in the middle illustrates the cross section of the solenoid assembly.

Figure 2.26.1 Drawing of the modified CF600 which is used for mounting the four legs of the solenoid clamp.

Figure 2.26.2 Drawing of the Teflon cover used in the solenoid clamp.

Figure 2.26.3 Drawing of the aluminum piece used in the solenoid clamp.

Figure 2.26.4 Drawing of modified CF600 flange used for covering the top of the photoelectron chamber. The 1/4" holes are for mounding MCP assembly.

Figure 2.26.5 Drawing of the modified CF600 flange. The high voltage electric feedthroughs are vacuum-welded.

Figure 2.27 Magnet assembly used in the photoelectron spectrometer.

Figure 2.27.1 Drawing of modified CF600 flange for fixing the permanent magnet.

Figure 2.27.2 Drawing of the Teflon housing used for holding the permanent magnet.

Figure 2.28 Equipotential line of the magnetic field created near the permanent magnet.

Figure 2.29 Assembly 2A.

Figure 2.29.1 Drawing of the base plate used for mounting the ion-lift assembly.

Figure 2.29.2 Drawing of the 6-way cross used in the laser interaction region to shield the stray magnetic and electric fields.

Figure 2.29.3 Drawing of the cone extension for blocking the stray fields.

Figure 2.30 Illustration of μ -metal shield installation.

Figure 2.30.1 Drawing of the outer shell of μ -metal tube.

Figure 2.30.2 Drawing of the inner shell of the μ -metal tube.

Figure 2.31 MCP assembly used for detecting photoelectrons.

Figure 2.31.1 Drawing of the vespel housing used for securing the microchannel plates.

Figure 2.32 Femtosecond laser system.

Figure 2.33 Cable connections for transmitting the triggering pulses

Figure 2.34 Pulse sequences used for synchronizing the molecular beam apparatus and the femtosecond laser system

Figure 2.35 Schematic representation of the experimental method

CHAPTER 3.

Femtochemistry of Mass-Selected Negative-Ion

Clusters of Dioxygen:

Charge-Transfer and Solvation Dynamics

3.1. Introduction

Spectroscopy of size-selected molecular clusters provides a unique approach to investigate solvation phenomena at the molecular level; for recent reviews see references [1-3]. For ions, mass selection provides an opportunity to study the energetics and dynamics, with the solvent number of atoms or molecules being well-defined. Homogeneous ionic clusters are of particular interest as they could exhibit unique features of electron and energy transfer, and solvation. For example, in a number of ionic cluster systems, such as $(\text{CO}_2)_n^-$, a dimeric core unit is found to be responsible for the observed photochemistry.⁴ In some other examples, such as Ar_n^+ and $(\text{H}_2\text{O})_n^-$, photoexcitation can lead to a charge-transfer to neutral solvent molecules, as shown by the Johnson group.^{5,6}

The relevant homogeneous system here is the anionic molecular-oxygen clusters studied by the groups of Johnson, Continetti, Märk and others.⁷⁻⁹ The O_4^- chromophore is suggested to be the core unit¹⁰, which is transparent in the near infrared region. However, with the addition of O_2 solvent molecules to the O_4^- core, cluster dissociation occurs upon infrared absorption.¹¹ Two mechanisms are proposed in the literature to account for the observed photodissociation of $(\text{O}_2)_n^-$ clusters: (i) Near-infrared excitation to a charge-transfer state which involves O_4^- and the solvent.¹¹ Following this charge transfer, the newly generated O_2^- ion exhibits a significant vibrational excitation, which by cooling leads to sequential evaporation of neutral O_2 molecules.¹² (ii) Excitation to low-lying repulsive states, which are not accessible in native O_4^- , but become possible in the larger $(\text{O}_2)_n^-$ ($n > 2$) clusters.⁸ In this case, vibrational excitation of product O_2^- can also be

observed. However, the time scale for the O_2^- release in these two mechanisms has to differ considerably.

In this chapter, we report study of the dissociation dynamics in real time of mass-selected clusters of molecular oxygen which was carried out by using femtosecond photoelectron (PE) spectroscopy. The method is capable of resolving the femtosecond dynamics of ions with mass selection as a function of size.^{13,14} For our study of $(O_2)_n^-$ clusters in the newly designed molecular beam machine, described here briefly, we identify two distinct dissociation channels which occur on drastically different time scales. We conclude that the preparation of the charge-transfer complex leads to the bifurcation of the wave packet, with liberation of the charge-accepted O_2^- in one channel and electron recombination which leads to O_4^- in the second channel. This second process is analogous to previous investigations of bimolecular charge-transfer reactions in neutral van der Waals clusters, which revealed the importance of reversible electron transfer.^{15,16} The influence of stepwise solvation by O_2 on the reaction timescale is also observed and is consistent with the aforementioned picture.

3.2. Experimental

Anionic oxygen clusters were generated by secondary electron attachment after the supersonic expansion. The pulsed electron gun with a tungsten filament (0.015") was used for thermionic electron generation. The anionic clusters were extracted to the field-free time-of-flight region by a pulsed electric field. A particular size was selected by an interleaved-comb massgate before entering the interaction-with-light region. The clusters of interest were then perpendicularly intercepted with femtosecond laser pulses, which

produces photofragments and photoelectrons. The nascent fragment ions were separated in time from the parent ions after reflection from the linear reflectron. The linear configuration of a reflectron provides the minimal deviation of the daughter-ion trajectories from the parent ions, which facilitate the analysis of the dissociation process by incorporating the relative intensity profiles of ion signals.¹⁸ (chapter 2) Photoelectrons were analyzed using a magnetic-bottle photoelectron spectrometer. Here, no decelerating field was applied to slow down the ion beam. Consequently, the resolution of the spectrometer is limited to 150-200 meV at 1 eV electron kinetic energy due to Doppler broadening. See chapter 2 for the resolution of magnetic bottle photoelectron spectrometer.

Intense femtosecond laser pulses (100 fs, 800 nm, 25 mJ/pulse, 20 Hz) were generated using a Ti:sapphire regenerative amplifier which is seeded with the output of a Ti:sapphire oscillator and pumped by the second harmonic (532 nm) of two Nd:YAG lasers. Twenty percent of the output power was used in these experiments to produce the 800 nm pump pulse with about 1.5 mJ and the 400 nm probe pulse (second harmonic generation using BBO crystal) with 0.8 mJ before the entrance window. Pump and probe pulses were collinearly directed into the molecular beam chamber, and the beam diameters of both were collimated to ~5 mm in order to achieve optimal overlap with the ion beam, minimizing multiphoton processes. We monitored the transients in real time by probing the time-dependent photoelectron spectrum of the nascent O_2^- fragment. We also studied the decay of the parent, which appears as a transient signal with a decay time constant.

3.3. Results

A mass spectrum of $(\text{O}_2)_n^-$ generated by the cluster ion source (no laser) is shown in Figure 3.1A. With 800 nm fs pulse, the fragment mass spectra of $(\text{O}_2)_n^-$ ($n = 3-5$) are displayed in Figure 3.1B. The irradiation of O_2^- and O_4^- with 800 nm pulse did not produce any detectable negatively charged fragments. The mass spectra of Figure 3.1B clearly indicate that the major anionic product of the $(\text{O}_2)_n^-$ ($n=3-5$) dissociation is the O_2^- fragment. Moreover, the intensity distribution shows the growth of O_4^- fragment with increasing cluster size. These results are in good agreement with previous photodissociation studies of $(\text{O}_2)_n^-$ at 1064 nm excitation.¹¹

Figure 3.2 shows the photoelectron spectra of $(\text{O}_2)_n^-$ clusters recorded at 400 nm (3.1 eV) probe irradiation. The photodetachment spectra of $(\text{O}_2)_n^-$ at this wavelength are similar to the previously reported spectra at 532 nm⁸, 355 nm^{8,11}, and 266 nm.⁸ The onset of the photoelectron spectrum (adiabatic electron affinity) of O_4^- is 0.5 eV shifted to higher electron binding energy with respect to the O_2^- PE spectrum, while ~ 0.1 eV shift is observed upon increasing the cluster size. Aside from the shifts, the shapes of the PE spectra of $(\text{O}_2)_n^-$ ($n = 3-5$) resemble that of O_4^- . These results, as with previous studies of thermochemical data¹⁰, photoelectron spectroscopy¹¹ and matrix isolation²¹, are consistent with the structure of the core being O_4^- solvated with neutral O_2 molecules.

Figure 3.3 shows the 2-D representation of the change in time of the electron binding energy (BE): The photon energy ($h\nu$) = BE + KE (kinetic energy). For all BEs, the temporal behavior is similar, displaying two distinct timescales; at lower BE, the behavior is that of a bi-exponential rise, while at higher BE, it becomes more of a decay transient due to the shift of the PE with size (see Fig. 3.2). We also recorded the entire

PE spectra for O_6^- , O_8^- and O_{10}^- as a function of time (not shown). We clearly see the increase of the envelope intensity upon going to longer delay times, and the envelope is in the energy range of O_2^- , consistent with its direct production. The O_2^- is vibrationally-excited, especially from O_6^- , in agreement with previous nanosecond work.¹²

The femtosecond transients of nascent O_2^- and the parent ion are shown in Figure 3.4. The transient was recorded by gating either at the positive intensity envelope of O_2^- (build-up) or at the negative intensity signal of the parent (O_2)_n⁻ (decay). Care was taken to exclude possible contributions of O_4^- fragments in the case of O_8^- and O_{10}^- by adjusting the position of the gate. All transients, including the decay of the parent (O_8^-), exhibit two distinct exponential components. The time constants differ by a factor of 6-10, and both time constants increase as the cluster size increases.

To quantify the analysis we fitted the data to a bi-exponential rise (or the parent decay), varying the amplitudes (A_1 and A_2) and time constants (τ_1 and τ_2); the response function, using the autocorrelation pulse measurement (FWHM: 100 ± 5 fs), was also included. The results are shown in Figure 3.4: For O_6^- , $\tau_1 = 110$ fs, $\tau_2 = 700$ fs, γ ($\equiv A_1/A_2$) = 4; for O_8^- , $\tau_1 = 230$ fs, $\tau_2 = 2400$ fs, $\gamma = 2.7$; for O_{10}^- , $\tau_1 = 420$ fs, $\tau_2 = 2700$ fs, $\gamma = 1.65$.

Based on studies of the power dependence of the pump pulse, the possibility of multiphoton processes was excluded because of the following: First, we observed a slope of ~ 0.5 in the plot of $\log(\text{signal})$ vs. $\log(I_{\text{pump}})$, consistent with previous nanosecond work¹¹, indicating a one-photon absorption (linear) and one-photon absorption/one-photon depletion by the same 800 nm wavelength; if two 800 nm pump photons are involved in the dissociation of the cluster (followed by 400 nm probe photodetachment of

O_2^-), then the slope will be ≥ 1 , maximum 2. Second, we also recorded the transient behavior at half the pump power and observed the same transients. Third, if the fast component is due to two pump photons to the higher-energy repulsive potential, we do not expect the dramatic change observed for the rates of O_6^- , O_8^- and O_{10}^- . Accordingly, the transient signal reported here is for a one-photon excitation at 800 nm, followed by a one-photon detachment at 400 nm (generated by SHG).

3.4. Discussion

The temporal behavior (with energy resolution) and the observed trends for the three solvated species, O_6^- , O_8^- and O_{10}^- , elucidate the presence of two pathways in the mechanism of cluster-ion fragmentation and solvent evaporation. The equilibrium structure of these clusters is not known, but experimental^{11,12} and *ab initio*²² calculations indicate that a core O_4^- is involved as a building block with solvation by neutral O_2 increasing as the cluster size increases. In O_6^- and larger clusters it has been shown by the Johnson's group that charge-transfer takes place, and in these clusters they observed photodissociation following infrared excitation at 1064 nm; since the spectrum of O_4^- and O_2^- do not show absorption in this region, the behavior is consistent with a charge transfer excitation.

The femtosecond excitation launches a wave packet in all of nuclear space. We only consider the relevant nuclear coordinates shown in Figure 3.5, for O_6^- . These are the O_2 – O_2 separations of O_4^- and the O_2^- separation from O_4 . The bifurcation of the wave packet is considered following the initial preparation from the strongly bound O_4^- core to O_2 . The influence of solvation by additional O_2 molecules on the nuclear motion is

illustrated by the caging barrier, schematically presented in Figure 3.5 at a long O_2 – O_2 distance.

Upon femtosecond excitation, electron transfer (ET) from the O_4^- core to the O_2 solvent occurs, with O_2^- vibrationally excited (see section III). This state of O_2^- can relax, either via autodetachment to form ground-state O_2 ($O_2^- \rightarrow O_2 + e^-$) or via coupling with O_4 , now-neutral core^{8,11,23} the autodetachment channel will not give a time-dependent rising signal as no photodetachment of O_2 will be possible. Thus the observed transient in this channel reflects the dynamics of O_2^- liberation. The importance of electron recombination (ER) has been recognized before in femtosecond dynamics of charge-transfer reactions.^{15,16} After charge-transfer excitation, back electron transfer to the O_4 core populates the excited complex onto a repulsive state which is not directly accessible by optical excitation in O_4^- at this wavelength. This repulsion leads to direct dissociation of the O_4^- core ion and the wave packet rapidly enters the region where the photodetachment signal of O_2^- is produced in 110 fs for O_6^- . This reaction path is depicted on the right hand side of Figure 3.5.

The other trajectories of the dynamics result from the bifurcation of the wave packet following electron transfer. Upon the formation of $O_2^-O_4$ by ET, the species must execute nuclear motions in order to break bonds along the ion induced-dipole coordinate corresponding to the O_2^- – O_4 reaction path (Fig. 3.5). The ps time scale reflects the dynamics of vibrational energy transfer in the solvent evaporation process. One more consideration must be addressed. As shown in Figure 3.2, O_2^- in our source exhibits a small amount of a hot band, reflecting a vibrational temperature roughly 800 K. If O_6^- produced in the source has a similar temperature, then the thermal averaging could in

principle give the appearance of a nonexponential rise. However, this is only expected when a near barrier crossing is involved.²⁴

For the two processes discussed above, it is expected that the degree of vibrational excitation in O_2^- should be somewhat different. However, we only monitor the vibrational changes in O_2^- as probed by its photoelectron-kinetic energy; the actual translational energy change in the recoil process, which can be observed in kinetic energy time of flight¹⁵, is not directly monitored here.

Solvation in the larger-sized clusters can be understood with the above picture in mind. The most noticeable experimental observation is the increase of both time constants with increasing cluster size, and the decrease in γ , the ratio of the amplitudes of the fast to slow components. The fast component is doubled in value for each additional solvent molecule, whereas the time constant for the slow component increases by a factor of three on going from O_6^- to O_8^- and then stays about the same, within the error bars, on going from O_8^- to O_{10}^- . As mentioned before, substantial vibrational cooling is observed for O_2^- from O_8^- or O_{10}^- as compared to O_6^- (from the PE spectra), which suggests that collisions between O_2^- and O_2 are effective during the reaction. Accordingly, in the case of core O_4^- dissociation resulting from electron recombination, the surrounding solvent O_2 molecules strongly influence the dissociation dynamics. This effect is visualized in terms of the kinematics of a collision with the solvent barrier (Fig. 3.5). The presence of solvent barrier also explains the observation of an increase in O_4^- fragment intensity for the larger clusters (Fig. 3.1B). On the other hand, for the slow channel, the time scale is dictated by the transfer of energy to the solvent and this evaporation-type process is

relatively slow and is not surprising that it does not change dramatically upon going from O_8^- to O_{10}^- .²⁵

3.5. Conclusion

The complexity of the reaction pathways for the ionic reaction of oxygen clusters is simplified by resolving in time and energy the photoelectron spectra of nascent and parent ions. We elucidate the role of electron transfer, electron recombination and nuclear motions on the femtosecond time scale. The stepwise solvation effect on reaction dynamics was also elucidated in this picture of wave packet bifurcation and solvent energy barrier. Future work will detail studies of solvation and will increase the photoelectron resolution in order to study vibrational structures near the transition state.

References

- ¹ A. W. Castlemann, Jr. and K. H. Bowen, *J. Phys. Chem.* **100**, 12911 (1996), and references therein.
- ² M. Nadal, S. Nandi, P. Wenthold, J. Kim, L. J. Andersen, Y. Ozaki, D. W. Boo, and W. C. Lineberger, in *Femtochemistry and femtobiology: ultrafast reaction dynamics at atomic-scale resolution: Nobel symposium 101*, edited by V. Sundström (Imperial college press, London, 1997), and references therein.
- ³ A. H. Zewail, *Angew. Chem. Int. Ed.* **39**, 2586 (2000), and references there in.
- ⁴ T. Tsukuda, M. A. Johnson, and T. Nagata, *Chem. Phys. Lett.* **268**, 429 (1997).
- ⁵ M. J. DeLuca and M. A. Johnson, *Chem. Phys. Lett.* **162**, 445 (1989).
- ⁶ P. Ayotte and M. A. Johnson, *J. Chem. Phys.* **106**, 811 (1997).
- ⁷ L. A. Posey, M. J. DeLuca, and M. A. Johnson, *Chem. Phys. Lett.* **131**, 170 (1986).
- ⁸ R. Li, K. A. Hanold, M. C. Garner, A. K. Luong, and R. E. Continetti, *Faraday Discuss.* **108**, 115 (1997).
- ⁹ S. Matejcik, P. Stampfli, A. Stamatovic, P. Scheier, and T. D. Märk, *J. Chem. Phys.* **111**, 3548 (1999).
- ¹⁰ K. Hiraoka, *J. Chem. Phys.* **89**, 3190 (1988).
- ¹¹ M. J. DeLuca, C.-C. Han, and M. A. Johnson, *J. Chem. Phys.* **93**, 268 (1990).
- ¹² C.-C. Han and M. A. Johnson, *Chem. Phys. Lett.* **189**, 460 (1992).
- ¹³ L. Lehr, M. T. Zanni, C. Frischkorn, R. Weinkauff, and D. M. Neumark, *Science* **284**, 635 (1999).
- ¹⁴ G. Ganteför, S. Kraus, and W. Eberhardt, *J. Electr. Spectr. Rel. Phen.* **88-91**, 35 (1998).
- ¹⁵ P. Y. Cheng, D. Zhong, and A. H. Zewail, *J. Chem. Phys.* **105**, 6216 (1996).
- ¹⁶ D. Zhong, T. M. Bernhardt, and A. H. Zewail, *J. Phys. Chem. A* **103**, 10093 (1999).
- ¹⁷ R. Weinkauff, K. Walter, C. Weickhardt, U. Boesl, and E. W. Schlag, *Z. Naturforsch.* **44a**, 1219 (1989).

- ¹⁸ B. Ernstberger, H. Krause, A. Kiermeier, and H. J. Neusser, *J. Chem. Phys.* **92**, 5285 (1990).
- ¹⁹ P. Kruit and F. H. Read, *J. Phys. E: Sci. Instrum.* **16**, 313 (1983).
- ²⁰ O. Cheshnovsky, S. H. Yang, C. L. Pettiette, M. J. Craycraft, and R. E. Smalley, *Rev. Sci. Instrum.* **58**, 2131 (1987).
- ²¹ G. V. Chertihin and L. Andrews, *J. Chem. Phys.* **108**, 6404 (1998).
- ²² J. A. A. Aquino, P. R. Taylor, and S. P. Walch, *J. Chem. Phys.* **114**, 3010 (2001).
- ²³ The excited O_2^- ions with $v'' \geq 4$ can undergo autodetachment since $v'' = 4$ state of O_2^- is higher than $v' = 0$ state of O_2 neutral. With pump pulse only, we observed the autodetachment signal of nascent O_2^- generated from the $(O_2)_n^-$ dissociation at 800 nm.
- ²⁴ N. F. Scherer and A. H. Zewail, *J. Chem Phys.* **87**, 97 (1987).
- ²⁵ M. Gutmann, D. M. Willberg, and A. H. Zewail, *J. Chem. Phys.* **97**, 8048 (1992).
- ²⁶ M. Allan, K. R. Asmis, D. B. Popović, M S., M. Stepanović, Nigel J. Mason, and J. A. Davies, *J. Phys. B: At. Mol. Opt. Phys.* **29**, 3487 (1996)

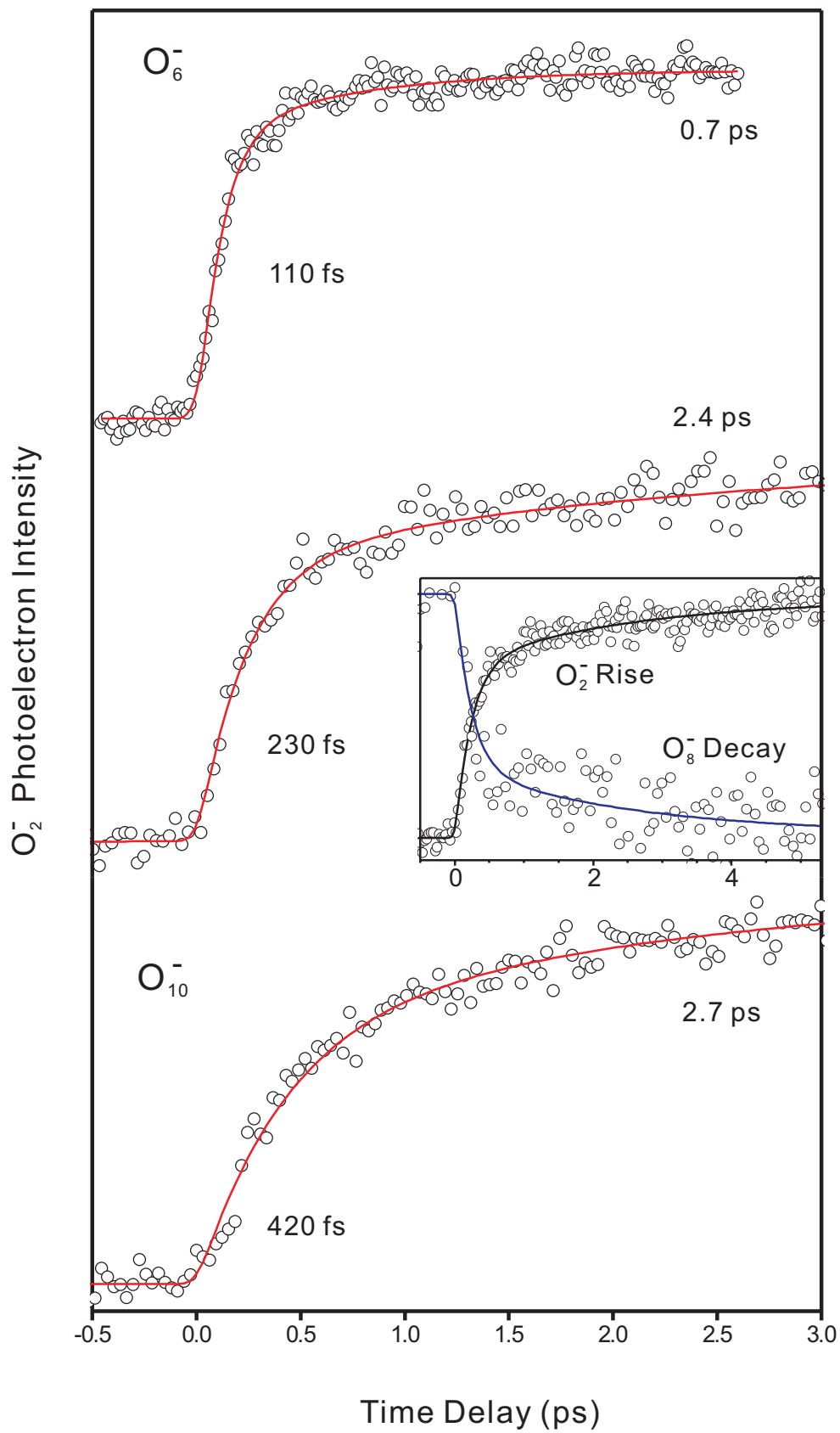


Figure 3.4

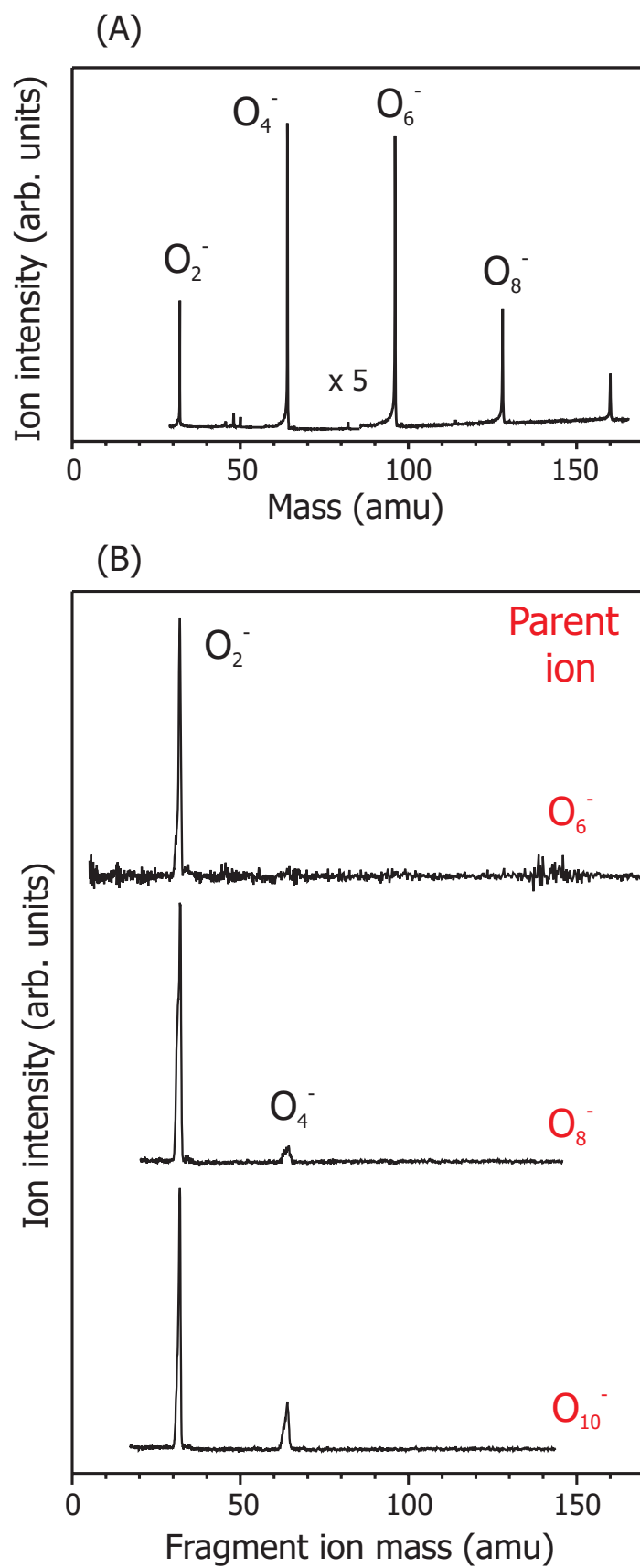


Figure 3.1

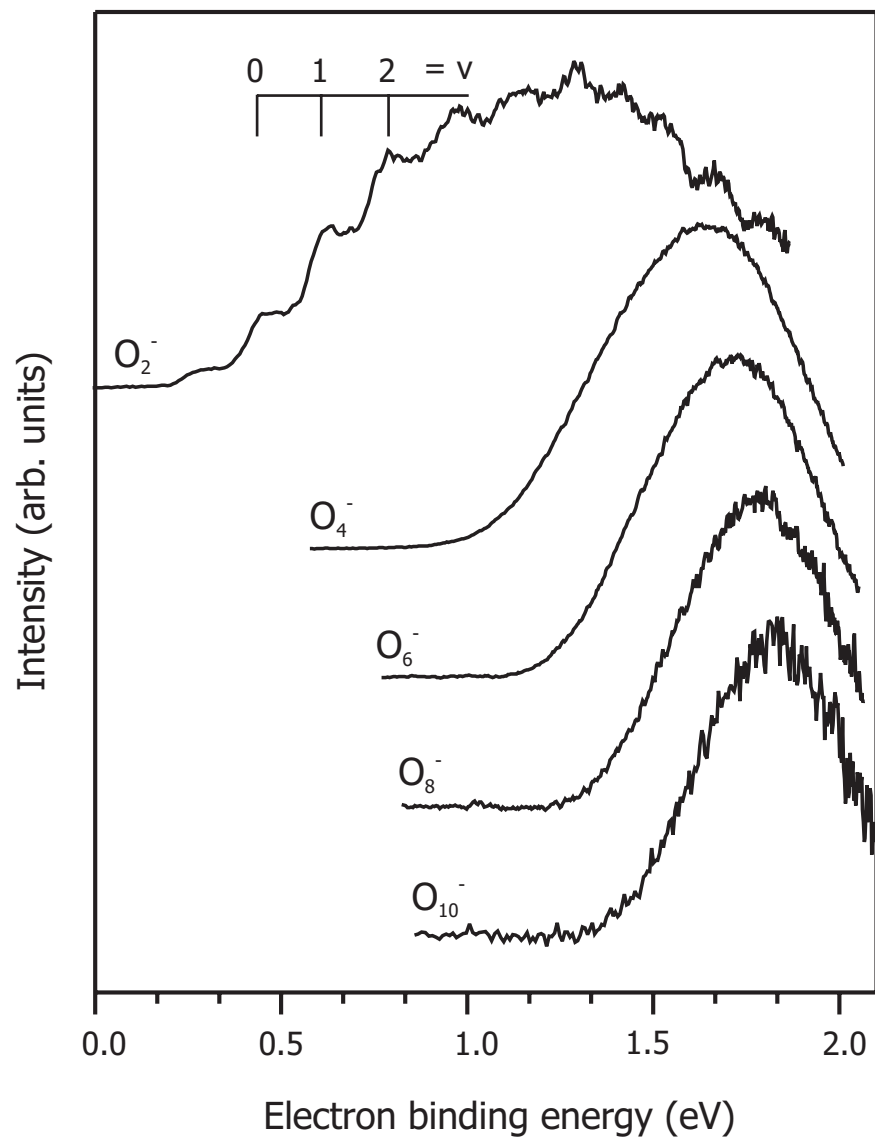


Figure 3.2

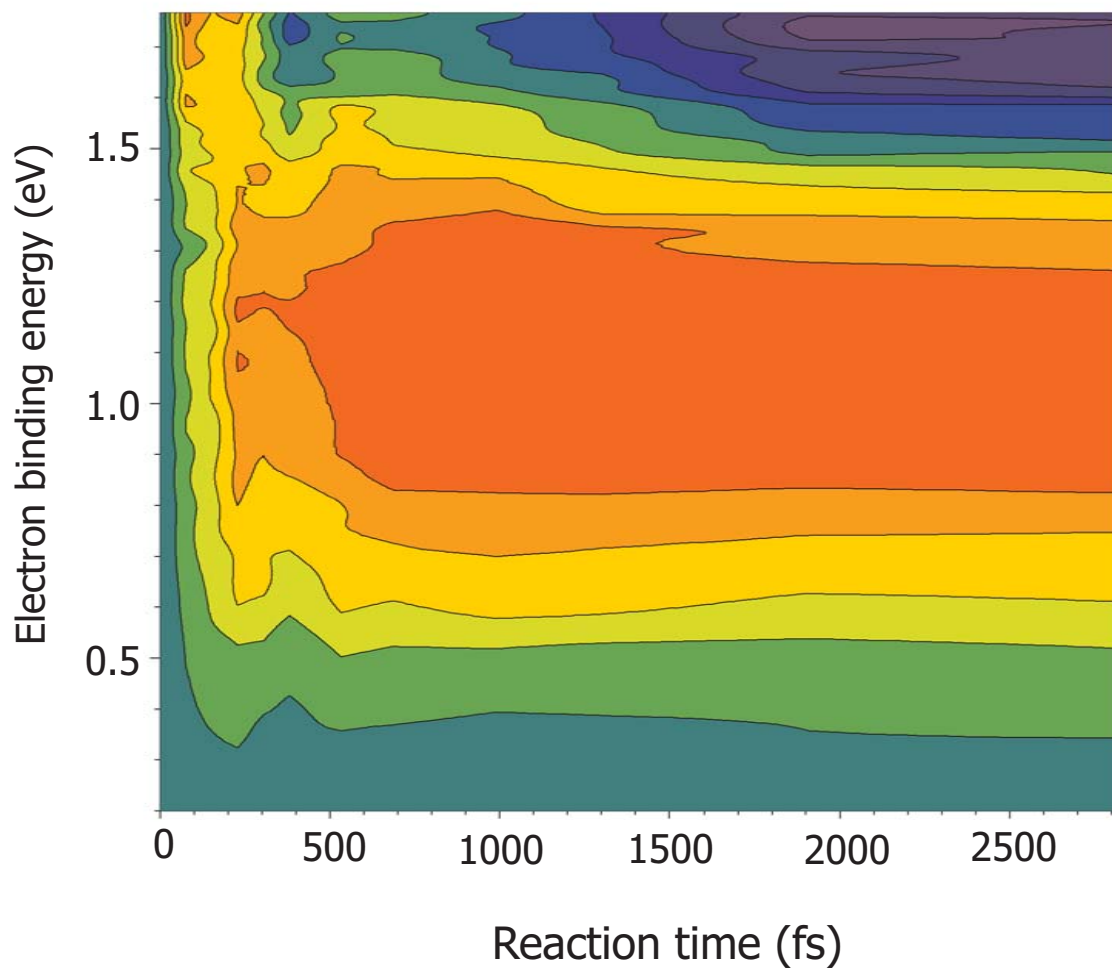


Figure 3.3

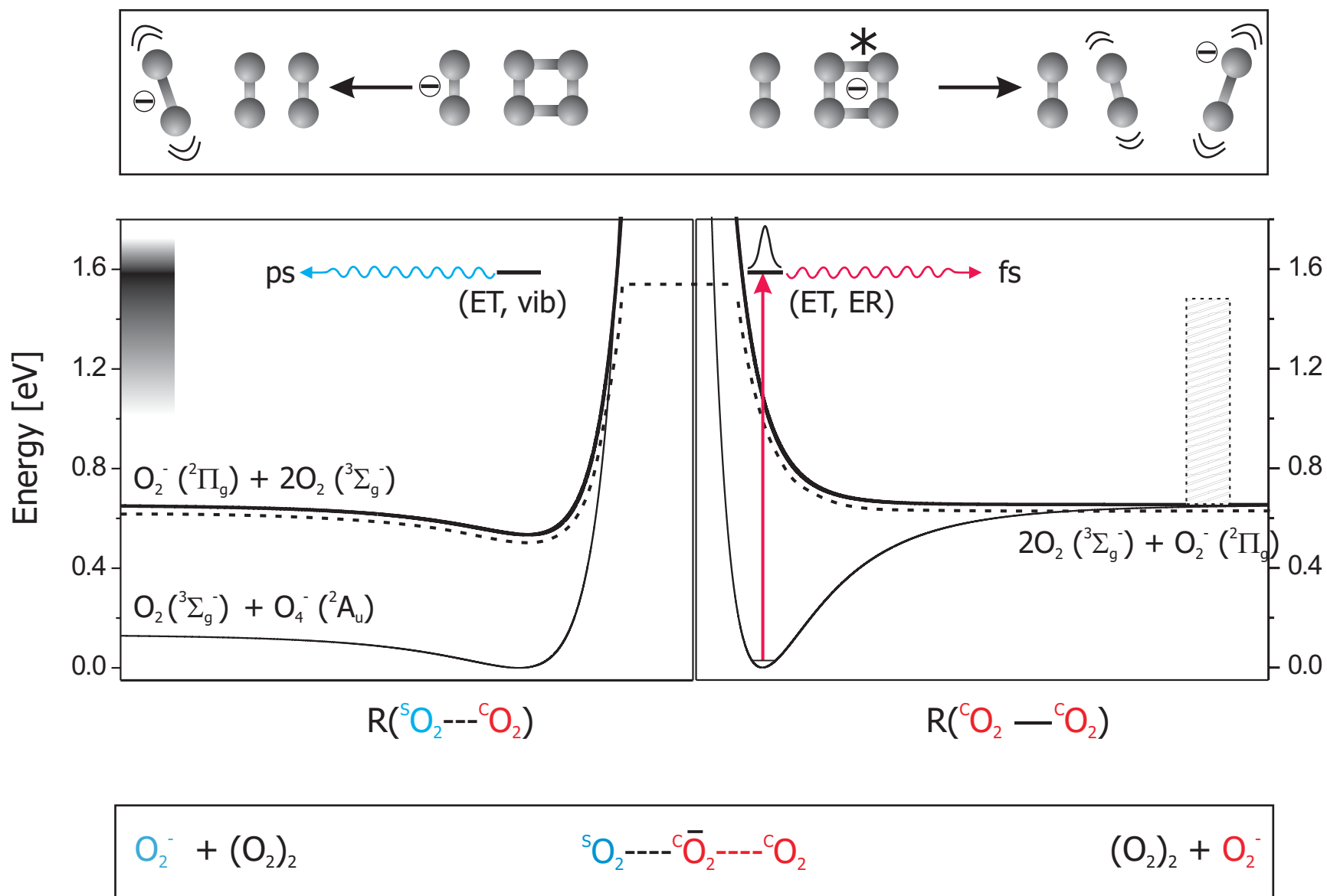


Figure 3.5

Figure captions

Figure 3.1

(A) Mass spectrum of anionic oxygen clusters generated by the ion source.

(B) Fragment ion mass spectra recorded utilizing the linear reflectron mass spectrometer.

The parent cluster size of the corresponding fragment spectrum is indicated on the right of each trace.

Figure 3.2

Photoelectron spectra at 3.1 eV laser energy (400 nm) of all investigated $(\text{O}_2)_n^-$ clusters.

The vibrational progression indicated in the O_2^- photoelectron spectrum originates from the $\text{O}_2 \text{X}^3\Sigma_g^- (v') \leftarrow \text{O}_2^- \Pi_g (v''=0)$ transition.¹¹

Figure 3.3

Two-dimensional contour plot of time-dependent photoelectron spectrum of the nascent O_2^- generated from the O_{10}^- dissociation, $\text{O}_{10}^- \rightarrow \text{O}_2^- + 4\text{O}_2$. In the contour plot, the intensity profile is indicated by the gray scale: The bright gray region in the contour plot corresponds to the positive envelop of the photoelectron spectrum, while the dark gray region indicates the negative envelop. Note that the contour is constructed from the total time-dependent signal (pump + probe) minus that of the reference (pump + probe) at $t = 0$.

Figure 3.4 Femtosecond transients of the $(\text{O}_2)_n^-$ photodissociation reaction at 800 nm excitation. Shown are the changes of the nascent O_2^- photoelectron signal as a function of the delay time between pump and probe laser pulses. We also display the parent ion decay signal as an inset for the case of O_8^- in order to compare with the product signal growth. All transient data are well fitted by a bi-exponential function, and the error bars are typically ± 50 fs for the fast component and ± 200 fs (for O_6^-) to ± 500 fs (for O_{10}^-) for the slow component. Note that the signal depicts a rise and any autodetachment of O_2^- to O_2 would appear as a decay at long times (see Ref. 26); the autodetachment threshold is at $v''=4$ of O_2^- and our O_2^- photoelectron spectra terminates near $v''=3$, confirming negligible population for observation of autodetachment.

Figure 3.5

A representation of two cuts in the O_6^- potential energy surface. On the left hand side of the figure, the potential is along the nuclear coordinate between the solvent O_2^- and core O_4 ($^{\text{S}}\text{O}_2 \cdots ^{\text{C}}\text{O}_2$); charge induced-dipole interaction. On the right hand side, the potential for the separation ($^{\text{C}}\text{O}_2 - ^{\text{C}}\text{O}_2$) of O_2^- from O_2 in core O_4^- is displayed; the solvent neutral O_2 is considered as a spectator, thus the dissociation energy of O_6^- (0.63 eV) is plotted in the asymptote even though O_4^- dissociation energy is 0.52 eV.¹¹ Note that the reaction in the box at the bottom implies symmetry along the dotted potential path, but because of the stability of O_4^- in contrast with O_4 there is some asymmetry (see references 8 and 22 for theoretical *ab initio* calculations). The hatched area in this panel represents the solvent barrier responsible for caging. The wave packet is launched as indicated, and the bifurcation is illustrated by the dotted path. The estimated energy range of the charge

transfer band is shown on the energy axis to the left; the width is determined by the range between the adiabatic electron affinity and vertical detachment energy of O_6^- , similar to estimates made for other systems.⁵

CHAPTER 4.

Femtosecond Dynamics of Solvated Oxygen Anions: Bifurcated Electron Transfer Dynamics Probed by Photoelectron Spectroscopy

4.1 Introduction

Studies of size-selected clusters provide valuable insights on the nature of solute-solvent interactions, with the hope of bridging the gap between the isolated gas-phase and condense-phase dynamics. These microscopic solvation processes, which may involve energy redistribution, electron transfer and vibrational predissociation, have been examined in a variety of ionic¹⁻⁸ and neutral⁹⁻¹³ clusters.

In the previous chapter, we reported on studies of O_2^- clusters, and in this paper we give a full account of the study and extend the scope to include clusters of O_6^- with a variety of solvents, $X = O_2, N_2, Xe$ or N_2O . Specifically, we report on the femtosecond (fs) time-resolved photoelectron (PE) spectra. The number of solvent molecules studied here is always one while in the accompanying paper the O_2 solvent composition varies from 3 to 10. These clusters are unique for a number of reasons: First, the O_6^- cluster is composed of the O_4^- core surrounded by a neutral O_2 molecule. Second, upon irradiation with 800 nm fs pulse, electron migrates from the O_4^- core to the neutral O_2 molecule; subsequently, an O_2^- fragment is generated via two different channels, as discussed in the previous chapter. The solvent, N_2, Xe or N_2O is weakly bound to the O_4^- core and not directly involved in electron migration process, as evidenced from the photoelectron spectra and the nascent fragments produced. Finally, for these clusters we can follow the change of the PE spectra with time.

In the present work, we examine the effect of the solvent on the observed rise of O_2^- and the change of the photoelectron spectra of $O_6^- \cdot X$. We consider the bifurcation of the initial wave packet to produce O_2^- in two channels and we compare the observed rates to calculations based on the statistical (RRKM) theory for the dissociation of $O_6^- \cdot X$,

through vibrational-energy redistribution, and the prompt dissociation through back electron transfer. Strong solvent dependence was evident in both the rates and the contribution of population in both channels.

4.2. Experimental

Negative ions were produced by a pulsed electron impact source. The pulsed supersonic expansion was crossed with 1.0 keV electron pulse (1.0 ms), and anions were produced by the secondary electron attachment. The ions passing through the skimmer (1.5 mm hole) were then accelerated to the field free region by applying electric pulse (-2.0 kV) to the two-stage repeller.¹⁴ The electric potential of the second stage repeller is adjusted so that the focus along the time-of-flight axis of the ion bunches is at the laser interaction region. The ions spatial distribution (perpendicular to the time-of-flight axis) was focused at the center hole of the MCP using an Einzel lens. A set of horizontal and vertical deflection plates were used to steer the ion beam.

In the field-free region, the ion bunches were separated by their masses, and the mass of interest was selected by the interleaved-comb massgate¹⁵ which provides a mass selection, by applying a high electric field (1.0 kV/1.0 mm) between two alternating wires. After mass selection, the ion bunch was intercepted with the femtosecond laser pulses, and the photoelectrons were collected by the magnetic bottle photoelectron spectrometer.¹⁶ The photofragments were detected by the linear reflectron time-of-flight mass spectrometer.¹⁷

Femtosecond laser pulses (110 fs, 800 nm) were generated from a Ti:Sapphire oscillator which was optically pumped by the second harmonic (532 nm) of a cw

Nd:YAG laser. The oscillator output was then amplified by the regenerative and multipass amplifiers. The amplified 800 nm light (20 Hz) was frequency doubled by a BBO crystal to generate 800 μ J of the 400 nm light. The remaining 800 nm output (1.5 mJ) was used as the pump pulse for photodissociating $O_6^- \cdot X$ clusters, while the 400 nm laser pulse was used as probe for photodetaching nascent anionic fragments. Black anodized light baffles were installed in order to reduce the background noise generated from the scattered light. In order to prevent multiphoton processes while maximizing the overlap between the laser pulse and ion beam, the laser beam waist was collimated only to 5 mm diameter. We also studied the power dependency (see paper II).

The $O_6^- \cdot X$ ($X = N_2, Xe$ or N_2O) anionic clusters were generated by crossing the electrons (1 keV) with the gas mixture of approximately 90 % of oxygen and 10 % of solvents (N_2, Xe or N_2O). The mixing ratio was maintained constant by utilizing mass flow controllers. The residual water trace was removed by passing the gas mixture through a cryotrap of -50 $^{\circ}C$.

4.3. Results

Figure 4.1 shows the mass spectra of $O_6^- \cdot X$ ($X = N_2, Xe$ or N_2O) recorded under the optimal ion-source conditions for generating $O_6^- \cdot X$. In this figure we show the clusters formed under our expansion conditions. The dominance of O_4^- and $O_4^- \cdot X$ indicates that the solvent is attached to the O_4^- core. Similar to our previous observation with O_6^- and higher clusters, upon irradiation by a 800 nm fs pulse, the $O_6^- \cdot X$ clusters produced the O_2^- fragment, whereas $O_4^- \cdot X_n$ ($n = 1,2; X = N_2, Xe$ or N_2O) did not generate any negatively charged fragment. This suggests that $O_4^- \cdot O_2$, not $O_4^- \cdot X$, is the essential

chromophore for the interaction with the 800 nm pulse. We did not observe the O_4^- fragment when the 800 nm pulse was used to excite $O_6^- \cdot X$ ($X = N_2, Xe$ or N_2O); for $O_6^- \cdot O_2$, a small amount of the O_4^- fragment was observed. The broad peaks of $O_4^- \cdot Xe$ and $O_6^- \cdot Xe$ are due to the presence of $^{128-136}Xe$ isotopes. In our experiment, $O_6^- \cdot ^{132}Xe$ was selectively intercepted with the laser pulse in order to avoid irradiating O_{14}^- whose mass is identical to $O_6^- \cdot ^{128}Xe$. This selection was verified by monitoring the depletion of the $O_6^- \cdot ^{132}Xe$ ion intensity in the reflectron time-of-flight mass spectrometer (not shown). Moreover, the absence of O_{14}^- in the interaction region between the laser and the ion beam was confirmed by comparing the $O_6^- \cdot Xe$ and O_{14}^- transients.

The photoelectron spectra of $O_6^- \cdot X$ at 400 nm (3.1 eV) are shown in Fig. 4.2A. The shapes of spectra resemble the photoelectron spectrum of O_6^- , but both the peak (vertical detachment energy (VDE)) and the onset (adiabatic electron affinity (AEA)) are shifted toward higher electron binding energies. The resemblance of the photoelectron profiles suggests that the solvent is attached to O_6^- by a weak interaction without altering its chemical properties. The increase in binding energy corresponds to the stabilization energy by the solvent X. Among the solvent molecules, O_6^- is stabilized most by N_2O and stabilized least by O_2 . We note that among the solvents, N_2O is the only one that has a dipole moment. The stabilization energy [$E_{st} = VDE(O_6^- \cdot X) - VDE(O_6^-)$] is listed in Table I, together with the literature values for the dipole and quadrupole moments and polarizabilities.^{8,18-21}

Figure 4.2B shows the photoelectron signals of $O_6^- \cdot X$ when the probe (400 nm) arrived 14 ps after the pump (800 nm). The pump/probe photoelectron spectra exhibit two peaks. The new peak (in contrast with 400 nm pulse only) at lower binding energy

corresponds to the photoelectron signal of the nascent O_2^- fragment which is dissociated from $O_6^- \cdot X$ by the 800 nm pulse. From the observed curve and knowledge of the position of the (0,0) and hot (0,1; 0,2 and 0,3) bands of O_2^- , we can estimate the relative population of the hot bands (see Fig 4.2B and ref. 22), and obtain the effective temperature; the Franck-Condon factors were deduced from a Morse potential approximation²³. The hot band tail was fitted with Gaussian functions with FWHM = 0.17 eV (our instrument resolution), and from the temperature values, the average internal energy ($k_B T$) of the nascent O_2^- was deduced.

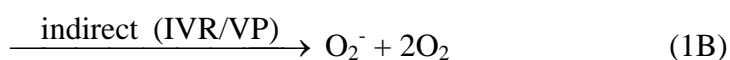
The onset of O_2^- generated from the dissociation of $O_6^- \cdot X$ are shifted toward a higher electron binding energy, when compared to the onset of O_2^- dissociated from O_6^- . The observed shift in Fig. 4.2B reflects the cooling of the nascent O_2^- fragment from parent $O_6^- \cdot X$. The degree of cooling varies with clusters $O_6^- \cdot X$ ($X = O_2, N_2, Xe$ or N_2O) as evident by the trend. This behavior is schematically illustrated in Figure 4.3, and the estimated temperatures are given in Table I. Figure 4.3 emphasizes the sensitivity of photoelectron spectra to changes in binding and temperature of nascent O_2^- product.

Figure 4.4 shows the femtosecond transients of O_2^- generated from the $O_6^- \cdot X$ dissociation. The transients were recorded by integrating the photoelectron signal of O_2^- (see Fig. 4.2B) at different time delays between pump and probe pulses. They exhibit bi-exponential rises with two distinct time constants for all clusters, but the time constants and amplitude ratios vary depending on the solvent. The time constants (τ_1 and τ_2) and the amplitude ratios ($\gamma \equiv A_1/A_2$) were obtained by fitting the transient data with a bi-exponential growth function, and the values are tabulated in Table I. In this treatment, the response function was included using the autocorrelation function of our pulse width

(110 fs) at 800 nm, however, we also checked for the values of the fit without convolution and obtained similar values for τ_1 , τ_2 and γ , except for the 200 fs component which without convolution becomes somewhat longer. These experiments were repeated many times, and all show the same general trend: the slow component increases in contribution, and its time constant increases as the solvent was changed from N_2 to N_2O , with O_2 and Xe being in the middle. In Figure 4.5, we plot the changes in τ_2 for these different solvents and the dependence on cooling, as discussed below.

4.4. Discussion

From the above results we conclude that the dynamics of solvated O_6^- follows the same energy landscape as in the case of bare O_6^- – a bifurcation of the wave packet motion in two different channels. Upon excitation at 800 nm, the electron in $O_4^- \bullet O_2$ migrates from the core to the solvent forming the $O_4 \bullet O_2^-$ complex; subsequently, $O_4 \bullet O_2^-$ dissociates via two different channels with distinct time constants. The fast component ($\tau_1=110$ fs) represents the direct dissociation, following electron recombination (ER) of O_4^- core on a repulsive potential surface. The slow component ($\tau_2 = 700$ fs) involves intramolecular vibrational-energy redistribution (IVR)/vibrational predissociation (VP) to liberate the negatively charged O_2^- solvent molecule from the charge transferred $O_4 \bullet O_2^-$ complex. The two steps can be written as follows:



The solvation of O_6^- by O_2 , N_2 , Xe or N_2O does not form a new chemical species, as discussed above. Accordingly, the same mechanism holds for the motion of the wave packet represented on the potential energy curves in Figure 4.6. Upper panel shows the S_{N2} type reaction, while the middle panel depicts the two channels described by equation 1. The wave packet preparation and its subsequent bifurcation on the two different potential energy surfaces (direct and indirect) are on different time scales, femtosecond (fs) and picosecond (ps). In the lower panel, the direct (right) and indirect (left) trajectories are represented schematically in a configuration space.

When O_6^- is solvated by an additional molecule, the fast component (equation 1A) slows down to approximately 200 fs, and the rate is nearly the same, regardless of solvent molecule. This trend suggests that the fast component is not significantly influenced by the vibrational/rotational degrees of freedom and that the rate is determined by electron recombination (ER) and the kinematics of the half-collision. For dissociation on a repulsive surface, the nuclear motion is expected to occur on the time scale of 50–200 fs.²⁴ However, electron recombination in $O_4 \bullet O_2^-$ could occur on this time scale or longer.

For O_6^- , where electron recombination is resonant, the effective rate of electron recombination and subsequent nuclear motion is about 110 fs. Addition of the solvent, which breaks the resonance, could yield a factor of 2 lengthening of τ_1 . Therefore, τ_1 is the overall time constant corresponding to ER and subsequent nuclear motion. The contribution due to kinematics appears to be insignificant in our particular systems since τ_1 does not vary with the mass of solvent X. Furthermore, Continetti and his coworkers have shown that two O_2 solvent molecules around O_4^- act essentially as spectators in the process of O_8^- dissociative photodetachment.²⁵ However, as shown in the accompanying

paper this kinematic effect becomes more significant as the cluster considerably increases in size.

The slow time constant (τ_2) increases by a factor of 3 to 10 when O_6^- is solvated. The slow time constant for $O_6^- \cdot N_2$, $O_6^- \cdot O_2$ and $O_6^- \cdot Xe$ were approximately the same (~ 2.0 ps), but τ_2 of $O_6^- \cdot N_2O$ was about three times longer (7.7 ps); the slow component for O_6^- gives $\tau_2 = 0.7$ ps. As described in equation (1B), the rate of indirect dissociation is determined by IVR, and we expect that the degree of IVR would be different for $O_6^- \cdot X$ clusters, depending on the composition (monatomic Xe; diatomic O_2 and N_2 ; triatomic N_2O) and binding through low-frequency modes.

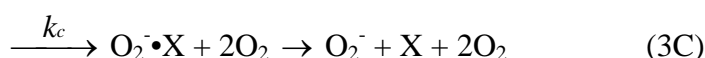
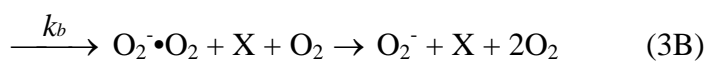
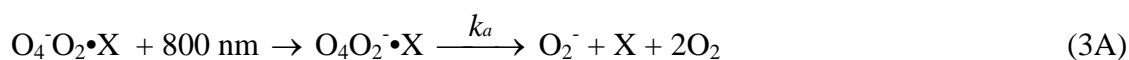
To examine the role of IVR, we made calculations of τ_2 using the statistical RRKM (Rice-Ramsperger-Kassel-Marcus) theory:

$$k = \sigma \frac{N^\#(E - D)}{h\rho(E)} \quad (2)$$

where σ is the degeneracy in the dissociation, h is Planck's constant, $N^\#(E - D)$ is the number of states at the transition state, and $\rho(E)$ is the density of states of the reactant at the total energy (see ref. 28). $N^\#(E - D)$ and $\rho(E)$ were approximated by using the intermolecular frequencies of $O_2^- \cdot X$. In other words, because the reaction coordinate on the excited potential involves $O_4O_2^- \cdot X$ we considered $O_2^- \cdot X$ for a full *ab initio* calculation and similarly for O_2^- with $2O_2$. The *ab initio* calculation was done using the unrestricted Hartree-Fock level of theory with 6-311+G* as the basis set. E is the energy of the excitation pulse minus the difference in energy (at the minimum of the potential) between

$O_2 \bullet O_4^-$ and $O_2^- \bullet O_4$. We took E to be the same for all clusters, since the stabilization by X is about the same for $O_2 \bullet O_4^-$ and $O_2^- \bullet O_4$.

In our calculations, three different dissociation channels were considered since all of them, shown below, can be observed in our probe window:



For $X = N_2$, Xe or N_2O , k_a , k_b and k_c were calculated using $\sigma = 1$, 2 and 1, respectively.

In the case of $X = O_2$, k_a and k_b were calculated using $\sigma = 1$ and 3. The τ_2 values calculated by the RRKM theory correspond to the reciprocal of the total rate constant ($k_{total} = k_a + k_b + k_c$). We found that k_b and k_c are dominant, consistent with the fact that the dissociation energy for 3(B) and 3(C) are smaller than that of 3(A). In the case of channel (3B) and (3C), subsequent dissociation of metastable $O_2^- \bullet X$ occurs. However, this subsequent dissociation will not appear in our transient because photoelectron signals of $O_2^- \bullet X$, as well as O_2^- , are integrated in our boxcar gate and the photodetachment cross section of O_2^- and $O_2^- \bullet X$ is about the same; the change from $O_2^- \bullet X$ to O_2^- is not sensitive enough to our probe. In all these calculations, the transition state was taken to be product-type, without variational adjustment.²⁶ The results show the trend shown in Figure 4.5 which parallels that of the experimental results, and the values are in Table I.

The amplitude ratio ($\gamma \equiv A_1/A_2$) varies as a function of the solvent X, which is also consistent with the solvent effect on the bifurcation process. Large γ value ($\gamma = A_1/A_2 > 1$) means that the direct process is more favored than the indirect one, and *vice versa*. The electron recombination (ER) is governed by the energetics of O_2^- and O_4 in the charge transferred $O_2^- \cdot O_4$ complex. The solvent effect on ER is mainly due to the dissipation of O_2^- internal energy to the solvent and the energetics. When the incipient O_2^- maintains its initial vibrational energy, electron recombination is most favored as observed in O_6^- ($\gamma = 4.0$). On the other hand, when O_2^- dissipates its internal energy to the solvent, the direct process decreases in contribution. Additionally, the energy between the HOMO of O_2^- and the LUMO of O_4 is influenced by the solvent and the gap increases as O_2^- becomes solvated. Thus, the amplitude ratio of the fast and slow component should be correlated, in part, to the degree of vibrational cooling.

A cooling factor can be defined to express the fraction of available energy that goes into the internal energy of O_2^- :

$$C = 1 - \frac{k_B T}{E - D_{(3A)}} \quad (4)$$

where k_B is the Boltzmann constant, T is the temperature of the nascent O_2^- fragment estimated from Figure 4.2B, E is defined above, and $D_{(3A)}$ is the dissociation energy of channel (4.2A). If O_2^- is very cold C goes to 1, and if it acquires most of the internal energy, C becomes 0. This trend is illustrated in the bottom panel of Figure 4.5 in which the branching ratio of the slow channel, $A_2/(A_1+A_2)$, is plotted against the cooling factor.

Among the solvents, the cooling factor of N₂O is larger than all others. The unique nature of N₂O compared to Xe, O₂ and N₂ is that O₂⁻•N₂O can effectively exchange energy via vibration-to-vibration and rotational couplings. The essential criteria of V-V transfer are near-resonance in energy and the infrared activity of the mode involved.^{27,28} Among the solvents studied, only N₂O fulfills these criteria.

4.5. Conclusion

We have investigated the solvent effect on O₆⁻ dissociation dynamics, and observed that the addition of one solvent (O₂, N₂, Xe or N₂O) gives very different effects on the dynamics of the nuclear motion, whose wave packet bifurcates in two channels. These real-time studies of the one-solvent dynamics provide the timescale for the distinctive processes of electron recombination and bond rupture, and vibrational predissociation – with both channels yielding O₂⁻. As with kinetic energy resolution²⁹, here the photoelectron resolution⁵ allows us to examine the dynamics following the bifurcation³⁰ in these pathways to O₂⁻. Manifestation of direct and indirect dissociations is clear in the change of the time scale with solvation, as the direct process is controlled by electron recombination and kinematics of the half collision, while the indirect process involves energy redistribution. We compare the experimental findings reported here with *ab initio* and statistical rate calculations in these finite-sized ionic clusters. These elementary processes observed in small clusters are expected to evolve as the number of solvent molecules increases, and this aspect will be discussed in the next chapter where we studied the homogeneous solvated and mass-selected (O₂)_n⁻, n = 3 to 10.

References

- ¹ A. W. Castleman, Jr. and K. H. Bowen, *J. Phys. Chem.* **100**, 12911 (1996), and references therein.
- ² A. Sanov, T. Sanford, S. Nandi, and W. C. Lineberger, *J. Chem. Phys.* **111**, 664 (1999), and references therein.
- ³ M. J. DeLuca, C.-C. Han, and M. A. Johnson, *J. Chem. Phys.* **93**, 268 (1990).
- ⁴ C.-C. Han and M. A. Johnson, *Chem. Phys. Lett.* **189**, 460 (1992).
- ⁵ B. J. Greenblatt, M. T. Zanni, and D. M. Neumark, *Science* **276**, 1675 (1997).
- ⁶ L. Lehr, M. T. Zanni, C. Frischkorn, R. Weinkauff, and D. M. Neumark, *Science* **284**, 635 (1999).
- ⁷ R. Li, K. A. Hanold, M. C. Garner, A. K. Luong, and R. E. Continetti, *Faraday Discuss.* **108**, 115 (1997).
- ⁸ K. Hiraoka, *Chem. Phys.* **125**, 439 (1988).
- ⁹ R. B. Gerber, A. B. McCoy, and A. Garcia-Vela, *Annu. Rev. Phys. Chem.* **45**, 275 (1994), and references therein.
- ¹⁰ D. M. Willberg, M. Gutmann, J. J. Breen, and A. H. Zewail, *J. Chem. Phys.* **96**, 198 (1992).
- ¹¹ M. Gutmann, D. M. Willberg, and A. H. Zewail, *J. Chem. Phys.* **97**, 8037 (1992).
- ¹² D. M. Willberg, M. Gutmann, E. E. Nikitin, and A. H. Zewail, *Chem. Phys. Lett.* **201**, 506 (1993).
- ¹³ Q. Liu, J.-K. Wang, and A. H. Zewail, *Nature* **364**, 427 (1993).
- ¹⁴ W. C. Wiley and I. H. McLaren, *Rev. Sci. Instrum.* **26**, 1150 (1955).
- ¹⁵ R. Weinkauff, K. Walter, C. Weickhardt, U. Boesl, and E. W. Schlag, *Z. Naturforsch.* **44a**, 1219 (1989).
- ¹⁶ P. Kruit and F. H. Read, *J. Phys. E: Sci. Instrum.* **16**, 313 (1983).
- ¹⁷ B. Ernstberger, H. Krause, A. Kiermeier, and H. J. Neusser, *J. Chem. Phys.* **92**, 5285 (1990).
- ¹⁸ A. G. Khrapak and K. F. Volykhin, *J. Exp. Theo. Phys.* **88**, 320 (1999).

- ¹⁹ L. H. Scharpen, J. S. Muentner, and V. W. Laurie, *J. Chem. Phys.* **53**, 2513 (1970).
- ²⁰ A. D. Buckingham, C. Graham, and J. H. Williams, *Mol. Phys.* **49**, 703 (1983).
- ²¹ Atomic and molecular polarizabilities, in *CRC Handbook of Chemistry and Physics*, 82 ed., edited by D. R. Lide (CRC Press, Boca Raton, Florida, 2001), **10**-165.
- ²² D. Spence and G. J. Schulz, *Phys. Rev. A* **2**, 1802 (1970).
- ²³ S. Matejcik, P. Stampfli, A. Stamatovic, P. Scheier, and T. D. Märk, *J. Chem. Phys.* **111**, 3548 (1999).
- ²⁴ A. H. Zewail, *J. Phys. Chem. A* **104**, 5660 (2000).
- ²⁵ T. G. Clements and R. E. Continetti, *Phys. Rev. Lett.* **89**, 033005 (2002).
- ²⁶ T. Bear and W. L. Hase, in *Unimolecular Reaction Dynamics: Theory and Experiments* (Oxford University Press, Inc., New York, 1996).
- ²⁷ J. A. Mack, K. Mikulecky, and A. M. Wodtke, *J. Chem. Phys.* **105**, 4105 (1996).
- ²⁸ M. Silva, R. Johgma, R. W. Field, and A. M. Wodtke, *Annu. Rev. Phys. Chem.* **52**, 811 (2001).
- ²⁹ D. Zhong, T. M. Bernhardt, and A. H. Zewail, *J. Phys. Chem. A* **103**, 10093 (1999), and references therein.
- ³⁰ K. B. Møller and A. H. Zewail, in *Essays in Contemporary Chemistry: From Molecular Structure towards Biology*, edited by G. Quinkert and M. V. Kisakürek (Verlag Helvetica Chimica Acta, Zurich, 2001), pp. 157-188.

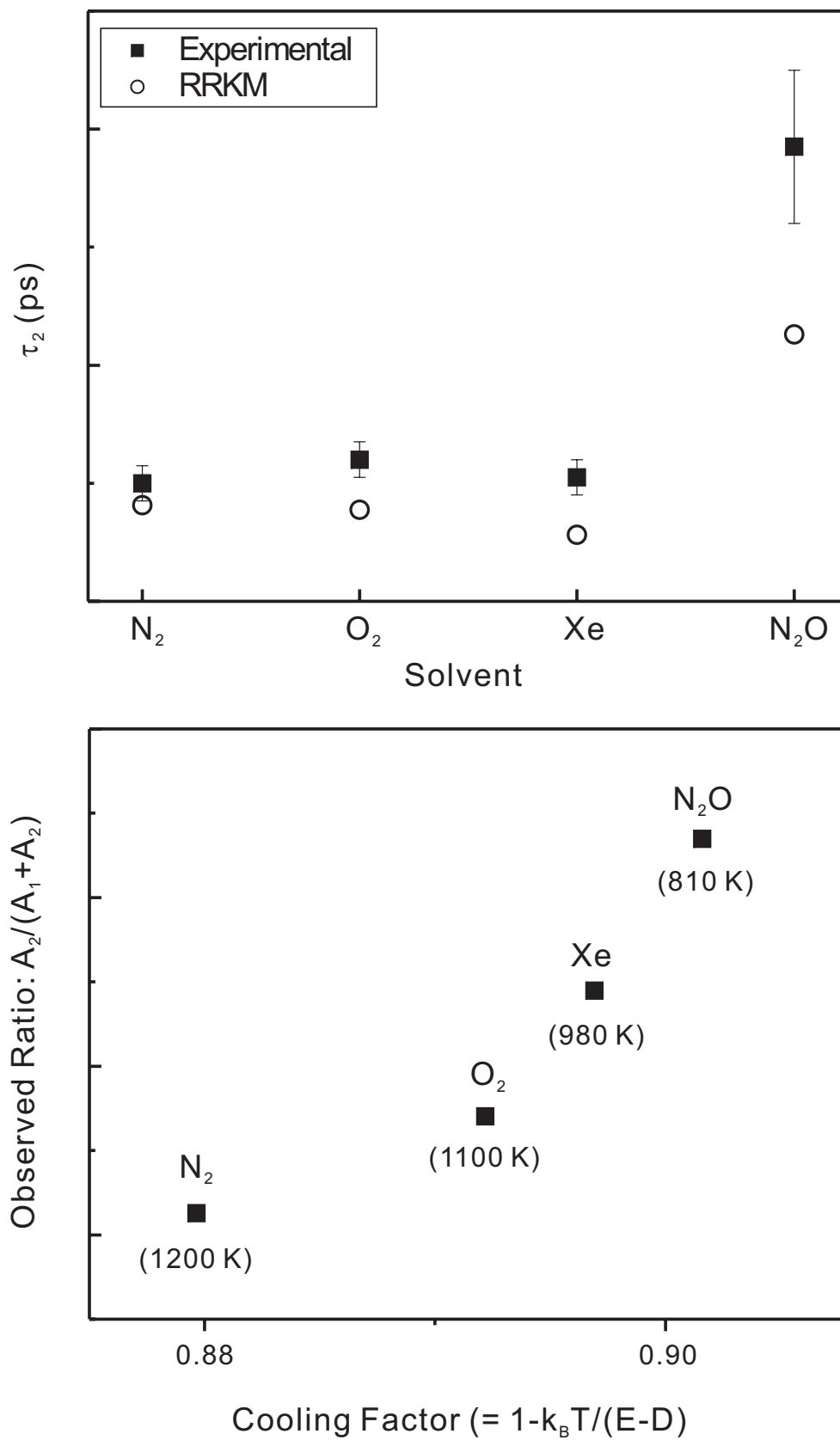


Figure 4.5

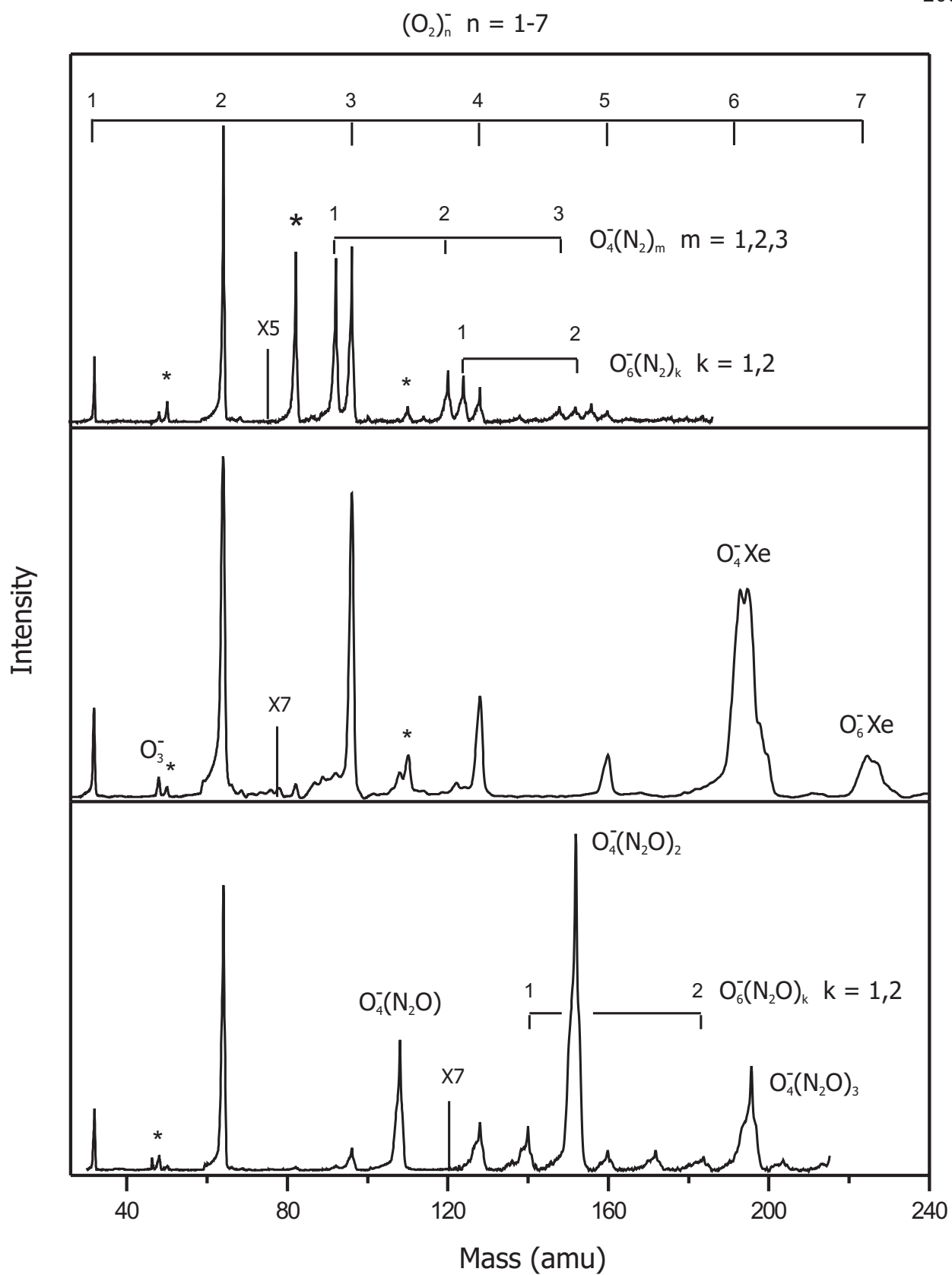


Figure 4.1

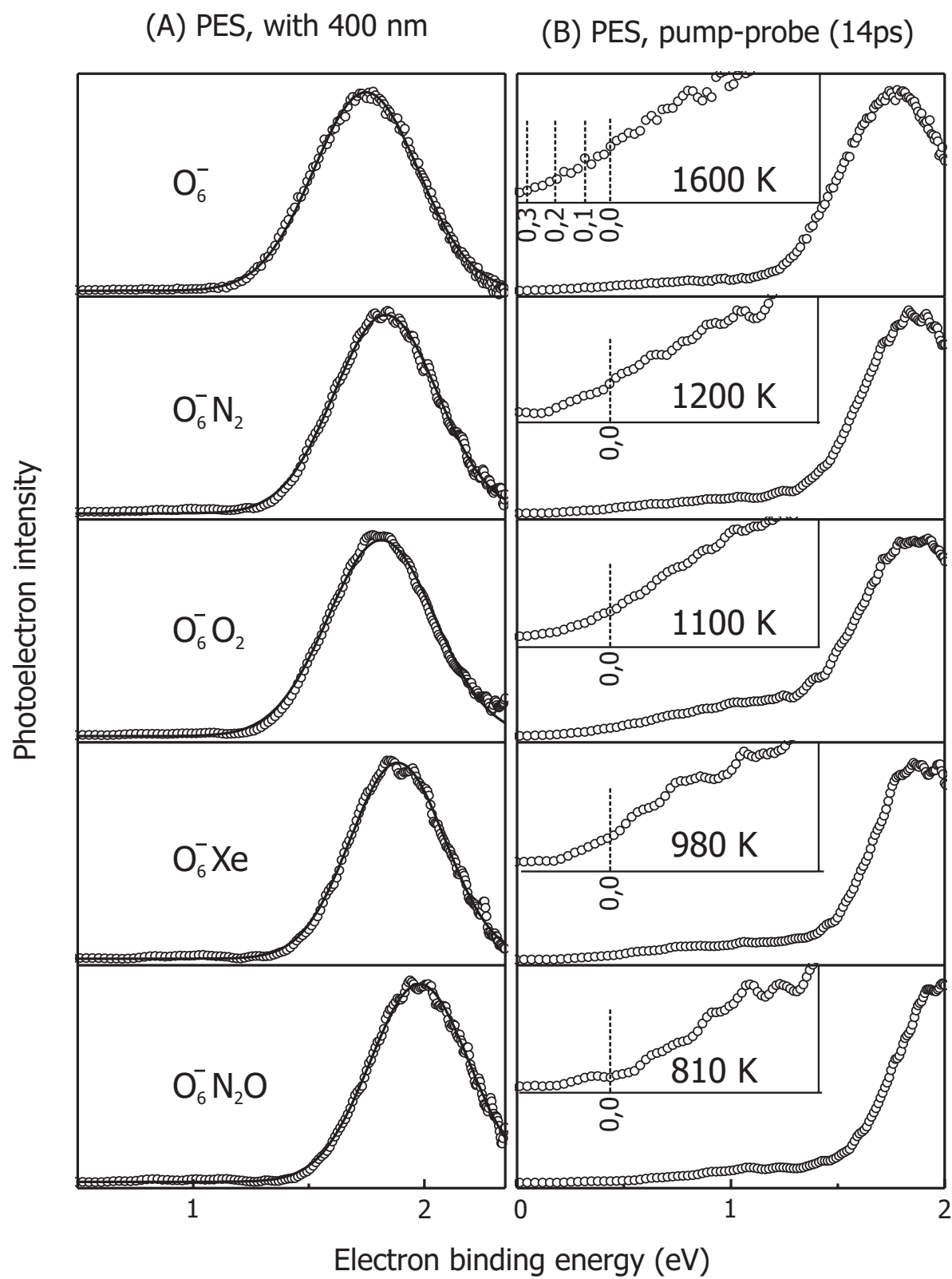


Figure 4.2

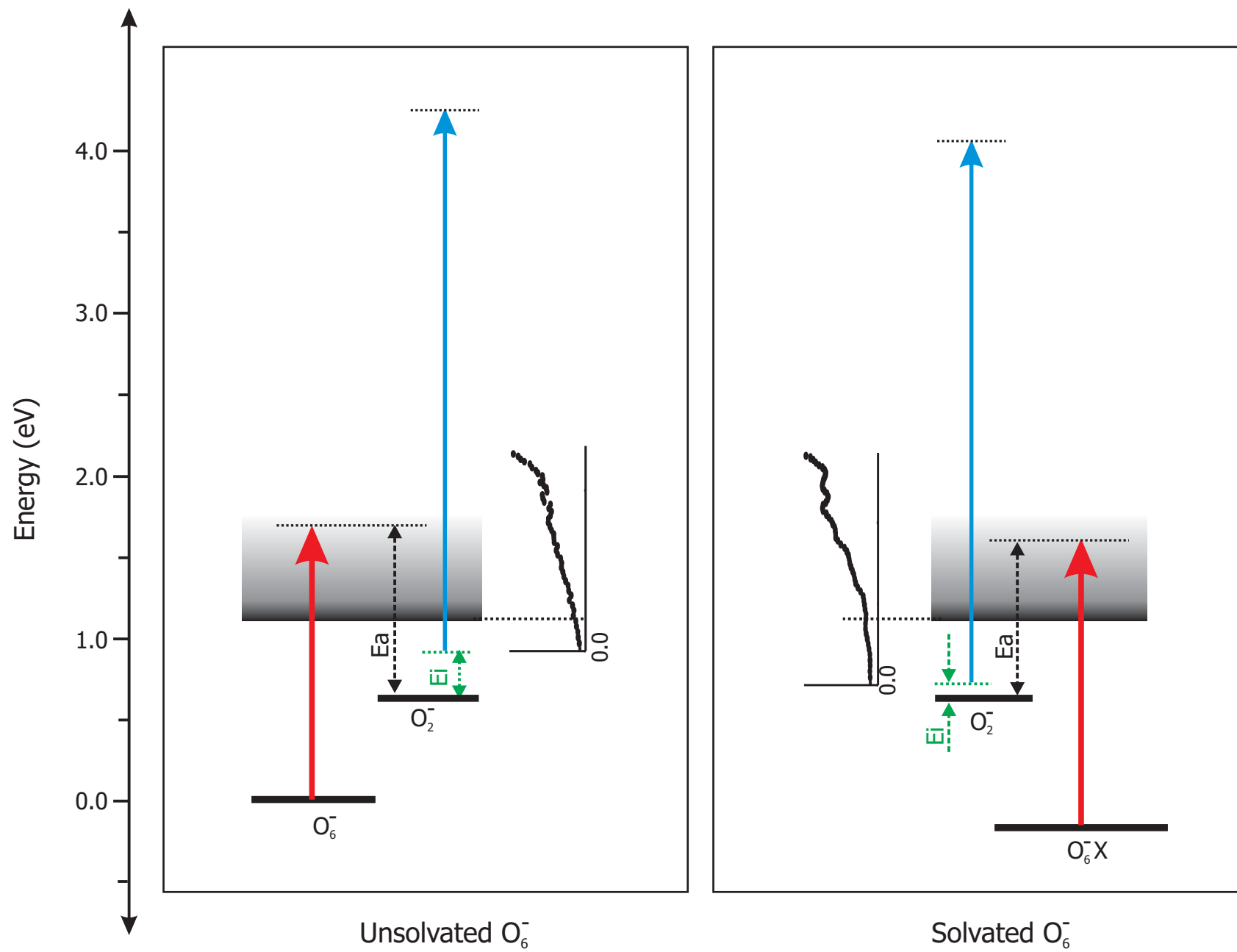


Figure 4.3

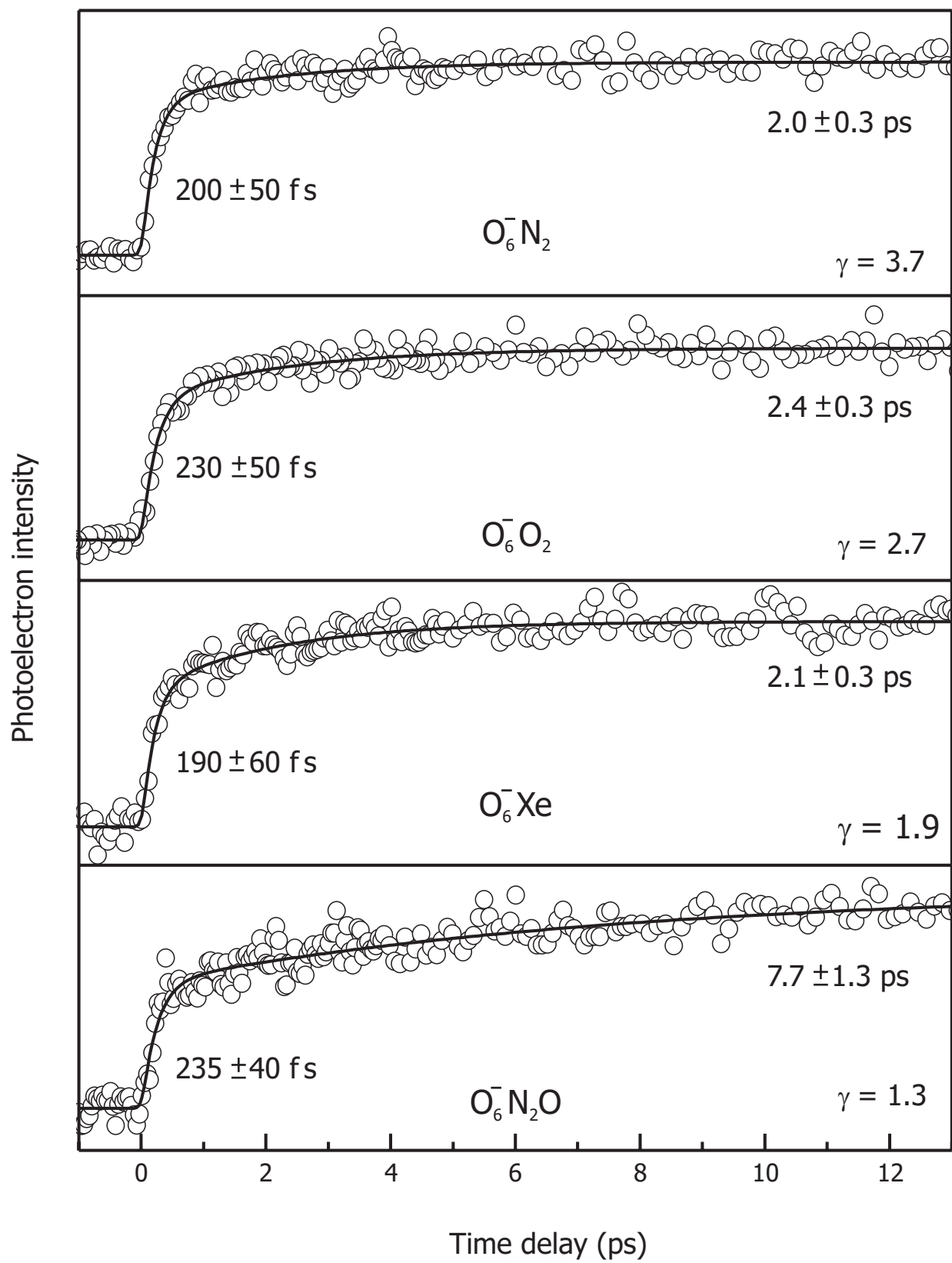


Figure 4.4

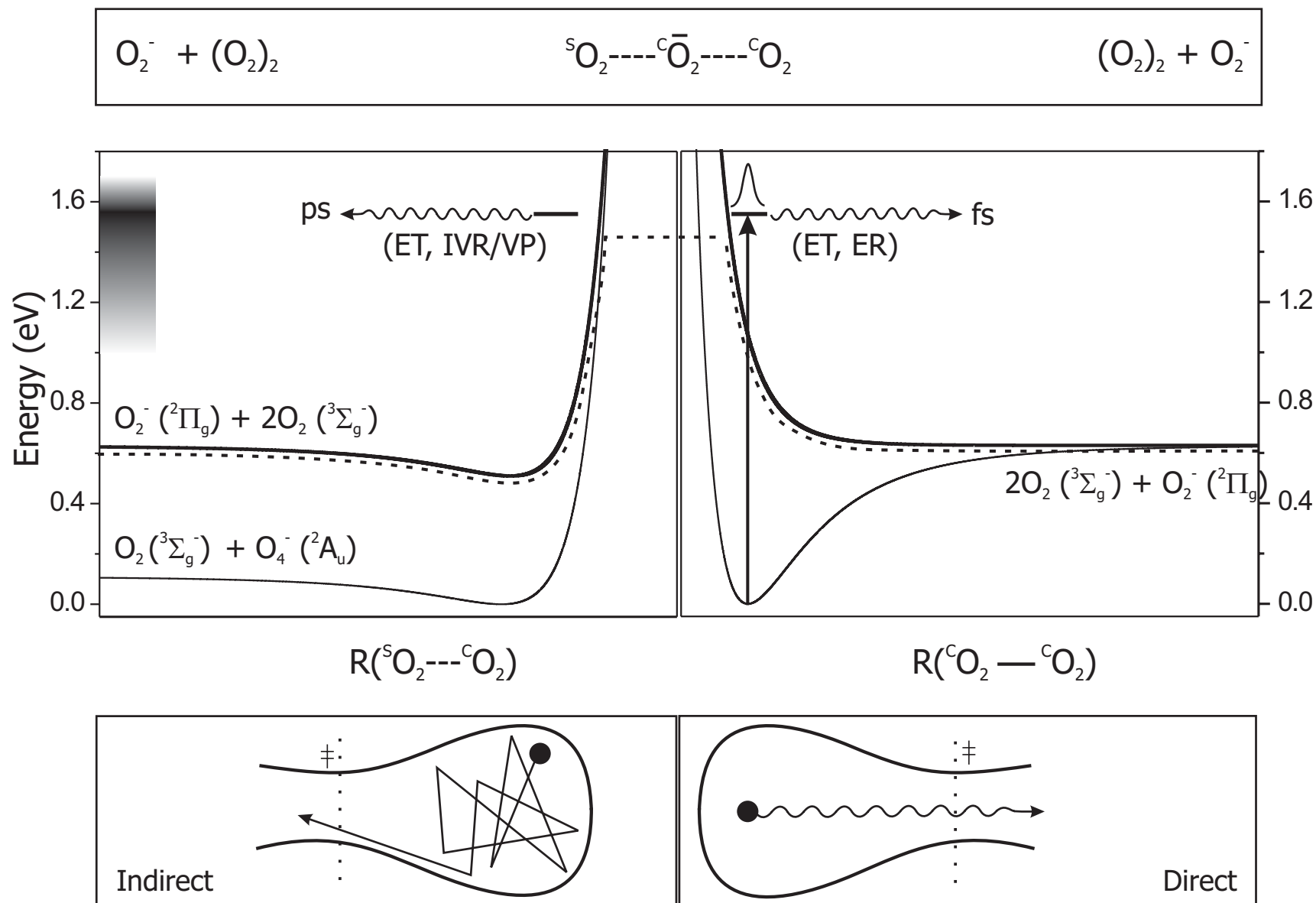


Table I. Summary of experimental results, RRKM calculations and literature values of dipole and quadrupole moments and polarizabilities

Solvent	Experimental results					RRKM	Literature values ^b		
	E_{st} [eV]	T [K]	γ	τ_1 [fs]	τ_2 [ps]	τ_2 [ps]	μ^a [D]	Θ^a [esu·cgs]	α^a [au]
none	—	1600	4.0	110	0.7	—	—	—	—
N ₂	0.08	1200	3.7	200	2.0	1.6	0	-14.7×10^{-27}	11.82
O ₂	0.06	1100	2.7	230	2.4	1.6	0	-4.0×10^{-27}	10.95
Xe	0.12	980	1.9	190	2.1	1.1	0	—	27.11
N ₂ O	0.23	810	1.3	235	7.7	4.5	0.16	-3.36×10^{-26}	20.35

^a μ , Θ and α refer to the dipole moment, quadrupole moment, and polarizability, respectively.

^b References are indicated in the parentheses: quadrupole moments and polarizabilities of N₂ and O₂ (8); polarizability of Xe (18); dipole moment (19), quadrupole moment (20) and polarizability (21) of N₂O.

Figure Captions

Figure 4.1

Time-of-flight mass spectra of $(\text{O}_2)_n^-(\text{X})_m$ ($\text{X} = \text{N}_2, \text{Xe}$ or N_2O) produced by electron impact source, under the optimized condition for the $\text{O}_6^-\cdot\text{X}$ ($\text{X} = \text{N}_2, \text{Xe}$ or N_2O) generation. The traces of $\text{O}_6^-\cdot(\text{H}_2\text{O})_m$ clusters are indicated by asterisks.

Figure 4.2

(A) Photoelectron spectra of $\text{O}_6^-\cdot\text{X}$ ($\text{X} = \text{O}_2, \text{N}_2, \text{Xe}$ or N_2O) with probe (400 nm) pulse only. The experimental results (open circles) are fitted to a Gaussian function (solid line) and the peak of the Gaussian function was assigned as the vertical detachment energy.

(B) Photoelectron spectra of $\text{O}_6^-\cdot\text{X}$ ($\text{X} = \text{O}_2, \text{N}_2, \text{Xe}$ or N_2O) collected when both the pump (800 nm) and probe (400 nm) pulses were present at a 14 ps delayed time. The photoelectron envelope at lower binding energy is that of the nascent O_2^- fragment, and the higher binding energy peak is due to the parent cluster excited by 400 nm light. The enlarged plots of the nascent O_2^- photoelectron profiles are presented as insets. The positions of hot bands and 0,0 band are indicated by the vertical lines, and the estimated temperature of O_2^- are given in the inset.

Figure 4.3

Energetics of electron detachment. The left-hand panel shows the PE spectrum of O_2^- fragment dissociated from unsolvated O_6^- , whereas the right-hand panel shows the PE spectrum of O_2^- fragment dissociated from solvated ones. The thick and thin vertical arrows represent the pump (800 nm) and probe (400 nm) photon energy, and the photoelectron spectra are shown on the vertical axes. E_i is the internal energy of O_2^- fragment, and E_a is the available energy acquired from the 800 nm pump pulse. E_a in O_6^- is larger than E_a of the solvated one because of the stabilization energy. The ground state of $O_6^- \cdot X$ is shifted downward with respect to O_6^- due to the stabilization energy by X. Notice that the origin (*i.e.* zero electron binding energy) of the spectrum is shifted relative to each other. The origin of O_2^- dissociated from O_6^- is shifted upward with respect to the O_2^- generated from $O_6^- \cdot X$ due to the difference in O_2^- internal energy.

Figure 4.4

Femtosecond time-resolved transients of O_2^- rise generated from the dissociation of $O_6^- \cdot X$ ($X = O_2, N_2, Xe$ or N_2O). The time-dependent signals (open circle) were fitted to a bi-exponential function (solid line); see text.

Figure 4.5

Upper panel: solvent dependence of the slow time constant (τ_2): experimental result (square) is plotted against the theoretical values (circle) estimated from the RRKM theory (see text). Lower panel: branching ratio of the slow component, as a function of cooling factor; the estimated temperatures are indicated (see text).

Figure 4.6

Upper panel: S_N2 type reaction pathway which is shown as the dotted line in the middle panel. Middle panel: A representation of two cuts in the O_6^- potential energy surface. On the left hand side of the figure, the potential is along the nuclear coordinate between the O_2^- and core O_4 ($^S O_2 \cdots ^C O_2$); charge induced-dipole interaction. On the right hand side, the potential for the separation ($^C O_2 - ^C O_2$) of O_2^- from O_2 in core O_4^- is displayed; the solvent neutral O_2 is considered as a spectator. The wave packet is prepared as indicated, and the bifurcation is illustrated by the dotted path. The estimated energy range of the charge transfer band is depicted by a shaded block on the vertical axis. Lower panel: The direct and indirect dynamics are represented schematically in the configuration space where the horizontal axis represents the reaction coordinate while the vertical axis describes all non-reactive coordinates.

CHAPTER 5.

Femtosecond Dynamics of Solvated Oxygen

Anions:

**Nature of Dissociation and Caging in Finite-Sized
Clusters**

5.1. Introduction

At the molecular level, van der Waals clusters have been considered as an ideal system to understand the solvation effect on dissociation and recombination dynamics. Since the proposal for caging by Franck and Rabinowitsch in 1930,¹ intensive efforts have been made to understand the recombination in solution, in vdW clusters and in dense fluids (see Refs. 2, 3 and references therein). Photoelectron (PE) spectroscopy of mass-selected anionic clusters makes possible the study of solvation systematically by increasing the number of solvent atoms or molecules. Prototypical examples include the $\text{Br}_2^-(\text{CO}_2)_n$ and $\text{I}_2^-(\text{CO}_2)_n$ clusters which were investigated both experimentally⁵⁻¹⁰ and theoretically¹¹⁻¹⁴. Neutral clusters were studied in this laboratory with focus on the time scale for the initial coherent caging and subsequent vibrational relaxation in solvent cages.¹⁵⁻¹⁹ However, studies of recombination have been mostly devoted to diatomic solute molecules in solvent clusters.

In this work, we investigate solvation effect on the dissociation and recombination dynamics by varying the number of solvent molecules in a homogeneous series of O_2^- clusters. The femtosecond (fs), time-resolved PE spectroscopy was used to follow the reaction dynamics of $(\text{O}_2)_n^-$, $n=3-10$ in real time, following excitation with 800 nm fs pulse. Two distinct time constants were obtained in the transient monitoring nascent fragment anions. The change of both time constants with the cluster size shows the different role of solvation in the two dissociation pathways, direct and indirect, discussed in chapter 4. The caging effect by the solvent is evident on the time scale of the direct dissociation, when the cluster size exceeds the threshold of O_{16}^- . For the indirect process, which occurs on a longer time scale than that of caging, the total rate is controlled by the

redistribution of energy and vibrational predissociation. We compare theory with experiments, deducing correlations which provide a connection to bulk-type behavior and to the electron transfer mechanism.

5.2. Experimental

The experimental procedure was discussed in the Chapter 2, and only a brief description is given here. The O_2^- clusters were produced by secondary electron attachment during the supersonic expansion of gas mixture (approximately 90 % oxygen and 10% Ar) at total backing pressure of 95 psig. The anionic clusters were collimated by the skimmer and then entered a two-stage accelerator. The ion bunches were accelerated by a pulsed high electric field (- 2.0 kV) into a field free region where the different masses of clusters were separated by their flight time.

The cluster of interest was irradiated by fs laser pulses, which produced photofragments and photoelectrons. The fragment ions were analyzed by a linear reflectron time-of-flight mass spectrometer, and the photoelectrons were collected by a magnetic-bottle PE spectrometer. To prevent multiphoton processes while maximizing the overlap between the laser pulses and the ion beam, the laser beam was collimated only to a 5 mm diameter in the laser interaction region.

The fs laser pulse at 800 nm (1.55 eV) was generated from a Ti:Sapphire oscillator. This output was amplified up to 6 mJ/pulse by a regenerative and a multipass amplifier. The amplified output was frequency-doubled by a BBO crystal, generating 800 μ J/pulse at 400 nm (3.1 eV). The remaining 800 nm output of 1.5 mJ/pulse was used as a

pump pulse to dissociate O_2^- clusters, while optically delayed 400 nm laser pulse was used as a probe to detach the electron from the nascent fragment anion.

Based on studies of the power dependence of the pump pulse, the possibility of multiphoton processes was excluded because of the following: First, we observed a slope of ~ 0.5 in the plot of $\log(\text{signal})$ vs. $\log(I_{\text{pump}})$, consistent with previous nanosecond work²⁰, indicating a one-photon absorption (linear) and one-photon absorption/one-photon depletion by the same 800 nm wavelength; if two 800nm pump photons are involved in the dissociation of the cluster (followed by 400nm probe photodetachment of O_2^-), then the slope will be ≥ 1 , with a maximum n value of 2. Second, we also recorded the transient behavior at half the pump power and observed the same transients. Accordingly, the transient signal reported here is for a one-photon excitation at 800 nm, followed by a one-photon detachment at 400 nm (generated by SHG).

5.3. Results

Figure 5.1 shows the PE spectra of O_2^- clusters using a 400 nm fs laser pulse. The vertical detachment energy (VDE) of each cluster is determined by fitting the observed peak to a single Gaussian function. The values obtained are plotted as a function of cluster size (Fig. 5.2). The increase of VDE with n indicates that the anionic clusters become more stable, compared to the corresponding neutral ones, as the number of O_2 molecules increases. As shown below, the plot of the VDE against $n^{-1/3}$, where n is the number of O_2 molecules of the negative ion cluster, follows the linear equation of $VDE = 2.53 - 1.13 \times n^{-1/3}$. The correlation gives a bulk value of the VDE (2.53 eV), when an electron is solvated by “infinite number” of O_2 molecules.²¹

The overall shape of the PE spectra (Fig. 5.1) resembles that of O_4^- , suggesting that additional O_2 molecules bind to O_4^- by weak interactions. The gradual increase of VDE without any abrupt shift (Fig. 5.2) implies no structural change in these clusters.²² In addition, the fact that all of the PE spectra are well fitted to a single Gaussian profile indicates that no other structural isomers with different core ion coexist, at least within our resolution. From these results, we conclude that the O_2^- clusters have a unique structure where O_4^- is a dimeric core and the rest of O_2 molecules form a solvent shell, which is consistent with previous observations.^{20,23}

Figure 5.3 shows fragment mass spectra of parent $(O_2)_n^-$, $n=6-10$, obtained upon irradiation with a 800 nm fs pulse. In the previous studies, we reported that the major anionic fragment in $(O_2)_n^-$, $n=3-5$ was found to be O_2^- , and the intensity of O_4^- was found to increase as the cluster size was increased. This trend continues here for larger clusters. The intensity ratio of O_4^- to O_2^- becomes larger reaching the 100 % level for $(O_2)_{10}^-$, as shown in the figure. No anionic fragments other than O_2^- and O_4^- were detected.²⁴

Figure 5.4 shows the *fragment* PE spectra obtained from the pump/probe PE spectrum at 400 ps time delay between the pump (800 nm) and probe (400 nm) pulses minus the pump/probe PE spectrum at time zero. The PE spectrum of O_4^- with 400 nm probe pulse only is also shown for comparison. The envelope of PE signal, as well as its onset, shifts toward higher electron binding energy (EBE) as the parent cluster size increases.

The transients obtained by detecting fragment anions are shown in Figure 5.5. The transients were recorded by integrating the entire PE signal of nascent fragment anions (shown in Fig. 5.4). We fitted the data to a bi-exponential rise, varying the amplitude (A_1

and A_2) and time constants (τ_1 and τ_2). The response function was included using the autocorrelation function of the pulse width (110 fs) at 800 nm. We also checked for the values of the fit without convolution and obtained similar values for τ_1 , τ_2 and γ . Figure 5.6 and 5.7 depict the behavior of the values of k_1 ($1/\tau_1$) and k_2 ($1/\tau_2$) as a function of n .

We note that the nascent fragment anions generated in the dissociation of large O_2^- clusters at 800 nm are not only O_2^- but also solvated O_2^- , i.e. $O_2^-(O_2)_m$ ($m < n-1$). The $O_2^-(O_2)_m$ subsequently transforms to O_2^- or O_4^- by evaporative dissociation which are the only fragments observed in our reflectron time-of-flight ($\sim 20 \mu\text{s}$) mass spectrometer. The existence of the fragment $O_2^-(O_2)_m$ is evidenced by the onset of the PE envelope in Figure 5.4, which was obtained at 400 ps time delay. The onset is shifted toward higher EBE by 0.1–0.3 eV with respect to that of cold O_2^- , which was attributed to the stabilization of O_2^- by solvation with O_2 molecules.

Unlike O_4^- where an excess electron is delocalized between two O_2 species, the electron in $O_2^-(O_2)_m$ is localized at one O_2 . The onset of O_4^- is 0.5 eV shifted to the higher EBE with respect to that of O_2^- , while the shift of $O_2^- \cdot O_2$ is not known experimentally. However, from the onset shift of $O_2^- \cdot N_2$ (0.26 eV),²⁵ we can roughly estimate the shift to be about 0.24 eV. With this estimated value, our probe window covered the region where the PE signal from $O_2^-(O_2)_m$, $m \leq 5$ could be detected. In order to separate different contributions from $O_2^-(O_2)_m$ to the transients we positioned a narrow gate at several different regions of the fragment PE envelope; the time constants were about the same. This is consistent with a significant overlap in the broad PE spectra of $O_2^-(O_2)_m$.

Figure 5.8 shows a series of time-dependent PE spectra at different time delays. Each PE spectrum is constructed by subtracting the pump/probe PE spectrum at time zero

from the pump/probe PE spectrum at a certain time delay. In Figure 5.8, several representative spectra are presented from a data set consisting of 20 measurements in order to clearly show the time-dependent behavior. For $(\text{O}_2)_6^-$ and $(\text{O}_2)_7^-$, the peak of fragment PE spectra shifts toward lower EBE with time. However, for $(\text{O}_2)_8^-$, $(\text{O}_2)_9^-$, and $(\text{O}_2)_{10}^-$ the peak moves at first toward lower EBE and then at 2–4 ps time delay the shift turns its direction toward higher EBE.

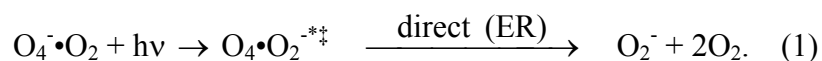
The peak positions were determined either from the pump/probe PE spectrum, which have the PE signals from both fragment and parent anions (each as a Gaussian), or from the fragment change represented by the rise of the fragment and depletion of the parent (each as a Gaussian). The behavior is shown in Figure 5.9. We then obtained the rate at which the EBE is decreasing or increasing by fitting the change in the fragment peak position as a function of time to an exponential decay or rise respectively. The time-dependent variation of the peak position is plotted in Figure 5.10.

5.4. Discussion

Two different pathways following the bifurcation of the initial wave packet were shown in the early communication and in the preceding paper to account for the observations made in all systems studied. For the larger clusters, the same picture holds because of the following findings: First, as discussed above O_4^- remains a dimeric core. Second, the pump pulse energy (1.55 eV) is sufficiently high to compensate for any stabilization by additional solvent molecules. Third, the transient exhibits two distinct rises with time constants vastly different and depend on the cluster size. In what follows we consider the dynamics in these two channels and the effect of microscopic solvation.

5.4.1. Electron Transfer and Solvation

As discussed in paper I, the initial process can be written as



Thus, τ_1 is the joint time constant for electron recombination and the nuclear motion that follows in dissociation. The electron recombination is on the fs time scale and occurs without involving major reorganization of molecules in the cluster. However, the addition of solvent molecules slows down the process by breaking the resonance between the reactant $\text{O}_2^-\bullet\text{O}_4$ and the product $\text{O}_2\bullet\text{O}_4^-$. Moreover, solvation will result in some charge delocalization and the weaker coupling is expected to increase the separation between O_2^- and O_4 . Both the asymmetry and separation changes will affect the energetics of the HOMO (O_2^-) and the LUMO (O_4).²⁶ The deceleration in the electron recombination is a significant factor in the increase of τ_1 , from O_6^- to $\text{O}_6^-\bullet\text{X}$. As the cluster size increases, we also expect the nuclear motion to be affected by the solvent confinement, as discussed elsewhere.²⁷ Below we shall discuss the change in τ_1 , with cluster size.

5.4.2. From Clusters to Bulk

In this section we consider the change in rates and vertical detachment energy as the cluster size increases. Bowen and his coworkers²⁸ obtained VDE of solvated anion

clusters $O^-(Ar)_{n=1-26,34}$ and estimated bulk parameters, such as the photoemission threshold, the photoconductivity threshold, and the bulk solvation energy. The theory by Jortner²⁹ makes the connection between cluster and bulk energetics. The expressions for VDE and the adiabatic electron affinity (AEA) have the $n^{-1/3}$ dependence which relates to the inverse of the radius of cluster for different n :

$$VDE(n) = VDE(\infty) - An^{-1/3} \quad (2A)$$

$$AEA(n) = AEA(\infty) - Bn^{-1/3} \quad , \quad (2B)$$

where the values at infinity are those of the bulk. The slope is given by

$$A = \frac{e^2}{2R_0} \left(1 - \frac{2}{\epsilon_0} + \frac{1}{\epsilon_\infty}\right) \quad (3A)$$

$$B = \frac{e^2}{2R_0} \left(1 - \frac{1}{\epsilon_0}\right) \quad , \quad (3B)$$

where e is the charge, R_0 is the effective radius of the solvent, ϵ_0 is the static dielectric constant, and ϵ_∞ is the corresponding high frequency dielectric constant.

In Figure 5.11 we present our data as plots of VDE and AEA of $(O_2)_n^-$, $n=2-10$ against $n^{-1/3}$. A linear relationship was obtained giving the following intercepts and slopes:

$$VDE(n) = 2.53 - 1.13n^{-1/3} \quad (4A)$$

$$AEA(n) = 2.33 - 1.79n^{-1/3} \quad (4B)$$

For the AEA of $(O_2)_n^-$, we used the values in refs. 20 and 23, for $n=2-6$; for the larger clusters, we obtained them from the PE spectra given in Figure 5.1. For our system, with $R_0 = 2.13 \text{ \AA}$, which is deduced from the bulk density of liquid O_2 ,³⁰ we obtained $\epsilon_0 = 2.13$ and $\epsilon_\infty = 3.65$. From the intercepts, we obtained the “bulk values” of VDE (2.53 eV) and AEA (2.33 eV). These values represent an effective bulk parameters extrapolated to from the mesoscopic properties of clusters. It is interesting that our ϵ_0 of 2.13 is larger than the bulk value of 1.568.³⁰

For the rates the behavior as a function of n is not linear, as shown in Figure 5.6. We replotted the data in Figure 5.12 to show the experimental behavior obtained for k_1 vs. $n^{1/3}$, which is related to the radius of the cluster by $R = R_0 n^{1/3}$. The agreement is surprisingly good and gives the following relationship:

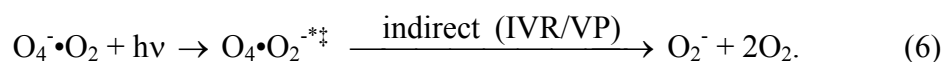
$$k_1 = 1.57 + 7.6 \exp(-7.3(n^{1/3} - 3^{1/3})) \quad (5)$$

where k_1 is in units of ps^{-1} and $3^{1/3}$ is related to the cluster radius of O_6^- which is the smallest cluster that undergoes recombination. The distance dependence is governed by the exponential form, and the value for “infinite” separation is the residual 1.57 ps^{-1} (0.64 ps); the maximum value is 9.17 ps^{-1} (0.11 ps). Considering the R_0 value of O_2 , we obtained the form $7.6 \exp(-\beta(r - r_m))$, with $\beta \sim 3 \text{ \AA}^{-1}$, and a pre-exponential of $7.6 \times 10^{12} \text{ sec}^{-1}$ (250 cm^{-1}). It is interesting to note the analogy with electron transfer in solution,

where β is typically 1.5 \AA^{-1} , in DNA which is less than 1 \AA^{-1} , and in vacuum which reaches $3\text{-}5 \text{ \AA}^{-1}$ (see refs. 31-33).

5.4.3. Evaporation and Solvation

As discussed in the previous Chapters, the second dynamical process involves energy redistribution and predissociation:



For this process, τ_2 is governed by the rate of intramolecular vibrational-energy redistribution among the vibrational modes of the cluster. Consequently, the plot of τ_2 as a function of cluster size is expected to exhibit quite a different behavior from that of τ_1 . As shown in Figures 5.6 and 5.7, except for an abrupt increase of τ_2 from $(\text{O}_2)_3^-$ to $(\text{O}_2)_4^-$, τ_2 gradually increases with the cluster size, without showing a saturation behavior up to $n=10$.

The dynamics of vibrational predissociation has been extensively studied in size-selected dihalogen-rare gas clusters.³⁴⁻³⁶ It is suggested that two pathways for vibrational-energy transfer determine the rates: One that involves direct energy transfer to the dissociative mode(s), i.e. direct vibrational predissociation (VP), while the other involves transfer of vibrational energy to non-reactive modes (IVR). Following this IVR, the energy in non-reactive modes is then channeled into the reaction coordinate.³⁶ In small clusters, VP is expected to be predominant, and the rate is governed by the

coupling between the initially prepared bound state and the final dissociation continuum.³⁷ For larger clusters, with the increase of the density of states, IVR plays a more important role.³⁸ It was shown that more quanta were needed to eject the first rare gas atom as the size of cluster increases.³⁶ Since IVR increases with cluster size, large clusters may reach a statistical limit, and the rate of vibrational predissociation can be successfully described by a statistical theory.

To test this hypothesis, we used the RRKM (Rice-Ramsperger-Kassel-Marcus) theory³⁹ to calculate the rate constant:

$$\frac{1}{\tau_2} \equiv k_2 = \sigma \frac{N^\ddagger(E-D)}{h\rho(E)}, \quad (7)$$

where σ is the degeneracy, h is Planck's constant, $N^\ddagger(E-D)$ is the number of states at the transition state, and $\rho(E)$ is the density of states of the reactant. The reaction coordinate involves $\text{O}_2^-(\text{O}_2)_{n-1}$, which is a charge transferred partner of the parent $\text{O}_4^-(\text{O}_2)_{n-2}$. We obtained the optimized structure and the vibrational frequencies of $\text{O}_2^-\cdot\text{O}_2$ using the unrestricted Hartree-Fock level of theory with 6-311+G* as a basis set⁴⁰. The calculated intermolecular frequencies of $\text{O}_2^-\cdot\text{O}_2$ were employed to obtain $N^\ddagger(E-D)$ and $\rho(E)$.

In calculating the effective rate constant, k_2 , we considered the following six dissociation channels:



Following the initial evaporative dissociation, further dissociation may occur. However, subsequent dissociations will not appear in our transient because the photodetachment cross-section of the fragments is about the same. The PE signal of the fragments is integrated in our boxcar gate which makes the probe insensitive to subsequent dissociations yielding smaller fragments.

In the above expression of k_2 , E is the energy of the excitation pulse minus the difference in energy (at the minimum of the potential) between $O_2^-(O_2)_{n-1}$ and $O_4^-(O_2)_{n-2}$. We took E to be the same for all clusters since the stabilization energy by O_2 molecules is about the same for $O_2^- \cdot O_2$ and O_4^- . The transition state for the reaction generating O_2^- and $O_2^- \cdot O_2$ was considered to be product-type and the dissociation energy D was deduced using the value of AEA of O_2^- and the estimated stabilization energy by O_2 . However, for the other channels yielding larger fragments, we assumed the same activation barrier height for the dissociation coordinate of $O_2^- \cdot O_2$. The σ value was 1 for the channel producing O_2^- , $(n-1)$ for channel producing $O_2^- \cdot O_2$, $(n-1)(n-2)/2!$ for channel producing $O_2^- \cdot 2O_2$, and so on.

The calculated rates are given in Figure 5.13. The agreement between the theoretical and experimental trend is reasonably good, except for the smallest cluster $(O_2)_3^-$. This indicates that significant degree of IVR precedes VP for $(O_2)_n^-$ ($n \geq 4$), and that “thermal” evaporation is dominant. The overestimation of the degeneracy factor σ , because of the lack of direct information on the anionic structure of the clusters, may account for the somewhat larger rate constants obtained theoretically for $n \geq 4$.

5.4.4. Recombination and Caging

The temporal behavior observed in the fragment PE spectra (Fig. 5.10) is consistent with previous observations in $\text{I}_2^-(\text{Ar})_n$ and $\text{I}_2^-(\text{CO}_2)_n$ made by Neumark and his coworkers.^{8,9} The shift toward lower EBE with time is attributed to the evaporation of solvent O_2 molecules around O_2^- which dissociates from O_4^- . In the case of $n = 8-10$, the gradient for the shift (solid lines in Fig. 5.10) is much steeper than that of $(\text{O}_2)_6^-$ and $(\text{O}_2)_7^-$. This efficient evaporation is because in these clusters of more complete solvent shell, the probability of hard collisions increases between the dissociating O_2^- and the solvent. The efficient energy transfer through these hard collisions rapidly heats up the solvent cage, which in turn makes effective evaporation of solvent molecules.⁴¹ The increase in EBE at 2–4 ps time delay for $n=8-10$ indicates the onset for recombination. Following the collision with the solvent cage, the O_2^- encounters the other O_2 and reforms O_4^- . The shift toward higher EBE, which approaches the asymptote at 10–20 ps, represents the bond reformation (recombination) and subsequent vibrational relaxation.

The recombination occurs at 2.5 ps for $(\text{O}_2)_{10}^-$ and at about 4 ps for $(\text{O}_2)_8^-$ and $(\text{O}_2)_9^-$. The time constant for effective vibrational relaxation also shows strong size-dependence: 12 ps for $(\text{O}_2)_8^-$, 4 ps for $(\text{O}_2)_9^-$, and 3 ps for $(\text{O}_2)_{10}^-$. This is because the larger number of solvent molecules around the reformed O_4^- provides an efficient energy bath with more density of states.⁴² The increase in the recombination rate for the larger clusters and the change in vibrational relaxation were observed in other systems.^{9,43}

Direct dissociation of O_4^- is primarily responsible for the recombination because the recombination time of $(\text{O}_2)_{10}^-$ (2.5 ps) is much shorter than the corresponding τ_2 (8.0 ps). Moreover, the recombination shows a threshold dependence on the cluster size, only

observed for the cluster size of $n \geq 8$. The time scale for bond breakage is critical for the subsequent recombination and solvent reorganization as pointed out in the study made in this laboratory on iodine-rare gas clusters.¹⁵⁻¹⁷ A slow dissociation gives solvent molecules enough time to absorb the energy, in this case of dissociating O_2^- , which softens the solvent wall; this soft solvent cage becomes ineffective to force the O_2^- back for recombination.

Johnson and his coworkers⁴⁴ recently reported that there exists a bound electronic excited state of O_4^- . However, we suggest that the recombination process, which is reflected as a peak shift in Figure 5.10, occurs along the ground potential energy surface for the following reasons. First, the dissociation asymptote of the electronic excited state is about 0.21 eV (1676 cm^{-1}) above that of the repulsive state. Therefore, the non-adiabatic transition from the repulsive state to the electronic excited state near the solvent wall is not likely to occur. Second, the excited state is located a little above the asymptote of the repulsive state. Hence, even though the recombination on the electronic excited state is possible through the curve crossing from the repulsive state following the collision with the solvent wall, the recombination process on this excited state will give rise to a small change in the peak position of fragment photoelectron spectrum and will not reproduce the behavior in Figure 5.10. Finally, vibrational or electronic predissociation, which begins at $\sim 242 \text{ cm}^{-1}$ above the band origin of the excited state, will make the recombination on this state much less efficient. If some trajectories of recombination occurs on the excited surface, then internal conversion to the ground state must be ultrafast in order to account for the results.

The striking feature observed in the recombination of O_4^- is that the rate of recombination is significantly slower than those found in other vdW clusters, given the fact that $(O_2)_n^-$, $n \geq 7$ has a complete solvent shell; we studied $(O_2)_{13}^-$ and the behavior is still similar to that of $(O_2)_{10}^-$. The prompt recombination was observed in vdW clusters of $I_2(Ar)_n$, $n = 8-40$ (660 fs),¹⁶ and the recombination began at 1 ps for $I_2^-(Ar)_{20}$ ^{8,41} and 500 fs for $I_2^-(CO_2)_{16}$ ⁹, where the first solvent shell is complete. Considering the significant quadrupole moment and the stronger binding energy of O_2 , than that of Ar (the binding energy of O_2 in $O_4^- \cdot O_2$ is ~ 0.1 eV, while that of Ar in $I_2^- \cdot Ar$ is 0.052 eV⁸), we can conclude that the solvent wall of O_2 molecules is stiffer and more cohesive than that of Ar. Thus, binding is not the cause of slow recombination.

We suggest that the slow recombination is due to the reorientation process of both O_2^- and O_2 to acquire the proper configuration for O_4^- reformation. Unlike recombination in the case of atoms, the recombination in the case involving two molecules (O_2 & O_2^-) requires a second coordinate, namely the angle (θ) between the two molecules involved. We present a schematic of this dependence in Figure 5.14. The non-adiabatic transition between the O_4^- repulsive surface (excited) and bound surface (ground) is θ -dependent and hence the transition to the ground state not only depends on the energetics in the asymptote region but also on the relative orientation. The reorientation may occur with relatively small energy change. However, the friction exerted by ion-induced dipole interaction between O_2^- and the solvent O_2 molecules may slow down the reorientation process.

5.5. Conclusion

In this chapter, we presented studies of the ultrafast dissociation and recombination dynamics of homogeneous O_2^- clusters, from O_6^- to O_{20}^- , using fs, time-resolved photoelectron spectroscopy. Dissociation and recombination of the mass-selected anionic clusters show solvation effects on two different time scales and dissociation pathways – a bifurcation of the wave packet in two channels of direct dissociation and vibrational predissociation. The emergence of bulk properties from clusters was examined and compared with theory – bulk-type behaviors were deduced from the correlation between vertical detachment energy, or adiabatic electron affinity, and the inverse radius of the cluster, $n^{-1/3}$. For the rates we found a dependence on the radius, $n^{1/3}$, and we related such striking behavior to the dynamics of electron recombination in the direct dissociation process. For vibrational dissociation, the solvent evaporation process, the experimental rates show reasonable agreement with the calculated values using a statistical theory. The reformation of the bond in solvent cages becomes evident as the cluster size increases. Our fs time resolution provides the time scale for the recombination and subsequent vibration relaxation, which vary with the cluster size. The measured rates reveal the unique feature in the recombination process between molecules, which is absent in the (atom+atom) bond reformation. The time scale for bond breakage is critical to the rate of bond reformation, and molecular orientations and solvent friction play a significant role, especially at longer times, longer than 1 ps.

References

- ¹ J. Franck and E. Rabinowitsch, *Trans. Faraday Soc.* **30**, 120 (1934).
- ² C. Lienau and A. H. Zewail, *J. Phys. Chem.* **100**, 18629 (1996), and references therein.
- ³ A. Materny, C. Lienau, and A. H. Zewail, *J. Phys. Chem.* **100**, 18650 (1996), and see the most recent reference 4.
- ⁴ J. Larsen, D. Madsen, J.-A. Poulsen, T. D. Poulsen, S. R. Keiding, and J. Thøgersen, *J. Chem. Phys.* **116**, 7997 (2002).
- ⁵ M. L. Alexander, N. E. Levinger, M. A. Johnson, D. Ray, and W. C. Lineberger, *J. Chem. Phys.* **88**, 6200 (1988).
- ⁶ J. M. Papanikolas, J. R. Gord, N. E. Levinger, D. Ray, V. Vorsa, and W. C. Lineberger, *J. Phys. Chem.* **95**, 8028 (1991).
- ⁷ B. J. Greenblatt, M. T. Zanni, and D. M. Neumark, *Science* **276**, 1675 (1997).
- ⁸ B. J. Greenblatt, M. T. Zanni, and D. M. Neumark, *J. Chem. Phys.* **111**, 10566 (1999).
- ⁹ B. J. Greenblatt, M. T. Zanni, and D. M. Neumark, *J. Chem. Phys.* **112**, 601 (2000).
- ¹⁰ A. Sanov, T. Sanford, S. Nandi, and W. C. Lineberger, *J. Chem. Phys.* **111**, 664 (1999).
- ¹¹ F. G. Amar and L. Perera, *Z. Phys. D* **20**, 173 (1991).
- ¹² V. S. Batista and D. F. Coker, *J. Chem. Phys.* **106**, 7102 (1997).
- ¹³ R. Parson, J. Faeder, and N. Delaney, *J. Phys. Chem.* **104**, 9653 (2000).
- ¹⁴ J. Ka and S. Shin, *J. Chem. Phys.* **109**, 10087 (1998).
- ¹⁵ Q. Liu, J.-K. Wang, and A. H. Zewail, *Nature* **364**, 427 (1993).
- ¹⁶ J.-K. Wang, Q. Liu, and A. H. Zewail, *J. Phys. Chem.* **99**, 11309 (1995).
- ¹⁷ Q. Liu, J.-K. Wang, and A. H. Zewail, *J. Phys. Chem.* **99**, 11321 (1995).
- ¹⁸ A. A. Heikal, S. H. Chong, J. S. Baskin, and A. H. Zewail, *Chem. Phys. Lett.* **242**, 380 (1995)
- ¹⁹ C. Wan, M. Gupta, J. S. Baskin, Z. H. Kim, and A. H. Zewail, *J. Chem. Phys.* **106** (10), 4353 (1997)

- ²⁰ M. J. DeLuca, C.-C. Han, and M. A. Johnson, *J. Chem. Phys.* **93**, 268 (1990).
- ²¹ R. N. Barnett, U. Landman, C. L. Cleveland, and J. Jortner, *Chem. Phys. Lett.* **145**, 382 (1988).
- ²² M. J. DeLuca, B. Niu, and M. A. Johnson, *J. Chem. Phys.* **88**, 5857 (1988).
- ²³ K. Hiraoka, *J. Chem. Phys.* **89**, 3190 (1988).
- ²⁴ The fragments $(\text{O}_2)_3^-$ and $(\text{O}_2)_4^-$, as well as O_2^- and O_4^- , were observed in the dissociation of parent $(\text{O}_2)_{13}^-$.
- ²⁵ L. A. Posey and M. A. Johnson, *J. Chem. Phys.* **88**, 5383 (1988).
- ²⁶ K. Ohta and K. Morokuma, *J. Phys. Chem.* **91**, 401 (1987).
- ²⁷ P. Y. Cheng, D. Zhong, and A. H. Zewail, *J. Chem. Phys.* **105**, 6216 (1996).
- ²⁸ S. T. Arnold, J. H. Hendricks, and K. H. Bowen, *J. Chem. Phys.* **102**, 39 (1995).
- ²⁹ J. Jortner, *Z. Phys. D* **24**, 247 (1992).
- ³⁰ *CRC Handbook of Chemistry and Physics*, 82 ed., edited by D. R. Lide (CRC, Boca Raton, FL, 2001), **6-139**, **6-152**.
- ³¹ C. Wan, T. Fiebig, O. Schiemann, J. K. Barton, and A. H. Zewail, *Proc. Natl. Acad. Sci. USA* **97**, 14052 (2000).
- ³² A. Ponce, H. B. Gray, and J. R. Winkler, *J. Am. Chem. Soc.* **122**, 8187 (2000).
- ³³ N. E. Miller, M. C. Wander, and R. J. Cave, *J. Phys. Chem. A* **103**, 1084 (1999).
- ³⁴ A. García-Vela, P. Villarreal, and G. Delgado-Barrio, *J. Chem. Phys.* **94**, 7868 (1991).
- ³⁵ M. Gutmann, D. M. Willberg, and A. H. Zewail, *J. Chem. Phys.* **97**, 8048 (1992).
- ³⁶ S. Fernandez Alberti, N. Halberstadt, J. A. Beswick, A. Bastida, J. Zúñiga, and A. Requena, *J. Chem. Phys.* **111**, 239 (1999).
- ³⁷ D. M. Willberg, M. Gutmann, J. J. Breen, and A. H. Zewail, *J. Chem. Phys.* **96**, 198 (1992).
- ³⁸ B. Miguel, A. Bastida, J. Zúñiga, A. Requena, and N. Halberstadt, *Faraday Discuss.* **118**, 257 (2001).
- ³⁹ P. J. Robinson and K. A. Holbrook, *Unimolecular reactions* (Wiley, New York, 1972).

- ⁴⁰ M. J. Frisch, G. W. Trucks, H. B. Schlegel *et al.* GAUSSIAN 98, Revision A.9, Gaussian, Inc., Pittsburgh, PA, 1998.
- ⁴¹ J. Faeder and R. Parson, *J. Chem. Phys.* **108**, 3909 (1998).
- ⁴² The difference in the asymptotes at 400 ps time delay (1.47 eV for $(\text{O}_2)_8^-$, 1.52 eV for $(\text{O}_2)_9^-$, and 1.61 eV for $(\text{O}_2)_{10}^-$) could be due to the degree of vibrational relaxation in different-sized clusters. However, considering the time constants for vibrational relaxation by solvent O_2 molecules (3-12 ps) and also the number of vibrational modes in O_4^- , an incomplete vibrational relaxation of O_4^- at 400 ps is unlikely. We suggest that the difference is due to the different contribution of the recombined product. It should be noted that the photoelectron spectrum of fragment anions is the sum of nascent fragment $\text{O}_2^-(\text{O}_2)_m$ from the dissociation and the $\text{O}_4^-(\text{O}_2)_k$ from the recombination, each with a different VDE value. The increased production of recombined $\text{O}_4^-(\text{O}_2)_k$ in larger clusters makes the asymptote value shift toward higher EBE.
- ⁴³ V. Vorsa, S. Nandi, P. J. Campagnola, M. Larsson, and W. C. Lineberger, *J. Chem. Phys.* **106**, 1402 (1997).
- ⁴⁴ J. A. Kelley, W. H. Robertson, and M. A. Johnson, *Chem. Phys. Lett.* **362**, 255 (2002).

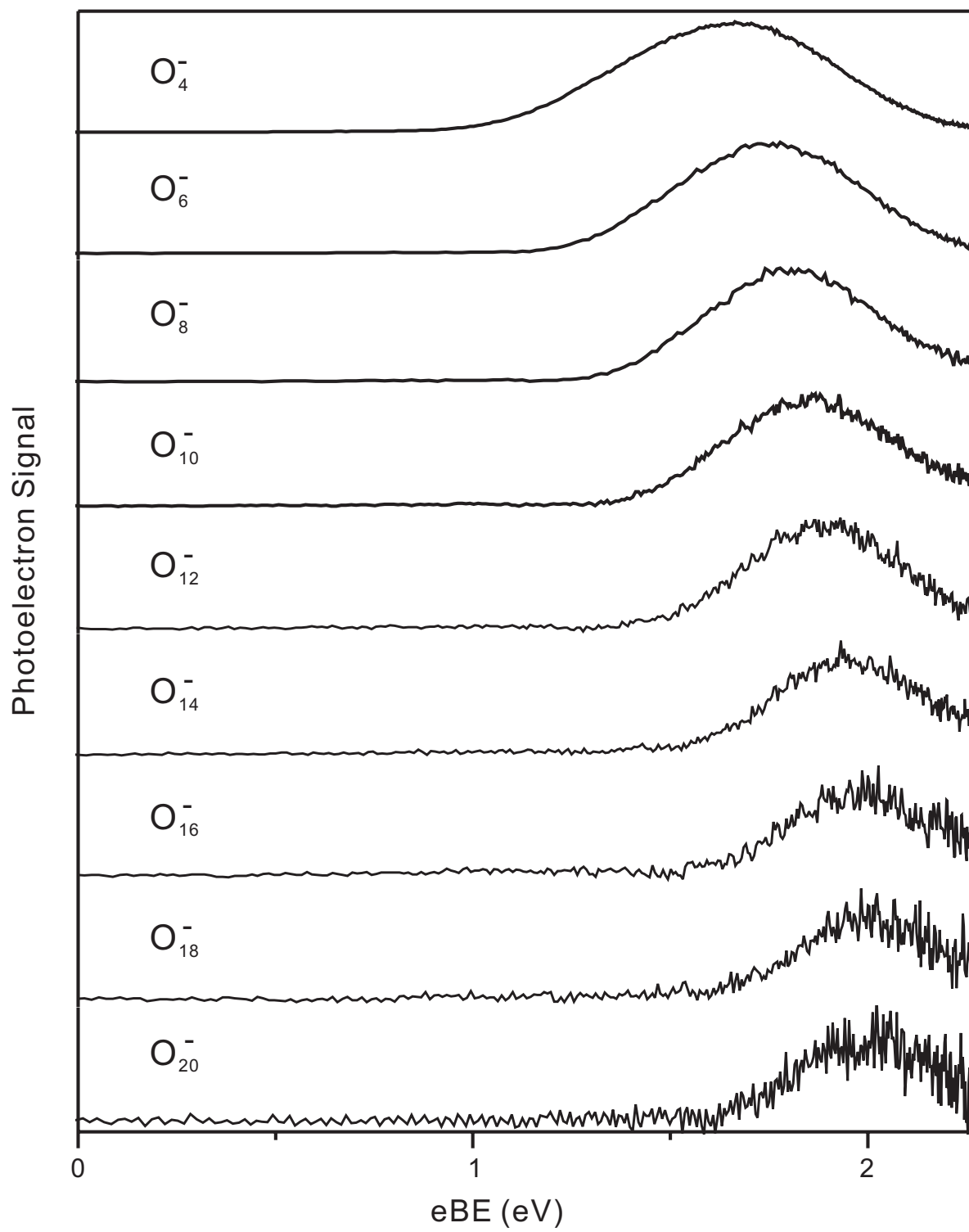


Figure 5.1

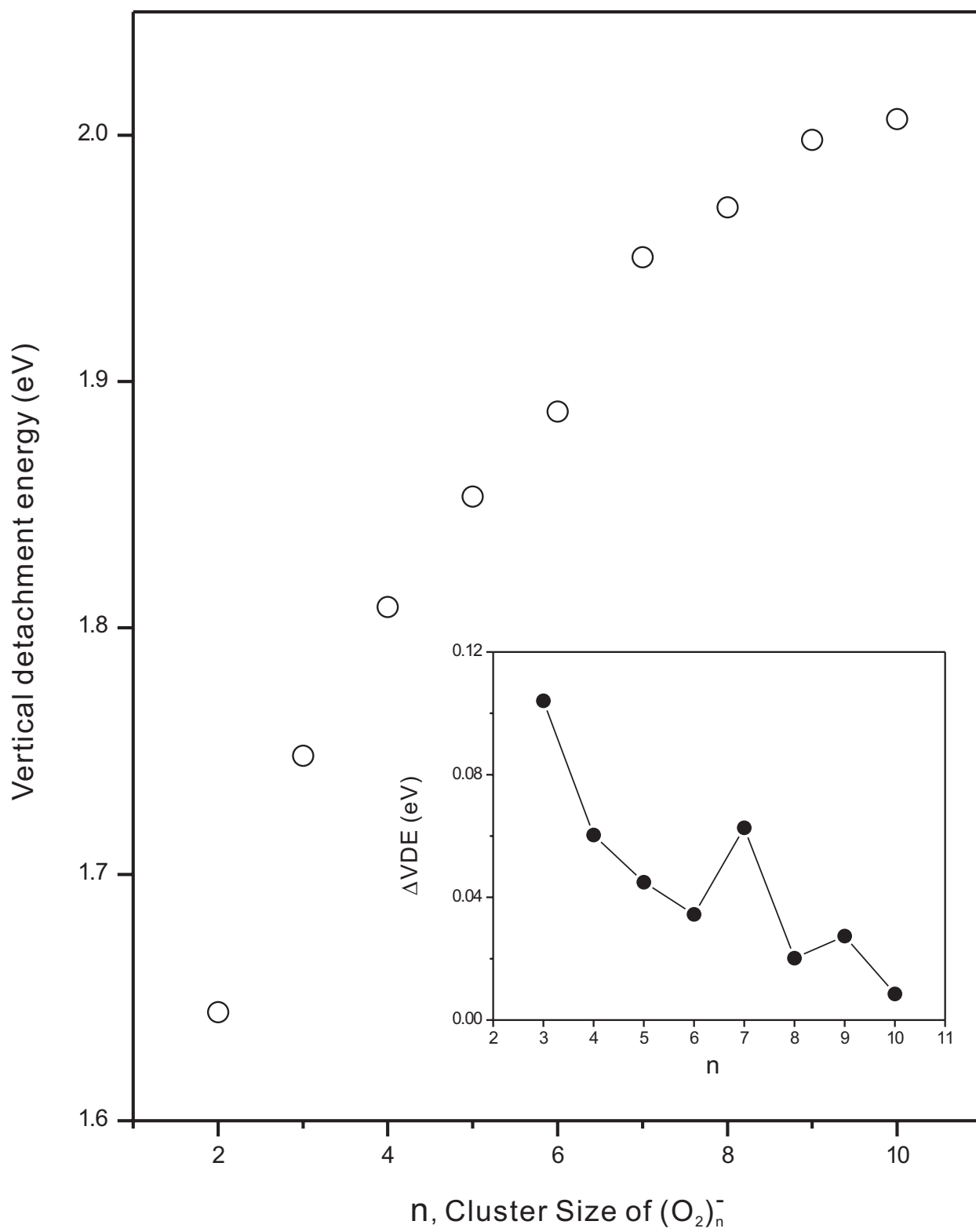


Figure 5.2

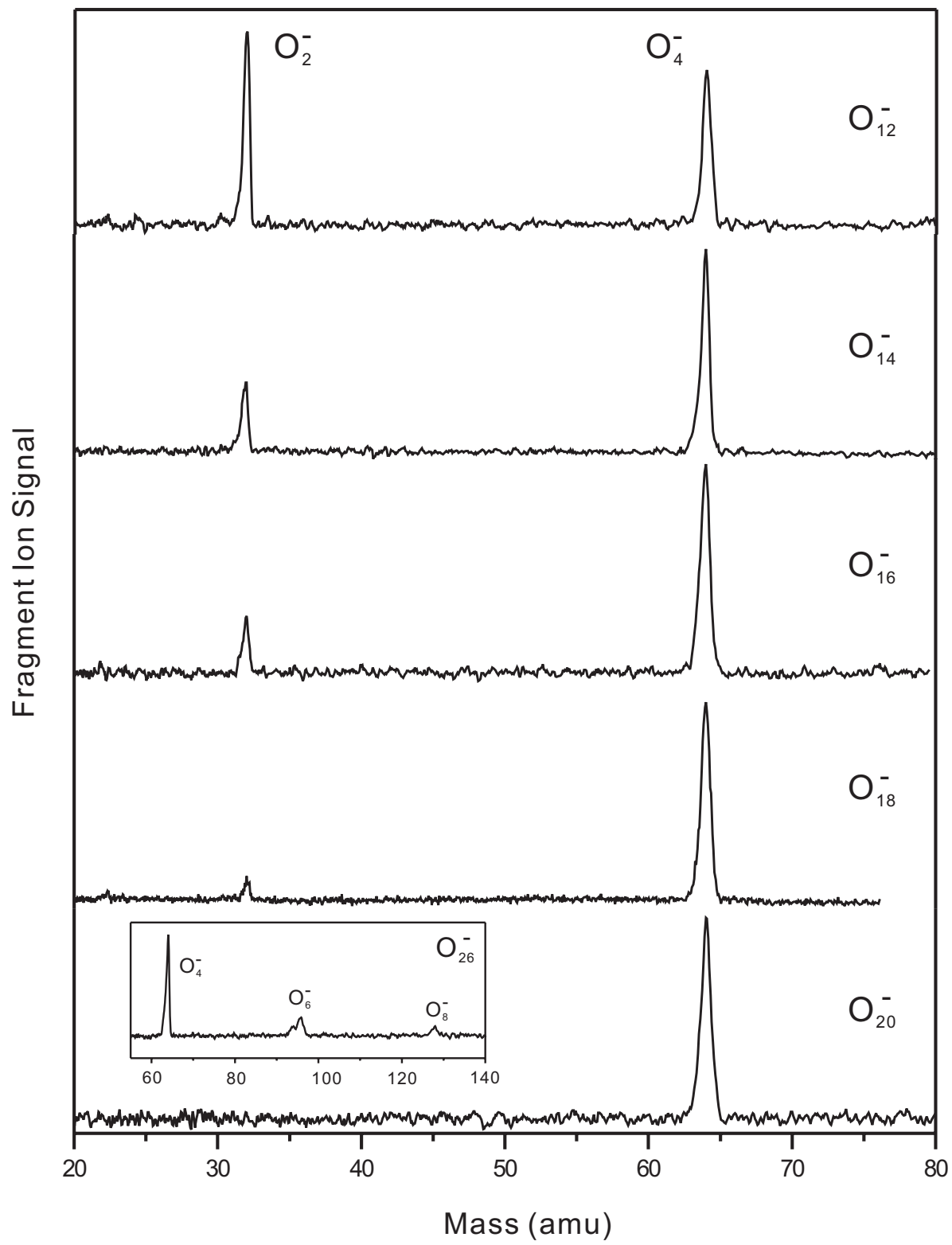


Figure 5.3

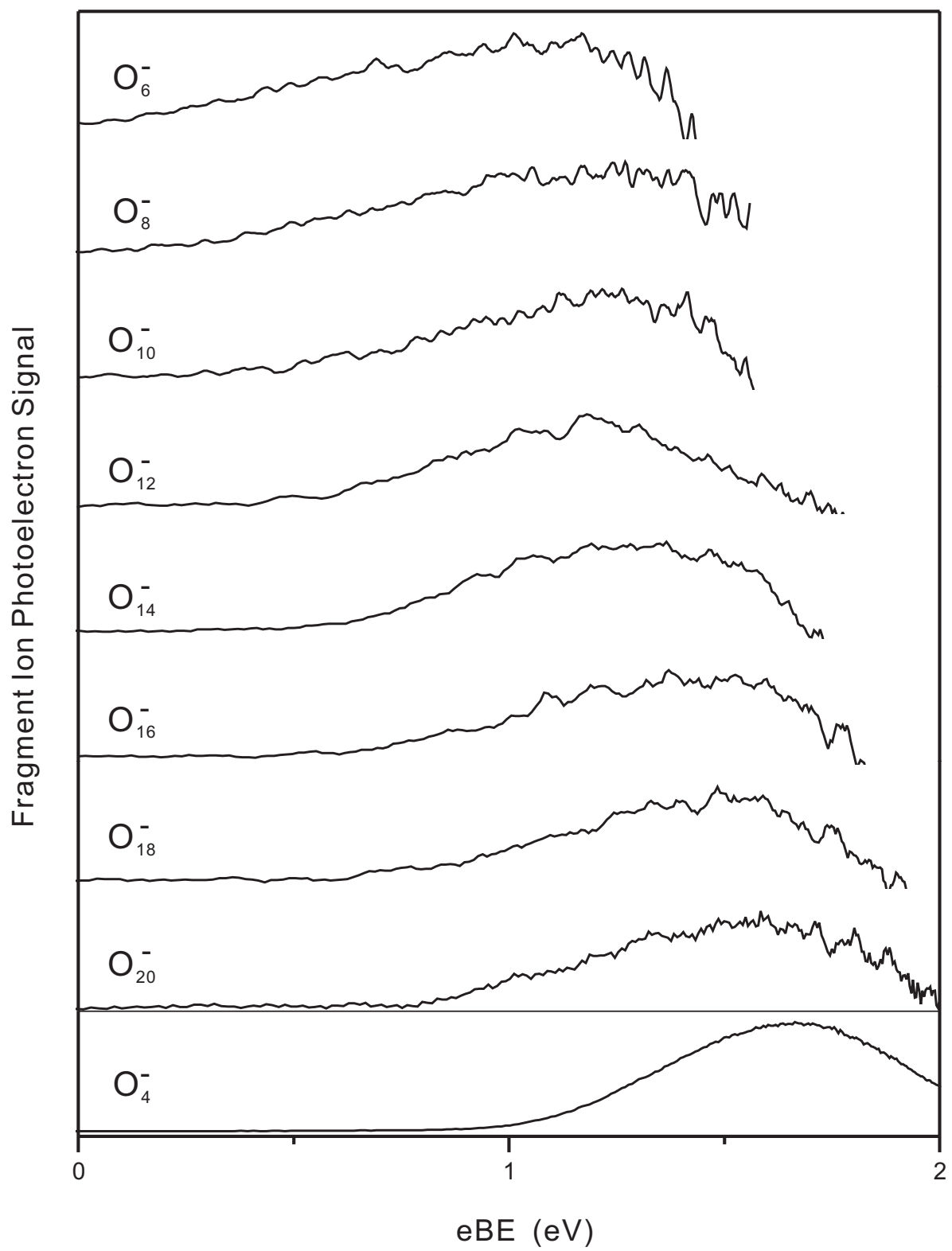
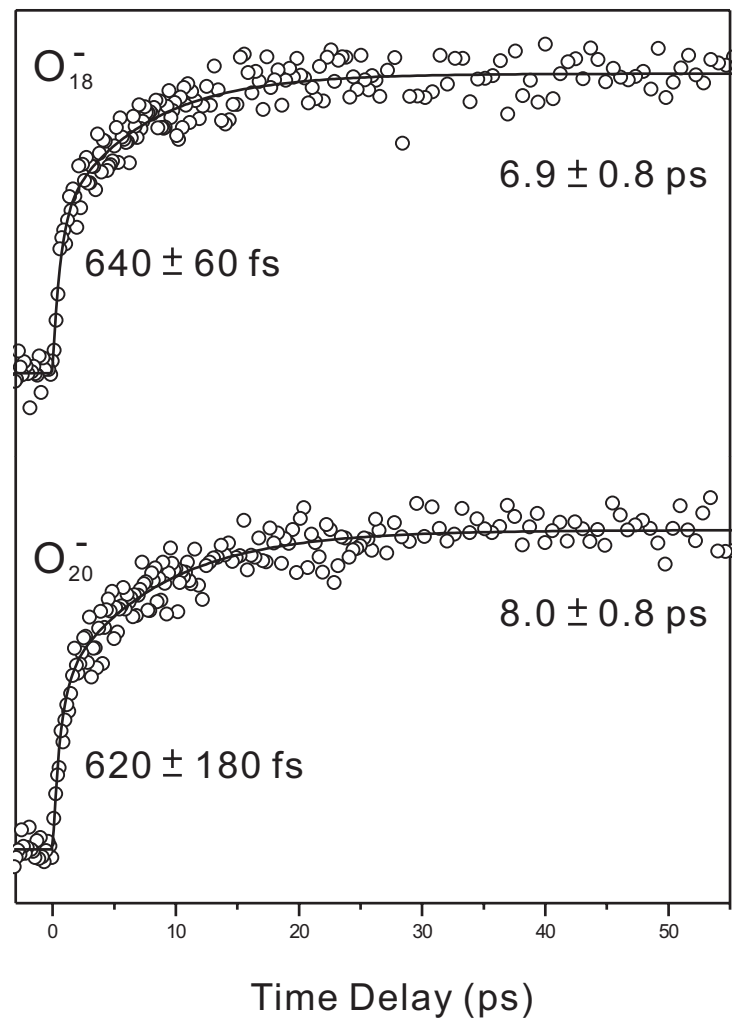
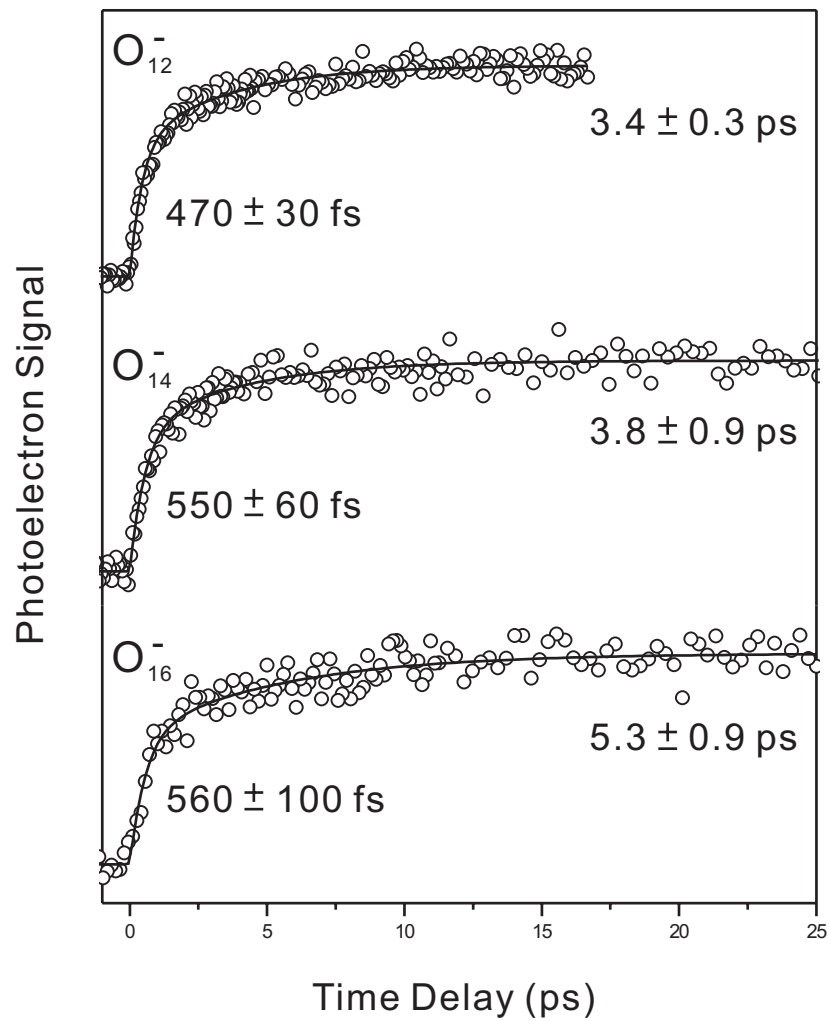


Figure 5.4



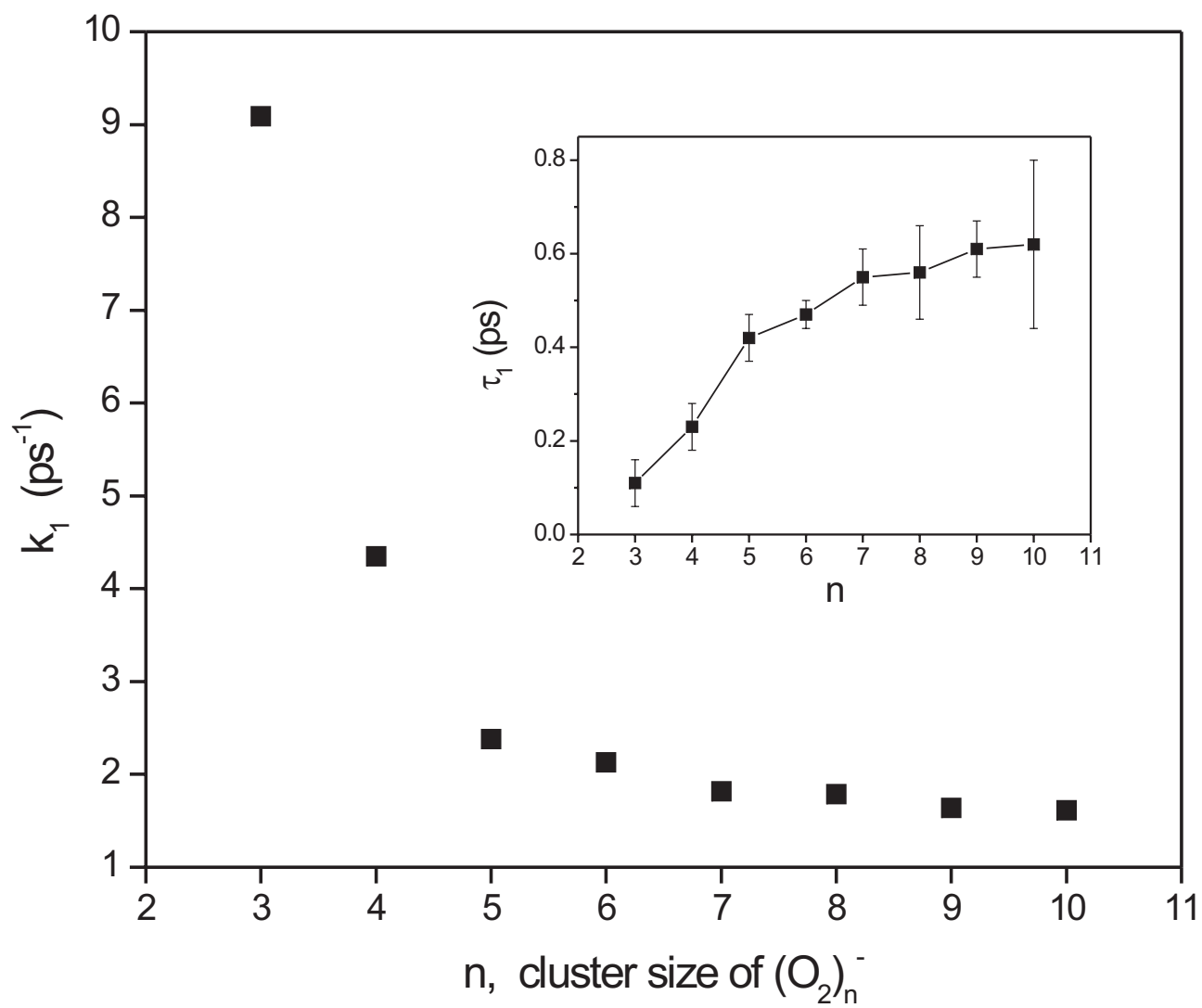


Figure 5.6

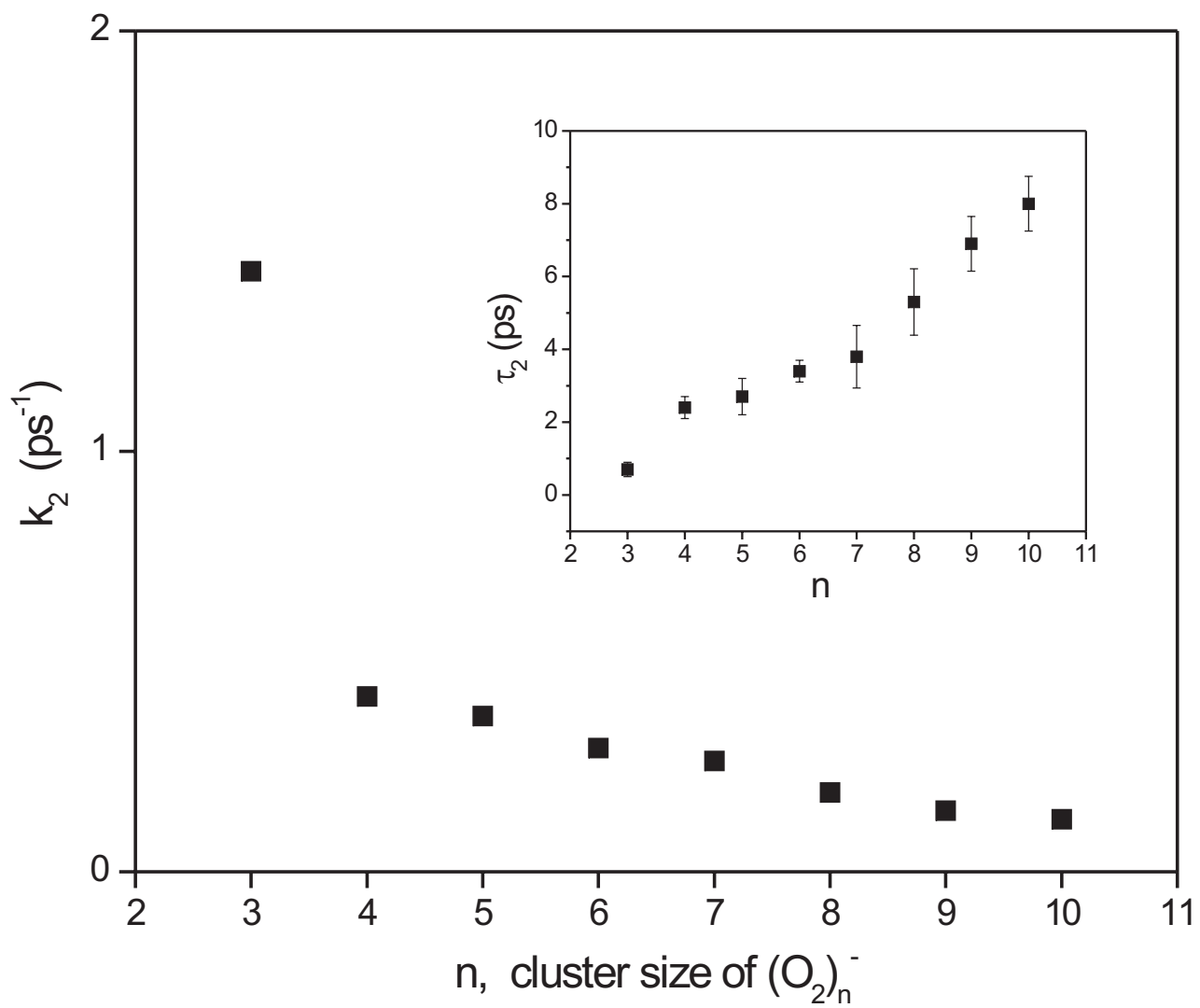


Figure 5.7

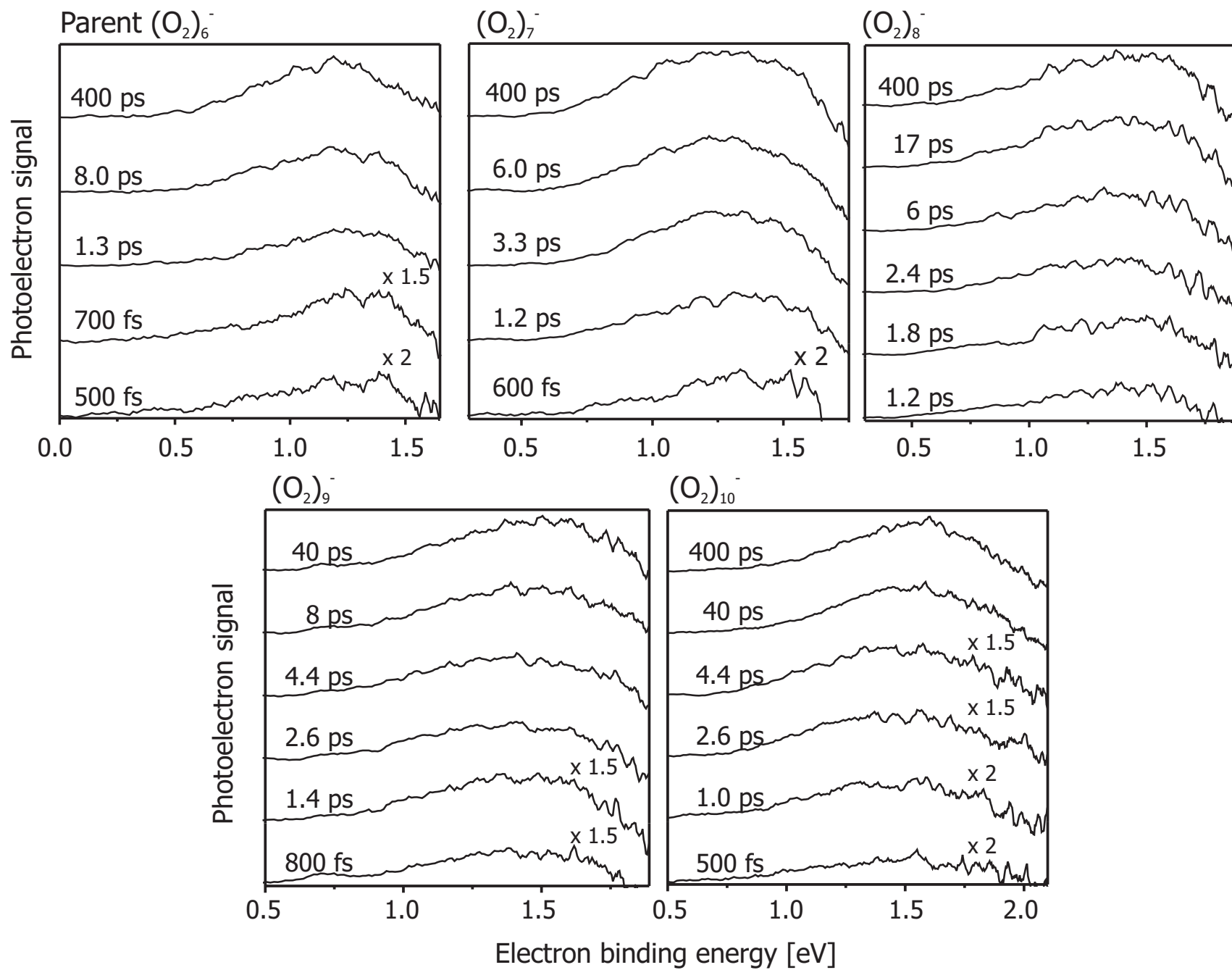


Figure 5.8

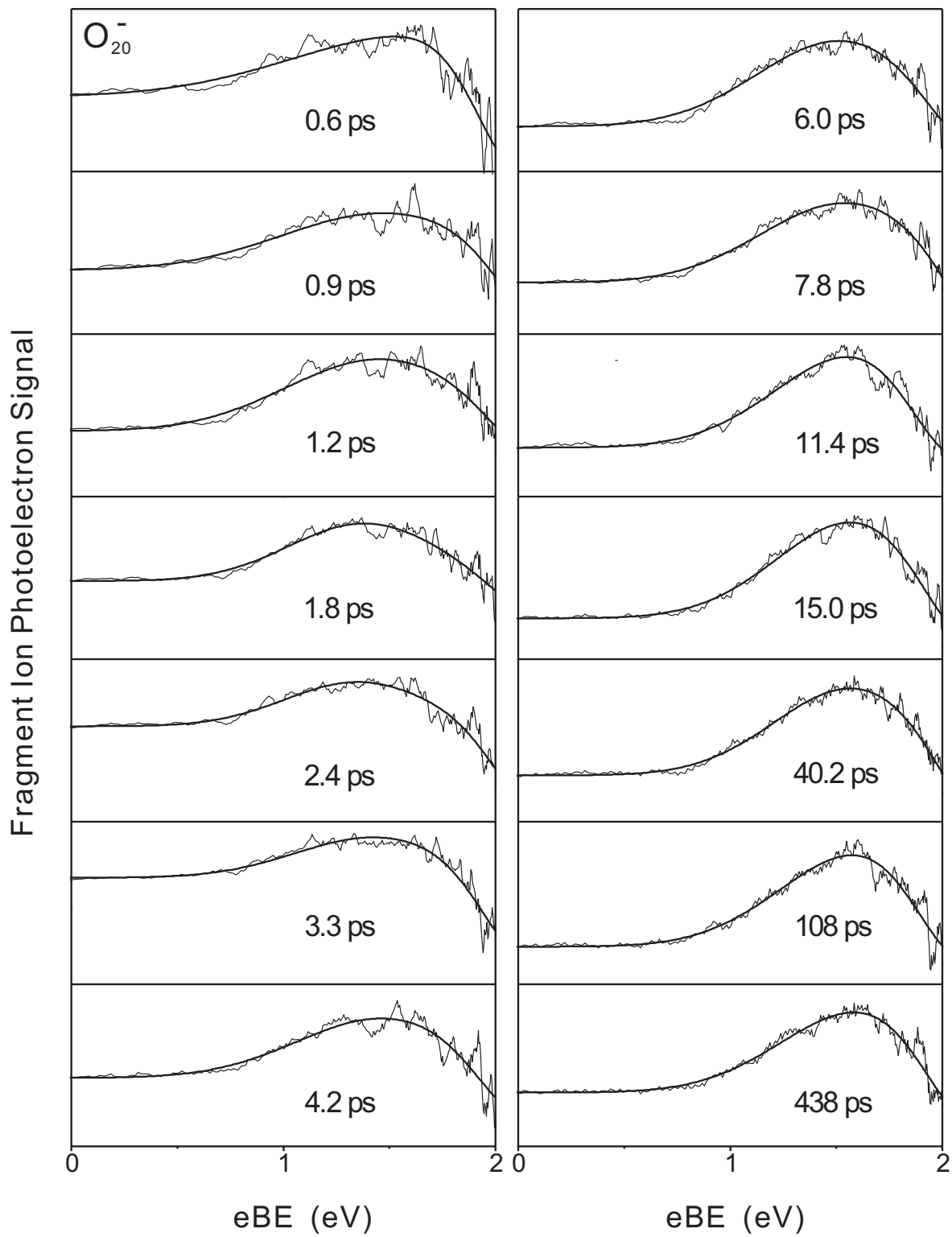


Figure 5.9

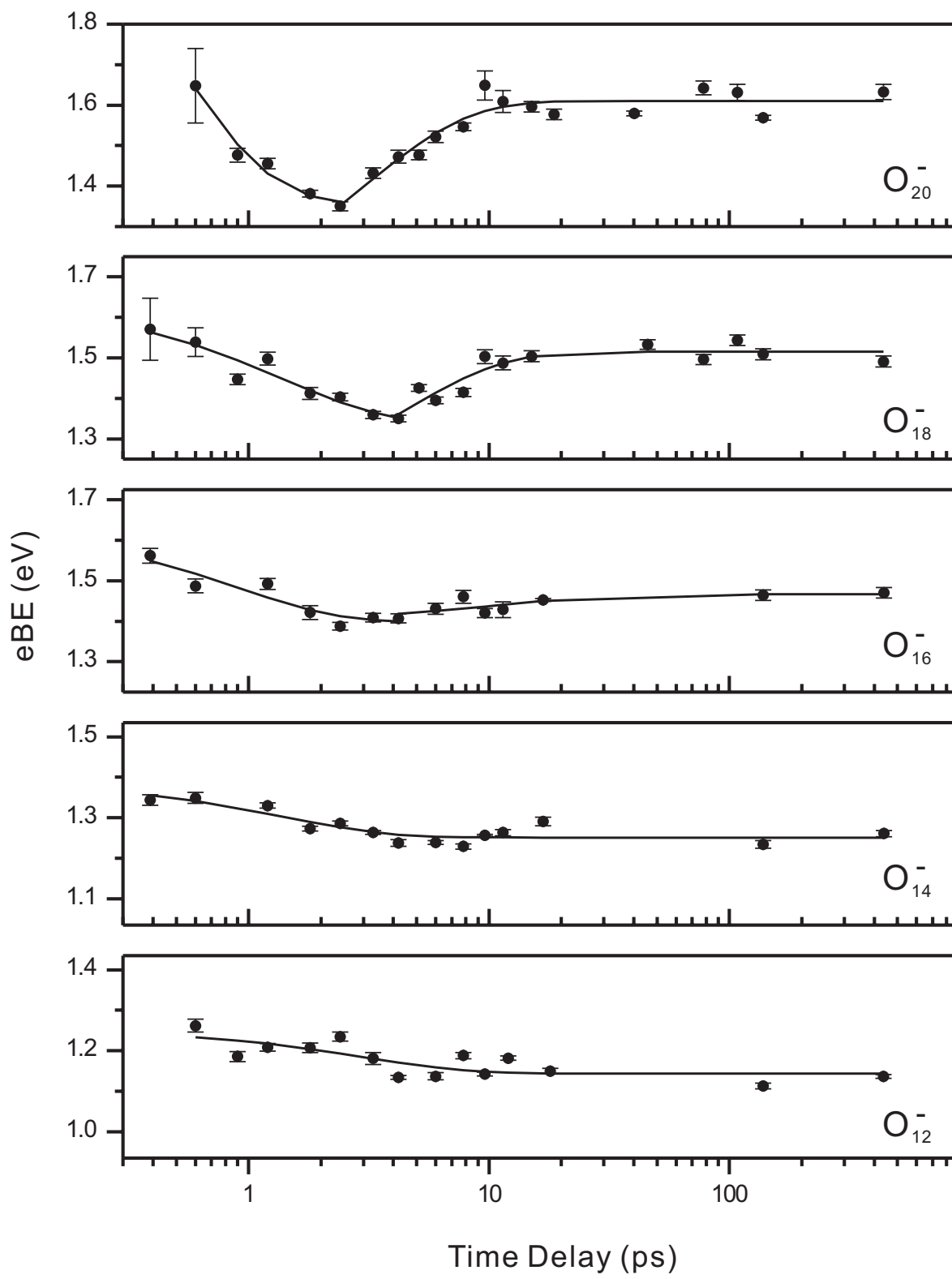


Figure 5.10

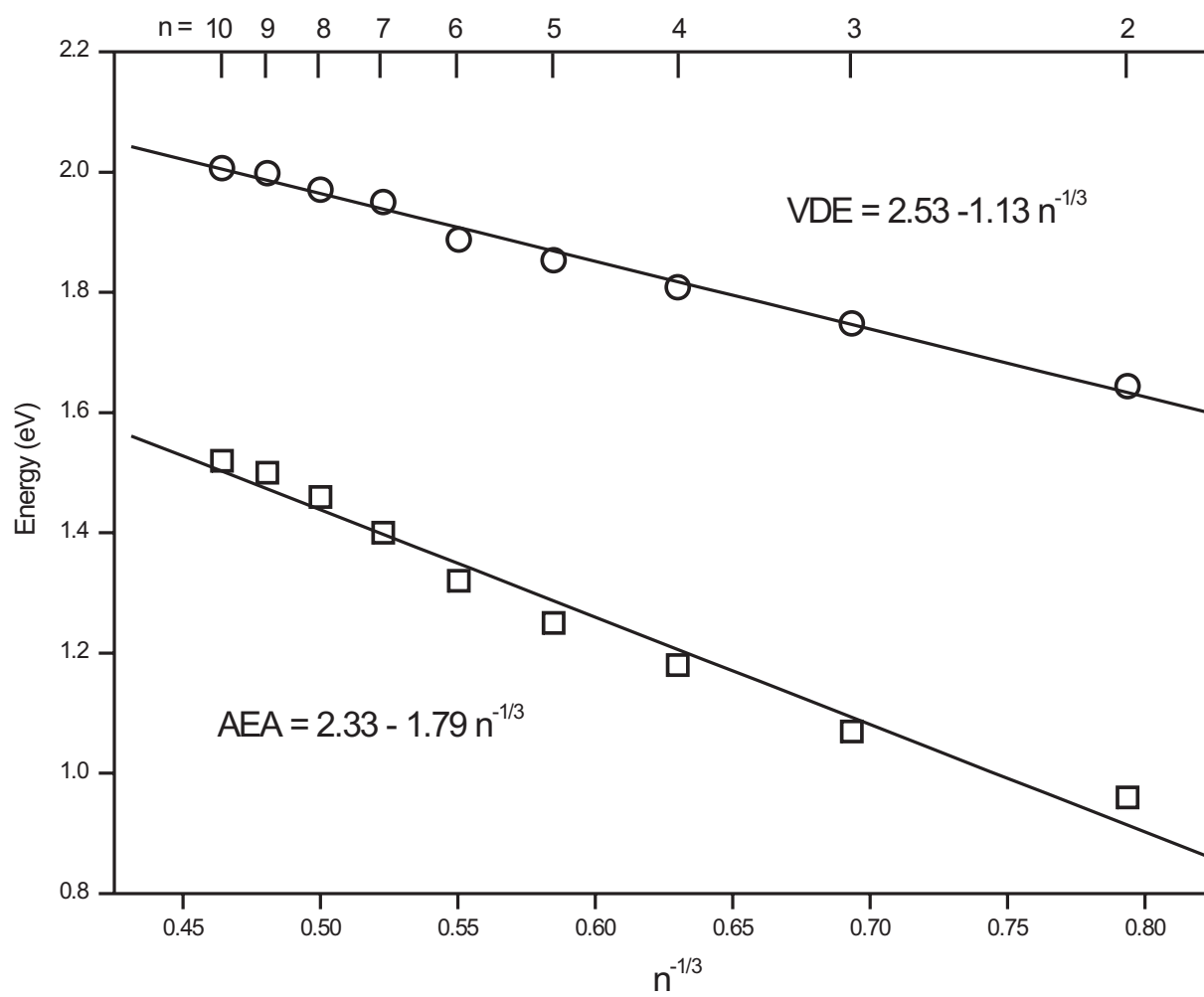


Figure 5.11

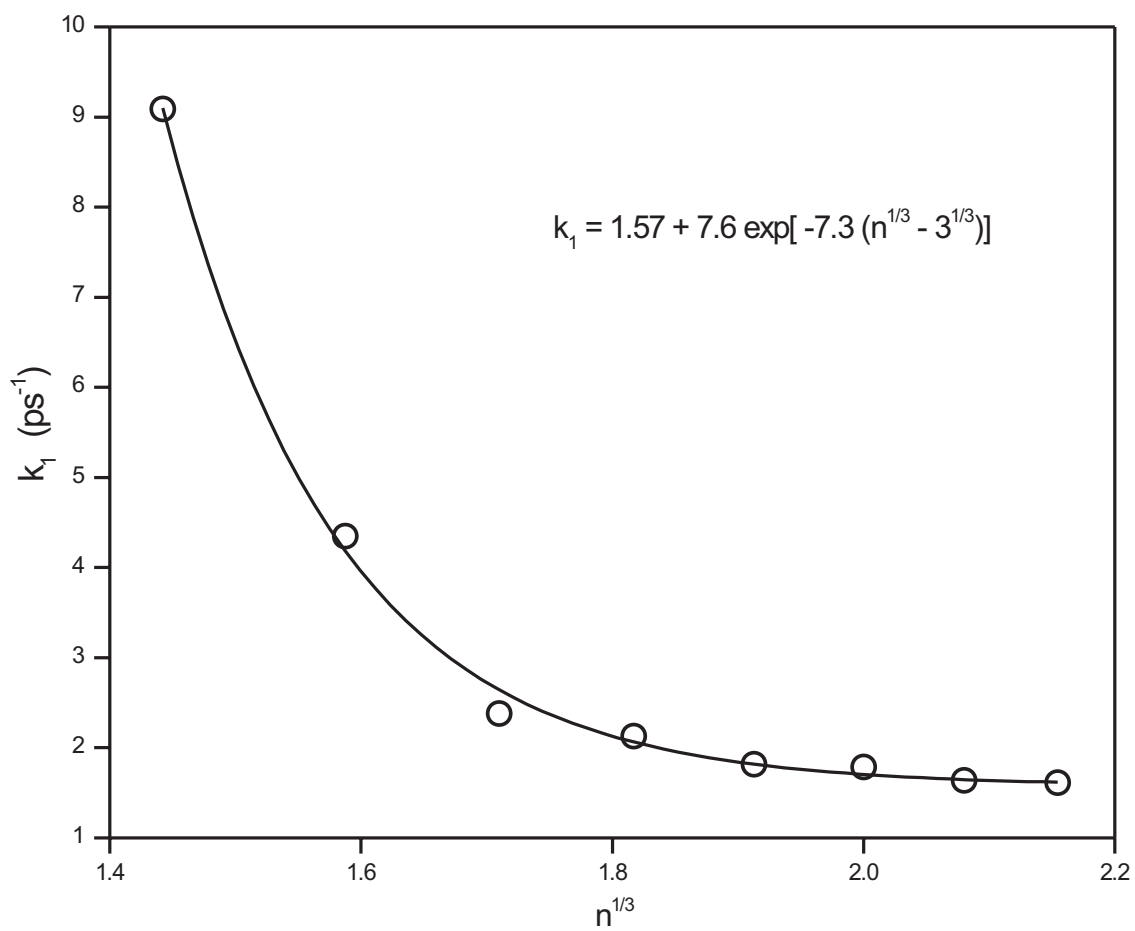


Figure 5.12

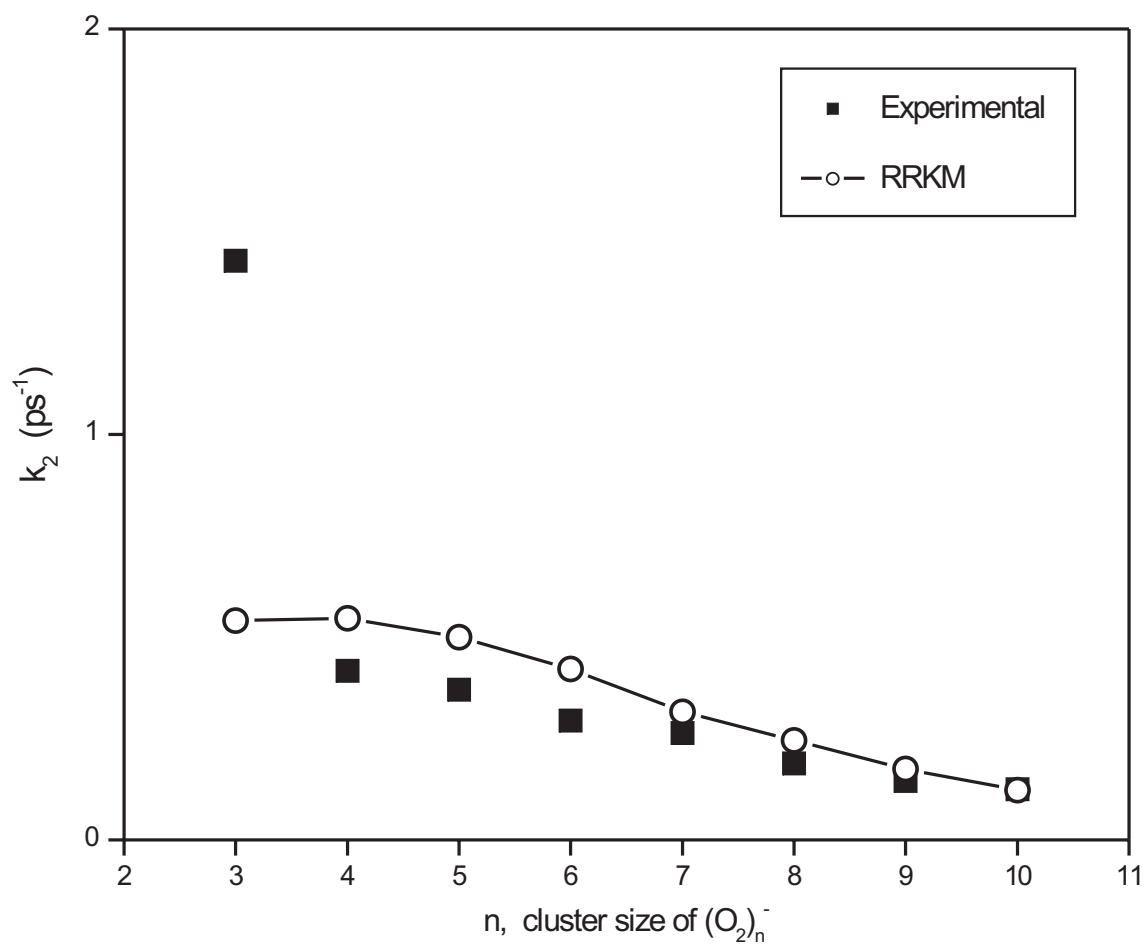


Figure 5.13

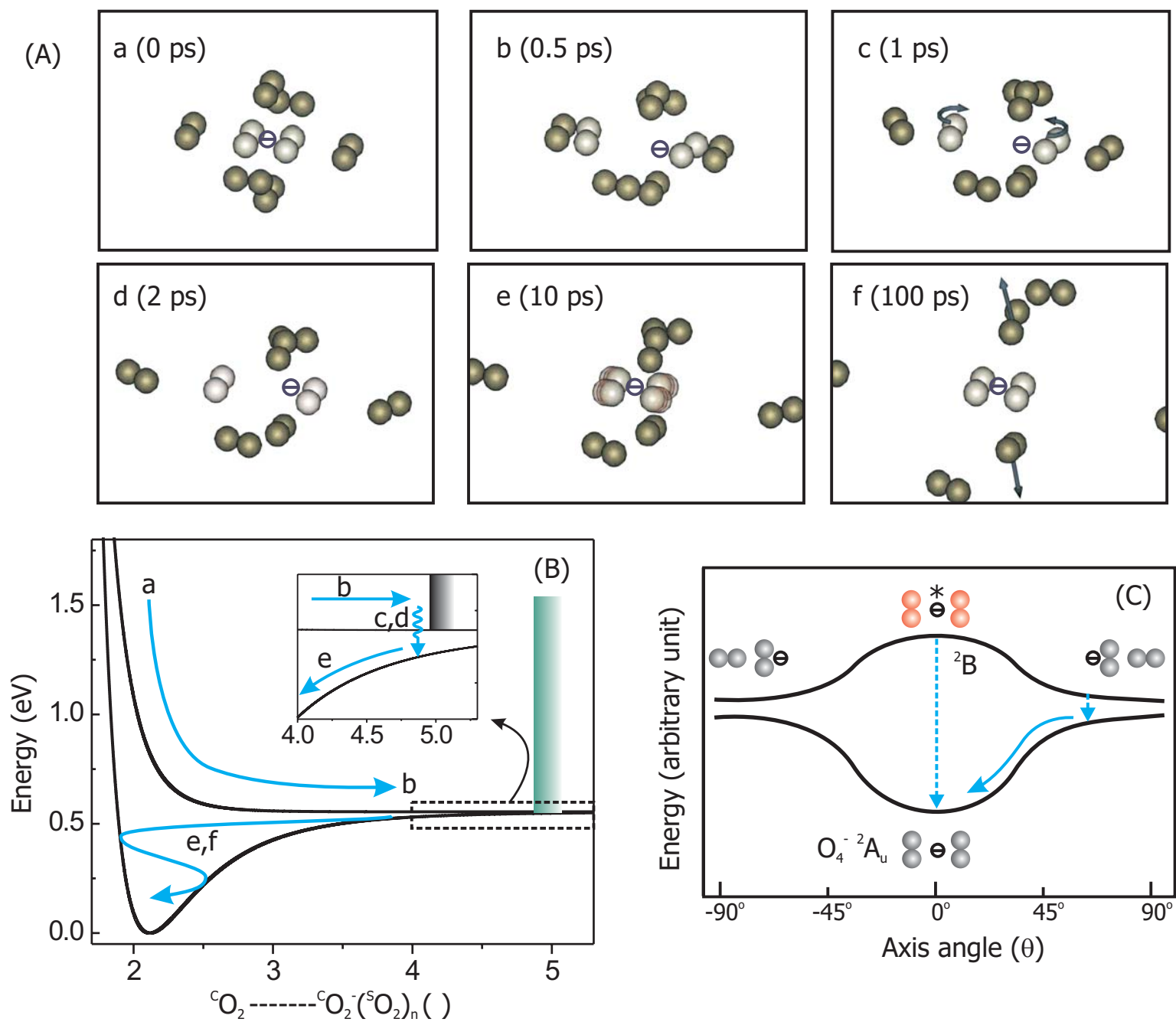


Figure Captions

Figure 5.1

PE spectra of $(\text{O}_2)_n^-$, $n = 2-10$ obtained by excitation at 400 nm with a fs pulse.

Figure 5.2

A plot of VDE vs. cluster size n . Inset: ΔVDE vs. n , $\Delta\text{VDE} = \text{VDE}(n) - \text{VDE}(n-1)$.

Figure 5.3

Fragment mass spectra observed from the dissociation of $(\text{O}_2)_n^-$, $n = 6-10$ using a 800 nm fs pulse. These mass spectra were obtained using the linear reflectron time-of-flight mass spectrometer. The parent cluster corresponding to each fragment spectrum is indicated on the right hand side. Inset: Fragment mass spectrum observed from the dissociation of $(\text{O}_2)_{26}^-$

Figure 5.4

Fragment PE spectra obtained from the differential fs pump/probe signal at 400 ps time delay and at time zero. The PE spectrum of $(\text{O}_2)_4^-$ (400 nm probe pulse only) is shown at the bottom for comparison. The parent anion corresponding to each fragment PE spectrum is indicated on the left hand side.

Figure 5.5

Femtosecond transients obtained by monitoring the fragment anions in the dissociation of $(\text{O}_2)_n^-$, $n = 6-10$ at 800 nm. All transients were fitted to a bi-exponential function. The τ_1 and τ_2 , and the ratio of amplitudes, γ ($\equiv A_1/A_2$), are indicated for each of the parent anion shown.

Figure 5.6

A plot of k_1 vs. cluster size n . The inset shows the corresponding dependence for τ_1 .

Figure 5.7

A plot of k_2 vs. cluster size n . The inset presents the corresponding dependence for τ_2 .

Figure 5.8

Time-dependent fragment PE spectra with the time delays indicated. The spectra were obtained as a differential pump/probe PE at the time delay given and that of time zero.

Figure 5.9

Time-dependent fragment PE spectra of parent O_{20}^- . The solid line is a Gaussian profile (see text for details).

Figure 5.10

A plot of the peak position in the fragment PE spectrum as a function of the time delay. The error bars are indicated for the peak position (see text). The solid line is a fit to indicate the rate at which energy changes with time (see text).

Figure 5.11

The experimental and theoretical fits for the change of vertical detachment energy (VDE) and adiabatic electron affinity (AEA) against $n^{-1/3}$. The best values are shown.

Figure 5.12

The plot of k_1 vs. $n^{1/3}$. The data are fitted to an exponential function with best values given in the figure.

Figure 5.13

The plot of k_2 vs. n . The open circles are the calculated rates using RRKM theory and the solid squares are the experimental results

Figure 5.14

Schematic representation of the dissociation and recombination dynamics in the O_{20}^- cluster. (A) Representation of snapshots at different times. The corresponding positions of the six frames are indicated on the potential energy surface in (B). The potential energy surface is sketched along the nuclear coordinate of forming O_4^- . The cO_2 and sO_2 represent the core O_2 and the solvent O_2 , respectively. The solvent wall is represented by a shaded bar. (C) A schematic diagram for the energetics of O_2^- and O_2 as a function of the angle between their molecular axes. The intermolecular distance is fixed to where the solvent wall is located. The dotted arrows represent the non-adiabatic transition from the repulsive surface to the ground state (2A_u) of O_4^- . The solid arrow describes the reorientation process.

CHAPTER 6.

**Femtosecond vectorial dynamics of anionic
clusters:**

**Heterogeneous clusters of azobenzene anion
solvated by oxygen molecules**

6.1. Introduction

Spectroscopy on mass-selected anionic clusters has been recognized as a versatile tool to carry out systematic studies on the stepwise solvation.¹⁻⁵ Rigorous mass-selection allows us to follow the evolution of bulk properties⁶⁻⁹ and examine the solvation dynamics as a function of cluster size.¹⁰⁻¹⁴ In earlier works, we have shown these aspects appeared in homogeneous and heterogeneous anionic oxygen clusters. In continuation of our efforts on oxygen-solvated anionic clusters, we have performed the femtosecond (fs) time-resolved photoelectron spectroscopy (PE) to study the photodissociation of *trans*-azobenzene anion (AB^-) solvated by oxygen molecules. In this contribution, we present the photodetachment of the isolated AB^- and its oxygen clusters and provide photochemical data of $AB^-(O_2)_n$, $n = 0 - 4$ in gas phase, including photoelectron spectra and photofragment patterns. Our focus was on the dissociation dynamics of these finite-sized clusters taking place in femtosecond time scale.

In our experiment, we excite $AB^-(O_2)_n$ with the 800 nm femtosecond pulse, which generates AB^- , and detect the photoelectron of the nascent AB^- fragment detached by the 400 nm fs pulse. With the pump-probe scheme, we monitored the bond dissociation between AB^- and O_2 in real time, by changing the time delay between the two pulses. We observed bi-exponential rise of AB^- in our transients and rationalized the subpicosecond component of the AB^- rise based on the time-dependent PE spectra. We propose that the fast channel occurs via electron transfer followed by ultrafast electron recombination and provide experimental evidences supporting this mechanism. emphasize the critical role of O_2 in photo-induced electron transfer.

In our current study, we demonstrated that structural evolution of finite-sized clusters could be monitored by implementing femtosecond time-resolved anisotropy. The fs time-resolved anisotropy has been developed as a reliable method to determine molecular structures and monitor the vectorial dynamics occurring in femtosecond and picosecond regime.¹⁵⁻¹⁸ We applied this technique to study the structure and rotational motion of $AB^-(O_2)_n$ clusters and recognized change in the location of O_2 with respect to AB^- , upon going from AB^-O_2 to AB^-O_4 . Cluster effect on the rotational motion is examined by measuring the dephasing time of the initial alignment. By incorporating the calculated structures of AB^-O_2 and AB^-O_4 , we elucidate the cluster size dependence on the anisotropy decay and deduced the direction of the transition dipole moment for the photodetachment (probe) process.

6.2. Experimental

The molecular beam apparatus and the femtosecond laser system have been described in the previous chapters, and only brief description of experimental set up is provided here. The negatively charged $(AB)_m(O_2)_n^-$ clusters were generated by crossing 1.0 keV electron to the supersonic expansion of azobenzene/oxygen mixtures. The azobenzene / O_2 gas mixture was prepared by blowing the oxygen gas (400 kPa) through the sample oven which contained the azobenzene (Aldrich, 98%) vapor at 100 °C. Pulsed electric field (-2.0 kV) was applied to the accelerator, and negatively charged species were extracted to the field free time-of-flight region where the negative ion bunches were separated in their masses. Mass selection was achieved by applying pulsed electric field (± 500 V) to the interleaved massgate¹⁹, prior to the light interaction. After mass

selection, the desired species were intercepted with femtosecond laser pulses in a perpendicular configuration, and photoelectron and photofragments were generated. Photoelectron was collected by the magnetic-bottle²⁰ photoelectron spectrometer, while the photofragments were detected by the linear reflectron mass spectrometer.

Femtosecond pulse (800 nm/110 fs) was generated from the Ti:Al₂O₃ oscillator and the 800 nm pulse was amplified up to 5mJ by the regenerative and the two-stage multi-pass amplifiers. The 800 nm femtosecond pulse was frequency doubled by passing the light through a BBO crystal to generate the 400 nm pulse. The remaining 800 nm femtosecond light was used for the pump pulse, while the 400 nm light was used for the probe. Time delay between pump and probe pulses was implemented by the Michelson interferometer type translational stage which was controlled by a computer. Typical pulse energy of the 800 nm and 400 nm pulses were 1.1 mJ and 0.4 mJ, respectively. Light was collimated down to 4.0 mm in order to achieve the optimal overlap between the molecular beam and light pulses without causing multiphoton process. For time-dependent anisotropy experiments, polarization of the pump pulse was rotated with respect to the polarization of the probe pulse which was parallel to the photoelectron detection axis.

The possibility of multiphoton processes was excluded, based on the following studies of the pump pulse power dependence: First, we observed a slope of about 0.7 in the plot of $\log(I_{\text{signal}})$ vs $\log(I_{\text{pump}})$, indicating a one-photon absorption (linear) of the 800 nm photon. Second, we also recorded the transient behavior at half the pump power and observed the same transients. Accordingly, the transient signal reported here is for a one-

photon excitation at 800 nm, followed by a one-photon detachment at 400 nm (generated by SHG).

6.3. Results

Mass spectrum of $(AB)_m^-(O_2)_n$ is shown in Figure 6.1. Small amount of $(O_2)_n^-$, H_2O and $AB^-(H_2O)_n$ are indicated by asterisk. The broad ion peak centered at mass ~ 383 au (indicated by a question mark) is two peaks at mass = 382 and 383, which were separated in the linear reflectron mass spectrometer (not shown). The peak at 382 can be assigned as $(AB)_2^-H_2O$ and the mass separation of 32 correspond to its oxygen clusters, but the mass peak of 383 was not identified. The ion peaks for $(AB)_m^-(O_2)_n$ were relatively broad in comparison to $(O_2)_n^-$ peaks, indicating the presence of metastable species in ion packets.

Negatively charged metastable species were detected without light by the linear reflectron mass spectrometer. The intensity distribution of the metastable species is presented in Fig. 6.2 by a histogram, and the amplitudes shown in the figure were normalized with respect to the parent ion intensity. The normalized intensity of metastable species were in the range of 1 ~ 2 %, and the largest one was $(AB)_2^-O_2$ generated from $(AB_2)^-O_4$ (2.2 %). There was no $(O_2)_n^-$ metastable species detected by the reflectron except for very small amount (0.1%) of O_4^- generated from AB^-O_4 , which suggests that the excess electron is localized in AB, and AB^- is solvated by neutral O_2 molecules. Figure 6.3 shows the photofragment distribution produced upon irradiation with the 800 nm fs pulse. The height of the histogram corresponds to the enhanced intensity of photofragments, which is obtained by subtracting the intensity of metastable

species and then dividing by the intensity of parent ions. There are three noticeable features in Fig. 6.3. First, AB^- is the major photofragment in all clusters (2 ~ 8 %). Second, no $(O_2)_n^-$ was detected except for very small amount of O_2^- (0.2 %) and O_4^- (0.2 %) generated from AB^-O_2 and AB^-O_4 . Third, when an oxygen molecule was not attached to AB^- (e.g. AB^- , AB_2^- and AB_3^- (not shown)), photodissociation did not occur at 800 nm.

Figure 6.4 shows the photoelectron (PE) spectra of unsolvated AB^- and $AB^-(O_2)_n$ clusters obtained by irradiating 400 nm (3.1 eV) pulse only. The PE spectrum of AB^- exhibits a broad Gaussian type profile with the onset (adiabatic electron affinity) of ~ 1.0 eV and the peak (vertical detachment energy) of about 1.54 eV, but we did not observe any vibrational structure in the PE spectrum with our energy resolution. Our estimated adiabatic electron affinity (AEA) is about twice larger than the previously reported value (0.56 eV) which was obtained from the bracketing experiments.²¹ The discrepancy can be due to small Frank-Condon overlap of 0-0 transitions, resulting in overestimation of AEA. However, the difference can be due to the uncertainty in the entropy factors from the previous experiment. Photoelectron spectrum of AB^-O_2 resembles the PE spectrum of the unsolvated AB^- , but the spectrum is shifted toward higher electron binding energy (AEA ~ 1.2 eV, VDE = 1.73 eV). This is another evidence that the excess electron is localized in the azobenzene molecule and O_2 is weakly bound to AB^- . PE spectra of larger clusters, $AB^-(O_2)_n$, $n = 2 - 4$ are quite different from the PE spectrum of AB^- . Peaks are significantly shifted toward higher electron binding energy, while the onsets are not much shifted: For AB^-O_4 , AEA ~ 1.2 and VDE = 1.95 eV; for AB^-O_6 , AEA ~ 1.2, VDE = 2.18 eV; for AB^-O_8 , AEA ~ 1.2, VDE = 2.28 eV. The PE profile at the lower

electron binding energy can be assigned as the PE spectrum of the metastable AB^- which is much easier to be photodetached compared to $AB^-(O_2)_n$, and the broad PE spectra of these clusters can be attributed to the overlap of the parent photoelectron and the metastable photoelectron profiles.

Figure 6.5 shows the time-dependent photoelectron (PE) spectra of $AB^-(O_2)_n$ which are constructed from the total time-dependent signal (pump + probe at $t \geq 0$) minus the reference (pump + probe at $t < 0$). The polarization of pump pulse was oriented 54.7° with respect to the probe pulse, to be consistent with the magic angle scans presented in Fig. 6.6. The time dependent photoelectron signals match with the photoelectron spectrum of unsolvated AB^- . (bottom panel of Fig. 6.5) For all clusters, AB^- signature appears within 100 fs, and the intensity of AB^- simply increases as time delay increases. We did not observe peak shift or broadening of the envelope in the time-dependent PE spectra.

The femtosecond transients of the nascent AB^- rise in the dissociation of $AB^-(O_2)_n$ are shown in Fig. 6.6, which were obtained by integrating the time-dependent photoelectron signals shown in Fig. 6.5. The width and position of the boxcar gate was carefully adjusted in order to integrate the PE signature of AB^- not the intermediate clusters, $AB^-(O_2)_{n-m}$, $m < n$. The transient scans were repeated many times with different gate positions and widths within the photoelectron profile of AB^- , but same transient behavior was observed. Hence, the time constants in Fig. 6.6 correspond to the time taken to strip off all the oxygen solvents around AB^- . The transients presented in Fig. 6.6 are the magic angle scans $[I_{//}(t) + 2I_{\perp}(t)]$ constructed from perpendicular and parallel scans, which eliminates effects due to molecular orientation. About the same transients

as Fig. 6.6 were obtained for AB^-O_2 and AB^-O_4 when pump pulse is oriented 54.7° (magic angle) with respect to the probe pulse. (not shown) We also performed the polarization-dependent scans of probe pulse with respect to the detection axis, and same results were obtained. For all clusters, the transients exhibit two distinct components, and both time constants increase with increasing cluster size. We fitted the transients to a bi-exponential growth function, varying time constants (τ_1 and τ_2) and the amplitudes (A_1 and A_2) with the fixed autocorrelation response time (FWHM = 150 fs): For AB^-O_2 , $\tau_1 = 320 \pm 30$, $\tau_2 = 1.8 \pm 0.3$ ps, $\gamma (\equiv A_1/A_2) = 3.5$; for AB^-O_4 , $\tau_1 = 570 \pm 20$ fs, $\tau_2 = 4.4 \pm 0.9$ ps, $\gamma = 6.8$; for AB^-O_6 , $\tau_1 = 680 \pm 20$ fs, $\tau_2 = 17.5 \pm 2.2$ ps, $\gamma = 4.6$; for AB^-O_8 , $\tau_1 = 800 \pm 30$ fs, $\tau_2 = 34 \pm 4.1$ ps, $\gamma = 2.8$.

The transient of AB^- rise is significantly dependent on the polarization angle between the pump and probe pulses. The transients with both parallel and perpendicular polarizations were obtained for all clusters, and the polarization dependence of AB^-O_2 was opposite to $\text{AB}^-(\text{O}_2)_n$, $n = 2 - 4$. From the parallel, $I_{\parallel}(t)$ and perpendicular, $I_{\perp}(t)$ scans, we obtained the time-dependent anisotropy, $r(t)$ as below:

$$r(t) = \frac{I_{\parallel}(t) - I_{\perp}(t)}{I_{\parallel}(t) + 2I_{\perp}(t)} \quad (1)$$

As we expected from Fig. 6.7, the time-dependent anisotropy decay of AB^-O_2 is opposite to the rest of larger clusters (Fig. 6.8): The anisotropy of AB^-O_2 starts at a negative value and approaches to zero, whereas the anisotropy of larger clusters start at positive values and decay to zero. This trend suggests that the transition dipole moments corresponding

to the pump and probe processes are perpendicular²² for $AB^{\cdot-}O_2$ and parallel for the other clusters. The decay time increase as cluster size increases, and the coherence time (τ_c), defined as the time taken to be one fourth of the initial anisotropy value¹⁵, were estimated and indicated in Fig. 6.8: 2.0 ps ($AB^{\cdot-}O_2$), 2.2 ps ($AB^{\cdot-}O_4$), 2.9 ps ($AB^{\cdot-}O_6$), 3.3 ps ($AB^{\cdot-}O_8$).

Figure 6.9 shows the geometry of $AB^{\cdot-}O_2$ and $AB^{\cdot-}O_4$ obtained from the *ab initio* calculations, using unrestricted B3LYP level of theory and 6-311G(d,p) as basis set. In both clusters, the excess charge is localized in the nitrogen atoms, and the geometry of azobenzene anion was about the same as the neutral azobenzene except for the elongated N-N bond distance. The oxygen molecules are located close to the N-N bond, and the midpoints of oxygen molecules in $AB^{\cdot-}O_2$ and $AB^{\cdot-}O_4$ are in the yz plane (see Fig. 6.9). The main difference between the two clusters is the location of oxygen molecules with respect to the z axis. The oxygen molecule in $AB^{\cdot-}O_2$ is located away from the z-axis (*i.e.* close to the plane of $AB^{\cdot-}$), whereas two oxygen molecules in $AB^{\cdot-}O_4$ are located near the z axis.

6.4. Discussion

Based on our experimental observations, we propose that the photodissociation of $AB^{\cdot-}(O_2)_n$, $n = 1 - 4$ occurs via electron transfer followed by ultrafast electron recombination as described below:



where $h\nu$ is the 800 nm pump photon energy, and $(AB\cdot O_2^-(O_2)_{n-1})^{*\ddagger}$ is charge transferred complex and ER stands for electron recombination. As discussed earlier in section III, our metastable study and photoelectron spectra of $AB^-(O_2)_n$ suggest that the excess electron is located in AB, and oxygen molecules are weakly bound to AB^- . Consistent result was obtained from the *ab initio* calculation which suggests that the excess electron is localized in the N-N double bond. For AB^-O_4 cluster, very small amount of metastable O_4^- was detected, which suggests that O_4^-AB is also generated, but not favored.

From the fragmentation study, it is inferred that when an oxygen molecule is attached to AB^- , there exists a charge transfer band around 1.55 eV (800nm) above the ground state of AB^-O_2 anion. Upon 800 nm excitation, electron migrates from AB^- to O_2 , forming $AB\cdot O_2^-$ followed by ultrafast electron recombination prior to dissociation. Clusters such as $(AB)_2^-$ and $(AB)_3^-$ did not dissociate although the binding energy between AB^- and AB is expected to be similar to the binding energy between AB^- and O_2^{23} , which implies that these clusters do not absorb 800 nm photon. On the contrary, AB^-O_2 can absorb the 800 nm photon by promoting the excess electron in AB^- to O_2 . In addition, small amount of O_2^- and O_4^- were generated for AB^-O_2 and AB^-O_4 besides the AB^- fragment, which supports the formation of the charge transferred complex, $AB\cdot O_2^- (O_2)_{n-1}$, but the predominant AB^- fragment indicates that the electron tends to transfer back to AB before dissociation occurs.

It is possible to think that O_2 perturbs the electronic state of AB^- such that an excited state of AB^- becomes accessible at 800 nm, without involving electron transfer and recombination processes. However, we think that the photo-induced intermolecular

electron transfer followed by ultrafast recombination is more probable for the absorption of 800 nm light and subsequent dissociation of $AB^-(O_2)_n$. The subject of electron transfer/recombination has been thoroughly investigated in this group for both neutral²⁴ and anionic clusters. Especially, we have found that oxygen play a significant role in the photo-induced electron transfer at 800 nm and examined this phenomenon in solvated oxygen anion: For example, we observed that $O_4^- \cdot X$, $X = Xe, N_2$ and N_2O does not dissociate while $O_4^- \cdot O_2$ dissociate at 800 nm.

There are two components with distinct time constants in the transient of AB^- rise with the fast component being the predominant one. The time scale of the fast (320 fs) component in AB^-O_2 reflects the direct bond dissociation of the reactive coordinate, $AB^- - O_2$. Since the pump process is involved in the charge transfer between AB^- and O_2 , the pump photon energy is likely to be deposited into the nuclear coordinate of $AB^- - O_2$. This energy is effectively used to break the bond between AB^- and O_2 , provided energy dissipation to other modes is not fast. Since the pump photon energy (1.55 eV) is much larger than the binding energy (~ 0.2 eV) of $AB^- - O_2$, the direct dissociation is expected to occur in femtosecond time scale. The small contribution of the slow component reflects the evaporation type predissociation of the remaining fractions.

The fast component (τ_1) is not significantly affected by the solvent size, in contrast to the slow component (τ_2). Upon going from AB^-O_2 to AB^-O_8 , τ_1 (320 \sim 800 fs) increases about three times while τ_2 (1.8 \sim 34 ps) increases about twenty times. As described earlier in section III, the time constants reported in Fig. 6.6 correspond to the time scales for all the oxygen molecules being removed from AB^- and leaving the naked AB^- . Surprisingly, the time scale of the fast component in AB^-O_8 is still subpicosecond,

implying that the production of AB^- is via a single bond breakage between AB^- and the conglomerated $(O_2)_n$, rather than one-by-one evaporation of oxygen molecules around AB^- . Moreover, our time dependent photoelectron spectra (Fig. 6.5) of $AB^-(O_2)_n$ show no apparent photoelectron signature (peak shift or broadening) of the intermediate $AB^-(O_2)_{n-m}$, $m < n$, which confirms that stepwise evaporation is not responsible for the fast process. Thus, the fast component of $AB^-(O_2)_n$, $n \geq 2$ describes the effective bond rupture between AB^- and $(O_2)_n$, and the delay in τ_1 with increasing solvent size can be ascribed to the perturbation of resonant electron recombination, as described in the previous chapters.

The contribution of the slow component increases (γ decreases) as cluster size gets larger, which is consistent with our mechanism that the fast process involves the electron transfer and recombination. The perturbation in electron recombination process hampers the rapid dissociation process and leaving more fractions undergo evaporative-type predissociation which is controlled by the intramolecular vibrational energy redistribution (IVR). The time scale of the slow components can be due to the stepwise evaporation of oxygen molecules as well as IVR. With our photoelectron spectrometer sensitivity, however we did not observe $AB^-(O_2)_{n-m}$, $m < n$ appearance in slow channel ($1 \sim 100$ ps). Note that fragmentation pattern in Fig 6.3 shows small amount of AB^-O_2 generated from AB^-O_4 and AB^-O_6 , however, the PE signature of AB^-O_2 was not detected in our time-dependent PE spectra. The PE signature of AB^-O_2 is likely to be embedded in the intense photoelectron profile of AB^- generated via fast channel.

As illustrated in Fig. 6.7, the transient of AB^- rise depends on the orientation of pump and probe polarizations, suggesting that the dissociation process exhibits time dependent vectorial dynamics. Based on our mechanism that pump pulse excitation

involves electron transfer from AB^- to O_2 , we can assume that pump pulse aligns AB^- (O_2)_n along the direction of electron motion. From the anisotropy values at time-zero (Fig. 6.8), we can determine the relative position of the electron receiving O_2 (\vec{r}_{AB-O_2}) with respect to the transition dipole moment of photodetachment process (\vec{d}_{PD}): For AB^-O_2 , $\vec{r}_{AB-O_2} \perp \vec{d}_{PD}$ and for AB^-O_4 , $\vec{r}_{AB-O_2} \parallel \vec{d}_{PD}$. Furthermore, incorporating the calculated structures of AB^-O_2 and AB^-O_4 , we can deduce the direction of \vec{d}_{PD} . According to *ab initio* structures illustrated in Fig. 6.9, O_2 in AB^-O_2 is located near the plane of the azobenzene molecule, whereas two oxygen molecules in AB^-O_4 are located perpendicular to the plane of AB^- . Thus, \vec{d}_{PD} is expected to be perpendicular to the plane of molecule, to be consistent with our anisotropy values and calculated structures. Characterizing the transition dipole moment of photodetachment process theoretical approach

For all clusters, the anisotropy values approach to zero within a few picoseconds, which indicates fast rotational dephasing of the initial alignment achieved by the pump pulse. The decay of the initial anisotropy can be attributed to the *inertial* motion of the clusters at finite temperature and the rotational motion of the nascent AB^- as a result of impulsive dissociation. In our system, the latter can be safely neglected, based on the following reasons: First, as shown in the *ab initio* structures of AB^-O_2 and AB^-O_4 , the lever arm distance (or impact parameter¹⁵) is almost zero with respect to the center of gyration. Second, if the force is along the \vec{r}_{AB-O_2} vector, then the interaction between O_2 and one of phenyl ring is expected to be small during the dissociation. Therefore, the force applied by impulsive dissociation results in translational motion of AB^- rather than rotation. The coherence time (τ_c) increases with increasing cluster size, and this trend can

be rationalized in terms of the *inertial* motion of the parent clusters since the torque effect is not significant as discussed above. In the first order approximation, molecules with larger moment of inertia (I) have slower angular velocity (ω) at a given temperature. [$k_B T \sim I\omega^2/2$] Provided the dissociation of $AB^-(O_2)_n$ does not affect the rotational motion of AB^- fragment, the angular velocity of the AB^- should be same as the angular velocity of non-dissociated $AB^-(O_2)_n$ to conserve its angular momentum.¹⁵ Therefore, the trend shown in τ_c simply follows the increase in moment of inertia, upon going from AB^-O_2 to AB^-O_8 .

Finally, it needs to be re-emphasized that the asymmetric solvation exhibited in $AB^-(O_2)_n$ is rather unique, in comparison to $I_2^-(CO_2)_n$. Parsons and his coworkers suggested that all four CO_2 molecules are in contact with I_2^- in $I_2^-(CO_2)_4$ which is analogous to $AB^-(O_2)_4$: Three oxygen molecules are around the waste of I_2^- and the fourth one is attached to one of I atoms, causing asymmetric charge distribution along the I_2 axis.²⁵ If $AB^-(O_2)_4$ has a similar solvent arrangement as $I_2^-(CO_2)_4$, it is not expected that all four O_2 molecules are stripped off in less than one picosecond. Instead, we propose that O_2 molecules tend to be clustered together, and the oxygen cluster $(O_2)_n$ sits on AB^- by forming a single bond between AB^- and $(O_2)_n$

One might speculate that the formation of the conglomerated $(O_2)_n$ is related to the tendency to form a dimeric O_4^- core^{26,27}, and we in fact found a few indirect evidences: First, no metastable form of AB^-O_2 was detected for AB^-O_6 and AB^-O_8 [Fig. 6.2]. The absence of metastable AB^-O_2 dictates that the second oxygen in AB^-O_4 is more tightly bound than the oxygen in AB^-O_2 . Second, O_4^- but not O_2^- was detected in photodissociation of AB^-O_4 . Third, we observed the change in the position of oxygen

molecules upon going from $AB^{\cdot-}O_2$ to $AB^{\cdot-}O_4$, favoring closer internuclear distance between two O_2 molecules.

6.5. Conclusion

In this article we have elucidated the dissociation dynamics of $AB^{\cdot-}(O_2)_n$, $n = 1 - 4$, involving photo-induced electron transfer, ultrafast electron recombination, bond rupture, and intramolecular vibrational energy redistribution. Evolution of these elementary processes as a function of cluster size was investigated by the femtosecond time-resolved photoelectron spectroscopy. Our femtosecond time resolution allows us to follow the structural evolution of $AB^{\cdot-}(O_2)_n$ upon going from $AB^{\cdot-}O_2$ to $AB^{\cdot-}O_8 - O_2$ in $AB^{\cdot-}O_2$ is located close to the plane of $AB^{\cdot-}$, whereas conglomerated $(O_2)_n$, $n = 2 - 4$ in larger clusters sits on the plane of $AB^{\cdot-}$. With *ab initio* calculations and our experimental data, we were able to unravel the complexity of rotational motion of the clusters and vectorial properties of transition dipole moments.

References

- ¹ A. W. Castleman, Jr. and K. H. Bowen, *J. Phys. Chem.* **100**, 12911 (1996).
- ² M. Nadal, S. Nandi, P. Wenthold, J. Kim, L. J. Andersen, Y. Ozaki, D. W. Boo, and W. C. Lineberger, in *Femtochemistry and femtobiology: ultrafast reaction dynamics at atomic-scale resolution: Nobel symposium 101101*, edited by V. Sundström (Imperial college press, London, 1997).
- ³ W. H. Robertson, E. G. Diken, E. A. Price, J. W. Shin, and M. A. Johnson, *Science* **299**, 1367 (2003).
- ⁴ R. Li, K. A. Hanold, M. C. Garner, A. K. Luong, and R. E. Continetti, *Faraday Discuss.* **108**, 115 (1997).
- ⁵ L. Lehr, M. T. Zanni, C. Frischkorn, R. Weinkauff, and D. M. Neumark, *Science* **284**, 635 (1999).
- ⁶ G. Markovich, L. Perera, M. L. Berkowitz, and O. Cheshnovsky, *J. Chem. Phys.* **105**, 2675 (1996).
- ⁷ S. T. Arnold, J. H. Hendricks, and K. H. Bowen, *J. Chem. Phys.* **102**, 39 (1995).
- ⁸ J. Li, X. Li, H. Z. Zhai, and L. S. Wang, *Science* **299**, 864 (2003).
- ⁹ M. Mitsui, A. Nakajima, and K. Kaya, *J. Chem. Phys.* **117**, 9740 (2002).
- ¹⁰ V. Vorsa, P. J. Campagnola, S. Nandi, M. Larsson, and W. C. Lineberger, *J. Chem. Phys.* **105**, 2298 (1996).
- ¹¹ A. Sanov, T. Sanford, S. Nandi, and W. C. Lineberger, *J. Chem. Phys.* **111**, 664 (1999).
- ¹² B. J. Greenblatt, M. T. Zanni, and N. D. M., *J. Chem. Phys.* **111**, 10566 (1999).
- ¹³ D. Ray, N. E. Levinger, J. M. Papanikolas, and W. C. Lineberger, *J. Chem. Phys.* **91**(10), 6533 (1989)
- ¹⁴ J. M. Papanikolas, V. Vorsa, M. E. Nadal, P. J. Campagnola, J. R. Gord, and W. C. Lineberger, *J. Chem. Phys.* **97** (9), 7002 (1992).
- ¹⁵ J. S. Baskin and A. H. Zewail, *J. Chem. Phys.* **98**, 3337 (1994).
- ¹⁶ J. S. Baskin and A. H. Zewail, *J. Phys. Chem. A* **105**, 3680 (2001).

- ¹⁷ P. M. Felker and A. H. Zewail, *J. Chem. Phys.* **86**, 2483 (1987).
- ¹⁸ A. H. Zewail, *Angew. Chem.* **39** (15), 2587 (2000)
- ¹⁹ R. Weinkauf, K. Walter, C. Weickhardt, U. Boesl, and E. W. Schlag, *Z. Naturforsch.* **44a**, 1219 (1989).
- ²⁰ P. Kruit and F. H. Read, *J. Phys. E: Sci. Instrum.* **16**, 313 (1983).
- ²¹ S. Ingemann, R. H. Fokkens, and N. M. M. Nibbering, *J. Org. Chem.* **56**, 607 (1991).
- ²² In this article, when the terms "perpendicular" and "parallel" were used to describe the orientations of transition dipole moments, "perpendicular" refers to an angle greater than 54.7 °, and "parallel" refers to an angle smaller than 54.7 °.
- ²³ The PE spectra of $(AB)_2^-$ and $(AB)_3^-$ resemble the PE spectra of AB^-O_2 with similar electron binding energy: For $(AB)_2^-$, AEA = 1.2 eV and VDE = 1.7 eV and for $(AB)_3^-$, AEA = 1.3 eV and VDE = 1.8 eV.
- ²⁴ D. Zhong, T. M. Bernhardt, and A. H. Zewail, *J. Phys. Chem. A* **103**, 10093 (1999).
- ²⁵ N. Delaney, J. Faeder, P. E. Maslen, and R. Parson, *J. Phys. Chem. A* **101**, 8147 (1997).
- ²⁶ M. J. DeLuca, C. C. Han, and M. A. Johnson, *J. Chem. Phys.* **93**, 268 (1990).
- ²⁷ C. R. Sherwood, K. A. Hanold, M. C. Garner, K. M. Strong, and R. E. Continetti, *J. Chem. Phys.* **105**, 10803 (1996).

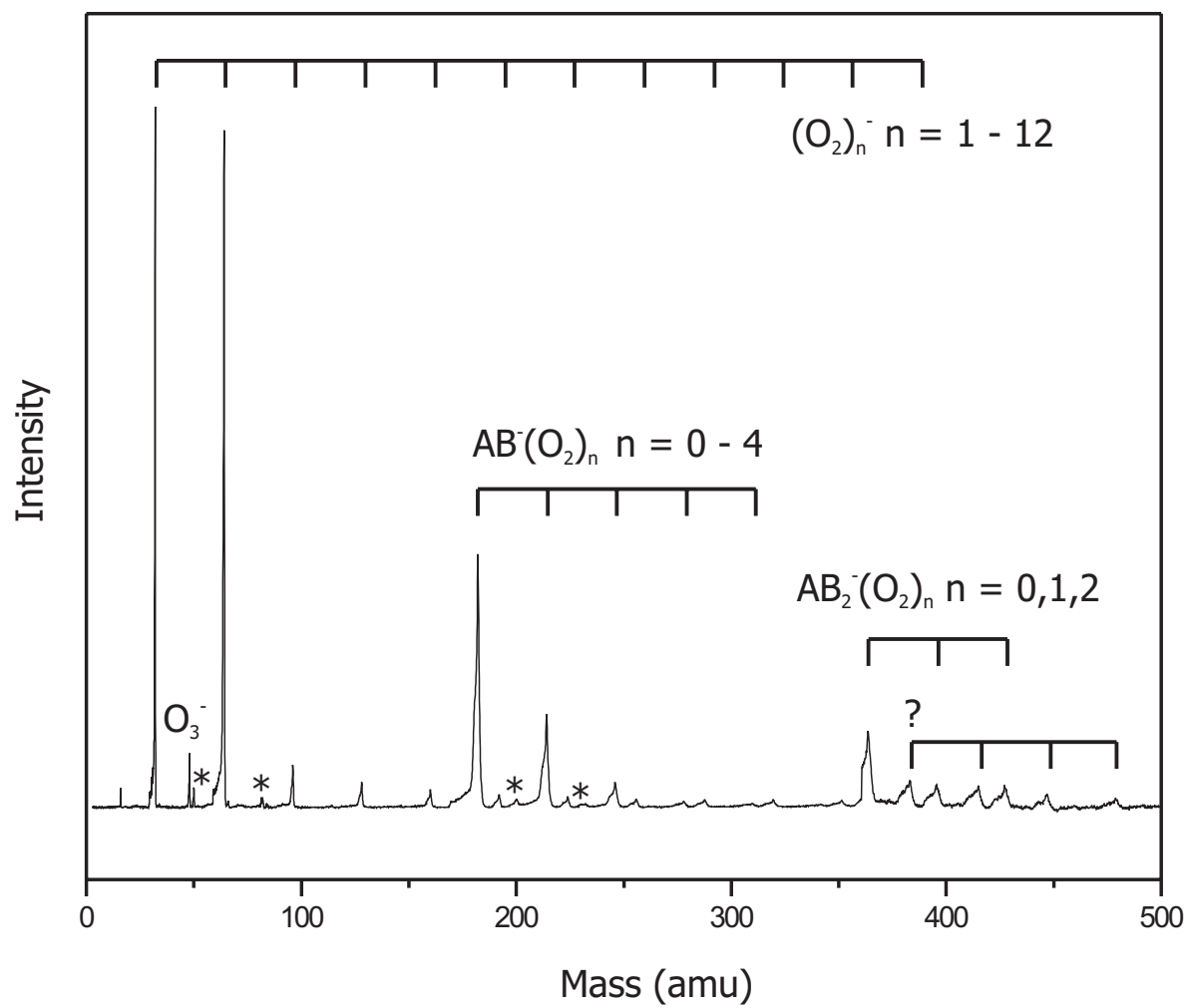


Figure 6.1

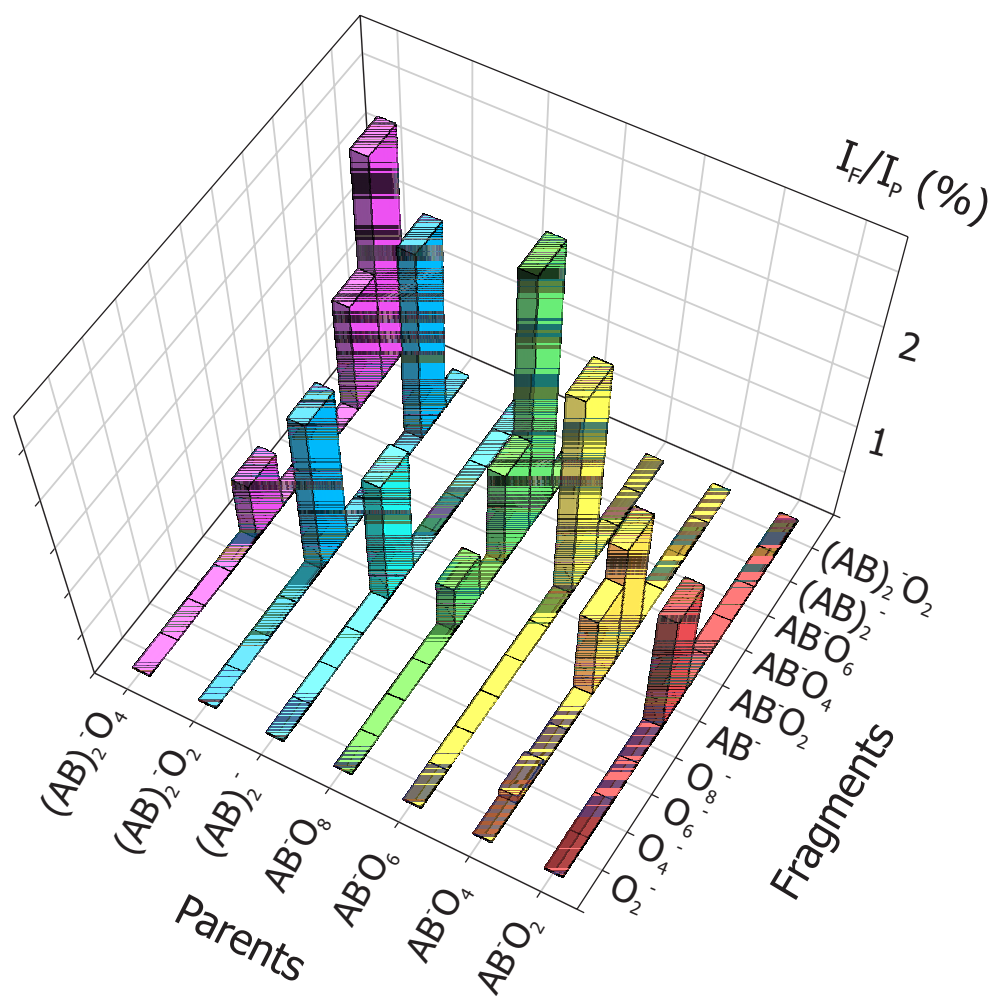


Figure 6.2

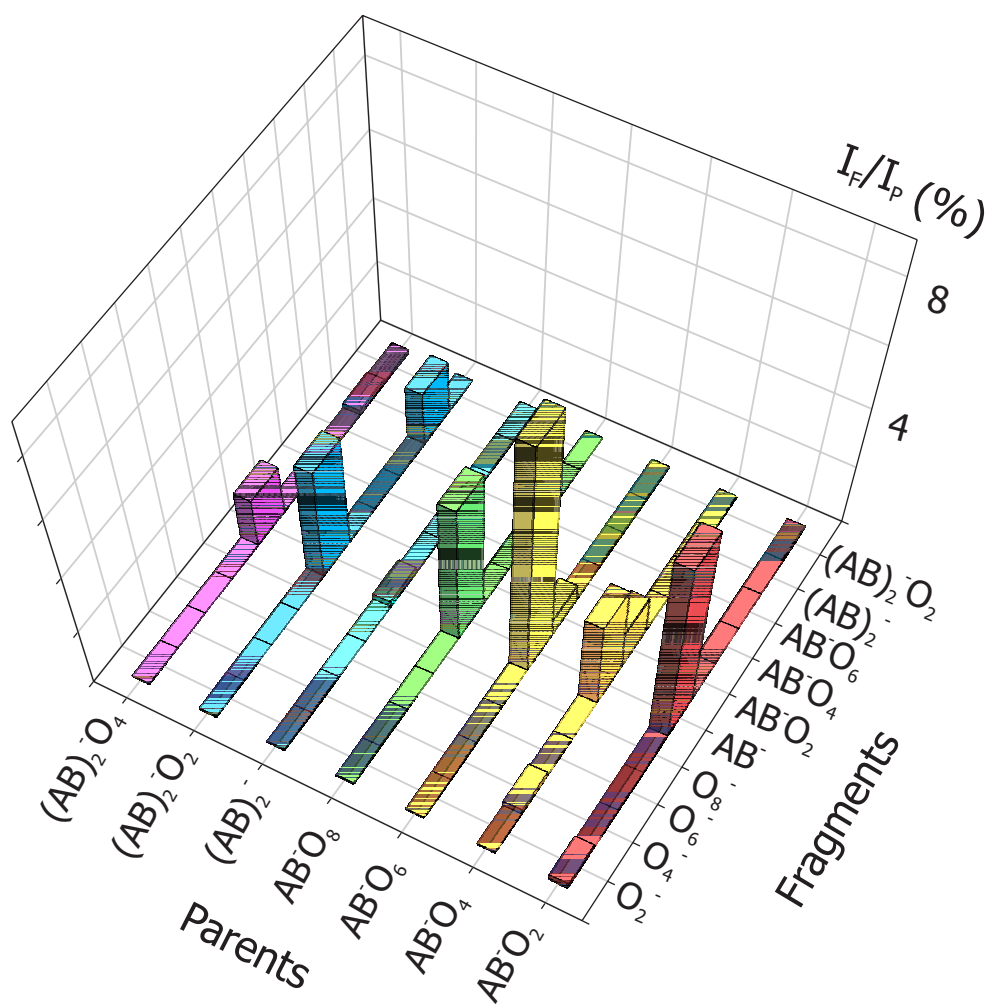


Figure 6.3

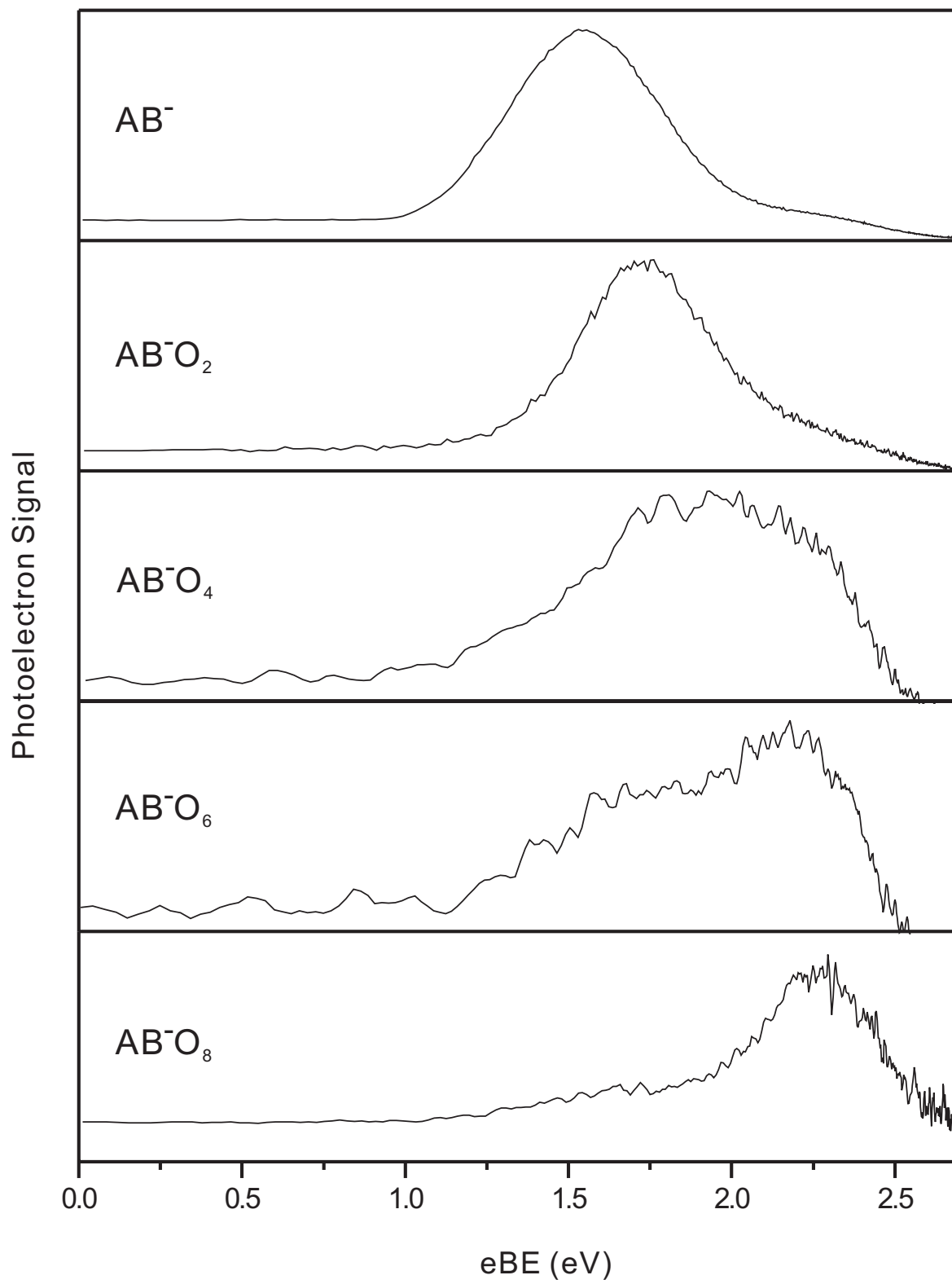


Figure 6.4

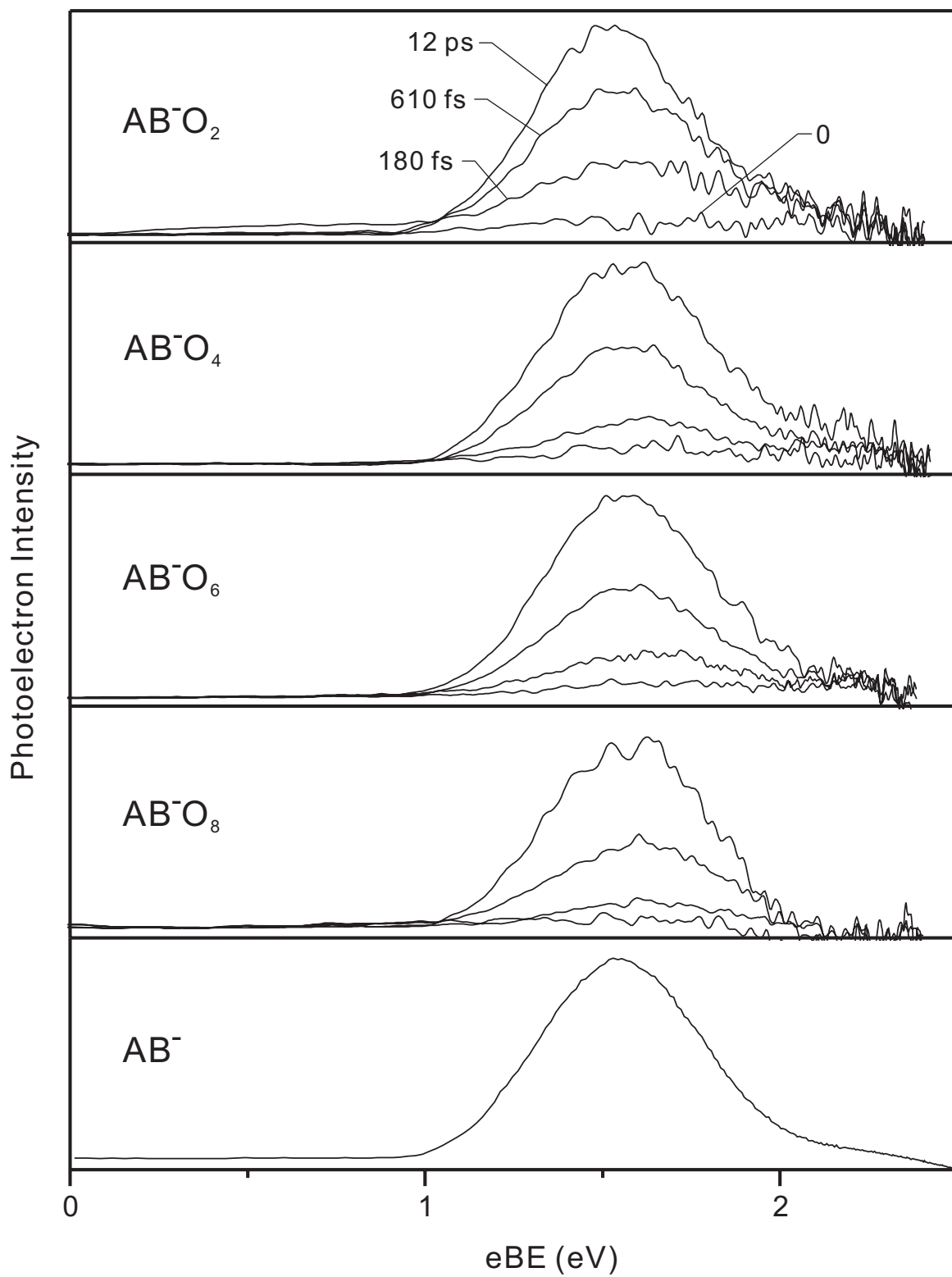


Figure 6.5

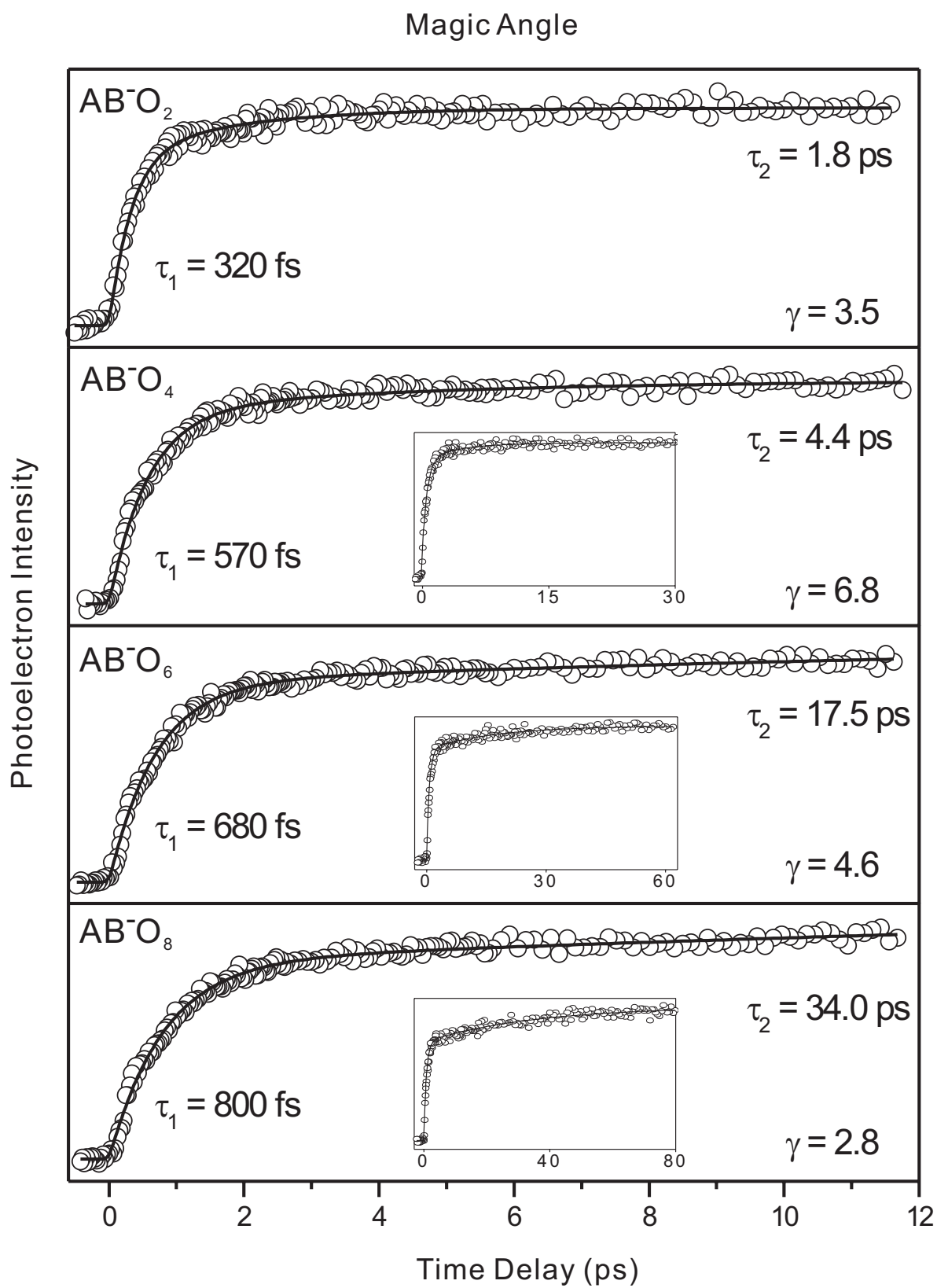


Figure 6.6

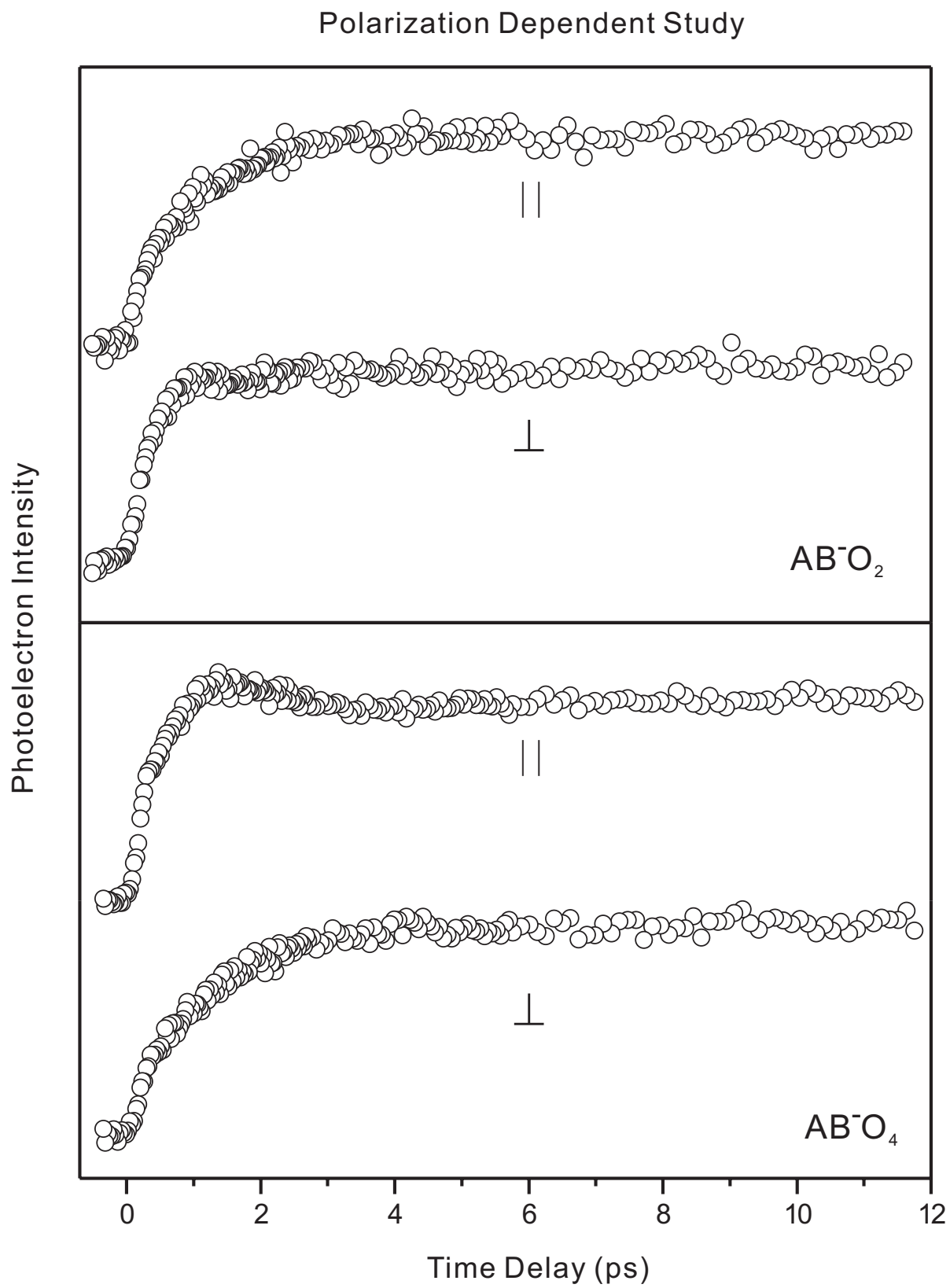


Figure 6.7

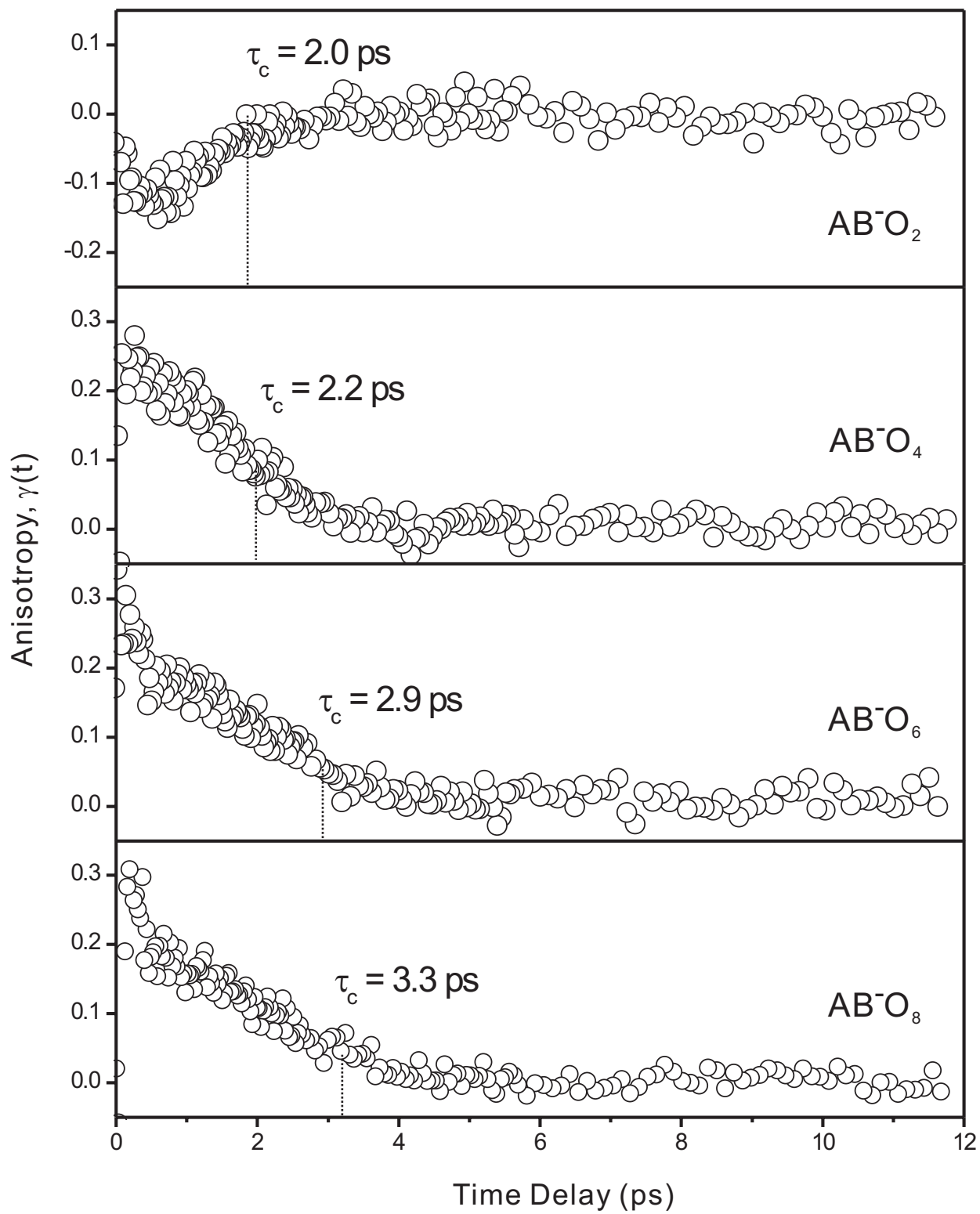


Figure 6.8

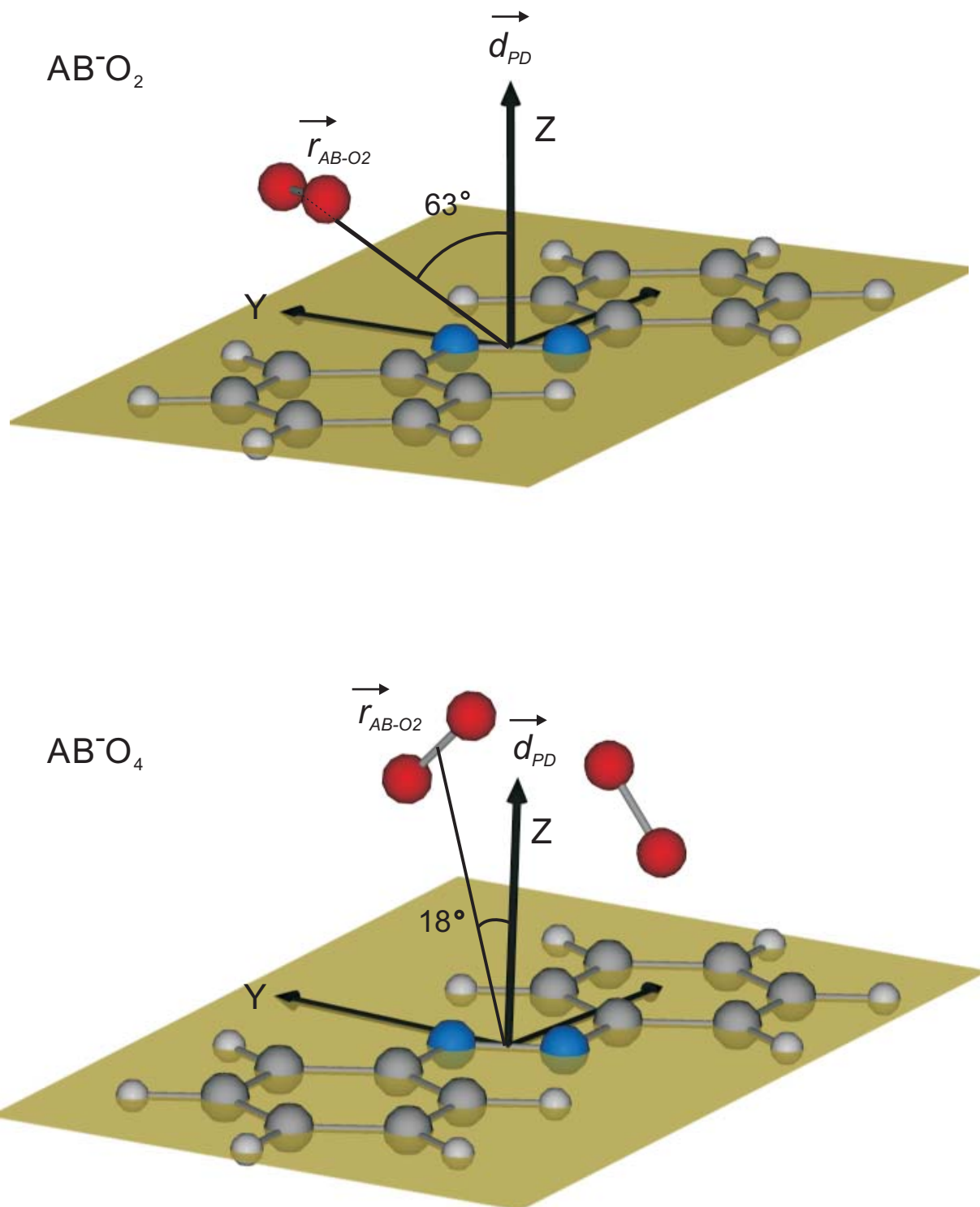


Figure 6.9

Figure Captions

Figure 6.1

Mass spectrum of $(AB)_m^-(O_2)_n$ generated by the pulsed electron impact source. The traces of $(O_2)_n^-H_2O$ and $AB^-(O_2)_n$ clusters are indicated by asterisks. The unidentified ion peak centered at mass = 383 au is indicated by a question mark. See text for details.

Figure 6.2

Metastable species detected by the linear reflectron time-of-flight mass spectrometer.

Figure 6.3

Photofragments generated at 800 nm. The vertical axis corresponds to the normalized fragment ion intensity (I_F) with respect to the parent ion intensity (I_P).

Figure 6.4

Photoelectron spectra of $AB^-(O_2)_n$, $n = 1 - 4$ obtained by excitation with a 400 nm (3.1 eV) fs pulse.

Figure 6.5

Time-dependent photoelectron (PE) spectra of $AB^-(O_2)_n$, $n = 1 - 4$. The spectra correspond to the total signal (pump + probe at $t \geq 0$) minus that of reference (pump + probe at $t < 0$). A set of four different time-dependent PE spectra at time delays of 12 ps, 610 fs, 180fs and 0 is presented in each panel, and the PE spectrum of AB^- obtained by irradiating the 400 nm pulse only was provided at the bottom for comparison. The amplitudes of the time-dependent PE spectra shown here are normalized according to our observed transients shown in Fig. 5.

Figure 6.6

Femtosecond transients obtained by monitoring the AB^- rise in the dissociation of $AB^-(O_2)_n$, $n = 1 - 4$ at 800 nm. The transients shown here are the constructed magic angle ($I_{\parallel} + 2I_{\perp}$) scans, and all transients were fitted to bi-exponential function. The τ_1 and τ_2 and the ratio of amplitudes, γ ($\equiv A_1/A_2$), are indicated. Long-range transient scans are presented as insets to illustrate the difference in τ_2 and γ .

Figure 6.7

Polarization-dependent transients of AB^- rise at 800 nm. Polarization of the probe pulse was fixed parallel to the photoelectron detection axis, while polarization of the pump pulse is rotated with respect to the polarization of the probe pulse. AB^-O_2 shows the polarization-dependent behavior opposite to the rest of larger clusters, $AB^-(O_2)_n$, $n = 2 - 4$, but only AB^-O_4 is provided for comparison.

Figure 6.8

Time-dependent anisotropy decay, $r(t) = (I_{\parallel} - I_{\perp}) / (I_{\parallel} + 2I_{\perp})$ obtained from parallel (I_{\parallel}) and perpendicular (I_{\perp}) transient scans. The estimated coherence times (τ_c) are indicated (see text for the definition of τ_c).

Figure 6.9

Calculated structures of AB^-O_2 and AB^-O_4 , using unrestricted B3LYP level of theory and 6-311G(d,p) as a basis set. The midpoints of O_2 molecules in AB^-O_2 and AB^-O_4 lie on the YZ plane. The force applied by the impulsive dissociation is expected to be along the \vec{r}_{AB-O_2} vector. The deduced transition dipole moment (\vec{d}_{PD}) for the photodetachment and the angle between \vec{r}_{AB-O_2} and \vec{d}_{PD} are indicated.

CHAPTER 7.

Femtosecond Dynamics of Hydrated Electrons in the Mesoscopic Water Clusters

7.1. Introduction

Dynamic nature of hydration has been recognized as a critical concept to elucidate the elementary processes exhibited in various aqueous solutions.^{1,2} The hydrated electron which is ubiquitous in physiological and biological systems is one of the simplest examples of solvation, but yet its photochemistry has not been clearly understood. Since Boag and Hart reported the spectroscopic evidence for the hydrated electron^{3,4}, numerous experimental⁵⁻¹² and theoretical¹³⁻¹⁸ works have been endeavored in order to understand the photochemical properties of the hydrated electron.

The research effort has been extended to the gas-phase analogue of hydrated electron, namely negatively charged water clusters, $(\text{H}_2\text{O})_n^-$. Since Harberland *et al.* have produced $(\text{H}_2\text{O})_n^-$ in the gas phase¹⁹, series of spectroscopic studies²⁰⁻³⁰ have been carried out for the size-selected $(\text{H}_2\text{O})_n^-$ clusters, with the hope of finding the smallest unit that represents the core motif^{31,32} of the bulk system. In spite of numerous experimental studies, there has been compelling arguments regarding the similarities between the clusters and the bulk system.^{15,23,26,28,29,33,34}

From the trend observed in the photoelectron spectra of $(\text{H}_2\text{O})_n^-$, Bowen and his coworkers proposed that $(\text{H}_2\text{O})_{11}^-$ is the embryonic hydrated electron showing the transition from the surface state to the internal state.²³ In contrast, Johnson and coworkers suggested that $(\text{H}_2\text{O})_{11}^-$ does not look like the core cavity but it has a linear 'chain-like' structure based on their infrared spectrum of $(\text{H}_2\text{O})_{11}^-$.²⁸ The recent *ab initio* calculation reported by Sobolewski and Domcke predicts that the excess electron is in the surface-state of $(\text{H}_2\text{O})_n^-$ for $n = 11$ and 14 .³⁴

In this paper, we report the femtosecond dynamics observed in hydrated electron clusters, $(\text{H}_2\text{O})_n^-$ ($n = 15, 20, 25$ and 30), which shows striking resemblance to the ultrafast dynamics of hydrated electrons in the bulk water. In our experiment, a desired size of $(\text{H}_2\text{O})_n^-$ was selectively intercepted by the 800 nm femtosecond laser pulse, which promoted the hydrated electron in the ground state to the upper electronic state(s). We followed the subsequent dynamics of this excited-state $(\text{H}_2\text{O})_n^-$ by monitoring the temporal evolution of the photoelectron spectrum generated by 400 nm probe pulse.

7.2. Experimental

Negatively charged water clusters, $(\text{H}_2\text{O})_n^-$ were generated by crossing continuous electron beam (1.0 keV) with the jet of $\text{H}_2\text{O}/\text{N}_2$ gas mixture which was prepared by blowing N_2 gas (250 kPa) through the sample vessel containing water vapor at room temperature. The $(\text{H}_2\text{O})_n^-$ clusters were directed into the field-free time-of-flight region by applying -2.0 kV electric pulse to the two-stage accelerator. In the field-free region, the $(\text{H}_2\text{O})_n^-$ clusters were separated by their masses, and the desired size of $(\text{H}_2\text{O})_n^-$ was intercepted with femtosecond laser pulses by adjusting the accelerator switching time with respect to the laser pulse arrival time.

The femtosecond laser pulse (110 fs) was generated from a Ti:Sapphire oscillator and amplified by the regenerative and the multi-pass amplifiers. The 800 nm pulse was frequency doubled by a BBO crystal to generate the second harmonic (400 nm). The remaining 800 nm was used as the pump pulse (excitation) while the 400 nm was used as the probe pulse (photodetachment). The photoelectrons were collected by the magnetic-

bottle photoelectron spectrometer, and the metastable and photofragment species were detected by the linear reflectron time-of-flight mass spectrometer. Femtosecond time-resolved transients were recorded by integrating the photoelectron intensity as a function of the pump-probe delay.

7.3. Results

Figure 7.1 shows the mass spectrum of $(\text{H}_2\text{O})_n^-$ clusters generated from the ion source. For all sizes of clusters, small amount of metastable $(\text{H}_2\text{O})_{n-1}^-$ and $(\text{H}_2\text{O})_{n-2}^-$ were detected without light, which suggests that $(\text{H}_2\text{O})_n^-$ clusters generated in the ion source are vibrationally hot, and up to two water molecules are evaporated during the flight time. Figure 7.2 shows the fragment mass-spectrum generated when a mass-selected ion was irradiated by 800 nm light. The positive and negative going peaks correspond to fragment-ion generation and parent-ion depletion, respectively. The negative going peaks of $(\text{H}_2\text{O})_{n-1}^-$ and $(\text{H}_2\text{O})_{n-2}^-$ in the fragment ion spectra are due to the presence of the metastable species.

The photoelectron (PE) spectra of $(\text{H}_2\text{O})_n^-$, $n = 15, 20, 25, 30,$ and 35 are shown in Fig. 7.3 and 7.4 which are obtained at 400 nm and 800 nm, respectively. Both onset and peak of the PE spectra shift toward low electron kinetic energy ($e\text{KE} = h\nu - \text{electron binding energy}$) as cluster size increases, and the breadth of PE spectrum becomes wider with increasing cluster size. The 800 nm spectra show a second peak at high eKE, which correspond to the PE signal generated by the two-photon absorption of 800 nm light. Compared to 400 nm spectra, the two-photon PE profiles are shifted to low eKE.

(Fig. 7.5) This shift is ascribed to the resonant process via bound excited states lying below detachment continuum.³⁰ The two-photon intensity decreases with decreasing cluster size, which implies that the excited state becomes detuned from the pump photon energy (1.55 eV).

Figure 7.6 displays the time-dependent PE spectra of $(\text{H}_2\text{O})_{35}^-$ at several time delays. Each spectrum is the difference spectrum which corresponds to the pump-probe PE signal minus the reference (pump-probe signal at 100 ps). It is clearly illustrated that the different regions of PE spectrum exhibit distinct temporal behaviors. At time zero, a small peak appears (upward arrow in Fig. 7.6) at eKE before the onset (region I), and this peak corresponds to PE signal generated by absorbing one photon of pump and one photon of probe light. The PE intensity near the onset (Region II; high eKE) decays with time, while the PE near the maximum of the spectrum (Region III; low eKE) displays an abrupt drop at time zero and a rise component.

To follow the temporal evolution shown in the PE spectrum of $(\text{H}_2\text{O})_{35}^-$, femtosecond time-resolved transients were recorded by integrating the PE intensity as a function of pump-probe delay. Three characteristic transients are obtained by integrating three different regions of the photoelectron profile. (Fig. 7.7 and 7.8) The 800-400 nm signal (Region I) shows a fast rise and a decay near time zero. Our observed data evidently displays the asymmetric shape of the transient signal which is fitted to a single exponential decay ($\tau_1 = 250$ fs) with a Gaussian convolution (FWHM = 300 fs).

The transient of region II shows a bi-exponential decay with two distinct time constants and a small contribution of a step-down offset. We fit the observed data with

bi-exponential decay and a step-function, and the time constants obtained for the two decay components are $\tau_2 = 1.1$ ps and $\tau_3 = 12$ ps. On the other hand, the transient of region III shows the sudden drop of the offset at time zero and an exponential rise at positive time delay. The observed data are fitted by a single exponential rise (940 fs) and a step-function. When the boxcar gate was located in between the position II and III, the transient shows just the step-down of the offset but no exponential rise or decay component.

Similar temporal behaviors were observed for $(\text{H}_2\text{O})_{30}^-$. Thus, the same kinetic equations as $(\text{H}_2\text{O})_{35}^-$ were used to fit the transients of $(\text{H}_2\text{O})_{30}^-$, and the following time constants were obtained: $\tau_1 = 150$ fs, $\tau_2 = 0.7$ ps, $\tau_3 = 13$ ps and $\tau_4 = 760$ fs. For $n = 15$, 20 and 25, the peak at region I and the rise component at region III are not observed, but the PE at region II exhibits bi-exponential decay (Fig. 7.9). The two time constants vary with cluster size, and the trends of τ_1 and τ_2 are shown in the Fig. 7.10.

7.4. Discussion

The temporal behaviors observed in the time-dependent photoelectron spectra elucidate the sequential relaxation pathways of internal conversion followed by solvent rearrangement and evaporation. Upon 800 nm excitation, most of $(\text{H}_2\text{O})_n^-$ clusters eject the excess electron by vertical detachment (step-down offset). But some fraction of $(\text{H}_2\text{O})_n^-$ clusters is promoted to the upper electronic state, which is evident in the observed fragmentation channel (Fig. 7.2) and the two-photon detachment (Fig 7.5 and Fig 7.6). Therefore, the transients reported here depict the dynamics of these $(\text{H}_2\text{O})_n^-$

clusters in which the excess electron remains bound after laser excitation.

Based on the energetics associated with the photoelectron spectrum, we assigned the region I as the PE originated from the upper electronic state(s), whereas the region II and III correspond to the photoelectrons generated from the high and low vibrational states of the electronic ground state.³⁶ (Fig. 7.11) With this picture in mind, the instantaneous rise and the fast decay shown in region I are viewed as the vertical excitation to the upper electronic state followed by rapid internal conversion to the electronic ground state. The decay time increases upon going from $(\text{H}_2\text{O})_{30}^-$ to $(\text{H}_2\text{O})_{35}^-$, but both time constants are comparable to the lifetime of the upper p -states measured for the hydrated electron in the bulk water.^{6,7,10,11} Like typical solvation process in condense process^{1,7,11}, the inertial solvent motions (libration) are expected to occur prior to the internal conversion, thus $1/\tau_1$ corresponds to the effective rate constant for the inertial solvent motion and the internal conversion. (Fig. 7.12)

The $(\text{H}_2\text{O})_n^-$ clusters in the high vibrational states decay via two different pathways with distinct time constants. Based on our measured time constants, the fast decay (τ_2) is attributed to the relaxation by solvent rearrangement (solvation) while the slow decay (τ_3) is understood by the evaporative dissociation. It is remarkable that our measured solvation time (τ_2) coincide with the typical time scale (~ 1 ps) of the solvation process by the diffusive rotation and translation of solvent exhibited in bulk systems.^{1,2}

As shown in Fig 7.9, the amplitude of the slow decay component (τ_3) increases with cluster size and shows a correlation with the fragment ion intensity detected in our mass spectrometer (Fig. 7.2), which is consistent with our decay mechanism by

evaporative dissociation. In addition, only up to three water molecules are removed upon 800 nm excitation, which is an indicative of pre-dissociation type evaporation.^{37,38}

If a repulsive-type bond rupture occurs in the cluster anions, small size fragment anions is likely to be generated by removing many solvent molecules.³⁸

Transient behavior at the region III shows depletion at time zero followed by partial recovery of the ground state $(\text{H}_2\text{O})_n^-$, and the difference in the offset corresponds to the photodetached electrons. The recovery time (τ_4) is very close to the fast decay (τ_2) of the high vibrational states, and we did not observe any slow rise component comparable to τ_3 . These experimental findings are consistent with our dynamic picture that the fast decay (τ_2) is due to solvation, while slow decay (τ_3) depicts the evaporation of water molecules.

For small clusters ($n = 15, 20$ and 25), photodetachment process dominates, and the transition to the bound electronic state is less favored, which accounts for the small amplitude of the decay component (region II) and the absence of the peak (region I) and the rise component (region III). Both τ_2 and τ_3 increase more or less with increasing cluster size, and this increasing progression can be explained as follow: In regards to τ_2 , it takes longer to rearrange more water molecules along the solvent coordinate. The time scale of τ_3 implies that intramolecular vibrational-energy redistribution will take place prior to evaporative dissociation hence the rate will be dictated by the density of states of the reactants (statistical limit).^{35,38}

7.5. Conclusion

In this work, we have presented the spectroscopic and kinetic data observed in the hydrated electron clusters, which displays the similar solvation dynamics to the hydrated electron in the bulk water. From the energy and time resolved photoelectron spectrum, the ultrafast processes occurring in the upper electronic states and the ground state were distinguished. With size-selecting capability, we also observed that the rates of solvation and evaporation decreases with increasing cluster size. Our experimental findings encourages the idea that understandings of mesoscopic properties will provide the molecular-level description of solvation phenomena exhibited in various condense-phase systems.

References

- ¹ S. K. Pal, J. Peon, B. Bagchi, and A. H. Zewail, *J. Phys. Chem. A* **106**, 12376 (2002).
- ² S. M. Bhattacharyya, Z.-G. Wang, and A. H. Zewail, *J. Phys. Chem. B* **107**, 13218 (2003).
- ³ E. J. Hart and J. W. Boag, *J. Am. Chem. Soc.* **84**, 4090 (1962).
- ⁴ E. J. Hart and M. Anbar, *The Hydrated Electron*. (Wiley-Interscience, New York, 1970).
- ⁵ A. Migus, Y. Gauduel, J. L. Martin, and A. Antonetti, *Phys. Rev. Lett.* **58**, 1559 (1987).
- ⁶ F. H. Long, H. Lu, and K. B. Eisenthal, *Phys. Rev. Lett.* **64**, 1469 (1990).
- ⁷ C. Silva, P. K. Walhout, K. Yokoyama, and P. F. Barbara, *Phys. Rev. Lett.* **80**, 1086 (1998).
- ⁸ A. Kummrow, M. F. Emde, A. Baltuska, M. S. Pshenichnikov, and D. A. Wiersma, *J. Phys. Chem. A* **102**, 4172 (1998).
- ⁹ K. Yokoyama, C. Silva, D. H. Son, P. K. Walhout, and P. F. Barbara, *J. Phys. Chem. A* **102**, 6957 (1998).
- ¹⁰ M. Assel, R. Laenen, and A. Laubereau, *J. Phys. Chem. A* **102**, 2256 (1998).
- ¹¹ R. Laenen, T. Roth, and A. Laubereau, *Phys. Rev. Lett.* **85**, 50 (2000).
- ¹² P. Kambhampati, D. H. Son, T. W. Kee, and P. F. Barbara, *J. Phys. Chem. A* **106**, 2374 (2002).
- ¹³ J. Schnitker and P. J. Rossky, *J. Chem. Phys.* **86**, 3471 (1987).
- ¹⁴ J. Schnitker, K. Motakabbir, P. J. Rossky, and R. Friesner, *Phys. Rev. Lett.* **60**, 456 (1988).
- ¹⁵ R. B. Barnett, U. Landman, C. L. Cleveland, and J. Jortner, *J. Chem. Phys.* **88**, 4429 (1988).
- ¹⁶ R. N. Barnett, U. Landman, and A. Nitzan, *J. Chem. Phys.* **89**, 2242 (1988).
- ¹⁷ F. J. Webster, J. Schnitker, M. S. Friedrichs, R. A. Friesner, and P. J. Rossky, *Phys. Rev. Lett.* **66**, 3172 (1991).
- ¹⁸ L. Turi and D. Borgis, *J. Chem. Phys.* **117**, 6186 (2002).

- ¹⁹ M. Armbruster, H. Haberland, and H. G. Schindler, *Phys. Rev. Lett.* **47**, 323 (1981).
- ²⁰ M. Knapp, O. Echt, D. Kreisler, and E. Recknagel, *J. Chem. Phys.* **85**, 636 (1986).
- ²¹ L. A. Posey and M. A. Johnson, *J. Chem. Phys.* **89**, 4807 (1988).
- ²² L. A. Posey, P. J. Campagnola, M. A. Johnson, G. H. Lee, J. G. Eaton, and K. H. Bowen, *J. Chem. Phys.* **91**, 6536 (1989).
- ²³ J. V. Coe, G. H. Lee, J. G. Eaton, S. T. Arnold, H. W. Sarkas, K. H. Bowen, C. Ludewigt, H. Haberland, and D. R. Worsnop, *J. Chem. Phys.* **92**, 3980 (1990).
- ²⁴ P. J. Campagnola, D. M. Cyr, and M. A. Johnson, *Chem. Phys. Lett.* **181**, 206 (1991).
- ²⁵ C. G. Bailey, J. Kim, and M. A. Johnson, *J. Phys. Chem.* **100**, 16782 (1996).
- ²⁶ P. Ayotte and M. A. Johnson, *J. Chem. Phys.* **106**, 811 (1997).
- ²⁷ P. Ayotte, C. G. Bailey, J. Kim, and M. A. Johnson, *J. Chem. Phys.* **108**, 444 (1998).
- ²⁸ P. Ayotte, G. H. Weddle, C. G. Bailey, M. A. Johnson, F. Vila, and K. D. Jordan, *J. Chem. Phys.* **110**, 6268 (1999).
- ²⁹ J. Kim, I. Becker, O. Cheshnovsky, and M. A. Johnson, *Chem. Phys. Lett.* **297**, 90 (1998).
- ³⁰ J. M. Weber, J. Kim, E. A. Woronowicz, G. H. Weddle, I. Becker, O. Cheshnovsky, and M. A. Johnson, *Chem. Phys. Lett.* **339**, 337 (2001).
- ³¹ L. Kevan, *Acc. Chem. Res.* **14**, 138 (1981).
- ³² H. Shiraishi, K. Ishigure, and K. Morokuma, *J. Chem. Phys.* **88**, 4637 (1988).
- ³³ J. Schnitker, P. J. Rossky, and G. A. Kenneywallace, *J. Chem. Phys.* **85**, 2986 (1986).
- ³⁴ A. L. Sobolewski and W. Domcke, *Phys. Chem. Chem. Phys.* **5**, 1130 (2003).
- ³⁵ It is expected that photodetachment of vibrationally excited $(\text{H}_2\text{O})_n^-$ generates photoelectrons at eKE before the onset. However, there is no apparent onset shift

was observed in the pump-probe signal compared to the PE spectrum obtained by the probe pulse only. This can be understood by the pre-existing hot band in the probe-only spectrum. As mentioned earlier, significant amount of vibrationally excited species are presented in the ion packet, which contributes the PE signals at high eKE (region II) in the probe-only spectrum.

³⁶ C. E. Klots, *J. Chem. Phys.* **83**, 5854 (1985).

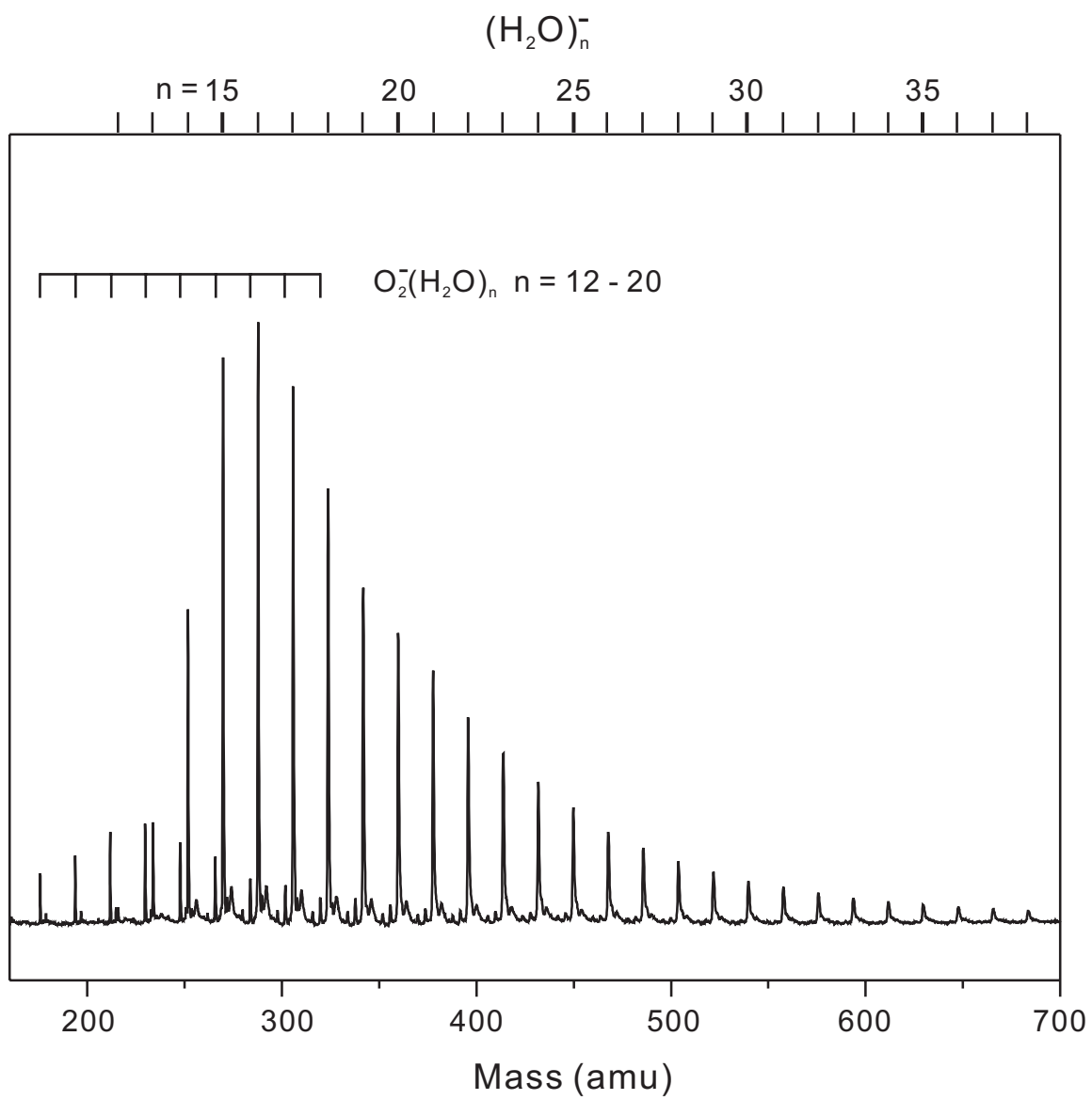


Figure 7.1

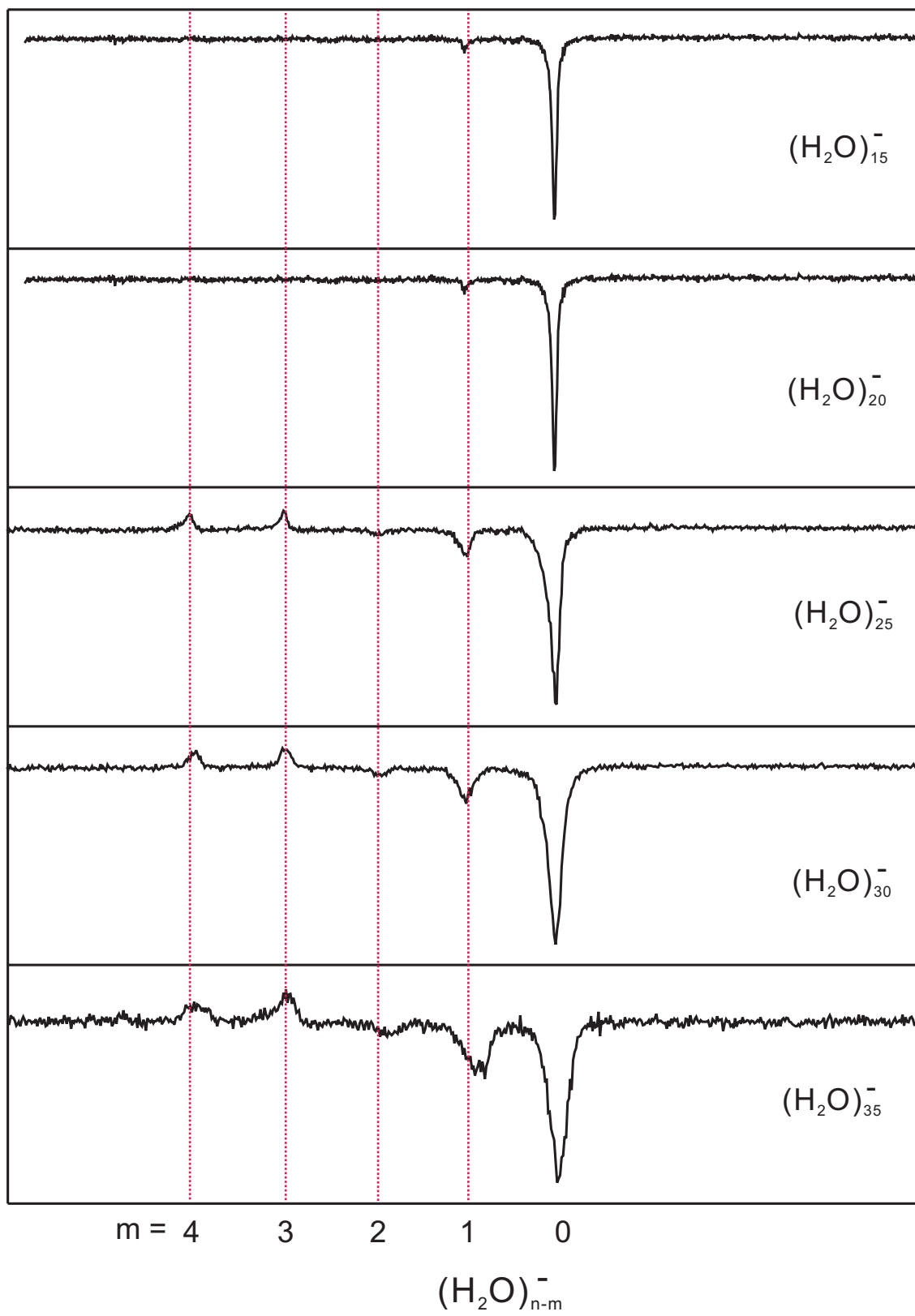


Figure 7.2

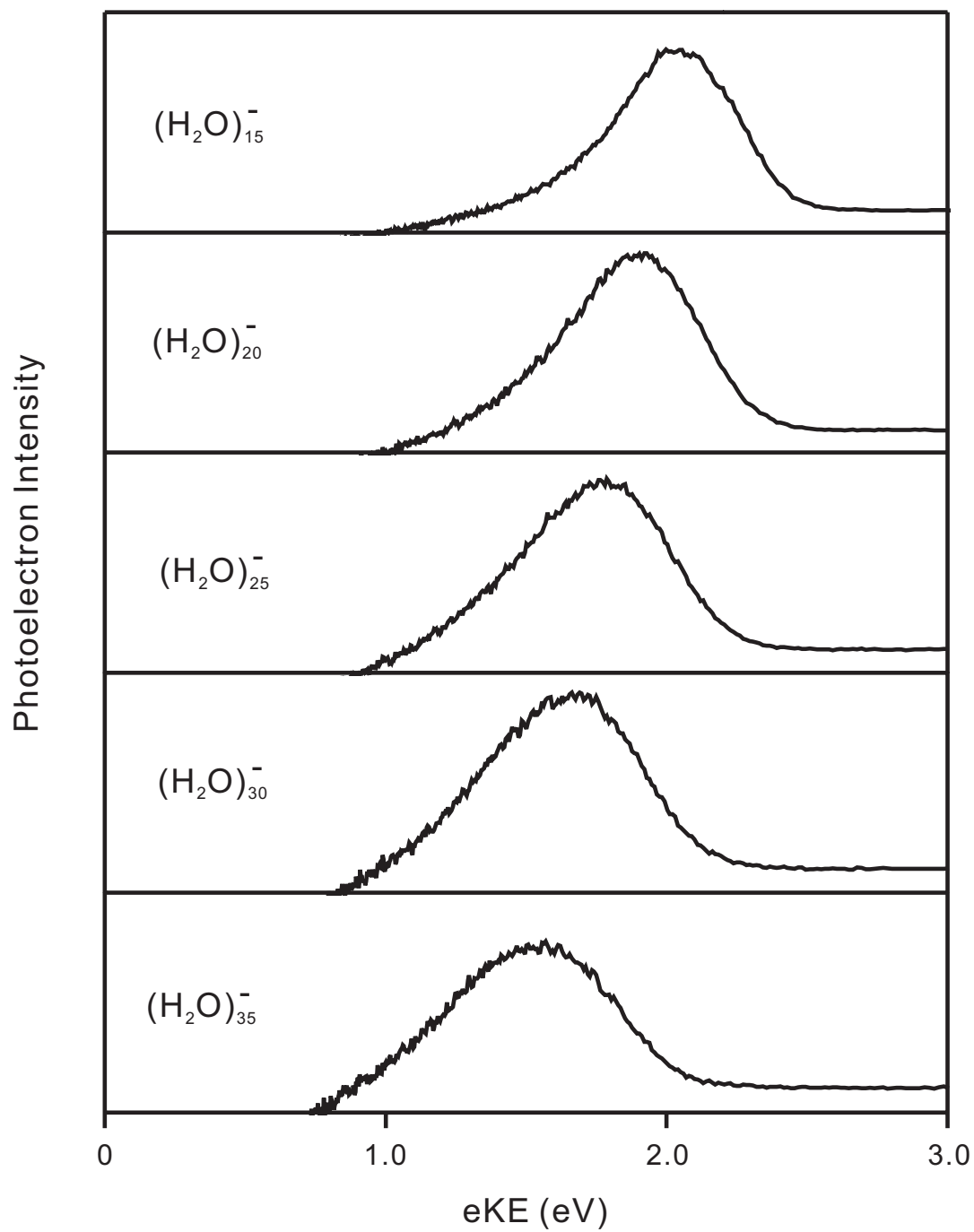


Figure 7.3

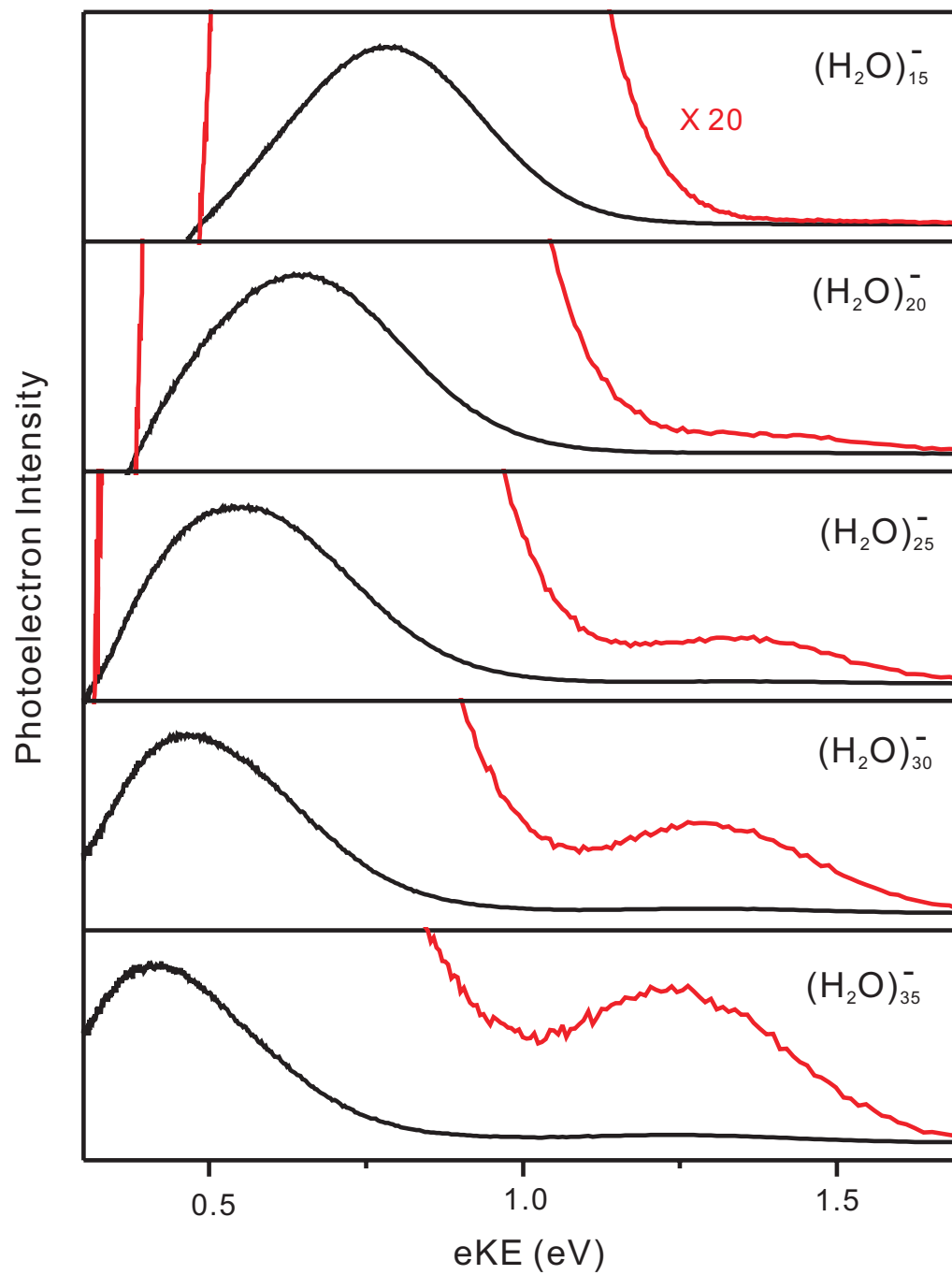


Figure 7.4

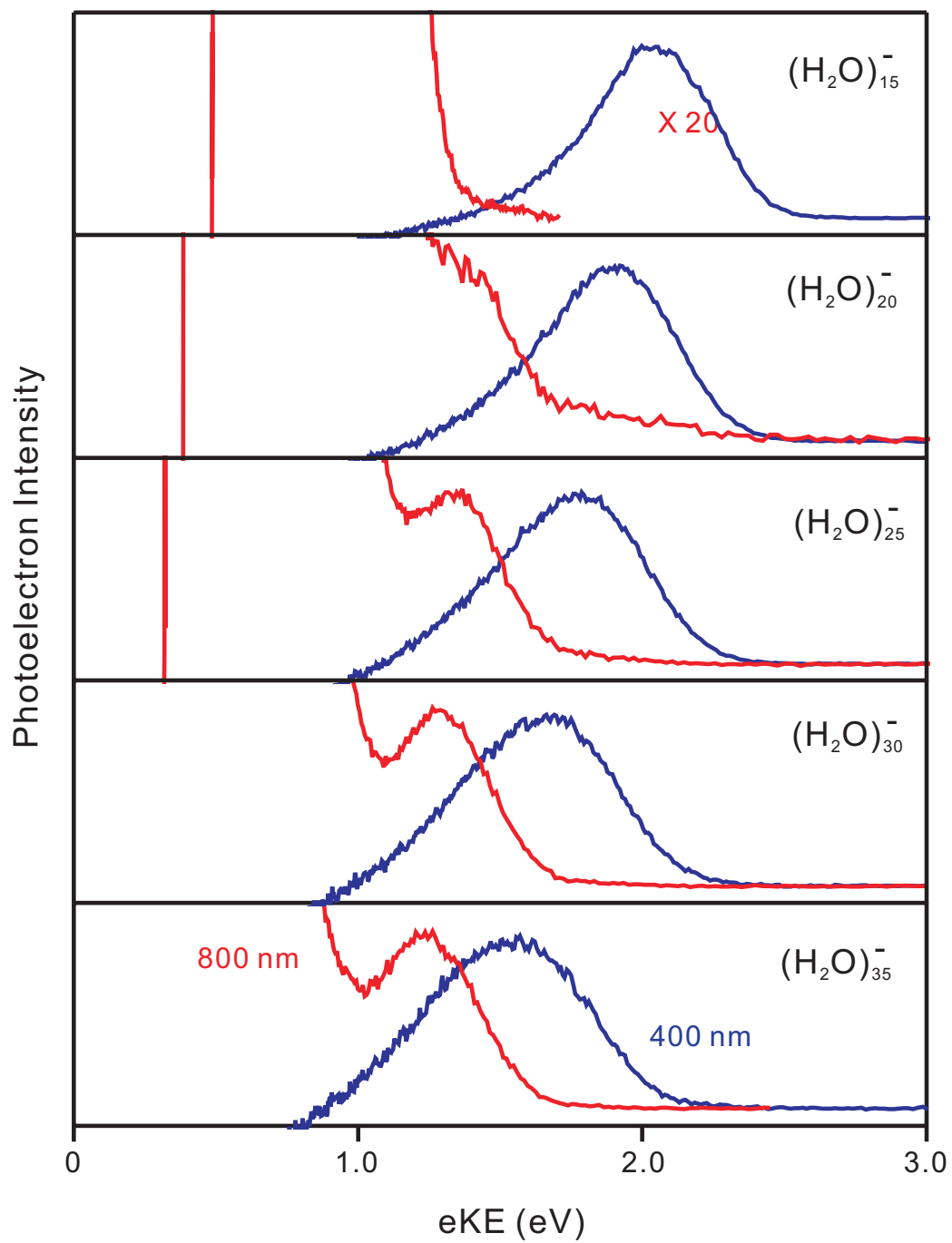


Figure 7.5

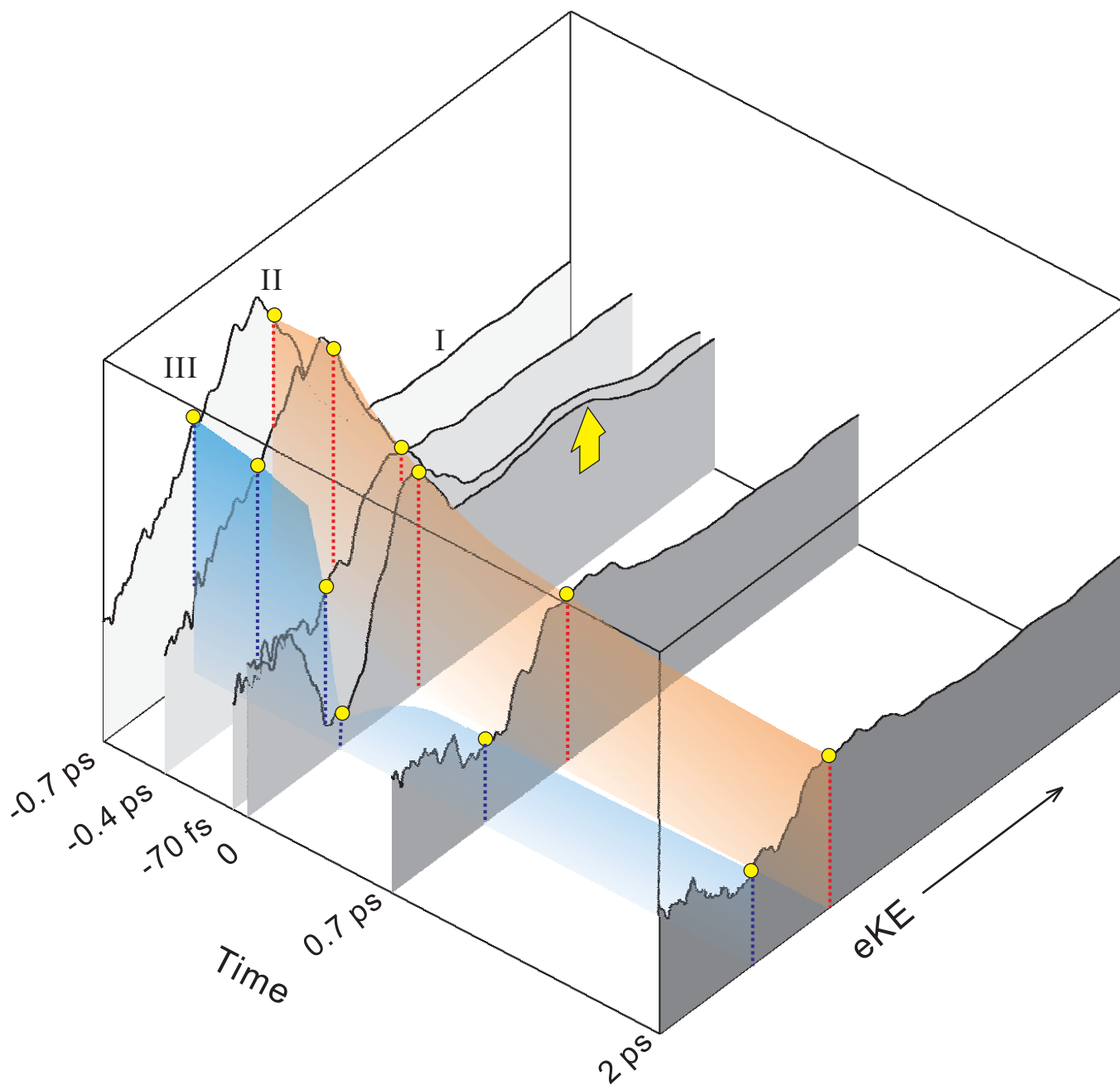


Figure 7.6

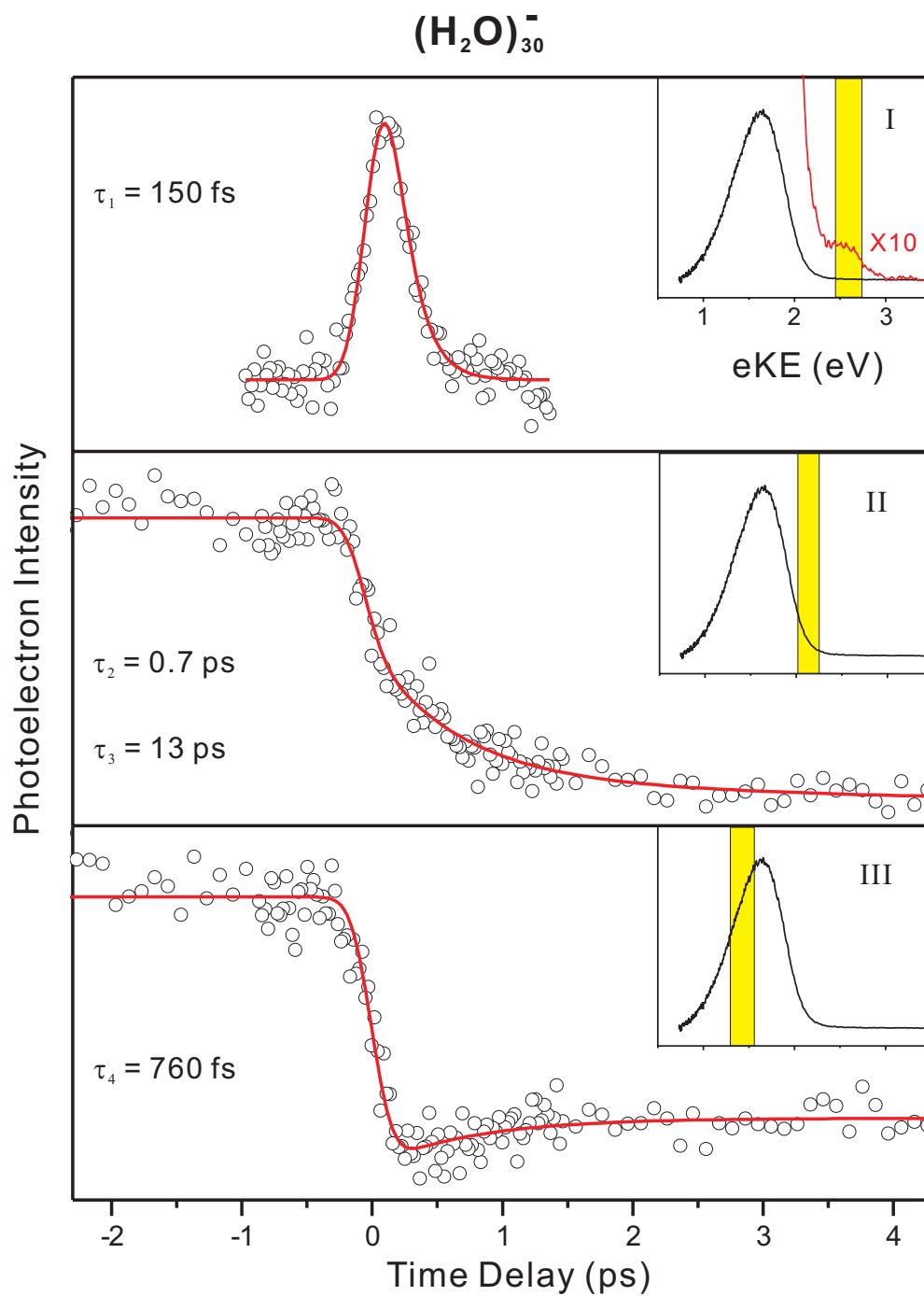


Figure 7.7

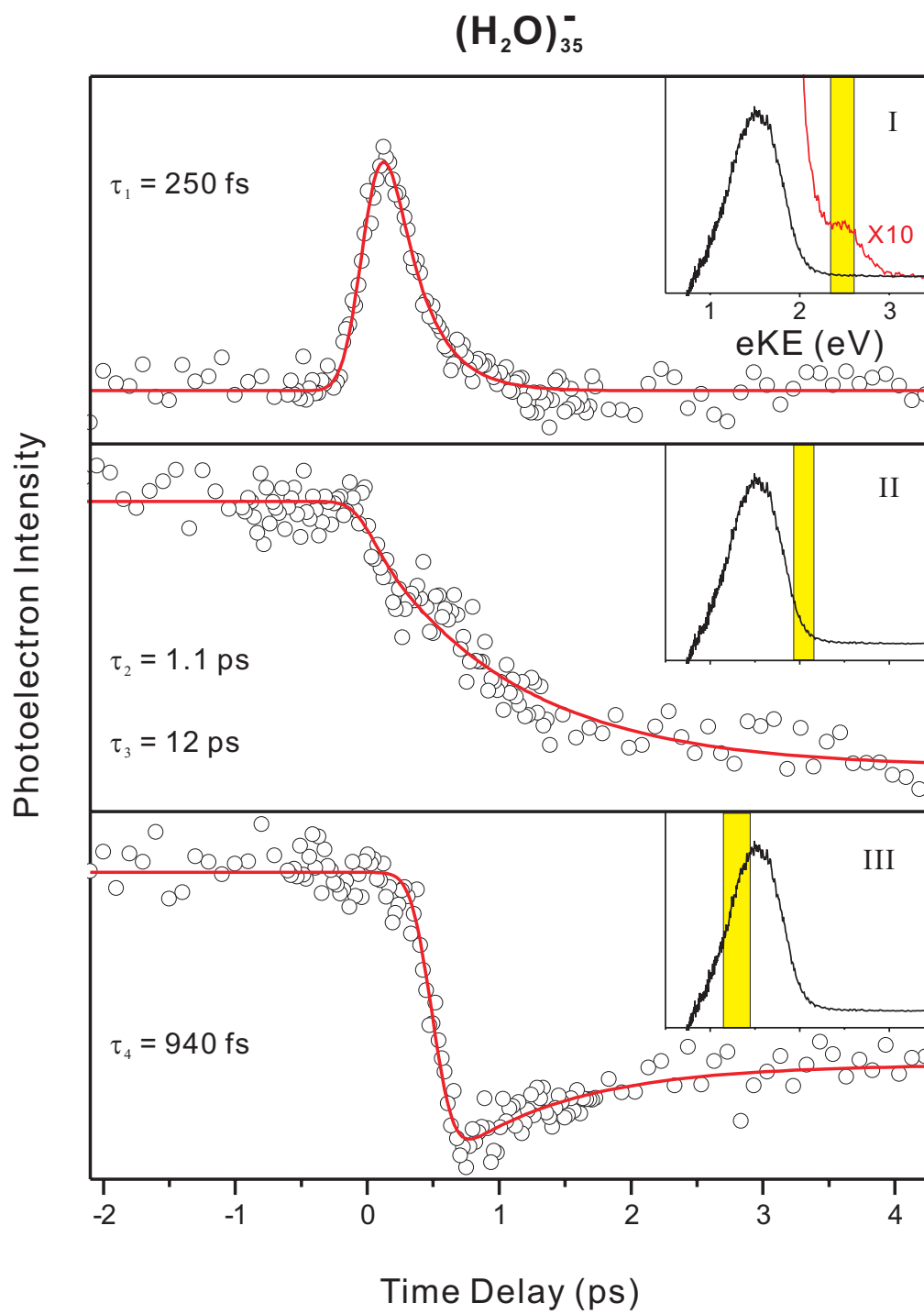


Figure 7.8

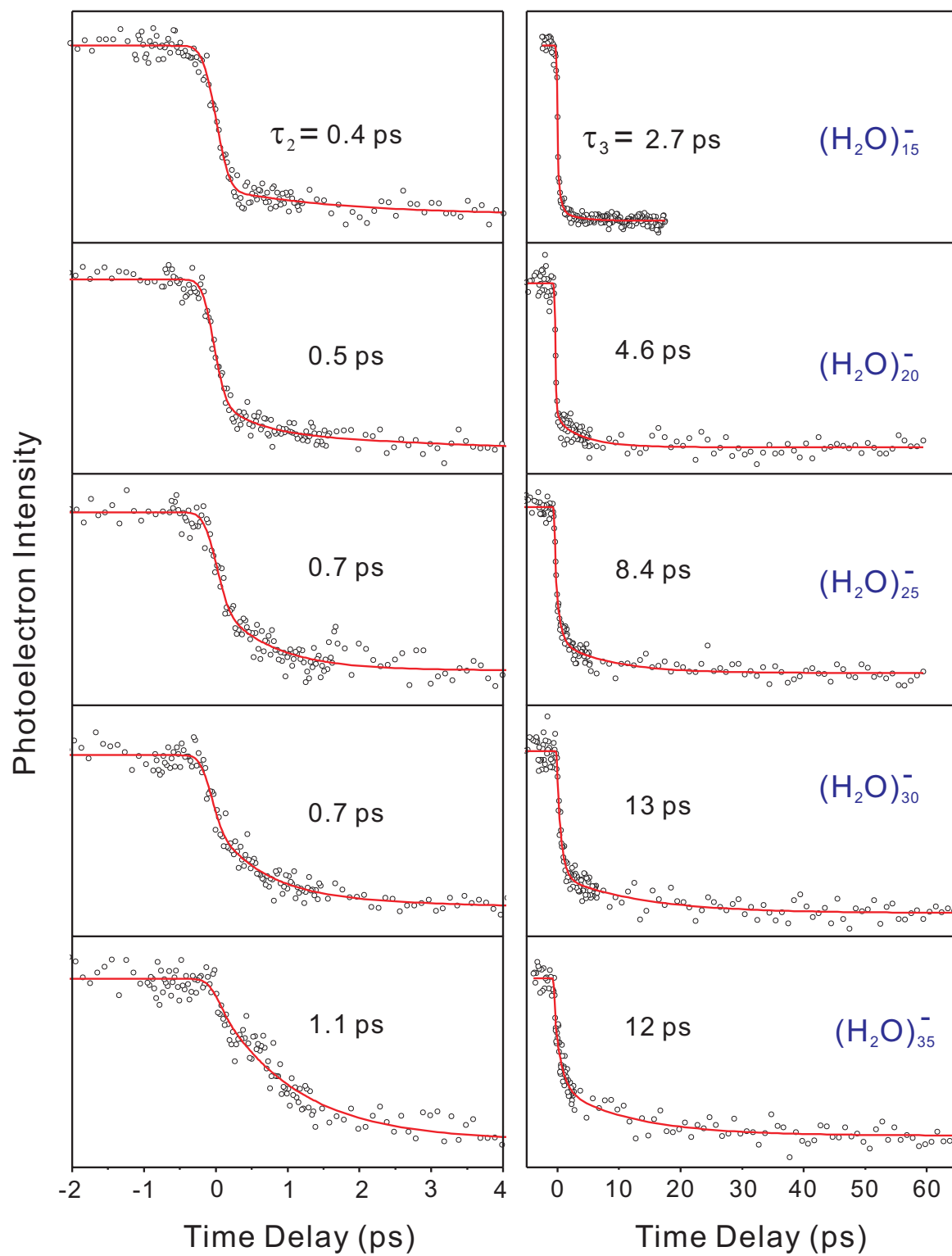


Figure 7.9

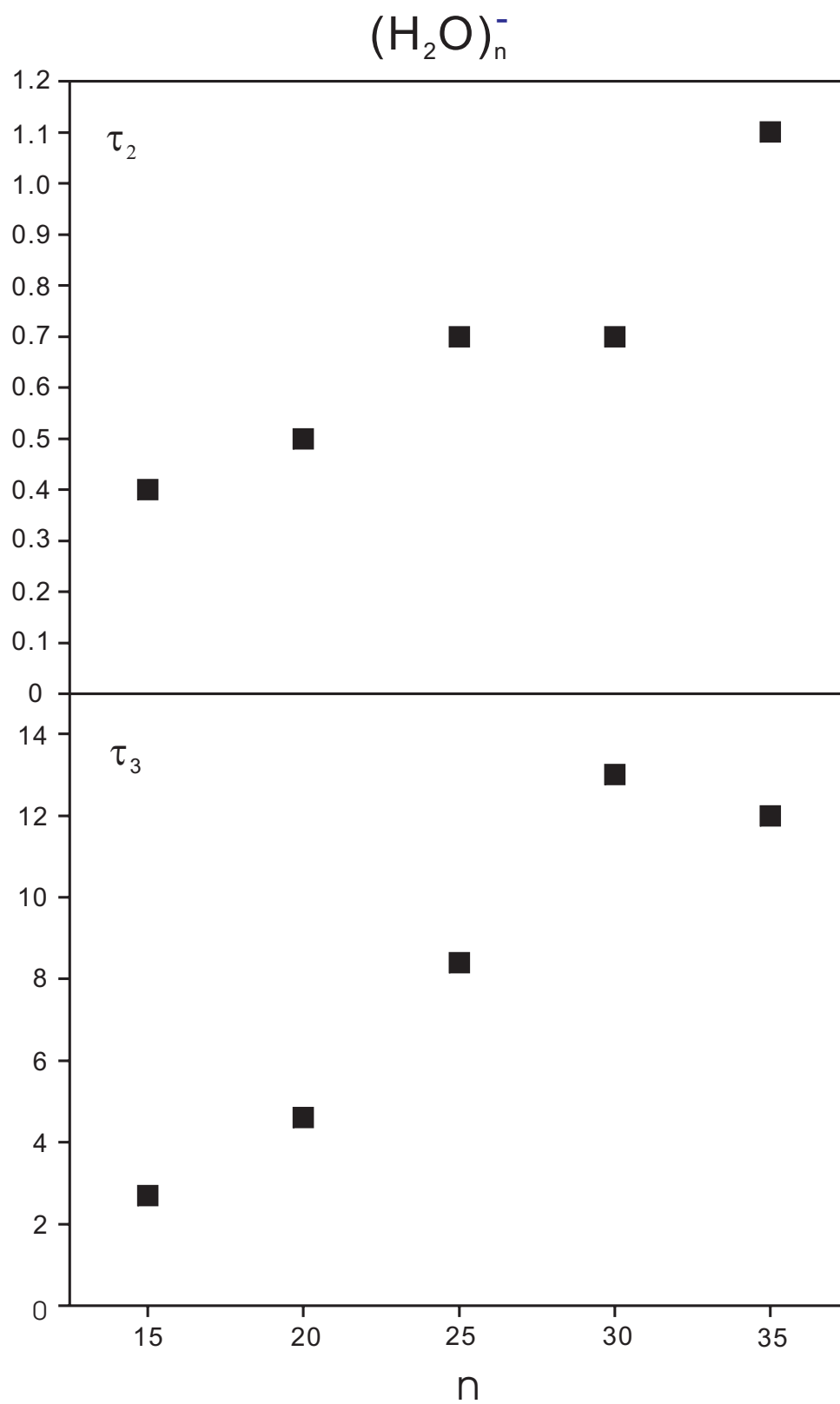


Figure 7.10

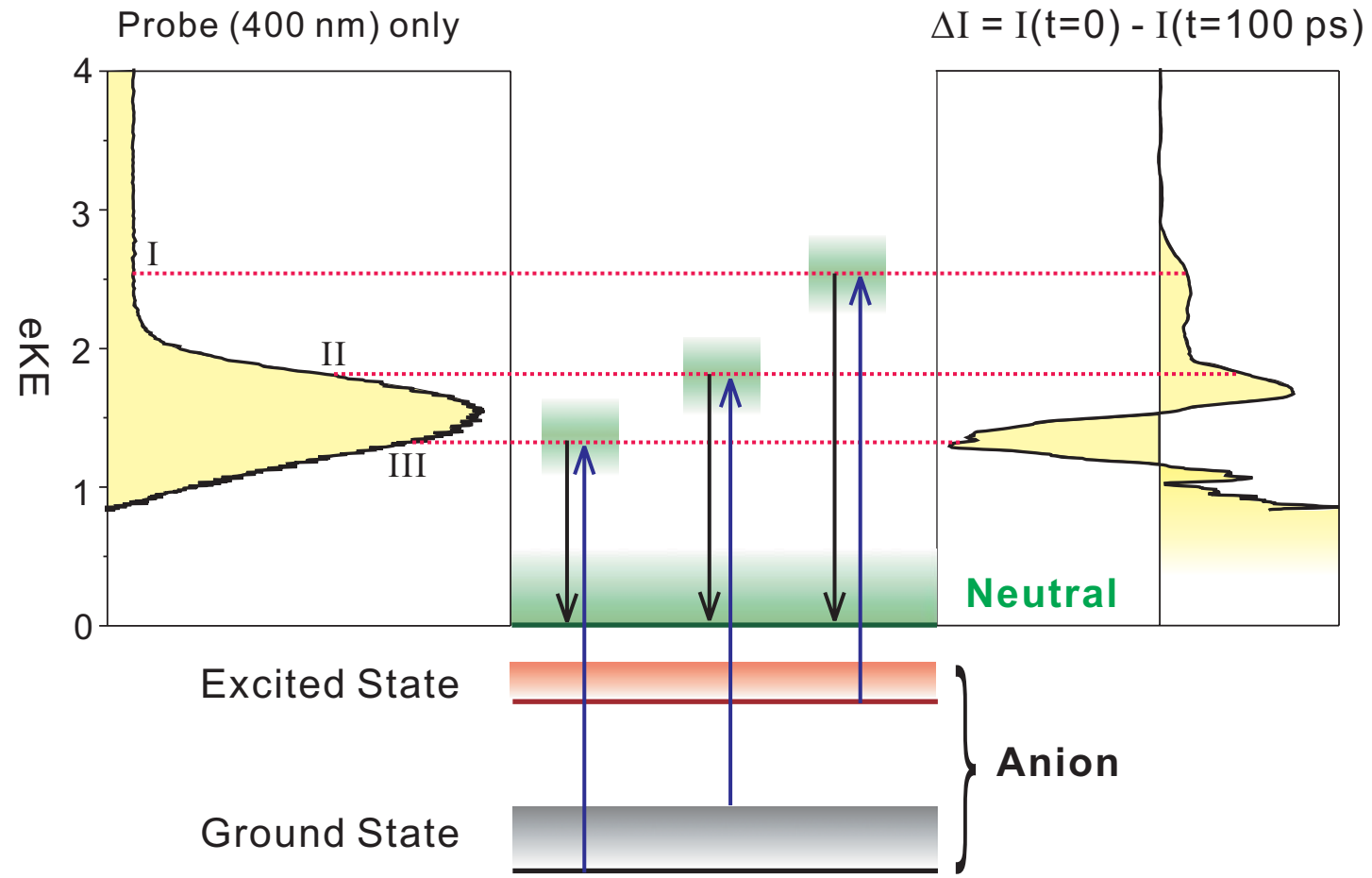


Figure 7.11

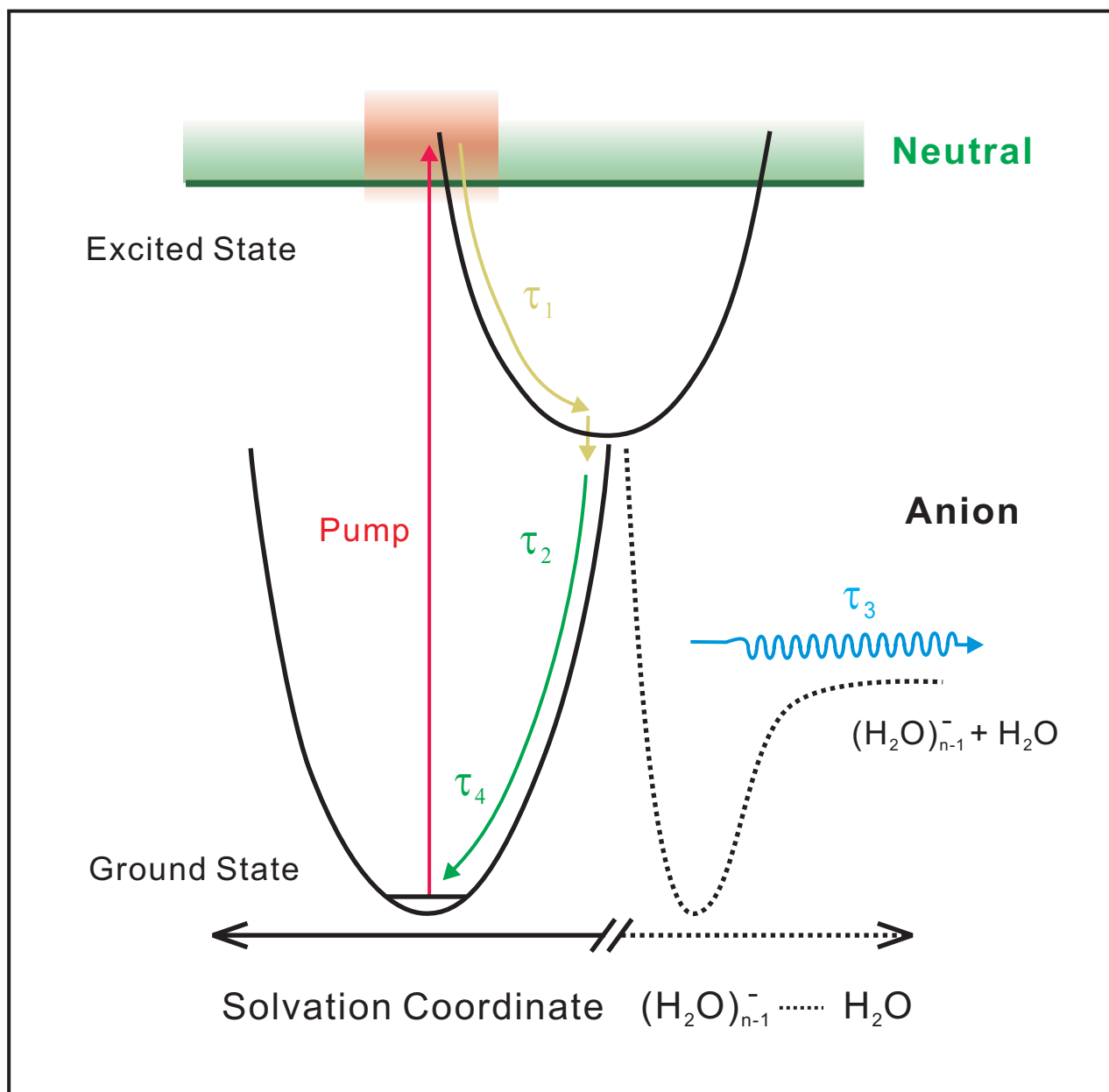


Figure 7.12

Figure Captions

Figure 7.1

Mass spectrum of $(\text{H}_2\text{O})_n^-$ generated by the ion source.

Figure 7.2

Fragment ion mass spectra of $(\text{H}_2\text{O})_n^-$, $n = 15, 20, 25, 30$ and 35 recorded by the linear reflectron mass spectrometer. The positive and negative going peaks correspond to fragment-ion generation and parent-ion depletion, respectively. The negative intensity of $(\text{H}_2\text{O})_{n-1}^-$ and $(\text{H}_2\text{O})_{n-2}^-$ is due to the depletion of metastable species.

Figure 7.3

Photoelectron (PE) spectra of $(\text{H}_2\text{O})_n^-$, $n = 15, 20, 25, 30$ and 35 obtained by irradiating 400 nm light.

Figure 7.4

Photoelectron spectra of $(\text{H}_2\text{O})_n^-$, $n = 15, 20, 25, 30$ and 35 obtained by irradiating 400 nm light 800 nm. The spectra in red are the twenty times enlarged spectra.

Figure 7.5

Overlays of 400 and 800 nm PE spectra illustrating the displacement between the 400 nm and two-photon 800 nm signals. The two-photon signal in 800 nm spectra are normalized with respect to the peak of 400 nm spectra.

Figure 7.6

Time-dependent photoelectron (PE) spectra at several time delays. The integrated regions of the PE intensity are marked by roman numbers. (see text for details) The yellow arrow indicated the 800-400 nm signal. The decay and rise trends observed in region II and III are illustrated by red and blue planes.

Figure 7.7

Femtosecond transients of $(\text{H}_2\text{O})_{30}^-$ obtained by integrating three different regions of photoelectron spectrum as a function of pump-probe delay. The insets are the PE spectrum of the probe only signal (400 nm), and the yellow rectangles indicate the integrated region. The inset in the top panel includes the pump-probe signal (red) at time zero to display the PE profile at region I.

Figure 7.8

Femtosecond transients of $(\text{H}_2\text{O})_{35}^-$ obtained by integrating three different regions of photoelectron spectrum. The insets are the PE spectrum of the probe only signal (400 nm), and the yellow rectangles indicate the integrated region. The inset in the top panel includes the pump-probe signal (red) at time zero to display the PE profile at region I.

Figure 7.9

Femtosecond transients of $(\text{H}_2\text{O})_n^-$, $n = 15, 20, 25, 30$ and 35 obtained by integrating the photoelectron signals at region II. The fast (τ_2) and slow (τ_3) time constants are shown in left and right panels, respectively.

Figure 7.10

Plots of τ_2 (fast decay) and τ_3 (slow decay) vs. number of water molecules, n .

Figure 7.11

Energy diagram illustrating the origin of the photoelectrons. The left panel is the PE spectrum at 400 nm while the right hand side spectrum is the difference spectrum obtained by subtracting pump-probe signal at 100 ps from the pump-probe signal at 0 ps. The upward arrows indicate the probe pulse energy and the downward arrows correspond to the kinetic energy of the detached electron (eKE). The shaded boxes centered at the tip of the arrows illustrate the band width of the photoelectron profiles.

Figure 7.12

Schematic representation of potential energy surfaces along the solvation coordinate. The curves (solid line) in left hand side correspond to the potential energy surfaces along the solvation coordinate while the curve (dotted line) at right represents the potential energy along the internuclear distance between the hydrated electron and a water molecule. The upward arrow represents the excitation by pump pulse and the relaxation and dissociation pathways are depicted by the color-labeled arrows with the corresponding time constants: yellow arrows - inertial motion (libration) of water molecules and internal conversion; blue arrow - evaporative dissociation; green arrow - solvent rearrangement.

CHAPTER 8.

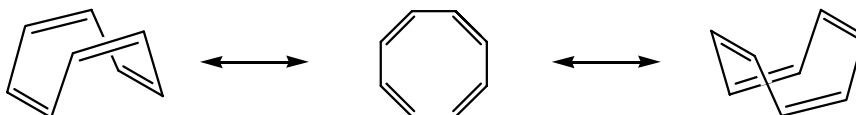
The Transition State of Thermal Organic Reactions: Direct Observation in Real-Time

8.1 Introduction

The motion of atoms during chemical reactions occurs on the femtosecond time scale, and only with this resolution can the transition state be frozen in time. Numerous examples of femtochemistry studies have been reported for reactions on excited surfaces and in all phases of matter (see, e.g. recent refs. 1 and 2). Combining the femtosecond time resolution and negative-ion-beam techniques provides a unique way to study the nuclear motions of *neutral* molecules in the electronic *ground* state, and this has been successful for Ag_3 and Ag_4 .³⁻⁷

Stable (positive electron affinity) negative ions prepared in the gas phase have their electronic states lying below the neutral ground state. Thus, coherent wave packets can be launched on this ground state by photodetaching the anion with a femtosecond laser pulse. Because the geometry of the anion and the neutral is different, vertical transition results in significant nuclear motions toward the equilibrium geometry of the ground state. This motion can be monitored in real time by using a second femtosecond laser pulse, with variable time delay, through ionization and detection with mass spectrometry.

In the present work, we report the femtosecond (fs) time-resolved dynamics of the transition state of the reaction of 1,3,5,7-cyclooctatetraene (COT):



This reaction of neutral COT on the *ground-state* potential is not a photochemical one, thus the transition state is that of thermal reactions. For this system a number of experimental and theoretical works have shown that neutral COT has a ‘tub-shaped’ (D_{2d}) structure in the electronic ground state,⁸⁻¹⁶ whereas the COT anion has a planar (D_{4h}) structure which resembles the geometry of neutral COT at the transition state of the ring inversion mode.¹⁷⁻²¹ From the photoelectron spectrum of COT^- , Lineberger and his coworkers showed that the vertical transition from COT^- can directly access the transition state of the ring inversion coordinate in the electronic ground state of neutral COT.²⁰

In our experiment, the coherent wave packet of the nuclear motion was launched from the negative ion using a 405 nm femtosecond pulse (Fig. 8.1). This negative ion was mass-selected, as shown in Figure 8.2, and with this 3.1 eV photon it photodetaches the anion to yield the transition state (TS) of the neutral reaction. The released electron carries most of the energy and the wave packet is launched directly at the transition state (Fig. 8.1). We then ionize the neutral COT with two photons of the probe pulse (270 nm), with variable time delay, and monitor the temporal evolution of the mass spectrum of COT^+ .

8.2. Experimental

Cyclooctatetraene anion (COT^-) was generated by crossing ~ 1 keV electron pulse with the gas mixture of $COT/O_2/Ar$. The COT vapor at 25 °C was expanded into a high vacuum chamber by flowing through pre-mixed Ar/O_2 gas (approximately 95% Ar and 5% oxygen) at a total backing pressure of 400 psig. Small amount of O_2 was introduced in the gas line, which produced more COT^- and stabilized the ion intensity. The ion

beam was collimated by a skimmer (1.0 mm hole) and then directed into the field-free time-of-flight region by applying -3.0 kV electric pulse to a two-stage accelerator. In the field-free region, ions were separated by their masses, and the anion packet of COT^- was intercepted with femtosecond laser pulses by adjusting the switching time of the ion accelerator with respect to the laser arrival time.

The femtosecond laser pulses (110 fs) at 810 nm and 820 nm were generated from a Ti:Sapphire oscillator, and amplified by the regenerative and the two-stage multi-pass amplifiers. The IR fundamental was split (50:50) and one of the beams was frequency doubled. The other beam was converted to the third harmonic by sequential doubling and sum-frequency mixing. The second harmonic (405 nm or 410 nm) was used as the pump pulse to photodetach COT^- , and the third harmonic (270 nm or 273 nm) was used as the probe pulse to ionize the nascent neutral COT by two-photon absorption. Positive ions generated in the laser interaction region were collected by the reflectron mass spectrometer, and the detached electron was analyzed by the magnetic-bottle PE spectrometer. Time-dependent transient was obtained by integrating the COT^+ ion peak as a function of the delay time between the pump and probe pulses (cross correlation 300 fs).

Ab initio calculations for the potential energy along the reactive coordinate (RI1) were made using the Gaussian 98 program at the B3LYP/cc-pVTZ level of theory.²² Wave packet motions were calculated by numerically solving the Schrödinger equation.

8.3. Results

Figure 8.2A shows the mass spectrum of negative ions generated from the anion source. The relative mixing ratio of O₂ gas was crucial for generating stable COT⁻ ion beam. Addition of small amount of oxygen increased the COT⁻ ion intensity, but mixing too much oxygen decreased COT⁻ and generated predominant oxygen anion clusters. The enhancement of COT⁻ in the presence of oxygen gas can be explained by the electron transfer reaction from O₂⁻ to COT.²³ Mass spectrum with higher resolution obtained by the reflectron time-of-flight mass spectrometer is shown as inset, and the mass peak at 105 a.u. corresponds to C₈H₈⁻ with one ¹³C isotope. No negatively charged metastable species was detected with the reflectron mass spectrometer, and photodissociation did not occur upon irradiation of pump and probe pulses.

Figure 8.2B shows the photoelectron spectrum of COT⁻ obtained at 405 nm. Our photoelectron spectrum is quite different from the spectrum reported by Lineberger group.²⁰ The onset of the spectrum is shifted toward lower electron binding energy and large intensity of the hot band below 1.1 eV is observed, which indicates there were significant amount of vibrationally hot COT⁻ in the ion beam. Therefore, the different spectral features appeared in our photoelectron spectrum such as broad peak width and discrepancy in peak positions are mainly due to the convolution of the photoelectron signals from the vibrationally excited COT⁻.²⁴ In addition, the broad spectral band width of the fs laser pulse and Doppler broadening in our photoelectron spectrometer lower the resolution of the photoelectron spectrum.

Based on the photoelectron spectrum of Lineberger group, the broad band profile below 1.5 eV is assigned to the transition to the electronic ground state (¹A_{1g}) of the

neutral D_{4h} COT, whereas the profile above 1.5 eV is assigned to the transition to the triplet state ($^3A_{2u}$) of D_{8h} COT. The new peaks at 1.0 eV and 1.5 eV were possibly originated from the $v'' = 1$ state of COT^- in the bond shifting mode.²⁵ The intense band above 1.1 eV is attributed to the formation of vibrationally hot neutral COT generated by the transition from the vibrationally excited state of COT^- . The photoelectron profile above 1.5 eV could be the extension of the ground state manifold; however, the higher vibrational state is not likely populated due to small Frank-Condon factors.

Figure 8.3A shows the positive ion mass spectrum obtained by illuminating COT^- with both pump and probe pulses at 160 fs time delay (maximum). Beside the predominant ion peak of $C_8H_8^+$, significant amount of fragment cations were detected. Since no metastable anion was presented in the ion beam and no fragment anion was generated by light, the fragment cations were generated from the subsequent dissociation of the parent COT^+ ion.²⁶ The intensity profile of the $C_8H_n^+$ ($n = 6 - 8$) and $C_6H_m^+$ ($m = 1 - 6$) is similar to the mass spectrum reported by other groups²⁶, but fragments smaller than C_6H_1 were not observed in our spectrometer.

As shown in Figure 8.1, two-photon absorption of probe pulse (9.1 ~ 9.2 eV) exceeds the sum of the adiabatic electron affinity (0.6 eV)^{23,28,29} and the ionization potential (8.0 eV)^{30,31} of COT. Thus it is energetically possible to generate the COT^+ cation directly from the COT^- anion by two-photon absorption of the probe pulse only. However, we observed the enhancement in the positive ion intensity when both pump and probe pulses were illuminated at positive time delays in which more neutral COT was generated by pump pulse. Since the total photon energy of one-photon of the pump and one-photon of the probe is not sufficient to generate COT^+ directly from COT^- , the

enhancement of COT^+ by pump pulse implies that two-photon ionization of the neutral COT is more favored than removal of two electron from COT^- .

Figure 8.3B is the time-dependent mass spectra of positive ions ($I - I_{t<0}$) obtained at three different time delays (0, 160 fs and 5.6 ps), which displays the increment of the positive ion signals compared to the ion signals at the negative time delay (-1 ps). The positive ion mass spectrum at -1 ps is similar to the mass spectrum generated by the probe pulse only, except that the ion intensity of COT^+ was slightly reduced while the intensity of C_8H_7^+ was increased. However, the difference was very small and no discernable change was observed for the smaller fragments. The intensity change in the two species implies that C_8H_7^+ is generated from the subsequent dissociation of the parent COT^+ by the pump pulse. Hence, it might be expected that more fragment cation is generated at a negative time delay than at a positive time delay. However, as illustrated in Fig. 8.3B, ion intensity of the fragments as well as the parent COT^+ were increased at the positive time delays. Therefore, enhancement of COT^+ signal at positive time delay is due to the generation of nascent neutral COT rather than the depletion of COT^+ by pump pulse.

In order to follow the temporal evolution, we recorded many such transients and the behavior is shown in Fig. 8.4 for gating at the mass of COT^+ . The observed transient exhibits two characteristics: (i) positive signal offset (shown by a thin line) and (ii) an apparent damped oscillatory behavior. The positive offset is understood because the detachment of electron from COT^- yields both the singlet and triplet states of COT, as evident in the PE spectrum. The offset is flat in our 12 ps scan (not shown), which is consistent with a long-lived triplet state ($\sim 100 \mu\text{s}$).³²

The oscillatory behavior is reminiscent of the transient behavior observed in this group for the photoisomerization reaction of *cis*-stilbene.³³ The transient fit shown in Fig. 8.4 was obtained using the following molecular response function with proper convolution:

$$M(t) = \exp(-\gamma \cdot t) \cdot \{a + b \cdot \cos[\omega(t) \cdot t]\} \quad (1)$$

where γ is the decay rate and a , b are constants. The time dependent frequency is $\omega(t) = 2\pi/(T_0 + k \cdot t)$, where T_0 is the initial period and k gives its change (dispersion) with time. From the fit we obtained $\gamma^{-1} = 750$ fs, $a/b = 2.6$, $T_0 = 750$ fs and $k = 0.5$. The residual sinusoidal component ($a = 0$) is shown in the bottom panel of Fig. 8.4.

8.4. Discussion

The temporal behavior observed in the femtosecond transient of COT^+ elucidates the nuclear motions on the electronic ground state potential energy surface (PES) of the neutral COT. The photodetachment by the pump pulse (3.1 eV) can reach the low-lying triplet state of the neutral COT which is located 1.6 eV above the ground state of COT^- .²⁰ Time evolution of the COT^+ signal could be originated from the dynamics occurring on this surface.³⁴ However, we think that the triplet state is not responsible for the temporal behavior observed in our transient. If the decay reflects the lifetime of the triplet state, COT^+ signal should decay exponentially with much longer time. The lifetime of 100 μs was measured for the low lying triplet state of COT in the condense phase³², and the triplet state lifetime of the isolated COT is expected to be longer.

The neutral COT can undergo thermal reactions in the electronic ground state, which isomerizes COT to two different bi-cyclic molecules.^{15,35,36} However, our time-dependent signal is not originated from the population decay of COT via the isomerization pathways because of the following reason: Although photodetachment of COT^- can produce vibrationally hot neutral COT, the internal energy of the nascent COT is not sufficient to overcome reaction barriers for the thermal isomerization processes. From our photoelectron spectrum, we estimated that the internal energy of the nascent COT can be as large as 0.9 eV, but the barrier height for the thermal isomerization processes are higher than 1.2 eV. Therefore, the femtosecond dynamics shown in the transient is related to the nuclear motion at the transition state of the ring inversion.

In a simplified picture, the energy landscape of the electronic ground state can be reduced to the one-dimensional potential energy surface of the ring inversion, and the nuclear motion of COT can be represented by a coherent wave packet on this surface. (Fig. 8.1) Upon photodetachment of COT^- by a femtosecond pulse, a coherent wave packet is launched near the transition state of the ring inversion, since the nuclei in the COT molecule were frozen in time during the photodetachment of an electron. Subsequently, the wave packet will move toward the equilibrium geometry (D_{2d}) of COT and then bounce back and forth along the ring inversion mode.

Recurring feature, however, was not observed in our transient, which is possibly due to the fast ring inversion motion. From the imaginary frequency ($90i \text{ cm}^{-1}$) of the transition state²⁰, the round trip period is estimated to be about 300 fs, which is in the range of our time resolution. In addition, the transitions from the vibrationally excited states of COT^- can make the recurring feature less pronounced. As shown in our

photoelectron spectrum of COT^- , significant amount of excited COT^- was photodetached by light. Therefore, it is likely that the observed transient is convoluted with multiple traces of many wave packet motions.

The 2.5 ps non-exponential decay is attributed to the wave packet dephasing and intramolecular vibrational-energy redistribution (IVR), and the picosecond time scale is rationalized by the effective coupling of ring inversion with other vibrational modes. Effective dephasing of a coherent wave packet is expected when it passes through the transition state of the ring inversion mode, because (1) the potential energy surface near the transition state exhibits significant degree of anharmonicity and (2) the spectral band width of our pump pulse is quite broad ($\sim 200 \text{ cm}^{-1}$). At longer time, kinetic energy of the wave packet will dissipate to other modes via IVR, and the wave packet will relax to the global minimum (D_{2d}) of COT .

In particular, the bond shifting mode (*i.e.* alternating bond mode between the single and double bond) is important in our study since the geometries of COT^- and the COT at the transition state of the ring inversion are different in the bond length ratio of the single to the double bonds.¹⁹ Based on our normal mode analysis, the vertical detachment will induce the nuclear motion along the bond shifting coordinate as well as the ring inversion mode, while the rest of modes will not be actuated. Moreover, the ring inversion and bond shifting modes are not fully decoupled, thus wave packet motion on the two-dimensional PES will be considered hereafter.

In order to elucidate the observed temporal behavior, we carried out both classical and quantum mechanical wave packet trajectory calculations on the two-dimensional potential energy surface (2D-PES) of the ring inversion (RI) and the bond shifting (BS)

modes. The 2D-PES was constructed by adding the two one-dimensional potentials (RI and BS) and introducing a coupling term which represents the barrier separating the two D_{2d} isomers across the BS coordinate. (Figure 8.5) The analytical functions describing the one-dimensional curves were obtained by incorporating the experimental values for the barrier heights and the DFT calculations. The coupling term is required since the auto-isomerization of tub-shaped COT (D_{2d}) across the BS coordinate requires severe nuclear rearrangement.^{37,38}

In the classical trajectory calculation, the molecular dynamics was followed by placing a particle on the 2D-PES described above. Many trajectories were simulated by varying the initial position of the wave packet. The trajectory and the round trip period were varied with the initial RI coordinate (RI_0). When the wave packet is placed exactly at the D_{4h} geometry ($RI_0 = 0$), wave packet stays at the saddle point region and oscillates along the BS mode only. When the initial RI coordinate is slightly off-centered, the wave packet moves along the RI. The round trip period becomes shorter at larger RI since the wave packet gets accelerated by the steeper gradient at larger RI_0 . However, within the RI range between 0.01° and 5° , which corresponds to the FWHM of the initial wave packet width, the simulation showed similar trajectories with the RI period of 300 ~ 500 fs.

For more rigorous calculation of the wave packet trajectories, we solved the time-dependent Schrödinger equation:

$$i\hbar \frac{\partial \Psi}{\partial t} = \left(-\frac{\hbar^2}{2m_{RI}} \frac{\partial^2}{\partial Q_{RI}^2} - \frac{\hbar^2}{2m_{BS}} \frac{\partial^2}{\partial Q_{BS}^2} + V \right) \Psi, \quad (\text{eq. 2})$$

where m_{RI} and m_{BS} denote the reduced masses corresponding to the nuclear coordinates of the ring inversion (Q_{RI}) and the bond shifting (Q_{BS}), and V is the two-dimensional potential energy surface described above. The initial wave packet Ψ was constructed by the product ($\Psi = \Psi_{RI} \otimes \Psi_{BS}$) of Ψ_{RI} and Ψ_{BS} which represent the nuclear wavefunctions of COT⁻ for the RI and BS modes. The time-dependent Schrödinger equation was solved numerically, using the Crank-Nicolson finite-difference method and the Douglas-Gunn alternating direction implicit (ADI) algorithm³⁹:

$$i\hbar \frac{\Psi^{n+1/2} - \Psi^n}{\Delta t} = \left(-\frac{\hbar^2}{2m_{RI}(\Delta Q_{RI})^2} \delta_{RI}^2 + V \right) \frac{\Psi^{n+1/2} + \Psi^n}{2} - \frac{\hbar^2}{2m_{BS}(\Delta Q_{BS})^2} \delta_{BS}^2 \Psi^n$$

$$i\hbar \frac{\Psi^{n+1} - \Psi^n}{\Delta t} = -\frac{\hbar^2}{2m_{RI}(\Delta Q_{RI})^2} \delta_{RI}^2 \left(\frac{\Psi^{n+1/2} + \Psi^n}{2} \right) + \left(-\frac{\hbar^2}{2m_{BS}(\Delta Q_{BS})^2} \delta_{BS}^2 + V \right) \frac{\Psi^{n+1} + \Psi^n}{2},$$

where Δ means the finite difference of a quantity, Ψ^n represents the probability amplitude at $t = n \cdot \Delta t$, and δ^2 is the finite-difference operator defined as $\delta^2 f = f_{n+1} - 2f_n + f_{n-1}$.

In the quantum mechanical calculation (Fig. 8.6), we observed that the initial wave packet motion begins along the BS coordinate with high-frequency oscillation, and the oscillation stays in the saddle point region for about 50 fs. It is inferred from the photoelectron spectrum of COT⁻ that the saddle point region along the RI coordinate is relatively flat.²⁰ Hence, the force exerted along this mode is weak, and it may take some time to gain enough momentum to leave the flat surface. Therefore, the broad peak

observed in our transient can be due to the delayed motion of a wave packet departing from the saddle point.

Ultrafast dephasing and rephasing of a wave packet was observed in the quantum mechanical trajectory calculation, and the first cycle of the dephasing-rephasing is presented in Figure 8.6. The wave packet becomes diffused throughout the potential energy surface in 100 fs, and then it regain its shape but with smaller amplitude, as it returns to the starting position. (320 fs) The dephasing becomes more pronounced after the second round trip (0.8 ps), but then rephasing of the wave packet occurs in the third round trip (1.1 ps). Unlike classical trajectory calculation, wave packet can propagate more pervasively by tunneling, and small barrier height across the BS mode (3 ~ 4 kcal/mol) permits effective tunneling through the D_{8h} transition state.^{8,37} Our quantum mechanical trajectory calculation shows that almost entire wave packet crosses the barrier in less than 100 fs. (not shown)

The dephasing-rephasing cycle recurs but with random variation of amplitude and period. To illustrate this point, we simulated a femtosecond transient by opening the probe window at the transition state of RI (upper panel in Figure 8.7). The 20 fs beat and the recurring envelope with ~ 350 fs interval correspond to the high frequency oscillation along the BS mode and the motion along the RI coordinate, respectively. Within 5 ps range, an exact repeating pattern was not observed, and the intensity does not come back to the original amplitude. The simulated transient exhibits a tendency of damping and broadening of the recurring envelope. However, the damping rate seems much slower compared to the observed transient (2.5 ps), which can be rationalized by ultrafast dephasing and subsequent IVR.

Quantum trajectory calculations were carried out for the wave packets prepared from the vibrationally excited states of COT^- ($v'' = 1, 2$ for the RI mode and $v'' = 1$ for the BS mode). Similar trends of damping and broadening were observed, but the rephasing periods were quite different. (Fig. 8.8) As discussed before, the convolution of these traces made the recurring feature less pronounced. In addition, several transients were obtained by changing the window position and size, and the trend of damping and broadening of the recurring feature was observed regardless of the position and the size of the probe window.

One more consideration must be addressed. Incorporating the BS mode provides more accurate description of the dynamical process of COT. For instance, the damping of the recurring feature was not observed in the trajectory calculation using one-dimensional potential energy curve, in which RI serves as the only reaction coordinate. The shortcoming of the one-dimensional picture has been recognized in this group, and extensive theoretical works have been elaborated on this subject.⁴⁰⁻⁴²

On a two-dimensional surface which includes both the reaction coordinate (Ring Inversion, RI1) and a second coordinate whose frequency is close to that of another ring inversion (RI2, $\sim 200 \text{ cm}^{-1}$), we obtained the snap shots shown in Fig. 8.10; the RI1 and RI2 coordinates correspond to the flipping motions along the single and double bonds, respectively (Fig. 8.9). From these quantum calculations we plotted the probability as a function of time, with the detection window located at the TS launching position. We can see that the prominent wave packet period is now in agreement with experiment (775 fs). However, we must account for the selectivity imposed on the window of detection along the harmonic transverse mode (RI2). This asymmetry of detection can be

rationalized by considering the multiple transition states shown in Fig. 8.10. COT, through bond shifting (BS, $\sim 1700\text{ cm}^{-1}$), can acquire a D_{8h} TS which is located only 4 kcal/mol from the D_{4h} geometry.¹⁹ As shown in Fig. 8.10, this ultrafast interconversion can induce such asymmetry. The two lowest-frequency normal modes (degenerate E_{2u}) at the D_{8h} geometry are linear combination of the first (reactive coordinate) and the second ring inversion modes, which suggests that Duschinsky rotation plays an important role, especially at the transition-state of the reactive coordinate.³⁷

8.5. Conclusion

In conclusion, we have demonstrated real-time probing of the transition-state dynamics of cyclooctatetraene in the electronic *ground state*. This transition state is unique in its definition for thermal reactions, and here it was directly accessed by detachment of the electron from the planar COT^- anion. The motion in the multidimensional nuclear space was monitored by ionization/mass spectrometry of neutral COT reaction. The oscillatory feature observed in the transients reflects trajectories of motion along the reaction coordinate, the ring inversion motion. With the aid of quantum calculations, we examined the nature of the modes involved and the energy landscape. These experiments should now be possible for applications to other ground-state thermal reactions with their transition states resolved in real time.

References

- ¹ *Femtochemistry and Femtobiology* (Ed.: A. Douhal, J. Santamaria), World Scientific, River Edge, New Jersey, **2002**.
- ² *Femtochemistry: with the Nobel Lecture of A. Zewail* (Ed.: F. S. De Schryver, S. De Feyter, G. Schweitzer), Wiley-VCH, Weinheim, **2001**.
- ³ S. Wolf, G. Sommerer, S. Rutz, E. Schreiber, T. Leisner, L. Wöste, R. S. Berry, *Phys. Rev. Lett.* **1995**, *74*, 4177-4180.
- ⁴ D. W. Boo, Y. Ozaki, L. H. Andersen, W. C. Lineberger, *J. Phys. Chem. A* **1997**, *101*, 6688-6696.
- ⁵ T. Leisner, S. Vajda, S. Wolf, L. Wöste, R. S. Berry, *J. Chem. Phys.* **1999**, *111*, 1017-1021.
- ⁶ H. Hess, S. Kwiet, L. Socaciu, S. Wolf, T. Leisner, L. Wöste, *Appl. Phys. B* **2000**, *71*, 337-341.
- ⁷ H. Hess, K. R. Asmis, T. Leisner, L. Wöste, *Eur. Phys. J. D* **2001**, *16*, 145-149.
- ⁸ F. A. L. Anet, *J. Am. Chem. Soc.* **1962**, *84*, 671-672.
- ⁹ M. Trættemberg, *Acta Chem. Scand.* **1966**, *20*, 1724-1726.
- ¹⁰ R. P. Frueholz, A. Kuppermann, *J. Chem. Phys.* **1978**, *69*, 3614-3621.
- ¹¹ D. A. Hrovat, J. H. Hammons, C. D. Stevenson, W. T. Borden, *J. Am. Chem. Soc.* **1997**, *119*, 9523-9526.
- ¹² C. D. Stevenson, E. C. Brown, D. A. Hrovat, W. T. Borden, *J. Am. Chem. Soc.* **1998**, *120*, 8864-8867.
- ¹³ J. L. Andrés, O. Castaño, A. Morreale, R. Palmeiro, R. Gomperts, *J. Chem. Phys.* **1998**, *108*, 203-207.
- ¹⁴ O. Castaño, R. Palmeiro, L. M. Frutos, J. Luisandrés, *J. Comput. Chem.* **2002**, *23*, 732-736.
- ¹⁵ M. Garavelli, F. Bernardi, A. Cembran, O. Castaño, L. M. Frutos, M. Merchán, M. Olivucci, *J. Am. Chem. Soc.* **2002**, *124*, 13770-13789.
- ¹⁶ L.-M. Frutos, O. Castaño, M. Merchán, *J. Phys. Chem. A* **2003**, *107*, 5472-5478.
- ¹⁷ M. J. S. Dewar, A. Harget, E. Haselbach, *J. Am. Chem. Soc.* **1969**, *91*, 7521-7523.
- ¹⁸ R. Gygax, H. L. McPeters, J. I. Brauman, *J. Am. Chem. Soc.* **1979**, *101*, 2567-2570

- ¹⁹ J. H. Hammons, D. A. Hrovat, W. T. Borden, *J. Am. Chem. Soc.* **1991**, *113*, 4500-4505.
- ²⁰ P. G. Wenthold, D. A. Hrovat, W. T. Borden, W. C. Lineberger, *Science* **1996**, *272*, 1456-1459.
- ²¹ T. M. Miller, A. A. Viggiano, A. E. S. Miller, *J. Phys. Chem. A* **2002**, *106*, 10200-10204.
- ²² Gaussian 98 (Revision A.9), M. J. Frisch, G.W. Trucks, H. B. Schlegel, G. E. Scuseria, M. A. Robb, J. R. Cheeseman, *et al.* Gaussian, Inc., Pittsburgh, PA, **1998**.
- ²³ S. Kato, H. S. Lee, R. Gareyev, P. G. Wenthold, W. C. Lineberger, C. H. DePuy, V. M. Bierbaum, *J. Am. Chem. Soc.* **1997**, *119*, 7863.
- ²⁴ It is important to note that the spectral signature of our photoelectron spectrum is more close to the photoelectron spectrum of $C_8H_6^-$ than COT^- which were obtained by Lineberger and his coworkers. However, it was experimentally verified that our photoelectron signature is solely from COT^- . First, the mass peak is at 104 amu and fragment anion was not observed with pump pulse. Second, positive ion spectrum shown in Figure 4(a) is almost identical to the COT^- ion spectra reported earlier. If $C_8H_6^-$ is intercepted with light instead of COT^- , the positive ion peak at 104 amu cannot be generated.
- ²⁵ Our calculation suggest that the energy spacing of the bond shifting between the ground and first vibrationally excited state in the bond shifting mode is about 0.08 eV.
- ²⁶ R. C. Dunbar, M. S. Kim, G. A. Olah, *J. Am. Chem. Soc.* **1979**, *101*, 1368.
- ²⁷ J. L. Franklin, S. R. Carroll, *J. Am. Chem. Soc.* **1969**, *91*, 5940.
- ²⁸ W. E. Wentworth, W. Ristau, *J. Phys. Chem.* **1969**, *73*, 2126.
- ²⁹ J. W. Denault, G. D. Chen, R. G. Cooks, *J. Am. Soc. Mass. Spectr.* **1998**, *9*, 1141.
- ³⁰ C. Batich, P. Bischof, E. Heilbronner, *J. Electron Spectrosc.* **1972**, *1*, 333.
- ³¹ M. Ohno, W. Vonniessen, E. Pairaud, J. Heinesch, J. Delwiche, *J. Electron Spectrosc.* **1995**, *73*, 261.
- ³² T. N. Das, K. I. Priyadarsini, *J. Chem. Soc. Faraday Trans.* **1994**, *90*, 963-968.
- ³³ S. Pedersen, L. Bañares, A. H. Zewail, *J. Chem. Phys.* **1992**, *97*, 8801-8804.
- ³⁴ In order to verify the involvement of the triplet state, we tried to obtain a transient using 810 nm (1.5 eV) light as the pump pulse, which selectively prepared the wave

packet on the electronic ground state. However, the time-dependent COT+ signal was not detected due to small photodetachment cross section at 810 nm.

- ³⁵ R. Huisgen, F. Mietzsch, *Angew. Chem., Int. Ed. Engl.* **1964**, 3, 83.
- ³⁶ H. –D. Maritn, T. R. Urbanek, *J. Walsh, Am. Chem. Soc.* **1985**, 107.
- ³⁷ D. A. Hrovat, W. T. Borden, *J. Am. Chem. Soc.* **1992**, 114, 5879.
- ³⁸ L. J. Schaad, J. Hu, *J. Am. Chem. Soc.* **1998**, 120, 1571.
- ³⁹ J. Douglas, J. E. Gunn, *Numerische. Mathematik* **1964**, 6, 428.
- ⁴⁰ M. H. Janssen, H. Dantus, H. Guo, A. H. Zewail, *Chem. Phys. Lett.* **1993**, 214, 281.
- ⁴¹ H. Guo, A. H. Zewail, *Can. J. Chem.* **1994**, 72, 947.
- ⁴² K. B. Møller, A. H. Zewail, *Essays in Contemporary Chemistry: From Molecular Structure towards Biology*; Verlag Helvetica Chimica Acta: Zurich, **2001**.

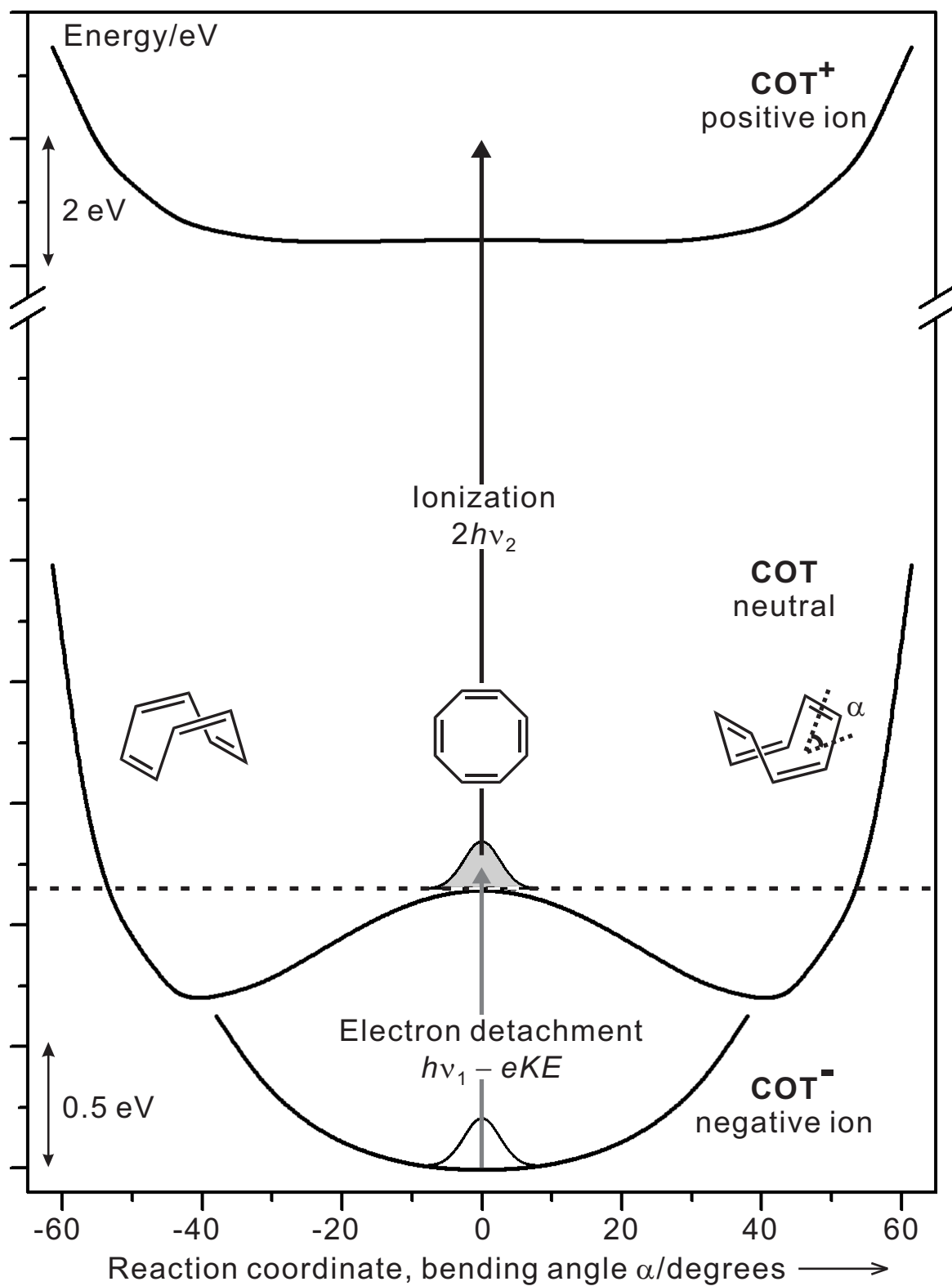
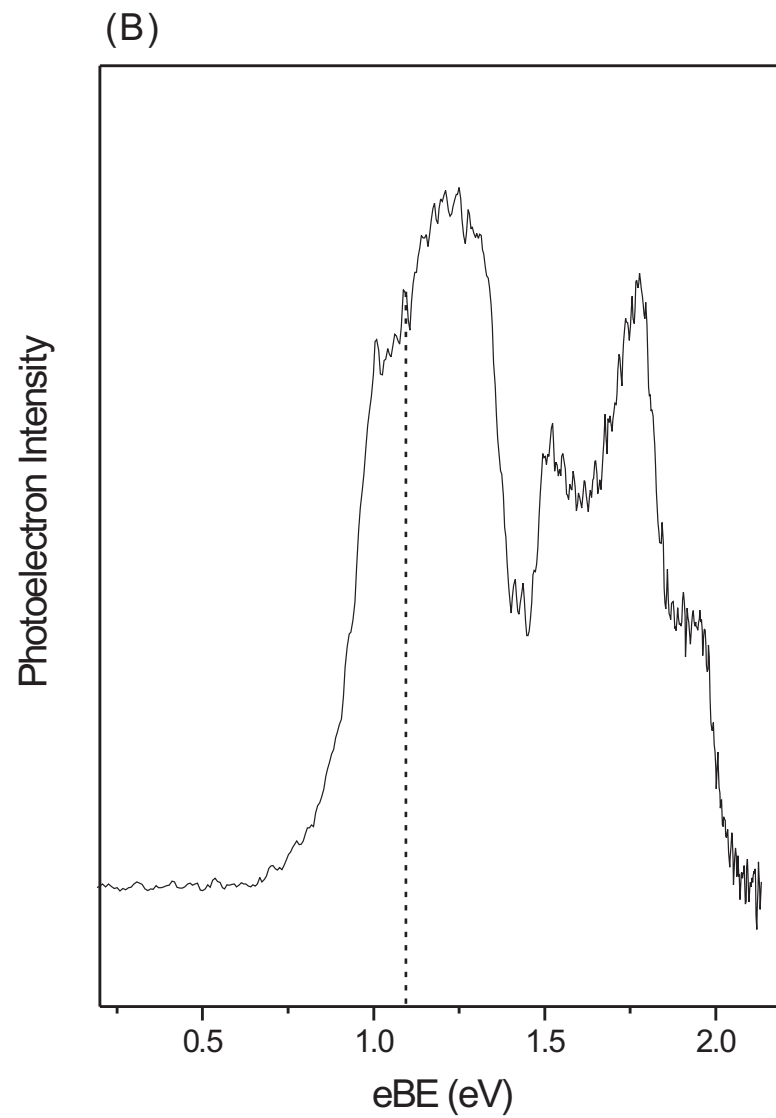
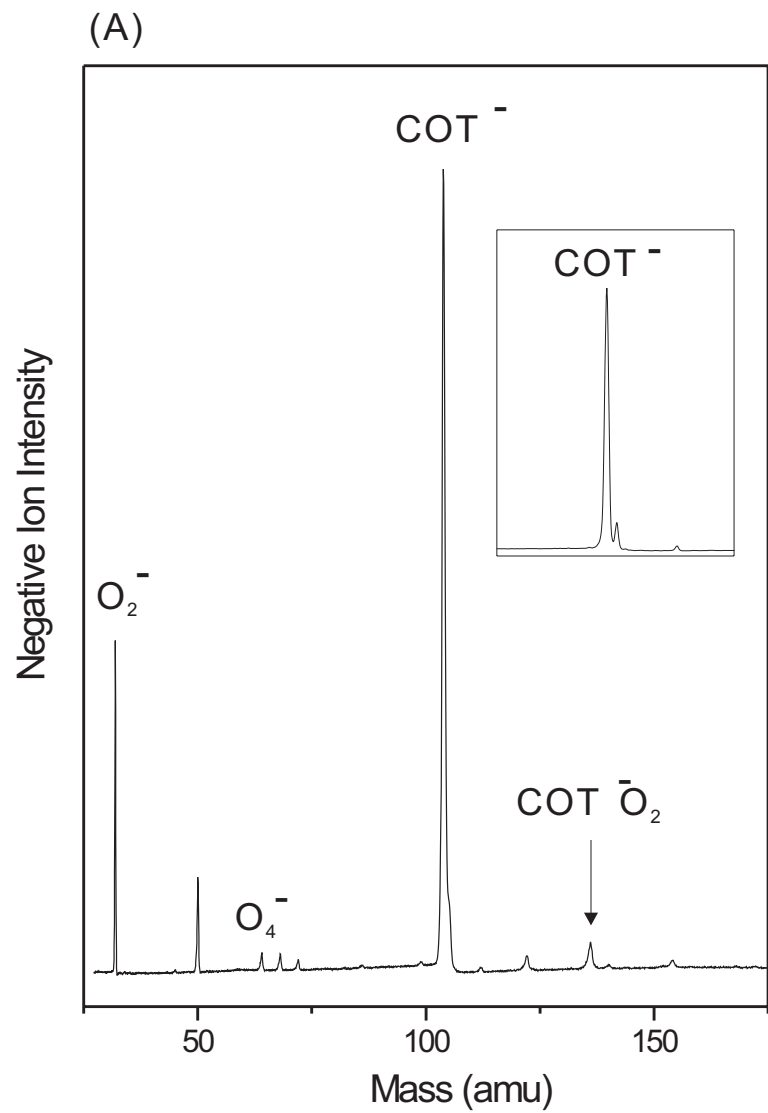


Figure 8.1



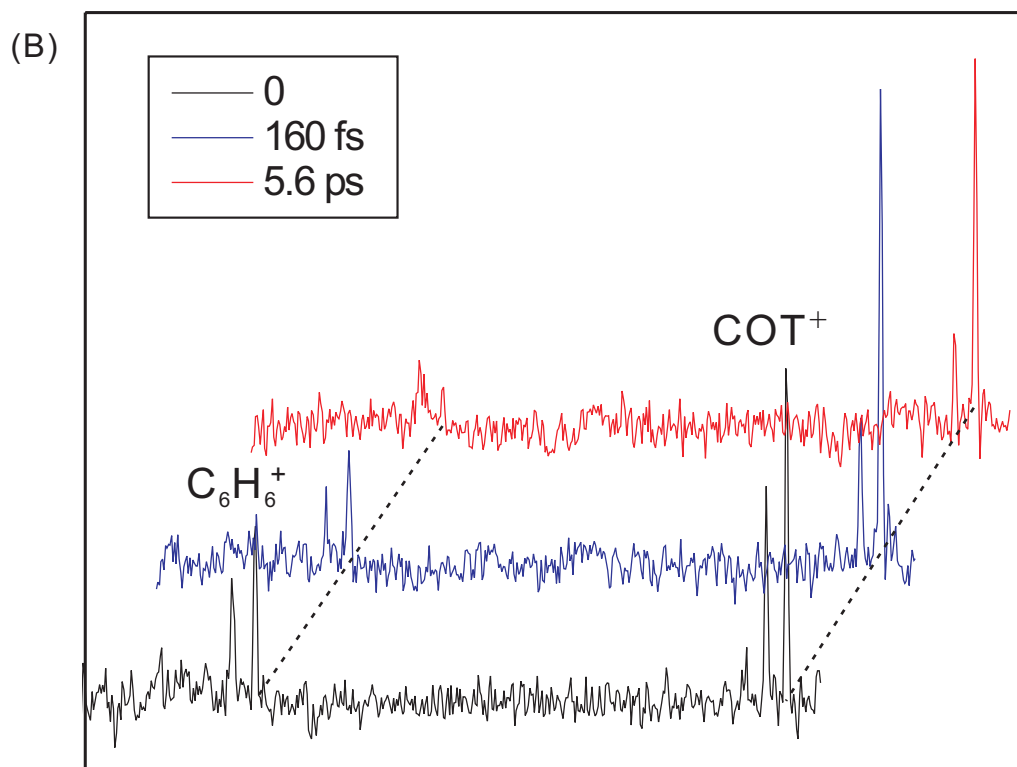
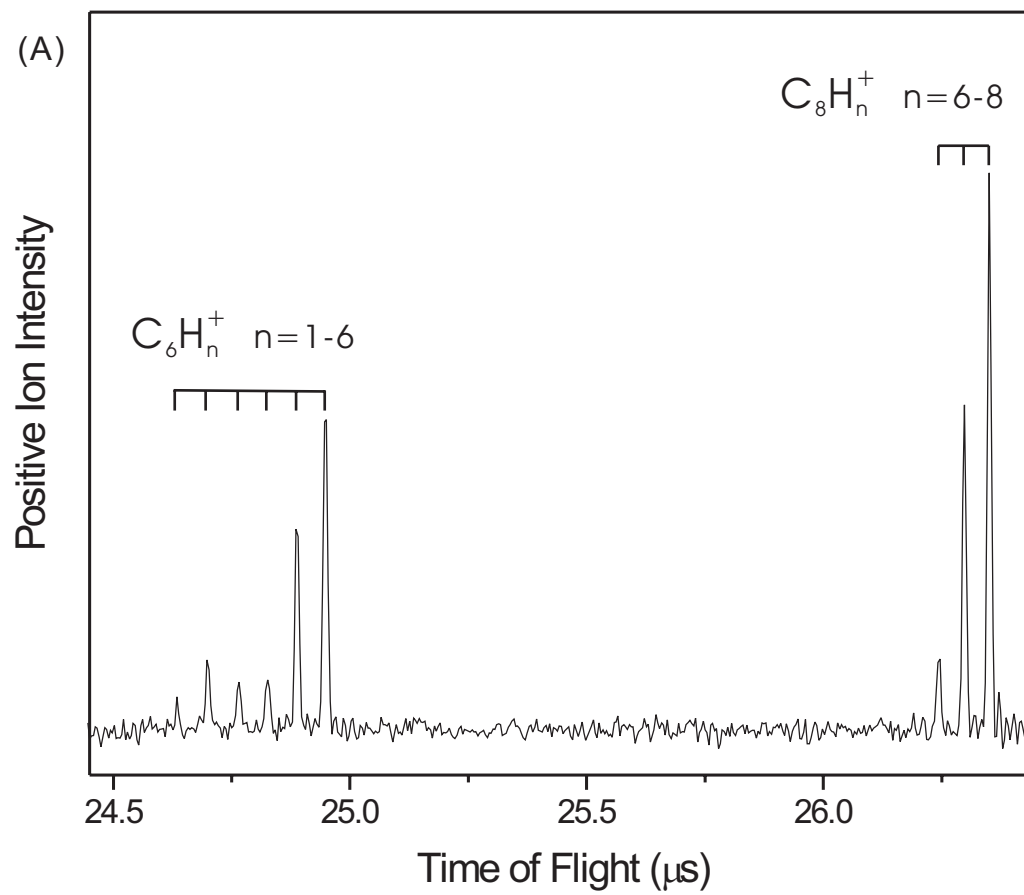


Figure 8.3

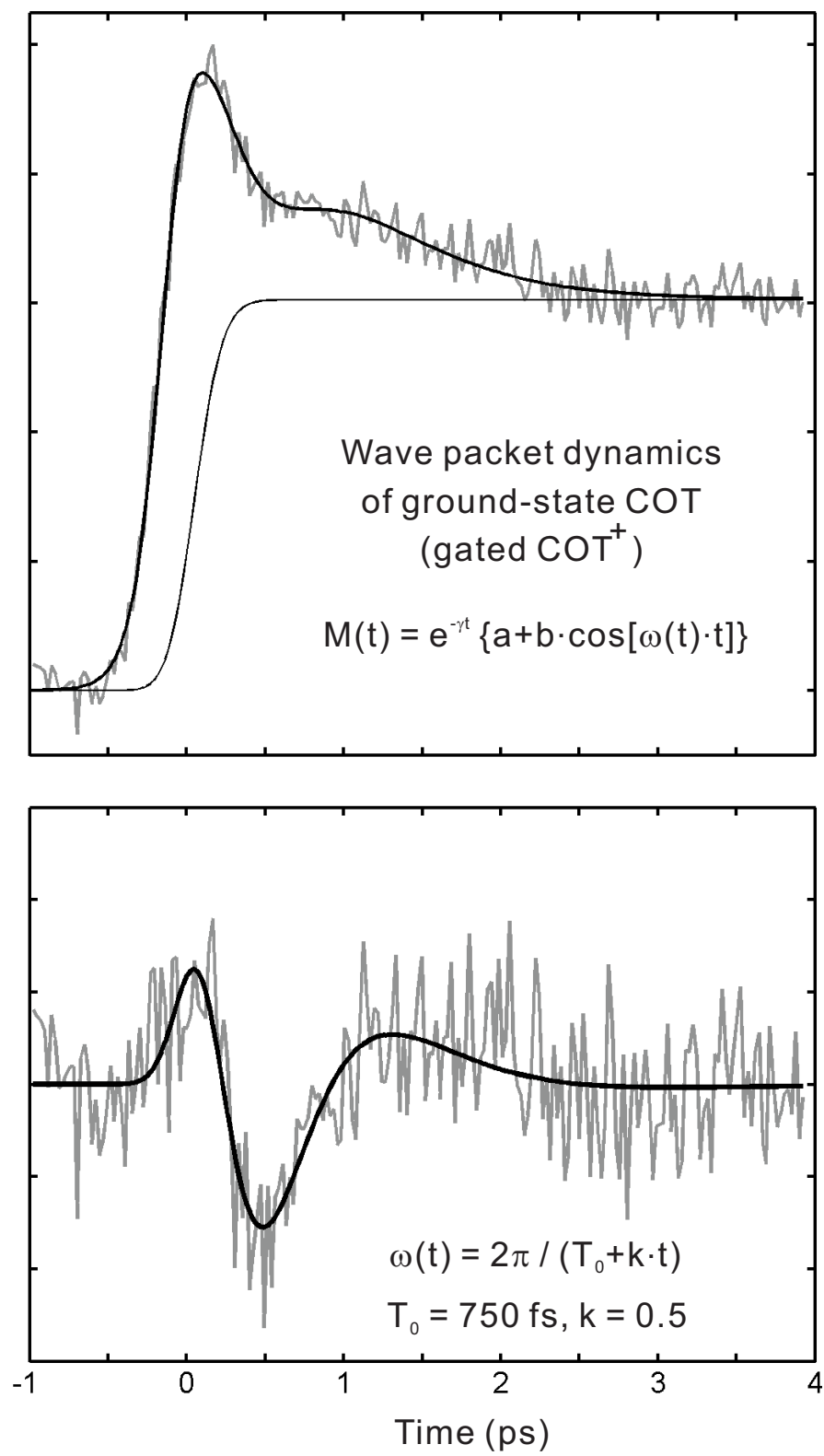


Figure 8.4

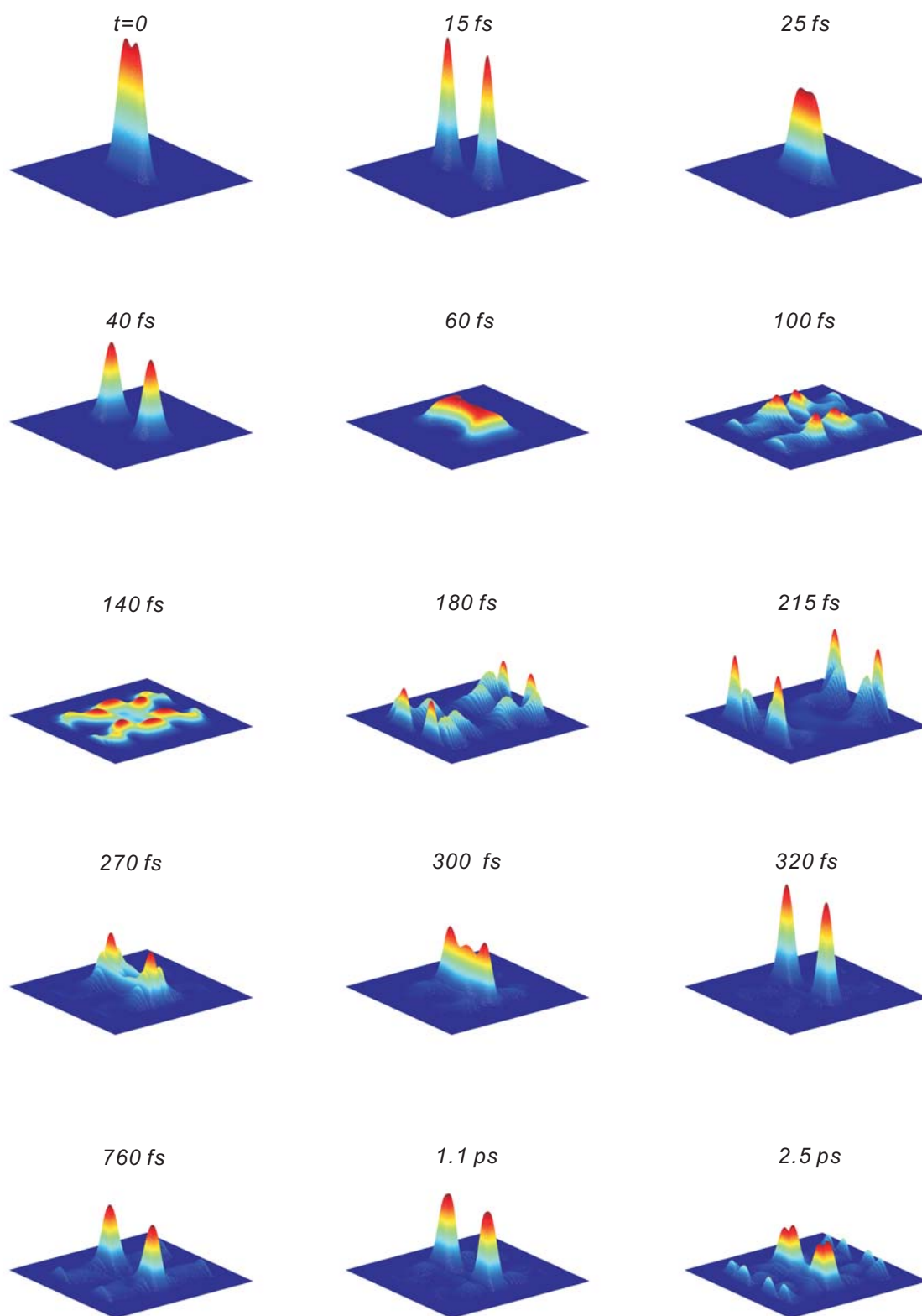


Figure 8.6

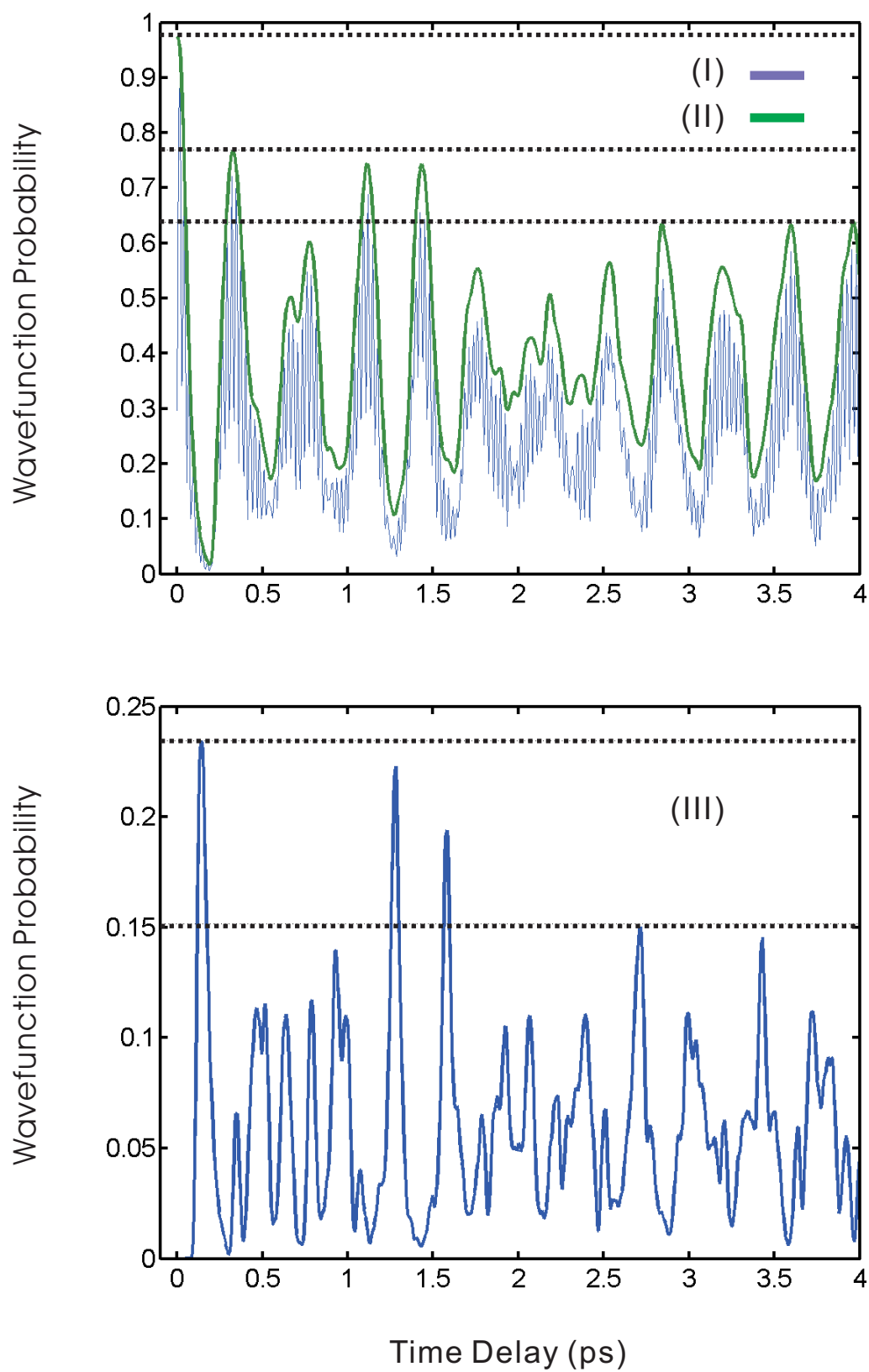


Figure 8.7

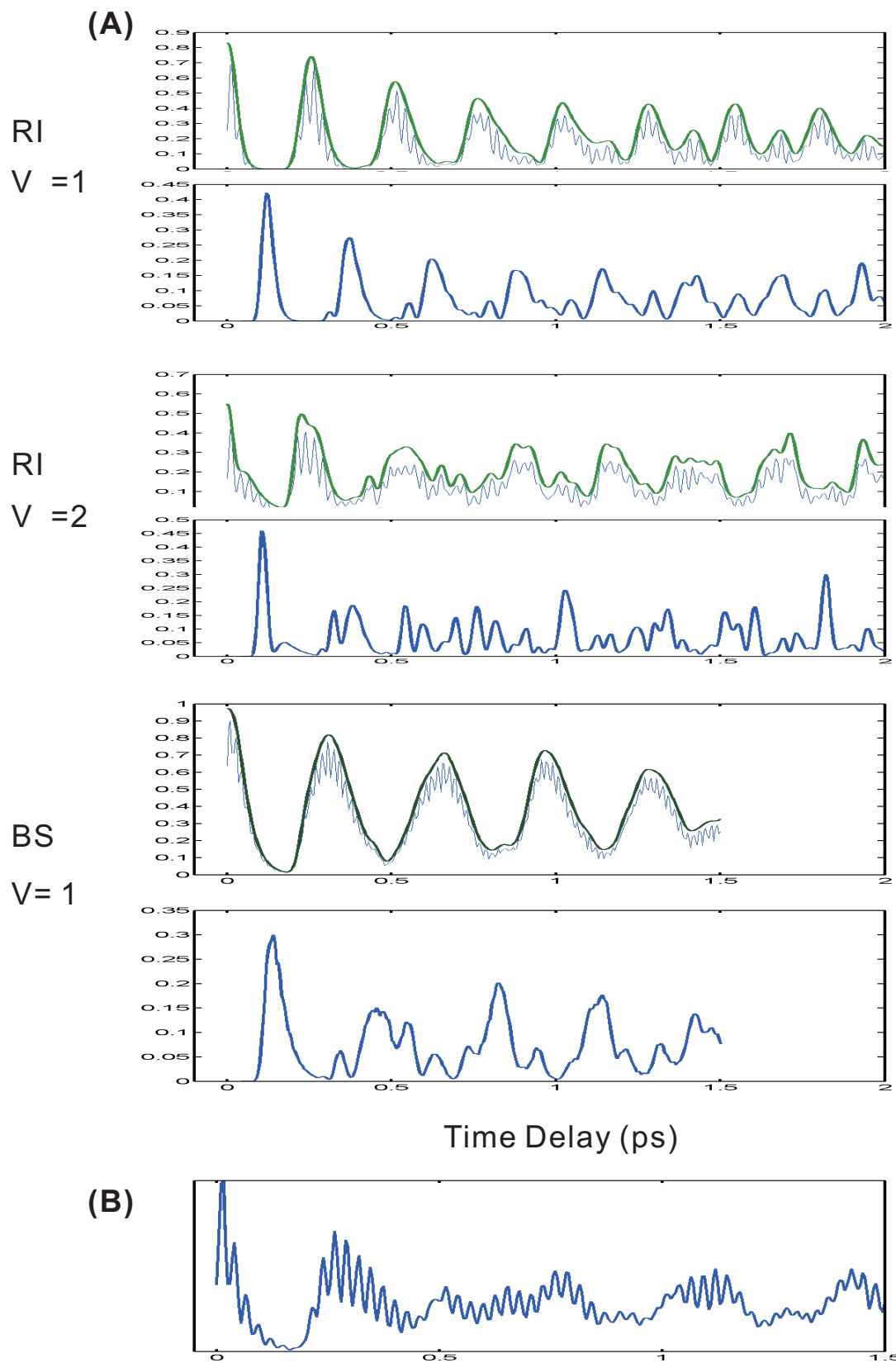


Figure 8.8

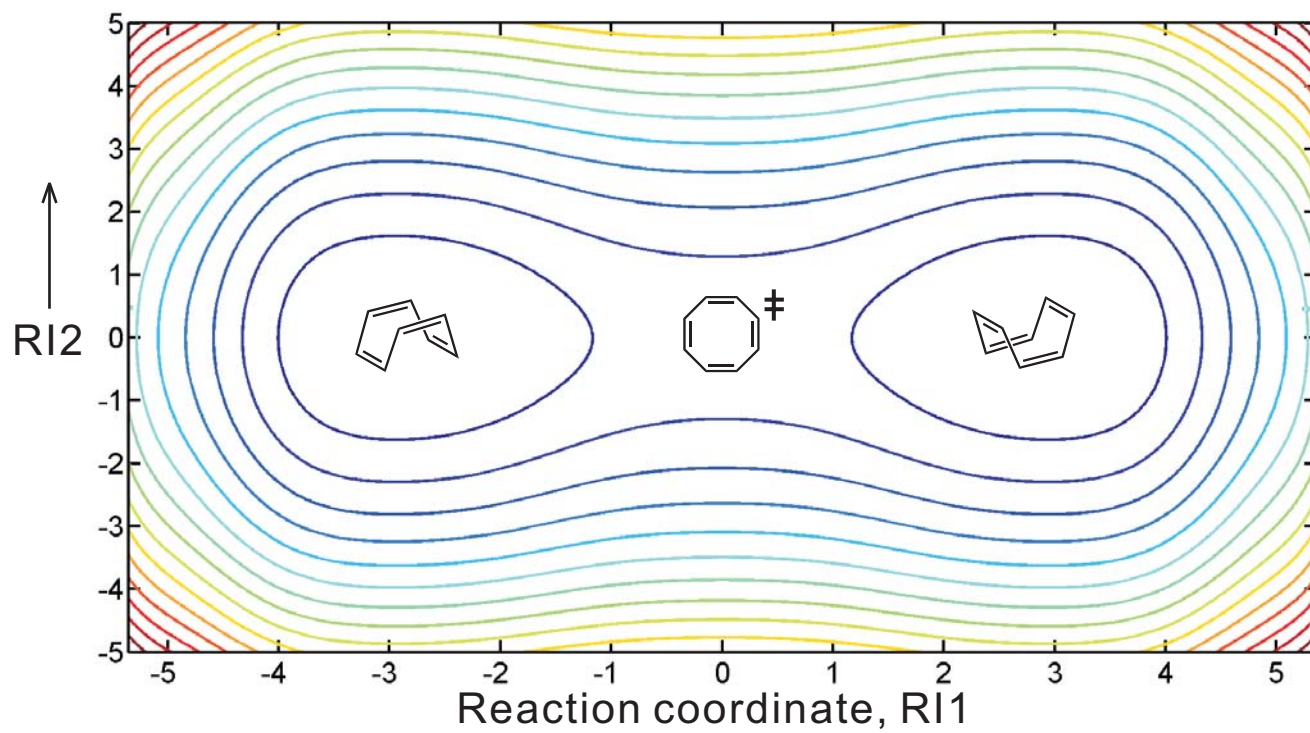


Figure 8.9

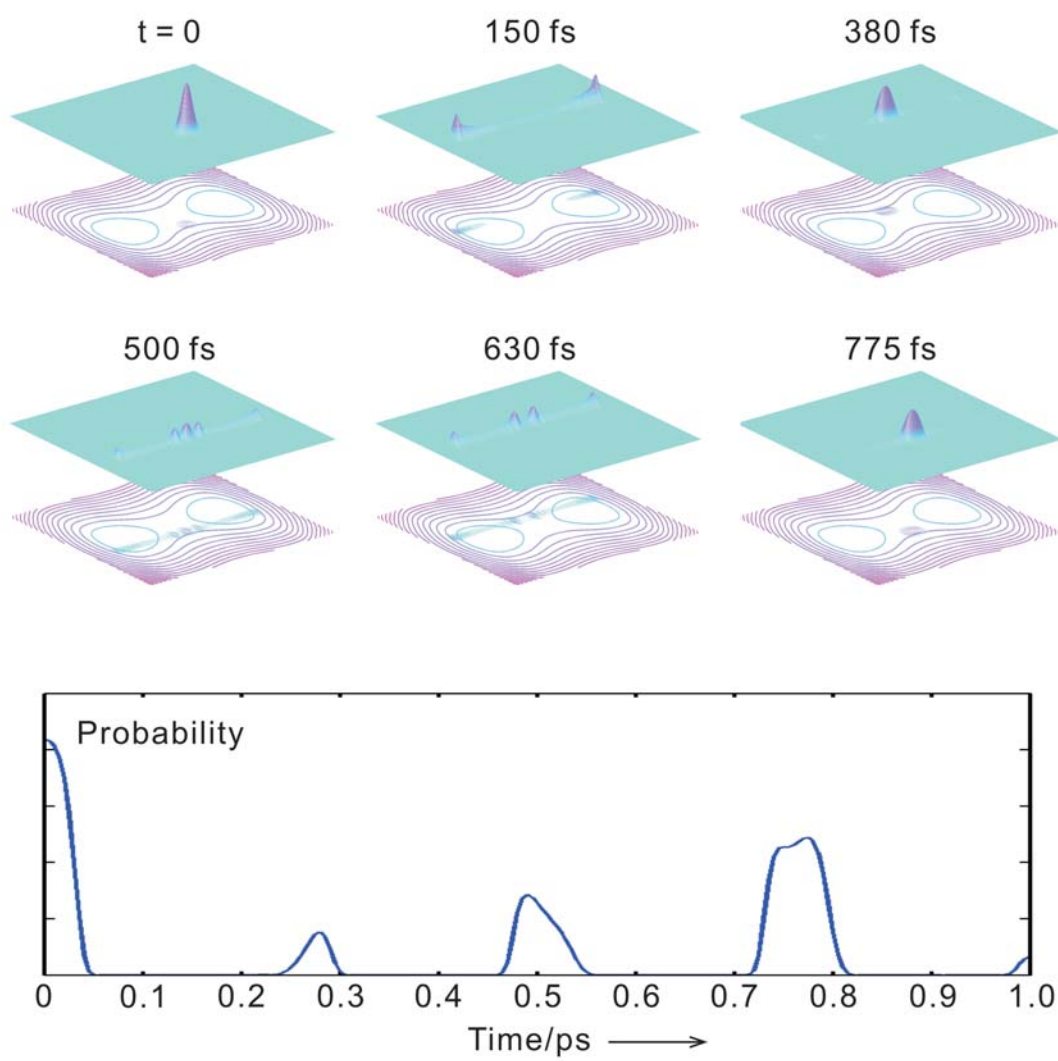


Figure 8.10

Figure Captions

Figure 8.1

Schematic illustration of the experiment, with calculated potential energies for COT^- , COT and COT^+ as a function of the bending angle (α). The electron detachment by the pump pulse and ionization by the probe pulse are indicated by upward arrows. The initial wave packet prepared by the pump pulse is indicated by a Gaussian profile at the transition state of the ring inversion mode.

Figure 8.2

(A) Mass spectrum of negative ions produced by the electron impact source. Inset: High-resolution mass spectrum obtained by the linear reflectron mass spectrometer.

(B) Photoelectron spectrum of COT^- generated by irradiating 405 nm fs pulse. The dotted line indicates the onset position (1.1 eV) of the photoelectron spectrum obtained by Lineberger group.

Figure 8.3

(A) Positive ion mass spectrum generated by intercepting COT^- with the pump and probe pulses at 160 fs.

(B) Time-dependent mass spectra of the positive ions obtained at three different delay times (0, 160 fs and 5.6 ps), which displays the increment of the positive ion signals with respect to the reference at -1 ps [$I(t) - I_{t<0}$]. With the pump and probe pulses we always observe enhancement of fragment cations as well as the parent COT^+ at all positive delay

times. Thus, the enhanced COT^+ signal is due to generating neutral COT by the pump pulse at positive delay, rather than depleting the background COT^+ at negative delay. If COT^+ is dissociated by the pump pulse at negative delay, the fragment ion signal should appear as a dip in the difference spectrum. Note that the peak for COT^+ first increases and then decreases with time.

Figure 8.4

Femtosecond transients of COT^+ generated by the pump-probe scheme described in Fig 8.1. The measured transient is shown together with the theoretical fit of the indicated equation. The oscillatory feature ($a = 0$) is illustrated in the bottom panel (see text for detail). As noted in the figure, there is a small contribution at negative time because of the reverse “probe-pump” signal. This is clear in our analysis because the initial peak is a factor of two broader than our cross correlation.

Figure 8.5

Potential contours of the ring inversion (RI1) and bond shift (BS) coordinates. The geometries of the COT isomers corresponding to the energy landscape are indicated.

Figure 8.6

Quantum mechanical calculation of the wave packet propagation, which is prepared from the $v'' = 0$ state of COT^- . (See text for details.) The iteration was carried out using the time interval, $\Delta t = 0.1$ fs in order to prevent the accumulation of error. The 15 frames represent the wave packet evolution in the first picosecond, which illustrates the

dephasing and rephasing of the wave packet. Note that the initial wave packet prepared on the 2D-PES has a small dip since potential energy curve of COT^- is a double-well along the BS mode.

Figure 8.7

Simulated transient of the wave packet motion prepared from the $v'' = 0$ state of COT^- . Three different time-dependent plots were generated by locating the probe window (*i.e.* integrating the wavefunction probability) at (i) at D_{4h} , (ii) at D_{4h} with larger window and (iii) turning point.

Figure 8.8

(A) The simulated transients of the wave packet motion prepared from the vibrationally excited state of COT^- ($v'' = 1$ and 2 for the RI mode and $v'' = 1$ for the BS mode) with three different probe windows: (i) at D_{4h} , (ii) at D_{4h} with larger window, and (iii) turning. (B) The convoluted transients with different probe windows. The relative contribution of the excited states was determined by assuming the population of the COT^- follows the Boltzmann distribution at 500 K.

Figure 8.9

Top: Representation of the two coordinates of ring inversion. Middle: Two-dimensional representation of the electronic ground-state potential energy surface along RI1 and RI2. The contour is constructed by adding two one-dimensional curves.

Figure 8.10

Snap shots of wave packet evolution on the two-dimensional contour (RI1, RI2). Note that the wave packet returns to the initial position at 775 fs. The bottom panel shows the simulated molecular response function obtained by opening the probe window at the initial wave packet position.

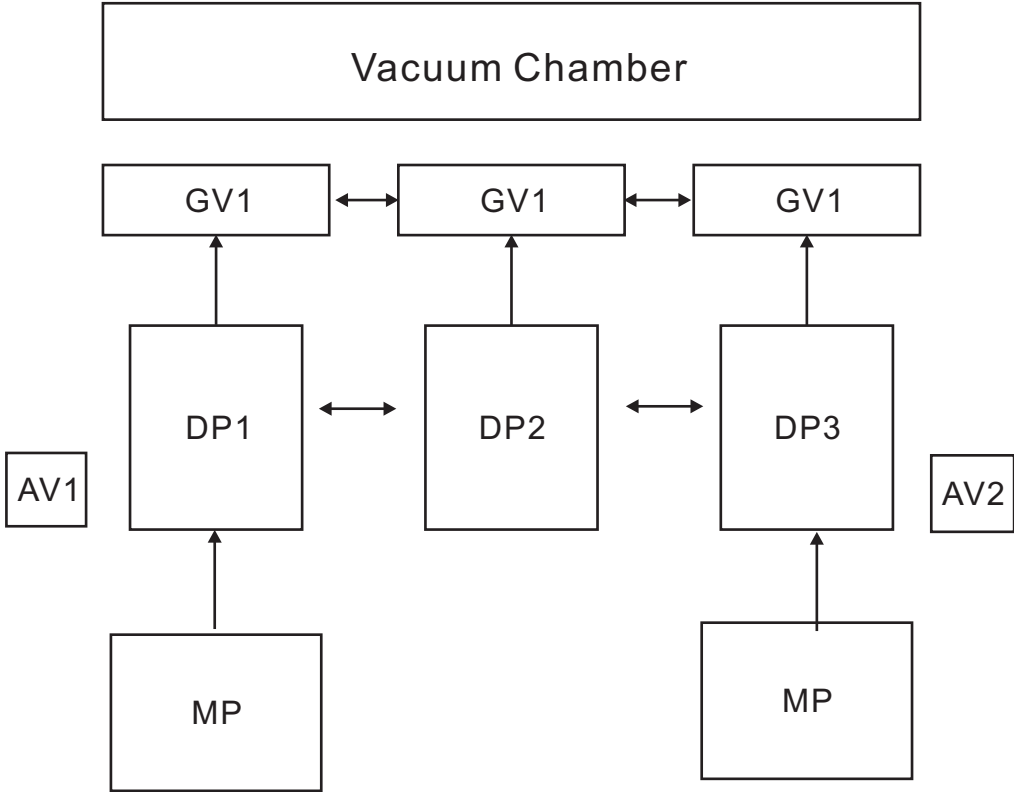
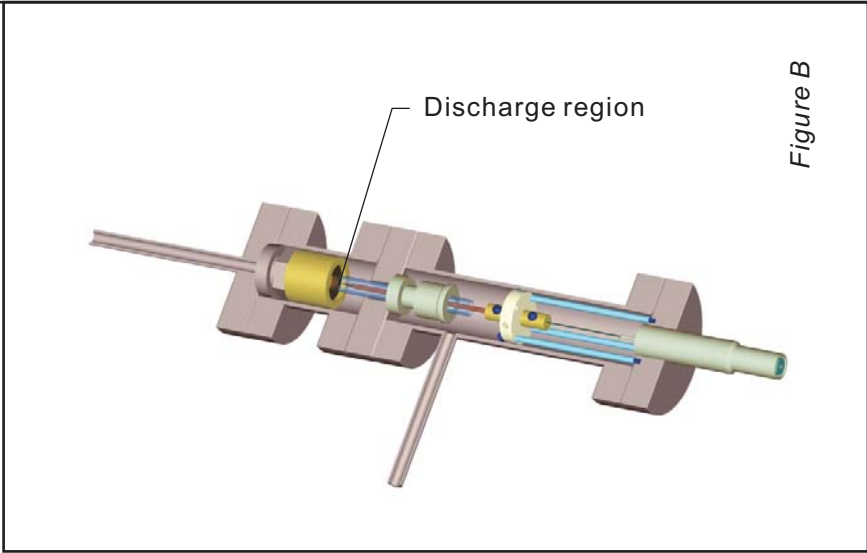
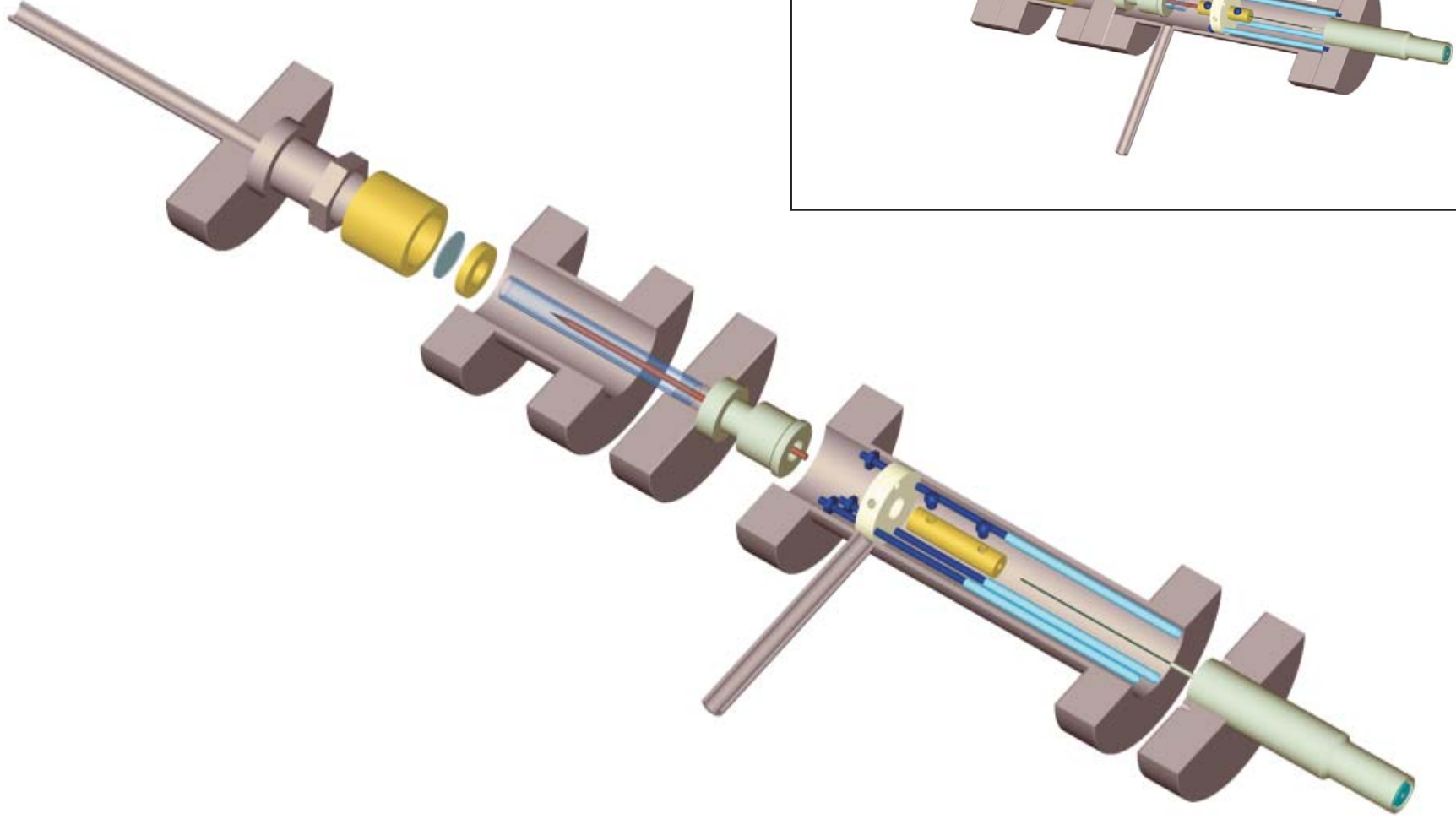


Figure A

Appendix B. Corona Discharge Source



Appendix C.

Parallelization Effect in the Magnetic Bottle Photoelectron Spectrometer

The gyroscopic motion of the electron in the non-uniform magnetic field can be decomposed into two simple motions: circular (spiral) motion induced by the Lorentz force and the linear vector orthogonal to the circular motion.

$$e \cdot v_{\perp} \cdot B = m \frac{v_{\perp}^2}{r} \quad (\text{C.1})$$

$$L = m \cdot r \cdot v_{\perp} \quad (\text{C.2})$$

$$L = m \cdot \frac{m \cdot v_{\perp}}{e \cdot B} \cdot v_{\perp} = \frac{m^2 \cdot v_{\perp}^2}{e \cdot B} = \frac{m^2 (v \cdot \sin \theta)^2}{e \cdot B} \quad (\text{C.3})$$

The adiabatic variation of the magnetic field suffices the conservation of angular momentum:

$$L_i = L_f \quad (\text{C.4})$$

$$\frac{m^2 (v \cdot \sin \theta_i)^2}{e B_i} = \frac{m^2 (v \cdot \sin \theta_f)^2}{e B_f} \quad (\text{C.5})$$

$$\frac{\sin \theta_f}{\sin \theta_i} = \sqrt{\frac{B_f}{B_i}} \quad (\text{C.6})$$

For electrons emitted in solid angle of 2π steradian, θ_i ranges from 0 to 90° . Therefore, the maximum angle in the weak magnetic field becomes

$$\theta_{f,\max} = \sin^{-1} \sqrt{\frac{B_f}{B_i}} \quad (\text{C.7})$$

Magnetic Mirror Effect in the Magnetic Bottle Photoelectron Spectrometer

For electron that emitted toward the strong magnetic field, electrons bounce back toward the weak magnetic field. Under the adiabatic variation of the magnetic field, the following relation holds:

$$\sin \theta_f = \sin \theta_i \cdot \sqrt{\frac{B_f}{B_i}} \quad (\text{C.8})$$